UNIVERSITY OF LIVERPOOL

Department of Chemistry

Functional Microporous Carbons for Energy and Environmental Applications

Thesis submitted in accordance with the requirements of the University of Liverpool for the degree of Doctor of Philosophy

Jet-Sing M. Lee

June 2018

ABSTRACT OF THESIS

Functional Microporous Carbons for Energy and Environmental Applications

By

Jet-Sing M. Lee

Department of Chemistry, University of Liverpool

Supervisor: Prof. Andrew I. Cooper FRS

Porous materials are useful in various energy and environmental applications such as electrodes for supercapacitive energy storage, gas storage media, and sieves for the removal of toxic chemicals. Carbonaceous materials derived from biomass have been widely used, but the properties obtained are variable as a result of the variation in the composition of the biomass often used to form them. The use of functionalised polymers as carbonisation precursors allows greater control of the structure and heteroatom doping in the resulting carbon. This thesis examines the largely unexplored route of carbonising porous organic networks, which have multiple advantages over non-porous and pre-carbonised analogues. This yields interesting properties for energy and gas storage applications. Only a few papers had been published in this area prior to the start of this PhD project, and there were no reports of carbonisation for the polymer networks investigated here. Thus, a range of methods and conditions were tested to prepare materials with excellent performance in their respective applications. This project also tackles the problem of toxic mercury contamination in water by developing microporous materials synthesised from low-cost, waste by-products.

Acknowledgements

First, I would like to express my sincere gratitude to my advisor, Prof. Andrew I. Cooper, for giving me the opportunity to undertake research in his group. His immense knowledge, flexibility, and near limitless resources has allowed me to have an enjoyable PhD experience, much academic freedom, and opportunity to develop my own ideas. I believe my mind-set has matured significantly since joining his group and I could not have imagined having a better mentor.

Many thanks go to Michael Briggs and Tom Hasell who have both been a huge support throughout my PhD. Their early support with paper writing, refining ideas, and general advice have been especially helpful. My sincere gratitude goes to Tzu-Ho "Henry" Wu for teaching me early electrochemistry and supercapacitor measurements out of his own free will. I believe if it was not for this, my PhD would have proceeded quite differently. I would like to thank Prof. Chi-Chang Hu, who I met through Henry, for giving me formal electrochemistry training with his group in Taiwan. I hope our collaboration can continue for many years to come.

Special thanks go to numerous people: Aled Roberts for sharing ideas about carbonisation, Ben Alston for sharing advice on electrochemistry, Rob Clowes for training in the use of numerous instruments and exceptional gas sorption advice, and Baltasar Bonillo Fernández for synthetic organic chemistry discussions and as the lone lab buddy on a Friday night. I am also grateful to Duncan Woods who helped me submit my thesis whilst I was away in Japan on a JSPS Fellowship.

I extend my great appreciation to Meera Vijayaraghavan for the high pressure CO_2 photos, Douglas Parker for the metal uptake experiments, Karl Dawson for HR-TEM, David Hesp, Thomas Whittles, and NEXUS Newcastle University for XPS measurements, and the technicians at the University of Liverpool for elemental analysis. I would also like to thank past and present members of the Cooper group for the discussions, events, and lively atmosphere throughout the four years. Being in a large and diverse group is not only intellectually stimulating but also enjoyable and fun.

Lastly, I would like to thank my parents, Ming Kiu "Connie" Lee and Man Hong "Simon" Lee, for their continuous support and encouragement throughout my life. They are the most selfless people I know, making many sacrifices for the sake of family and for the future of their children. I hope with this PhD, I can make them proud of their son and the future ahead of me.

Table of Contents

List of Publications

The thesis is based on the following papers, which are referred to by their Roman numerals below.

I. J.-S. M. Lee, A. I. Cooper, in preparation.
"**Advances in Conjugated Microporous Polymers**"

II. J.-S. M. Lee, T.-H. Wu, B. Alston, M. E. Briggs, T. Hasell, C.-C. Hu, A. I. Cooper, *J. Mater. Chem. A* **2016**, *4*, 7665–7673.
"**Porosity-Engineered Carbons for Supercapacitive Energy Storage Using Conjugated Microporous Polymer Precursors**"

III. J.-S. M. Lee, M. E. Briggs, C.-C. Hu, A. I. Cooper, *Nano Energy* **2018**, *46*, 277–289.
"**Controlling Electric Double-Layer Capacitance and Pseudocapacitance in Heteroatom-Doped Carbons from Hypercrosslinked Polymers**"

IV. J.-S. M. Lee, M. E. Briggs, T. Hasell, A. I. Cooper, *Adv. Mater.* **2016**, *28*, 9804–9810.
"**Hyperporous Carbons from Hypercrosslinked Polymers**"

V. J.-S. M. Lee, D. J. Parker, A. I. Cooper, T. Hasell, *J. Mater. Chem. A* **2017**, *5*, 18603–18609.
"**High Surface Area Sulfur-Doped Microporous Carbons from Inverse Vulcanised Polymers**"

My Contribution to these Papers

Paper I: I participated in the planning of the review. I wrote the initial manuscript and contributed to the continued drafts.

Paper II: I participated in the planning of the study, performed all the experimental work, characterisation except for SEM, Raman spectroscopy, XPS, and HR-TEM, and carried out the data analysis. I wrote the initial manuscript, contributed to the continued drafts, and formulated the initial response to referees.

Paper III: I participated in the planning of the study, performed all the experimental work, characterisation except for XPS and ICP-OES, and carried out the data analysis. I wrote the initial manuscript, contributed to the continued drafts, and formulated the response to referees.

Paper VI: I participated in the planning of the study, performed all the experimental work except for the high pressure swelling experiment, performed characterisation except for Raman spectroscopy, XPS, and ICP-OES, and carried out the data analysis. I wrote the initial manuscript, contributed to the continued drafts, and formulated the initial response to referees.

Paper V: I participated in the planning of the study, performed all the experimental work except for the ion uptake experiments, characterisation except for HR-TEM, and carried out the data analysis. I wrote the initial manuscript, contributed to the continued drafts, and formulated the initial response to referees.

Also Published

Y.-i. Fujiwara, J.-S. M. Lee, M. Tsujimoto, K. Kongpatpanich, T. Pila, K.-i. Iimura, N. Tobori, S. Kitagawa, S. Horike, *Chem. Mater*. **2018**, *30*, 1830–1834.
"**Fabrication of ε-Fe_2N Catalytic Sites in Porous Carbons Derived from an Iron−Triazolate Crystal**"

N. Hernández-Ibáñez, J.-S. M. Lee, J. Iniesta, V. M. Leguey, M. E. Briggs, A. I. Cooper, E. Madrid, F. Marken, *J. Electroanal. Chem.* **2018**, *819*, 46–50.
"**pH Effects on Molecular Hydrogen Storage in Porous Organic Cages Deposited onto Platinum Electrodes**"

T. Banerjee, T. Bennett, K. Butler, T. Easun, M. Eddaoudi, R. Forgan, L. Gagliardi, C. Hendon, M. Jorge, C. Lamberti, J.-S. M. Lee, K. Leus, J. Li, W. Lin, M. Ranocchiari, N. Rosi, J. G. Santaclara, S. Shevlin, K. Svane, V. Ting, M. v. d. Veen, P. V. D. Voort, A. Walsh, D. Woods, O. M. Yaghi, G. Zhu, *Faraday Discuss*. **2017**, *201*, 87–99.
"**Electronic, Magnetic and Photophysical Properties of MOFs and COFs: General Discussion**"

M. Addicoat, T. Bennett, K. Chapman, D. Denysenko, M. Dincă, H. Doan, T. L. Easun, M. Eddaoudi, O. Farha, L. Gagliardi, F. Haase, A. H. Farmahini, C. Hendon, M. Jorge, S. Kitagawa, C. Lamberti, J.-S. M. Lee, K. Leus, J. Li, W. Lin, X. Liu, G. Lloyd, C. Lu, S. Ma, J. P. H Perez, M. Ranocchiari, N. Rosi, I. Stassen, V. Ting, M. V. D.Veen, P. V. D. Voort, C. M. L. Vande Velde, D. Volkmer, S. Vornholt, A. Walsh, O. M. Yaghi, *Faraday Discuss*. **2017**, *201*, 175–194.
"**New Directions in Gas Sorption and Separation with MOFs: General Discussion**"

M. Addicoat, K. Butler, O. Farha, L. Gagliardi, A. H. Farmahini, C. Hendon, M. Jorge, S. Kitagawa, C. Lamberti, J.-S. M. Lee, J. Li, X. Liu, S. Moggach, M. Ranocchiari, L. Sarkisov, S. Shevlin, I. Stassen, K. Svane, D. Volkmer, A. Walsh, C. Wilmer, O. M. Yaghi, *Faraday Discuss*. **2017**, *201*, 233–245.
"**MOFs Modelling and Theory: General Discussion**"

F. Carraro, K. Chapman, Z. Chen, M. Dincă, T. Easun, M. Eddaoudi, O. Farha, R. Forgan, L. Gagliardi, F. Haase, D. Harris, S. Kitagawa, J. Knichal, C. Lamberti, J.-S. M. Lee, K. Leus, J. Li, W. Lin, G. Lloyd, J. R. Long, C. Lu, S. Ma, L. McHugh, J. P. H. Perez, M. Ranocchiari, N. Rosi, M. Rosseinsky, M. R. Ryder, V. Ting, M. v. d. Veen, P. V. D. Voort, D. Volkmer, A. Walsh, D. Woods, O. M. Yaghi, *Faraday Discuss*. **2017**, *201*, 369–394.
"**Catalysis in MOFs: General Discussion**"

C. B. Meier, R. S. Sprick, A. Monti, P. Guiglion, J.-S. M. Lee, M. A. Zwijnenburg, A. I. Cooper, *Polymer* **2017**, *126*, 283–290.
"**Structure-Property Relationships for Covalent Triazine-Based Frameworks: The Effect of Spacer Length on Photocatalytic Hydrogen Evolution from Water**"

A. D. Roberts, J.-S. M. Lee, S. Y. Wong, X. Li, H. Zhang, *J. Mater. Chem. A* **2017**, *5*, 2811–2820.
"**Nitrogen-Rich Activated Carbon Monoliths *via* Ice-Templating with High CO_2 and H_2 Adsorption Capacities**"

G. Wilson, M. Trusler, J. Yao, J.-S. M. Lee, R. Graham, N. Mac Dowell, R. Cuellar-Franca, G. Dowson, P. Fennell, P. Styring, J. Gibbins, M. Mazzotti, S. Brandani, C. Müller, R. Hubble, *Faraday Discuss*. **2016**, *192*, 561–579.
"**End Use and Disposal of CO_2 – Storage or Utilisation?: General Discussion**"

B. Smit, P.Styring, G. Wilson, G. Rochelle, F. Donat, J. Yao, M. Trusler, C. Adjiman, S. Lyth, J.-S. M. Lee, T. Hills, P. Brandl, M. Gazzani, R. Cuellar-Franca, P. Fennell, D. Sutter, M. Bui, C. Scholes, G. Dowson, J. Gibbins, L. Joss, G. Maitland, S. Brandani, P.Garcia-Gutierrez, Y. Zhang, C. Müller, G. Jackson, R. Ocone, L. Joos, R. Bell, R. Graham, *Faraday Discuss*. **2016**, *192*, 493–509.
"**Modelling – from Molecules to Mega-Scale: General Discussion**"

B. Smit, R. Graham, P. Styring, J. Yao, P. Clough, J.-S. M. Lee, N. MacDowell, S. Lyth, G. Rochelle, T. Hills, G. Wilson, C. Petit, J. Kemper, R. Cuellar-Franca, G. Dowson, M. Gazzani, P. Fennell, D. Sutter, C. Scholes, A. Azapagic, R. Bell, J. Gibbins, M. Mazzotti, G. Maitland, S. Brandani, R. Ocone, M. Mota-Martinez, M. Dunstan, P. Liang, R. Anantharaman, L. Joss, J. Stolaroff, *Faraday Discuss*. **2016**, *192*, 303–335
"**CCS – A Technology for the Future: General Discussion**"

J.-S. M. Lee, G. Rochelle, P. Styring, P. Fennell, G. Wilson, M. Trusler, P. Clough, J. Blamey, M. Dunstan, N. MacDowell, S.Lyth, J. Yao, T. Hills, M. Gazzani, P. Brandl, R. Anantharaman, S. Brandani, J. Stolaroff, M. Mazzotti, G. Maitland, C. Müller, G. Dowson, J. Gibbins, R. Ocone, K. Sedransk Campbell, M. Erans, L. Zheng, D. Sutter, A. Armutlulu, B. Smit, *Faraday Discuss*. **2016**, *192*, 125–151.
"**CCS – A Technology for Now: General Discussion**"

R. Dryfe, G. Z. Chen, D. Bayer, M. Jonsson-Niedziolka, R. McCreery, J. Macpherson, H. Abruna, Y. Gogotsi, C.-C. Hu, F. Beguin, L. Hardwick, J. Foord, M. Duca, E. Howe, K. Holt, M. Alvarez-Guerra, P. R. Unwin, T. Rabbow, M. Shaffer, J.-S. M. Lee, E. Frackowiak, F. Qiu, B. Dyatkin, P. A. Ash, K. Stevenson, D. Guldi, P. Bergonzo, *Faraday Discuss.* **2014**, *172*, 117–137.
"**The Many Faces of Carbon in Electrochemistry: General Discussion**"

M. Giardiello, T. McDonald, J.-S. M. Lee, A. D. Roberts, A. Owen, S. P. Rannard, *Green Chem.* **2013**, *15*, 1590–1599.
"**Reactions of Hydrophobic Organic Nanoparticle Mixtures in Water: Nanoparticle-on-Nanoparticle Oxidative Dye Bleaching**"

Abbreviations

Δ	heating temperature
ε_r	electrolyte dielectric constant
ε_0	permittivity of vacuum
η	coulombic efficiency
θ	fractional occupancy
1-D	one-dimensional
2-D	two-dimensional
3-D	three-dimensional
A	area
A_g	adsorbate gas
A_s	surface area
a_0	effective size of counter-ions
a_s	specific surface area
b	pore radius
Ben	benzene
BET	Brunauer–Emmett–Teller
bipy	2,2'-bipyridine
C	capacitance
CCS	carbon capture and storage
CDC	carbide-derived carbon
C_{DL}	double-layer capacitance
C_e	equilibrium concentration
C_H	Helmholtz capacitance
C_G	Gouy-Chapmann capacitance
c	BET constant
c_i	charge of ion
CMP	conjugated microporous polymer
CNT	carbon nanotube
COD	1,5-cyclooctadiene
COF	covalent organic framework
C_P	pseudocapacitance
C_s	specific capacitance
C_{s2}	specific capacitance in two-electrode configuration
C_{sc}	specific capacitance from Galvanostatic charge-discharge

C_{sc2}	specific capacitance from Galvanostatic charge-discharge in two-electrode configuration
C_{si}	specific capacitance from impedance spectroscopy
C_{si2}	specific capacitance from impedance spectroscopy in two-electrode configuration
C_{sv}	specific capacitance from cyclic voltammetry
C_{sv2}	specific capacitance from cyclic voltammetry in two-electrode configuration
$C_{S,T,M}$	maximum total specific capacitance
CTF	covalent triazine framework
CV	cyclic voltammetry
D	disordered
d	diameter
DC	direct current
DCPD	dicyclopentadiene
DCE	dichloroethane
DCM	dichloromethane
DFT	density functional theory
DI	deionised
DIB	1,3-diisopropenyl benzene
DMF	*N*,*N*-dimethylformamide
DOE	Department of Energy
E	potential
E_1	heat of adsorption for first layer
EDCC	electric double-cylinder capacitor
EDL	electrical double-layer
EDLC	electric double-layer capacitance
E_H	potential *vs.* standard hydrogen electrode
EIS	electrochemical impedance spectroscopy
E_L	heat of adsorption for second layer and beyond
EOF	element organic framework
ESR	equivalent series resistance
EWCC	electric wire-in-cylinder capacitor
f	frequency
FDA	formaldehyde dimethyl acetal
FE-SEM	field emission scanning electron microscope
G	graphitic
GCD	galvanostatic charge-discharge
HCP	hypercrosslinked polymer

HCP-Ani	hypercrosslinked aniline
HCP-Ben	hypercrosslinked benzene
HCP-Py	hypercrosslinked pyrrole
HCP-Th	hypercrosslinked thiophene
I	current
I	molar ionic strength
ICP	inductively coupled plasma
ICP-OES	inductively coupled plasma optical emission spectrometry
ICP-MS	inductively coupled plasma mass spectrometry
IEA	International Energy Agency
IHP	inner Helmholtz plane
IPCC	Intergovernmental Panel on Climate Change
iR	internal resistance
IUPAC	International Union of Pure and Applied Chemistry
K	equilibrium rate constant
K	adsorption parameter
k_a	adsorption rate constant
k_d	desorption rate constant
m	mass
MOF	metal-organic framework
M_w	weight-average molecular weight
N_A	Avagadro's number
NL-DFT	non-local density functional theory
NMP	*N*-methyl-2-pyrrolidone
OHP	outer Helmholtz plane
P	pressure
PAF	porous aromatic framework
PAni	polyaniline
PC	pseudocapacitance
PEDOT	poly(3,4-ethylenedioxythiophene)
PIM	polymer of intrinsic microporosity
POP	porous organic polymer
PPN	porous polymer network
PPy	polypyrrole
PSD	pore size distribution
PTh	polythiophene

PVDF	polyvinylidene fluoride
Py	pyrrole
q	charge
q_A	mg adsorbate per g absorbent
q_a	anodic charge
q_c	cathodic charge
q_H	Helmholtz charge
q_G	Gouy-Chapmann charge
q_S	solution charge
Q_{sat}	maximum capacity
q_T	total charge
r_a	rate of adsorption
r_d	rate of desorption
s	scan rate
SA_{BET}	BET surface area
SA_{Lang}	Langmuir surface area
S-DCPD	sulfur-dicyclopentadiene
SEM	scanning electron microscopy
SHE	standard hydrogen electrode
t	time
t_c	charge time
t_d	discharge time
TEM	transmission electron microscopy
TGA	thermogravimetric analysis
Th	thiophene
UNEP	United Nations Environment Programme
V	potential
v	scan rate
V_{max}	maximum voltage
V_{tot}	total pore volume
XPS	X-ray photoelectron spectroscopy
Z	real part of resistance
Z”	imaginary part of resistance
z_i	charge of ion
ZIF	zeolitic imidazolate framework

List of Schemes

List of Figures

List of Tables

Chapter 1

Introduction and Background Literature

Some of the contents in this chapter are taken from **Paper I**.

J.-S. M. Lee, A. I. Cooper, "Advances in Conjugated Microporous Polymers", in preparation.

1.1 Introduction

In the opening lecture at the 2003 Energy and Nanotechnology Conference, Nobel laureate Prof. Richard E. Smalley presented a list entitled "Humanity's Top Ten Problems for Next 50 Years".[1] Within this list, energy was given top priority because the availability of cheap, sustainable energy is seen as key to solving the rest of the problems:

1. Energy
2. Water
3. Food
4. Environment
5. Poverty
6. Terrorism and war
7. Disease
8. Education
9. Democracy
10. Population

Followed by energy is the issue of water scarcity and pollution. Billions of people live without reliable access to clean water for personal and agricultural use: a rising problem with an ever increasing population. Our planet has an extensive supply of water, however, most of it contains salts and other hazardous chemicals. The United Nations Environment Programme (UNEP) has implemented various strategies to tackle environmental issues, which is 4th on the priority list with human activity thought to be responsible for substantial increases in greenhouse gas emissions.

Research into energy storage,[2] hydrogen storage,[3] carbon dioxide capture,[4] and removal of pollutants in water[5] is interesting due to the potential societal impact associated with any significant advancement. Over the last few decades, porous materials have showed excellent performances for these applications, driving development in this field and making it an important area of research.

1.2 Porosity

Porosity is not a new concept: it has existed in nature for millennia in structures such as rocks, biological tissues, and charcoal. The word "porous" is typically used to describe a material that possesses permanent voids that may be interconnected and are permeable to liquids or gases; that is, it typically

has a practical connotation. In modern times, porous materials are of major importance in many fields of science and technology and there has been an explosion in the number of new advanced porous functional materials that has been developed. The International Union of Pure and Applied Chemistry (IUPAC) classified porous materials into three types based on the diameter (d) of their pore sizes: microporous (d < 2 nm), mesoporous (2 nm < d < 50 nm), and macroporous (d > 50 nm).[6] Porous materials with a significant proportion of pores spanning more than one of these classes in an ordered manner can be defined as having hierarchical porosity.[7] The term nanoporous has also been used for materials with pores of 100 nm or smaller.[8] Ultramicroporous can be used for pores smaller than 0.7 nm.[9] High amounts of these small pores leads to high surface areas, that is, the amount of surface which is accessible to liquids, gases, charges, etc. This is commonly quantified by a Brunauer–Emmett–Teller (BET) surface area value (detailed discussion in Chapter 2).

The diameter and distribution of the pore size significantly impacts what application a material will be suitable for. For instance, in macroporous materials, guest molecule diffusion is governed by molecule-molecule interactions, whilst interaction of the guest to pore wall is negligible. By contrast, microporous materials are entirely driven by molecule-pore wall interactions by influence of the forces exerted from the walls, and leads the motion of "absorbed" molecules with no unabsorbed "bulk" fluid region.[10] This is important for the storage of gases[3, 4] and also storage of electrical charges in supercapacitors,[11] which favours high surface areas. Mesoporous materials are driven by a combination of molecule-molecule and molecule-pore wall interactions. A level of mesoporosity in the material can be preferable as it aids diffusion of guests to the micropore regions, and therefore affords faster kinetics.[11]

1.3 Porous Materials

Many different synthetic porous materials have been produced for a variety of applications. Zeolites are inorganic porous frameworks that are a staple product in society, having a large global market with uses that range from detergents to the removal of radioactive particles from nuclear waste. Another class of inorganic-containing porous solids are hybrid metal-organic frameworks (MOFs — also known as porous coordination polymers, PCPs).[12] MOFs are extended, typically crystalline frameworks constructed with metal ions or clusters which provide directional bonding to the organic ligand through the preferential geometry and coordination number of the metal, and forms voids within the structure giving rise to porosity. Zeolites and MOFs both incorporate metals, but there is also a range of purely organic porous materials. In porous MOFs, metal ions coordinated to organic linkers, which are usually aromatic, imparts both rigidity and directionality. Porous organic materials also need to be rigid and somewhat directional to prevent collapse of the porous structure. This can be achieved by careful choice

of the molecular building blocks, and not all porous materials need to be extended networks. For example, porous organic cages are discrete porous molecules where the molecular cage is synthesised first and then assembled in the solid state in a separate step.[13] They are a unique class of solution-processable molecular materials where porosity arises via interconnection of intrinsic cavities, which can be modified by changing the solid state packing of the cage molecules. Polymers of intrinsic microporosity (PIMs) are a rare example of porosity in a one-dimensional polymer, achieved through inefficient packing of the twisted polymer backbone.[14] A wide range of porous organic polymer (POP) networks have been introduced over the past two decades (**Figure 1.1**), such as crystalline covalent organic frameworks (COFs)[15-17] and various amorphous networks, such as hypercrosslinked polymers (HCPs),[18, 19, 20] covalent triazine frameworks (CTFs),[21-23] porous aromatic frameworks (PAFs),[24-26] and conjugated microporous polymers (CMPs).[27-29]

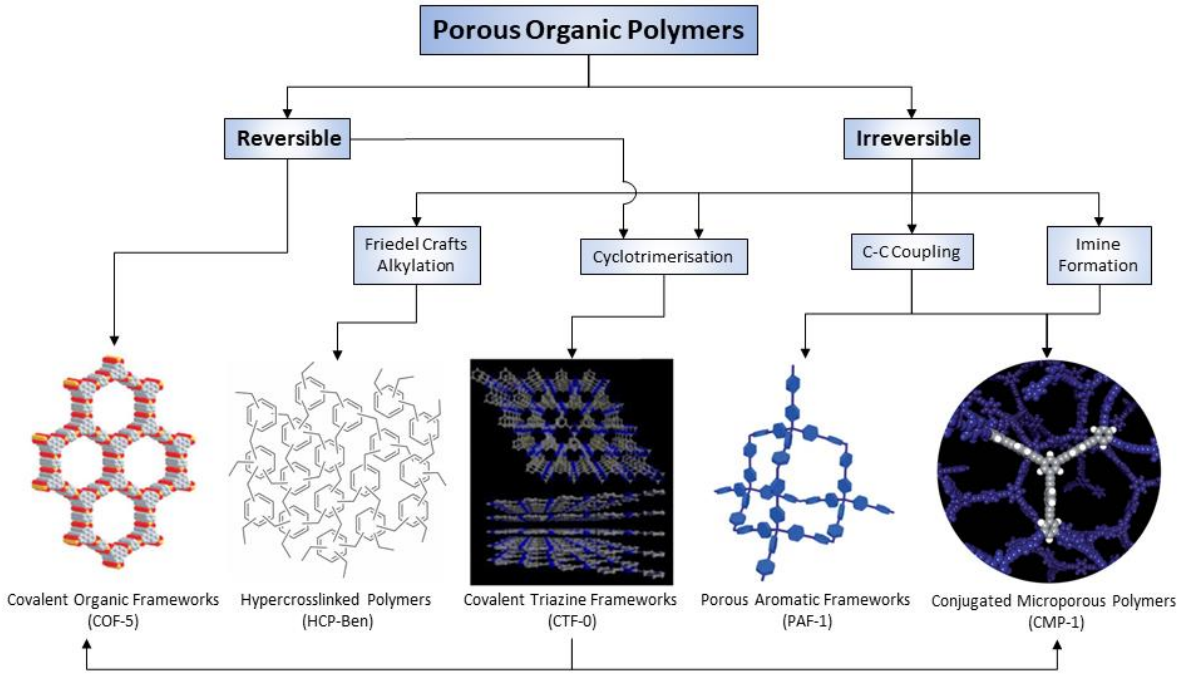

Figure 1.1 Types of porous organic polymers and their coupling chemistries. Porous polymers from left to right: covalent organic frameworks (COFs),[15] hypercrosslinked polymers (HCPs),[19] covalent triazine frameworks (CTFs),[23] porous aromatic frameworks (PAFs),[26] and conjugated microporous polymers (CMPs).[27]

1.4 Porous Organic Polymers

Each sub-class of material generally favours particular network formation reactions, with the exception of COFs and a small number of CTFs, which are synthesised under thermodynamic control using

reversible reaction conditions; the other POP networks usually yield amorphous materials (**Figure 1.2**). While these various materials are structurally different, they are united by their high porosity, construction from lightweight elements, and their strong, covalently bonded two- or three-dimensional (2-D, 3-D) structures.

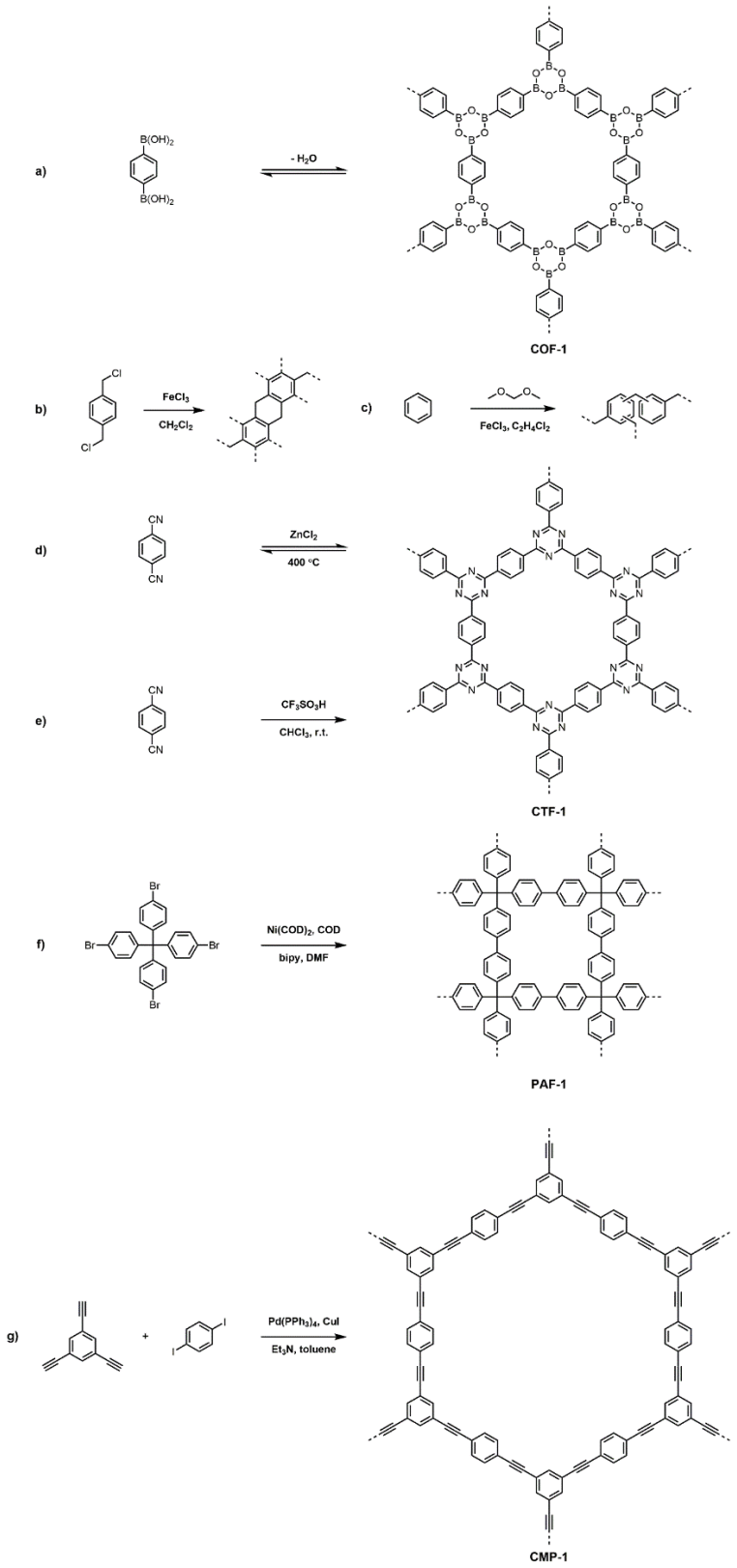

Figure 1.2 Example synthesis schemes of each type of porous organic polymer network: (a) COFs (b) HCPs (via self-polycondensation), (c) HCPs (via use of external crosslinker), (d) crystalline CTFs, (e) amorphous CTFs, (f) PAFs, (g) CMPs.

Davankov *et al.* reported the first example of HCPs back in 1969.[30] These materials became industrially important with Purolite International Ltd. (UK, USA) producing them as Hypersol-Macronet®, 25 years later. HCPs were developed initially using linear polystyrene as a precursor with different crosslinkers such as divinylbenzene,[31] *p*-xylylene dichloride,[32] and chloromethyl methyl ether,[33] yielding BET surface areas of up to 1106 $m^2 g^{-1}$.[34] Each crosslinker can react with two phenyl rings via a Friedel-Crafts alkylation reaction to form a network.[35] The extent of the crosslinking in the HCP prevents complete collapse upon solvent removal and provides permanent porosity. HCPs are known to swell in most liquids and gases as this relives the strain in the system. Very recently, HCPs with BET surface areas up to 3002 $m^2 g^{-1}$ was reported through an approach that gives layered, exfoliable materials.[36] An important paper was published in 1992 by Webster *et al.*, who reported a HCP that used similar bonding principles to later CMPs, although in that case, the conjugation between the aromatic rings was broken by a carbinol centre.[37]

In 2002, McKeown and Budd reported the first PIMs.[38] The porous properties of these 1-D polymers are derived from their high rigidity, combined with a randomly contorted backbone, therefore disrupting the ability of the polymer to pack efficiently. The porosity observed in PIMs arises from the poor packing of the linear polymer chain in contrast to the permanent porosity of 3-D polymer networks; this allows PIMs to be solution processable, which is still a rare feature among porous solids.

COFs were first reported in 2005 by Yaghi *et al*., and they are built through using reversible covalent bonds, which allows the formation of an ordered, crystalline porous framework:[15] COFs are effectively the covalent analogue of MOFs. There has been rapid growth in the field of COFs since their initial discovery, with a number of new synthetic routes developed. BET surface areas as high as 4210 $m^2 g^{-1}$ were reported for COF-103,[39] although this material most likely has relatively low stability. Certain imine-based COFs could also be thought of as crystalline CMPs since the imine linkages provide conjugation. (Likewise, CMPs are, in a sense, amorphous COFs.) Very recently, an aldol derived COF/CMP was published.[40]

CMPs are unique among porous materials because they possess extended π-conjugation throughout the porous 3-D network. PAFs,[24-26] which are closely related to CMPs and formed using similar coupling chemistries to CMPs, do not possess extended π-conjugation. Porous polymer networks (PPNs) is another term used to describe PAFs.[41] Element-organic frameworks (EOFs) are non-carbon core-containing (*e.g.*, Si, Sn, Bi, Sb, P) analogues to PAFs and are formed using organo-metallic coupling routes.[42] CTFs might also be considered to be a sub-class of CMPs as they are microporous and have extended π-conjugation, though they were developed separately and their formation chemistry is quite different.[21]

1.4.1 Conjugated Microporous Polymers

CMPs are 3-D semiconducting polymers in which rigid aromatic groups are linked together, either directly or via double or triple bonds to afford π-conjugated microporous networks.[28] Conjugation arises from the alternation of single and double-/triple-bonds throughout the extended network, which offers useful electronic properties to the porous polymer. In almost all examples so far, covalent bonds in CMPs are formed irreversibly and the polymerisation proceeds via a kinetic route; hence all CMPs (excluding any imine COFs) are amorphous.

In 2007, Jiang *et al*. reported the synthesis of microporous poly(aryleneethynylene) networks; these were the first examples of what have since become known as CMPs.[27] Since their discovery, many scientists across the world have contributed to the field of CMP chemistry, leading to a strong growth in their rate of discovery and the identification of new functions (**Figure 1.3**).

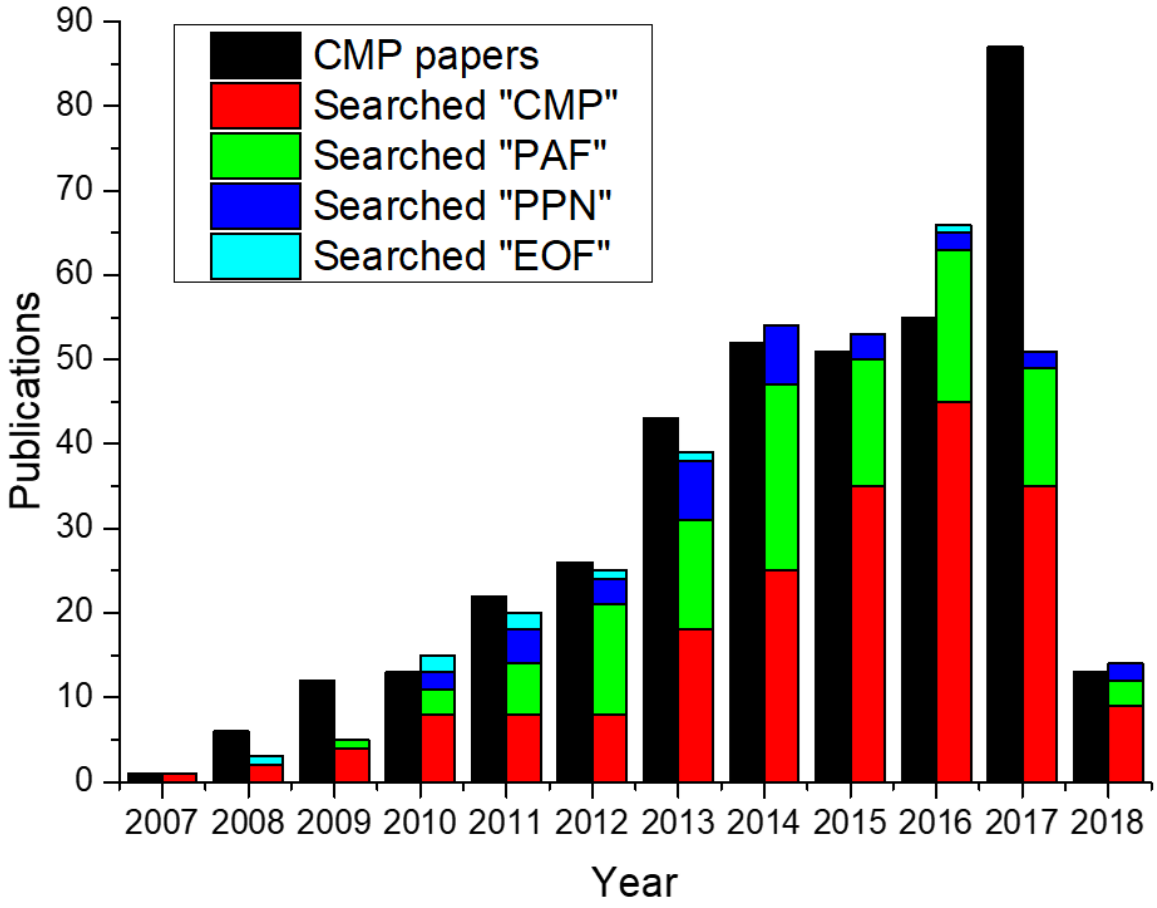

Figure 1.3 Publications of CMPs on a yearly basis and related materials since discovery (assessed 1st March 2018). "CMP papers" (black) was found from CMP-specific papers which cite key classic CMP literature. Searched terms are from the title search with Web of Science, Thomson Reuters database.

The growth is benefitted by the ability of CMPs to be used across a diverse range of applications, stemming from the combination of extended conjugation, high porosity, ease of tunability, and their good chemical and thermal stabilities. In fact, CMPs have been reported for gas storage and separations,[27, 43] encapsulation of chemicals,[44] heterogeneous catalysis,[45] photocatalysis,[46] light emittance,[47, 48] chemosensing,[49, 50, 51] energy storage,[52, 53, 54] and water splitting.[55] The large variety of molecular building blocks available or easily accessible allows the control of functionality and structure of CMPs, which is important in accessing particular properties.

1.4.1.1 Synthesis of CMPs

CMP networks can be formed through the reaction of two or more different monomers or, in some cases, by homocoupling of a single monomer. The most common approach so far is the combination of a "core" of C_3 symmetry with a "linker" with C_2 symmetry, as put forward in the first CMPs.[27] Homocoupling of trifunctional or polyfunctional monomers can also result in 3-D porous networks, with the most well-known example being PAFs, which are formed from the homocoupling of tetrafunctional, tetrahedral monomers.[24] 2-D monomers afford 3-D polymers due to free rotation of the core-linker bond during reaction and subsequent reactions may not form the complete 2-D pore. The absence of reversibility in these kinetic couplings mean the structure cannot be corrected to a more thermodynamically stable product (*c.f.*, COFs). Many 3-D building blocks, such as the tetrahedral monomers used in PAFs, cannot be used to synthesise CMPs because the tetrahedral node breaks the extended π-conjugation. There are, however, strategies to avoid this, such as the use of spirobifluorene linkers.[56]

The scope to customise CMPs is near limitless. There are extensive options for tuning pore structure, morphology, and optoelectronics by varying the monomer geometry, or by incorporating different heteroatoms or metals; it is also possible to post-synthetically modify.[57] A wide range of reactive coupling groups has been used for CMP synthesis including halogens, boronic acids, alkynes, alkenes, nitriles, amine, aldehydes, and activated phenol-substituted aromatic monomers. The various reaction methods used to synthesise CMPs are summarised in **Figure 1.4**. The most common CMP forming reactions are Sonogashira-Hagihara coupling,[27, 58-60] Suzuki-Miyaura coupling,[61] and Yamamoto coupling.[24, 62] Other reactions that have been reported for the synthesis of CMPs include the Heck reaction,[50, 51] cyclotrimerisation,[21-23, 63, 64] phenazine ring fusion,[52] Schiff-base reaction,[65, 66] alkyne metathesis,[67] oxidative coupling,[60, 68] electropolymerisation,[54, 69, 70] and by hypercrosslinking linear polymers.[71]

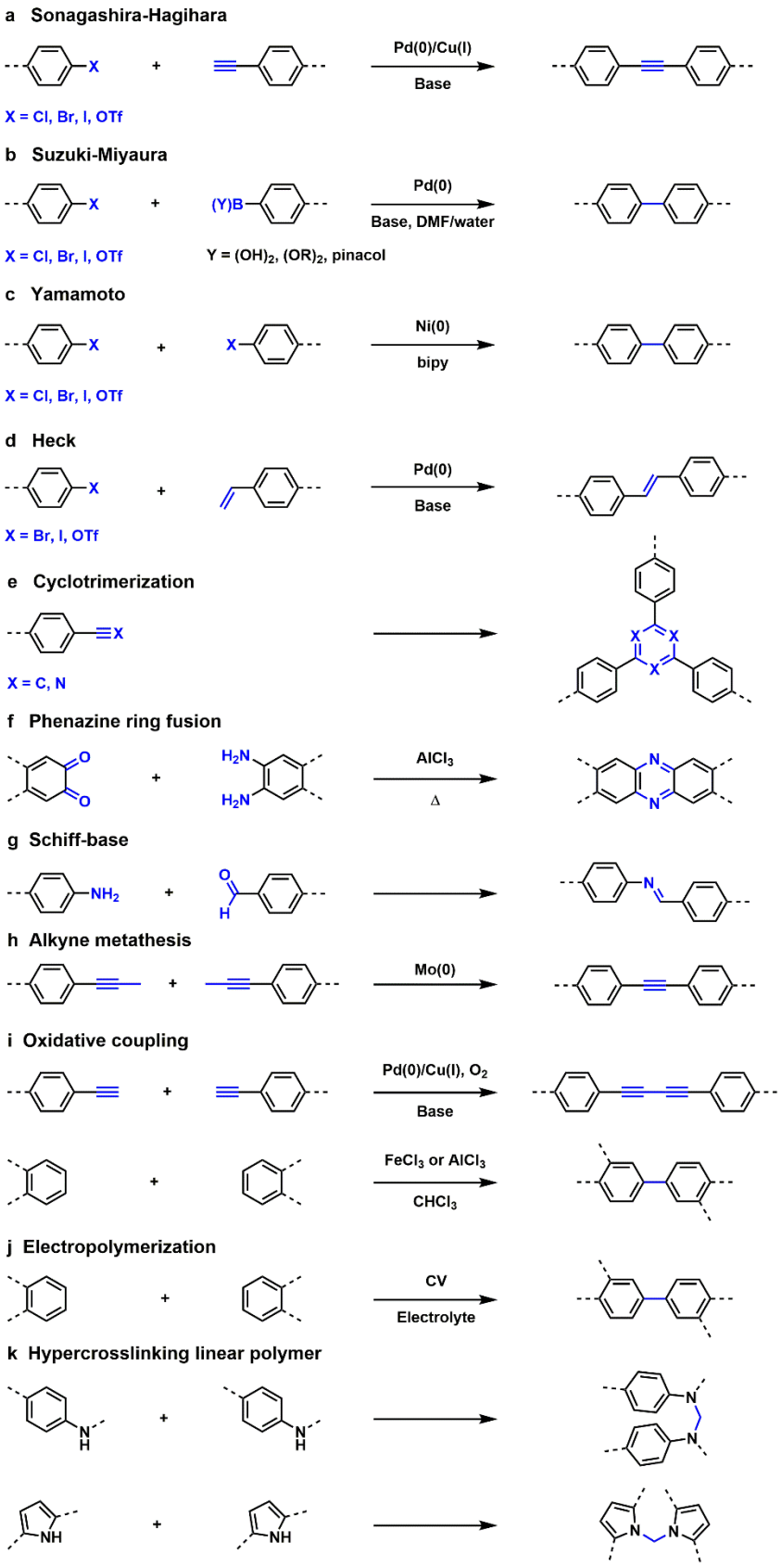

Figure 1.4 Reaction schemes for the synthesis of CMPs. (a) Sonogashira-Hagihara; (b) Suzuki-Miyaura; (c) Yamamoto; (d) Heck; (e) cyclotrimerization; (f) phenazine ring fusion; (g) Schiff-base; (h) alkyne metathesis; (i) oxidative coupling; (j) electropolymerisation; and (k) hypercrosslinking linear polymers.

Sonogashira-Hagihara Coupling

The first CMPs were prepared using Sonogashira-Hagihara cross-coupling.[27] The reaction mechanism is complex,[72] involving many steps common to metal-coupling reactions, *i.e.*, oxidative addition, transmetallation, isomerisation, and reductive elimination (**Figure 1.5**).[73] This reaction couples an aryl halide with an alkyne-containing monomer using a palladium catalyst and a copper co-catalyst, often tetrakis-(triphenylphosphine)palladium(0) and copper(I) iodide, in the presence of an amine base (**Figure 1.4a**). The presence of a Cu co-catalyst is used in the coupling due to the improved reactivity,[74] although copper-free Sonogashira-Hagihara reactions are also known.[58] Four solvents were studied initially for this chemistry: *N*,*N*-dimethylformamide (DMF), 1,4-dioxane, tetrahydrofuran (THF), and toluene. In general, it was found that CMPs formed in DMF possess the highest surface areas and levels of microporosity.[59] Alkynes can also be homocoupled using similar reaction conditions.[60] This can be a drawback in cross-couplings reactions as incomplete oxygen removal can afford homocoupled alkynes within the polymer, which can change its properties.[75] Hence, rigorous anaerobic and anhydrous conditions should be employed.

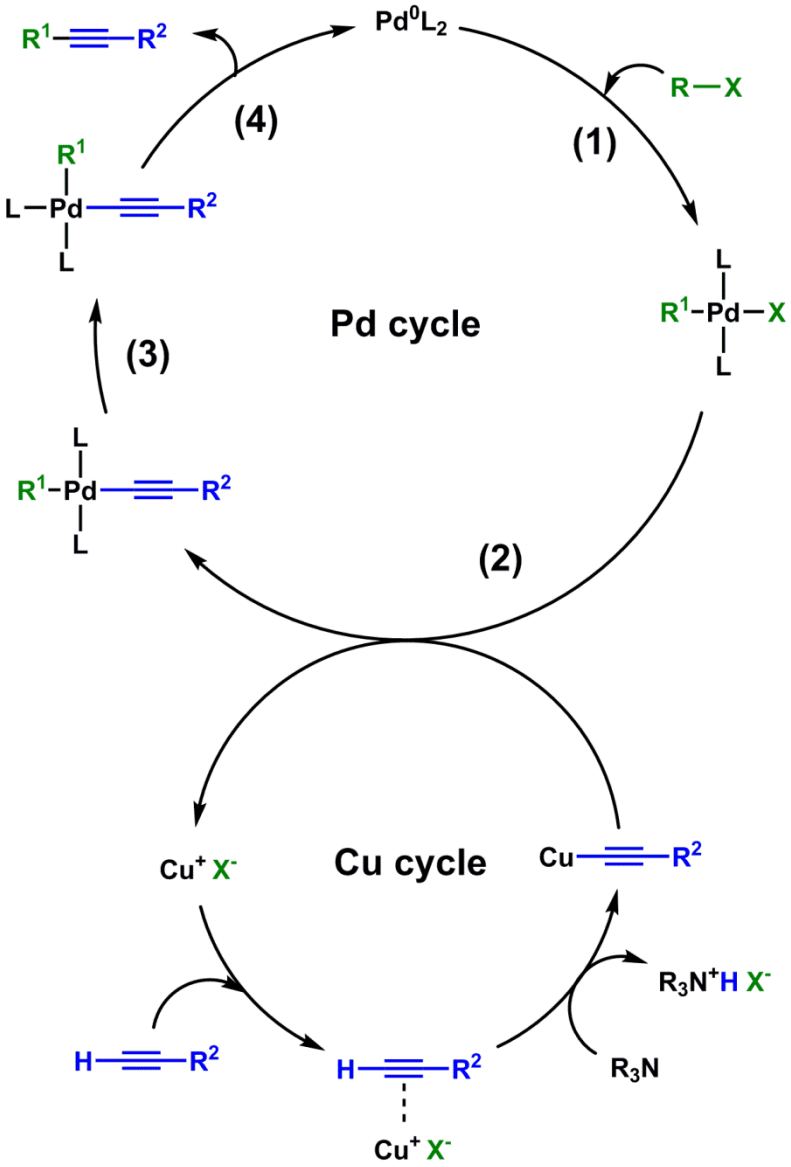

Figure 1.5 Supposed catalytic cycle for the Sonogashira-Hagihara reaction. (1) Oxidative addition. (2) Transmetallation. (3) *trans-cis* Isomerisation. (4) Reductive elimination. Green compound represents the aryl halide and blue compound represents the alkyne.

Suzuki-Miyaura Coupling

The Suzuki-Miyaura cross-coupling reaction was discovered as a method to form aryl bonds in 1979.[76] The reaction uses a Pd(0) catalyst such as tetrakis(triphenylphosphine)-palladium(0) to couple an aryl-boron monomer with an aryl halide or sulfonate in the presence of a mild base, such as K_2CO_3 in a water/organic solvent mixture (**Figure 1.4b**).[61] This method has various advantageous including commercial availability of boronic acids, wide functional group compatibility, and mild reaction conditions, and hence the potential for scale-up. A downside is that Suzuki-Miyaura cross-couplings are oxygen sensitive, which can lead to homocoupling and deboronated by-products. To tackle this, the reaction should be thoroughly degassed.[77]

Yamamoto Coupling

In Yamamoto coupling, aryl halides with at least 3 reactive sites are coupled together with bis(cyclooctadiene)nickel(0) ($Ni(COD)_2$) (**Figure 1.4c**).[62] The advantage of this coupling method is that only a single, halogen-functionalized monomer is required, leading to a simple reaction procedure. There are a diverse range of aryl halide monomers therefore many porous networks can be designed through Yamamoto couplings, including CMPs.[47, 62] When using 3-D monomers, Yamamoto reactions can induce very inefficient packing to give remarkably high surface areas and porosity, as observed with PAF-1 and its analogues.[24] A drawback of this route that may preclude scale up is the high sensitivity to water, which often necessitates reactions to be done in glovebox.

Heck Coupling

The Heck reaction, also known as the Mizoroki-Heck reaction, forms a C=C bond between two units by coupling an unsaturated halide with a primary alkene in the presence of a Pd catalyst and base. CMPs produced from this reaction commonly use tetrakis-(triphenylphosphine)palladium(0), K_2CO_3 base, and DMF solvent under anaerobic conditions (**Figure 1.4d**).[50] Suzuki-Heck one-pot reactions have also been utilised to form similar CMP products.[51] The method utilises aryl halides as the monomer where some are substituted with an alkene functional group via Suzuki-Miyaura, and then reacts with the remaining aryl halide via Heck reaction.

Cyclotrimerisation Reactions

Cyclotrimerisations typically form 6-membered aromatic rings from either three alkyne or three nitrile containing monomers to form benzene or C_3N_3, *s*-triazine rings, respectively. The use of disubstituted alkynes or nitriles results in an extended network (**Figure 1.4e**).[63] Cyclotrimerisations using nitrile containing monomers can be carried out under ionothermal conditions in molten $ZnCl_2$ at temperatures of over 400 °C.[21, 23, 64] However, such harsh conditions rules out the use of all but the most stable monomers and a degree of carbonisation can occur. The use of Brønsted acid catalysed trimerisations was also developed, which allows the reaction to proceed at room temperature or at modest temperature under microwave heating.[22] This method uses trifluoromethanesulfonic acid with $CHCl_3$ as the solvent, or it could occur by microwave synthesis without the use of any solvent. Microwave-assisted reactions allow much shorter reaction times to tens of minutes at microwave outputs of 120–460 W. A recent report allowed the formation of triazines through a low-temperature polycondensation approach.[78]

Phenazine Ring Fusion

Ladder-type polymers have been produced since 1966 via phenazine ring fusions.[79] The reaction links aryl *o*-diamines and aryl *o*-diketones at temperatures of 250 °C in specific, high-boiling solvents, such

as *N*,*N*-dimethylacetamide, hexamethylphosphoramide, and 116% polyphosphoric acid. More recently, phenazine ring fusion has been used to produce Aza-CMPs.[52] The reported method uses C_2 + C_6 monomers to create a 3-D ladder CMP network in the presence of $AlCl_3$ at high temperatures (300–500 °C) in an evacuated ampule (**Figure 1.4f**). Recently, a mild solvothermal method was developed to prepare Aza-CMPs by refluxing the monomers in a 1:4 mixture of dioxane and acetic acid.[80]

Schiff-Base Condensations

Schiff-base reactions have been used to synthesise both CMPs and imine-based COFs.[16] The reaction is metal free, reducing cost and avoids any trace metals residues in the CMP networks. The reaction forms an imine bond from amine and aldehyde-functionalised monomers (**Figure 1.4g**).[65] A benefit of Schiff-base chemistry is that the products are N-rich, which is advantageous for applications such as selective CO_2 adsorption.[66]

Alkyne Metathesis

In 1968, Bailey *et al*. reported the first alkyne metathesis reaction using catalytic tungsten oxide on silica at 350 °C.[81] The method was used to produce CMPs using a Mo(VI) based catalyst in $CHCl_3$ at mild temperatures (**Figure 1.4h**).[67] Although the reaction is reversible, to date CMP produced by this method have only been reported to be semi-crystalline. This reaction is different to homocoupling terminal alkynes in that only one alkyne group remains in the product, rather than a diyne, between the two linked monomers.

Oxidative coupling

Terminal alkynes can be coupled together using Sonogashira-Hagihara conditions (Pd(II)/Cu(I), Et_3N, solvent) in presence of O_2 (**Figure 1.4i**).[60] In addition, CMPs can be produced by oxidative Scholl reactions of electron-rich aromatics using a Lewis acid catalyst, commonly $FeCl_3$ or $AlCl_3$ in $CHCl_3$ solvent.[68] This method, which was first observed by Friedel and Crafts over a hundred years ago,[82] uses relatively inexpensive catalysts, which simplifies production and reduces costs.

Electropolymerisation

Oxidative coupling can also be performed via an electrochemical route using cyclic voltammetry (CV) to yield CMP films (**Figure 1.4j**).[54, 69, 70] Ma *et al.* reported the first synthesis of electropolymerised CMPs using a carbazole functionalised monomer with Bu_4NPF_6 in acetonitrile/CH_2Cl_2 electrolyte using multi-cycling CV in the potential range -0.8 to 0.97 V (*vs.* Ag/Ag^+) at a scan rate of 50 mV s^{-1}. The onset oxidative potential of the monomer is observed at 0.93 V, which was attributed to the oxidation of the carbazole groups. A new peak was later observed at a lower potential with increasing cycles due to the formation of dimeric carbazoles and growth of the CMP film on the electrode.[69]

Hypercrosslinking Linear Conjugated Polymers

An interesting approach to produce CMPs is hypercrosslinking of pre-formed linear conjugated polymers (**Figure 1.4k**). Reacting linear polyaniline or linear polypyrrole with a crosslinker resulted in BET surface areas as high as 632 and 732 $m^2 g^{-1}$, respectively.[71] The reaction method, choice of solvent, and choice of crosslinker greatly affected the resultant porosity.

1.4.2 Hypercrosslinked Polymers

HCPs are diverse, microporous polymer materials that were initially discovered by Davankov *et al*. in 1969.[30] They are the oldest type of POP network and still receive high levels of research interest. Their rapid growth can be prescribed to the many advantages such as the diverse synthetic methods, ease of functionalisation, high surface areas, chemical and thermal stabilities, mild synthesis conditions, and low reagent costs. In particular, the last two advantages make HCPs favourable compared to the other POPs. Many classes of microporous polymers use costly starting materials (*e.g.*, PAFs, many MOFs, and CMPs) or expensive catalysts for their preparation (*e.g.*, CMPs, PAFs). The synthesis of HCPs is mainly based on Friedel-Crafts chemistry which uses cheap Lewis acid catalysts, such as $FeCl_3$, and the monomers are also cheap and simple. Other POP networks require synthesis under rigorous anhydrous and anaerobic conditions (*e.g.*, PAFs), which makes scale-up challenging. The combination of low-cost reactions and ease of synthesis conditions for HCPs make them scalable.[83]

1.4.2.1 Synthesis of HCPs

Friedel-Crafts reactions are mainly utilised in the synthesis of HCPs. Numerous HCPs have been reported using three different synthesis strategies: post-crosslinking polystyrene-based precursors, one-step self-polycondensation, or external crosslinking of aromatic monomers. The crosslinking of polystyrene-based precursors generally proceeds in two crucial steps: (1) the complete dissolution or swelling of polymer precursors and then (2) intensive crosslinking.[84] Upon drying the material, this creates a flexible and strained porous structure as a result of the high number of weak bridges produced from the crosslinking reaction (**Figure 1.6**). Thereby, the inner-stress can be relieved by occupation of solvent and HCPs are able to swell.[85] The swelling mechanism has been utilised for high pressure CO_2 capture[86] and uptake of chemicals.[87]

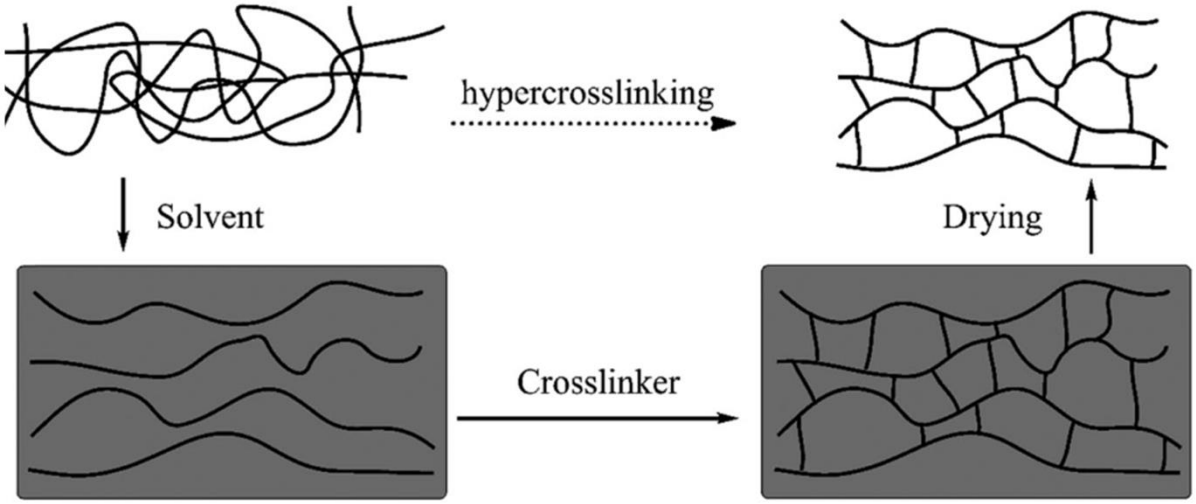

Figure 1.6 Schematic representation of post-crosslinking polystyrene-based precursors. Figure reprinted from literature source.[84]

The post-crosslinking of polystyrene-based precursors has been widely studied with many crosslinking agents. A simple methylene bridge can be made between two styrene rings in the presence of a Friedel-Crafts catalyst and formaldehyde dimethyl ether (FDA) crosslinking agent (**Figure 1.7a**).[85] This type of reaction can also proceed through the incorporation of a reactive group onto the styrene unit, such as an olefin or a chloromethyl group, which react under the Friedel-Crafts conditions (**Figure 1.7b**).[85] However, the approach can be quite limited as the use of polystyrene-based precursors limits synthetic diversity.

One-step self-polycondensation reactions allow greater precursor freedom, allowing the use of molecules that contain crosslink-able halogens or methyl ester groups to undergo Friedel-Crafts reactions (**Figure 1.7c**).[20] Co-monomers can also be utilised in order to add functionality and create more diverse HCPs (**Figure 1.7d**).[88] However, the strict requirement that the monomers must contain these specific functionalities can limit the choices of precursors, or may require multi-step organic synthesis to prepare these monomers which uses large volumes of reagents and solvents associated with further purification steps and high cost.

To overcome the limitations of previous methods which either require a polystyrene-based precursor or halogen-functionalised monomers, the Tan group developed the preparation of HCPs by using a simple external crosslinking strategy; the "knitting" approach utilised FDA as an external crosslinker for simple aromatic compounds, such as benzene, to build methylene bridges between the aromatic monomers. The Lewis acid catalysed Friedel-Crafts alkylation reaction is most commonly carried out with $FeCl_3$ in DCE (**Figure 1.7e**),[89] and proceeds by the mechanism shown in **Figure 1.8**. This simple

one-step route can also be utilised with a range of heteroaromatic molecules, such as thiophene, pyrrole, and furan, which can add functionality to the resultant HCP (**Figure 1.7f**).[90]

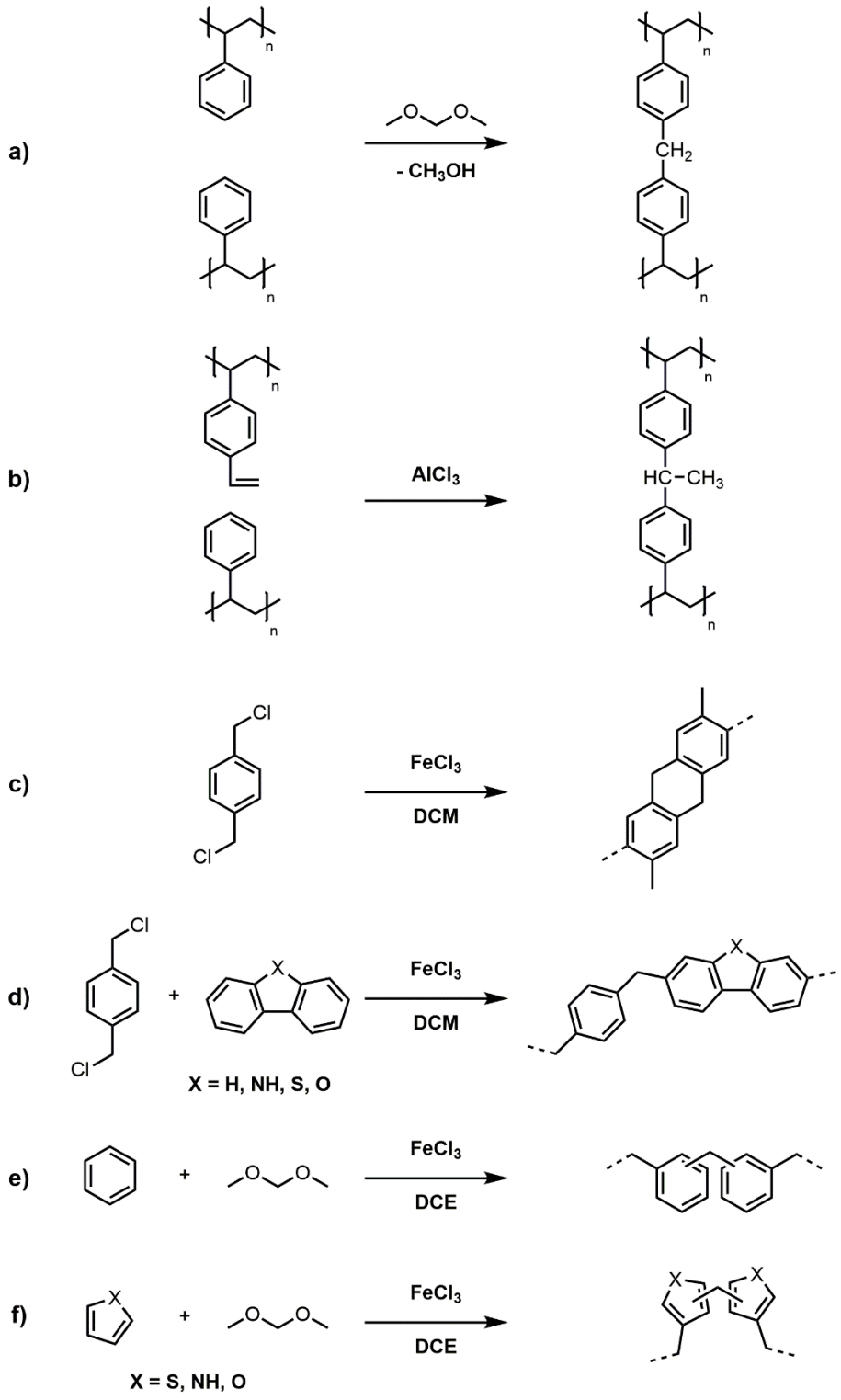

Figure 1.7 Reaction schemes for the synthesis of HCPs. (a) Post-crosslinking of polystyrene with external crosslinker, FDA; (b) Post-crosslinking of polystyrene with internal double bond group; (c) Self-polycondensation reaction; (d) Polycondensation with a co-monomer; (e) Knitting reaction of benzene; and (f) Knitting reaction of heterocycles.

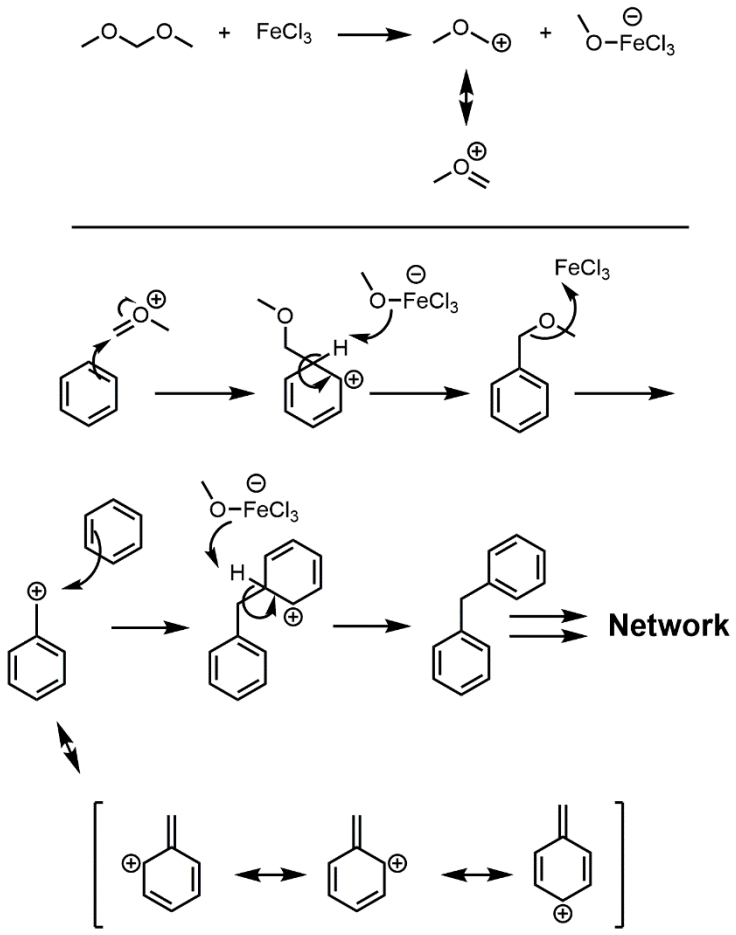

Figure 1.8 Mechanism for the HCP knitting method of benzene.

1.5 Carbon

Carbon, originating from Latin *carbo* and French *charbon* meaning charcoal, is the fourth most abundant element in the universe by mass.[91] It is also the second most abundant element in the human body. Carbon exists in various allotropes, such as diamond, graphite, and amorphous carbon. The different forms of carbon possess varying physical properties.

Diamond is built from purely sp^3 hybridised carbon atoms (**Figure 1.9a**) and is known for its extreme hardness, high thermal conductivity, and its transparent and colourless form – making it the most popular gemstone.[92] Graphite has a planar, sp^2 structure which is layered (**Figure 1.9b**). It is the softest naturally occurring material due to its weak interlayer interaction, which allows the graphene layers to "slide" over one another; it is this property that gives rise to its use as a lubricant in industry. The aromaticity of graphite layers allows free movement of the valence electrons and gives rise to electric conductivity.[93]

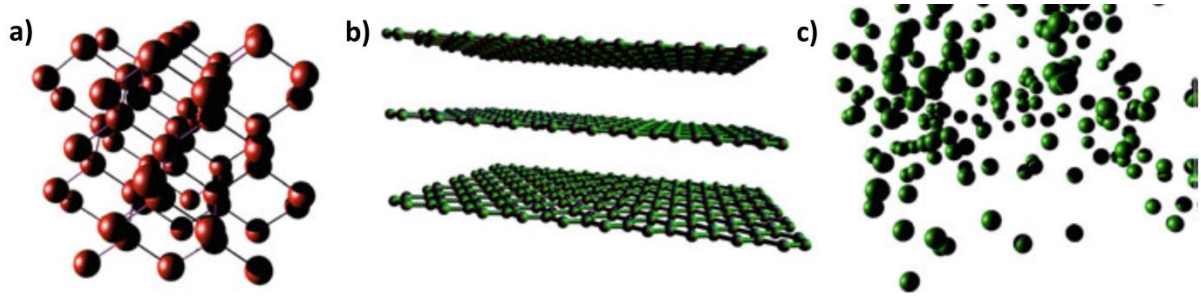

Figure 1.9 Allotropes of carbon. (a) Diamond; (b) Graphite; and (c) Amorphous carbon. Figure reprinted from literature source.[91]

Amorphous carbons lack long range crystallinity (**Figure 1.9c**). A spectrum exists between truly amorphous carbon and single crystal graphite, and are classified as disordered, semi-graphitic, or polycrystalline. Semi-graphitic carbon contains some graphitic domains but lacks sufficient order to be considered graphite (**Figure 1.10**). Various degrees of orientation exist such as planar orientation for graphite, axial orientation for carbon fibres, point orientation for carbon blacks, and random orientation for activated carbons.[94]

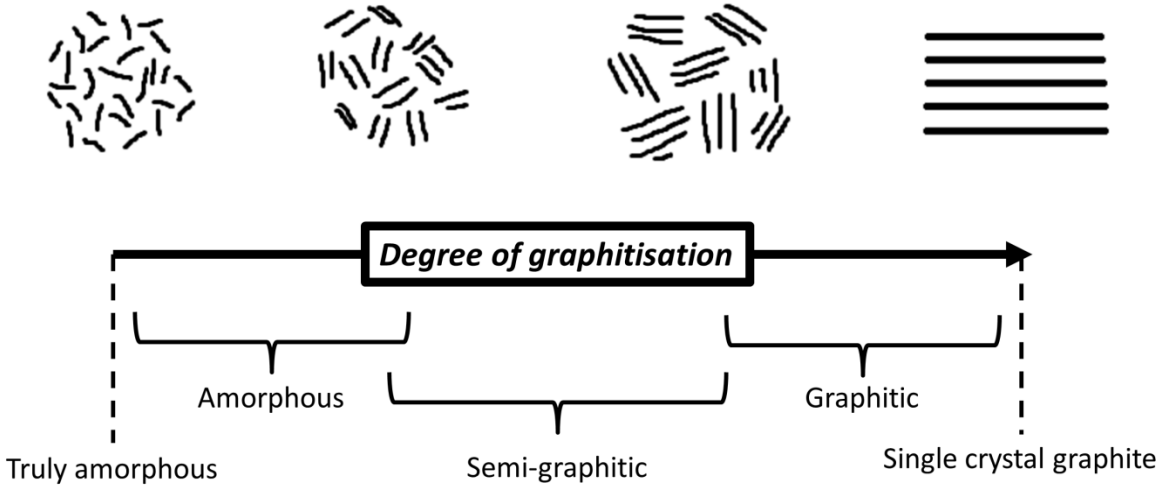

Figure 1.10 Spectrum of semi-graphitic carbons between truly amorphous carbon and single crystal graphite.

1.5.1 Carbonisation

Pyrolysis is the thermochemical decomposition of an organic material at elevated temperatures in an inert atmosphere. High purity N_2 or Ar is commonly used and the reaction must be carried out in the absence of oxygen as combustion would occur. The word is derived from the Greek terms for fire "*pyro*" and separating "*lysis*".

Carbonisation is the conversion of an organic material into carbon. The term pyrolysis is commonly used when heating materials at relatively low temperatures to yield a solid richer in carbon content. Carbonisation can be defined as extreme pyrolysis, with temperatures ranging from 600 to 1300 °C,[95] which leaves mostly carbon as the residue. The reaction mechanism is complex and involves simultaneous dehydrogenation, condensation, hydrogen transfer, isomerisation, and aromatisation reactions throughout the material.[95] The inherent difficulty associated with monitoring the many cascade reactions has led to numerous theories being proposed for the carbonisation reaction mechanisms. At higher carbonisation temperatures, graphite-like crystallites are prone to form through further condensation and lateral π- π stacking.[95, 96] Very high temperature carbonisation reactions (~2000–3000 °C) can lead to the fusion of graphitic crystallites to form graphitic carbon (known as graphitisation), or can form glass-like carbon if the carbon is not graphitisable.[95, 97]

The choice of precursors to generate carbonaceous materials is almost limitless. However, in order to undergo successful and high yielding carbonisation reactions, some general rules should be followed, namely:

1. **The carbonisation precursor should have high carbon content**, preferably with a high degree of sp^2 and/or *sp* hybridised carbon. Non-carbon species are readily removed during carbonisation so low carbon-containing feedstocks result in low yields. sp^3 hybridised carbons are very likely to decompose and will not contribute to the yield or can undergo dehydrogenation to form sp^2 and/or *sp* hybridised carbon.[96]
2. **The carbonisation precursor should have a relatively high molecular weight.** Feedstocks with low molecular weight are more volatile, thus they are more prone to sublimation resulting in low yield. An exception to this rule is if the material undergoes *in situ* polymerisation, prior to higher carbonisation temperatures. Such is the case for glucose which polymerises at a low pyrolysis temperature of 150 °C.[98]
3. **The carbonisation precursor should be crosslinked or undergo *in situ* crosslinking prior to carbonisation.** Related to the second rule, high molecular weight materials are less prone to sublimation before reaching their carbonisation temperature. Therefore small molecules with functional groups should be crosslinked and formed into a network in order to preserve functionality. Crosslinking can be performed through various methods such as pre-oxidation of the precursor[99] or chemically crosslinking the material prior to carbonisation — as is the case in this thesis.

Carbonaceous materials have been studied for many years because of their use in a vast range of applications.[100] This is largely due to the ease and variety of tuning methods available to synthesise these materials. Out of all the properties, pore structure and surface chemistry are probably the most desirable features to be controlled.

1.5.2 Porous Carbon Methodology

The family of porous carbons is diverse. Its complex pore structure (**Figure 1.11**), not only in size but also morphology, is important for applications. The large variety of porous carbons available allows access to many applications such as gas separation,[101] water purification,[102] catalysis,[103] electromagnetic interface shielding,[104] and energy storage in batteries,[105] supercapacitors,[106] and fuel cells.[107]

Porous carbons are appealing because of their relatively low cost and their ease of preparation from a variety of natural and synthetic precursors. Porous carbons are noted for their high surface areas (>1000 m^2 g^{-1}) and pore volumes (>0.5 cm^3 g^{-1}); they also have good chemical, thermal, and mechanical stability, high electrical conductivity, and they can be processed for various applications.[108] Activated carbon is a highly porous carbon, synthesised via activation. Porous carbonaceous materials are traditionally prepared by the following methods:

1. Direct carbonisation[109, 110-113]
2. Template method[114-121, 122-125]
3. Physical activation[126-130]
4. Chemical activation[131-142]

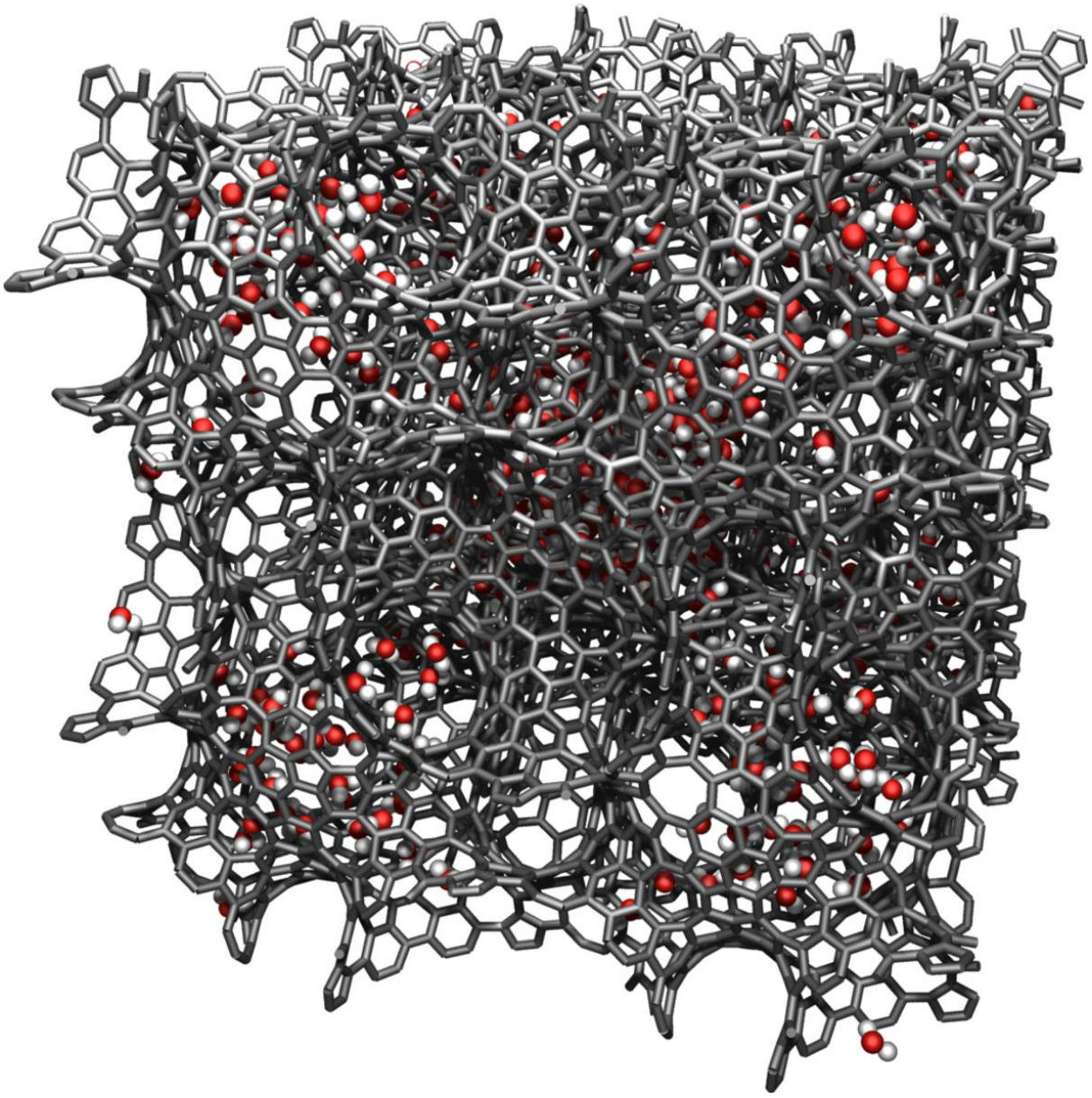

Figure 1.11 The complexity of a porous carbon nanostructure, with H_2O molecules diffusing in the pores for supercapacitor application. Activated carbons are often random structured folds of graphene-like sheets to create porosity. Molecular dynamics image simulation generated by Oak Ridge National Laboratory, U.S. Dept. of Energy.

1.5.2.1 Direct Carbonisation

The direct carbonisation method (or pyrolysis) is the simplest of all methods to prepare porous carbons. The carbonisation precursor is heated directly under an inert gas (N_2 or Ar) which converts the material into a carbon with often relatively low porosity compared to activated carbons. The advantages are that the method involves a single step and is cheap. In order to tune the resultant carbon, the carbonisation temperature and precursor should be carefully considered. Porosity characteristics are strongly

dependent on the carbonisation temperature, with higher temperatures generally yielding increasingly porous carbons.[109] However, pore collapse have been observed when too high a temperature is used.[110] Functional precursors such as N-containing molecules,[111] heterocyclic polymers,[112] and MOFs[113] have been used to produce heteroatom- and/or metal-doped carbons.

1.5.2.2 Templating Method

The template carbonisation method generally uses a scaffold that incorporates the natural or synthetic precursor to be carbonised, and then the scaffold is discarded. The scaffold itself is nanostructured, therefore the resultant carbon structure can be designed (**Figure 1.12**).[143] This method is popular in producing precisely controlled carbon structures at the nanometre level.[114] These often ordered structures cannot usually be produced using the other carbonisation methods.

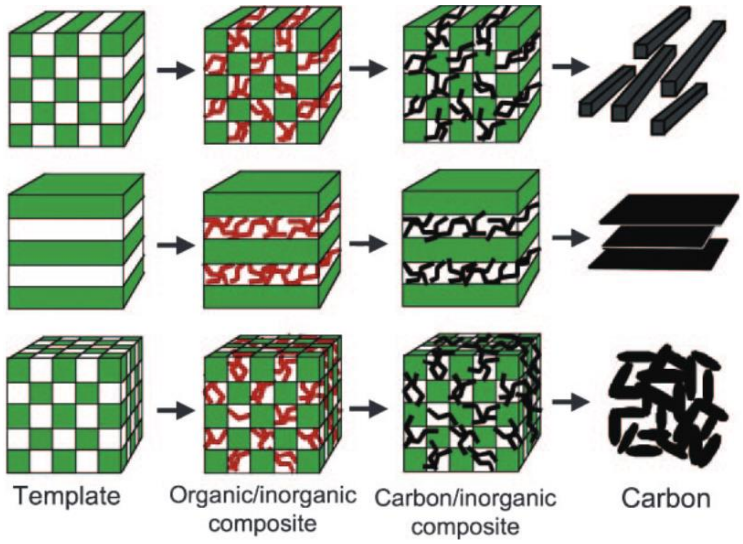

Figure 1.12 The concept of the template carbonisation method using template materials with different nanospace dimensions. The red and black parts correspond to an organic compound (as a carbon precursor) and carbon, respectively. Figure reprinted from literature source.[143]

There are two main types of templating methods, categorised as hard or soft templating. Hard templating was first reported by Knox *et al*. in 1986.[115] It requires a preformed porous scaffold, such as a MOF,[118] zeolite,[117] metal oxide,[116] mesoporous silica,[119] or spheres of polystyrene,[120] which the carbonisation precursor is loaded into and then carbonised. The porous scaffold is then removed through acid or base etching,[121] leaving a carbon material with the shape of the scaffold pore structure. The disadvantages of hard templating are that they usually involve several steps and are costly. The method involves the preparation of the scaffold which itself might be synthetically exhausting and expensive, and its subsequent removal, often using dangerous reagents such as HF.[114] The amount of template required

is also commonly more than twice the mass of carbon produced — all limiting factors for commercialisation.

Soft templating disregards the use of preformed scaffolds. Rather, they involve the self-assembly of organic-organic species such as surfactants,[124] or block-copolymers,[123] which are structure-directing to form lyotropic phases in the presence of the carbonisation precursor solution.[125] First reported by Dai *et al*. in 2004,[122] there has been rapid growth in this field due to the cost-effectiveness and fewer synthetic steps required by this method to produce porous carbons compared with hard templating. Though soft templating has advantages, there are still various problems with this method. For example, the structure-directing polymer must provide a driving force for micelle formation, and the interaction between the precursor and one of the blocks in the templating block-copolymer must be strong, in order to prevent macrophase separation. The precursor should be able to crosslink prior to carbonisation, in order to stabilise the framework. Finally, the crosslinked precursor should have greater thermal stability than the template so that it can be removed without collapse of the porous carbon structure.[125] These rules greatly limit the choice of carbon precursor and applicable templates.

1.5.2.3 Physical Activation

The physical activation process occurs by partial gasification of carbon with a mildly oxidising gas (*e.g.*, air, steam, or CO_2) at 350–1000 °C, after initial pyrolysis of the precursor.[126] The first pyrolysis step is required in order to remove the maximum amount of oxygen and hydrogen elements.[127] The active oxygen species in the activating gas then burns away by-products trapped in the pyrolysed carbon pores, which leads to further opening of pores. Additionally, the oxidising gas burns away the more reactive carbon regions present in the structure, generating CO and CO_2. The extent of this process is dependent on the activation temperature used, length of activation time, and the nature of the gas deployed. Higher activation temperatures and longer activation times generally leads to larger porosity development; however, this is commonly accompanied by a broadening of the pore size distribution (PSD).[126]

The use of air (O_2) as an activating agent has its pros and cons. The reaction of O_2 with carbon is highly exothermic. This makes the activation speed difficult to control and can result in excessive burn-off, therefore, reducing the carbonisation yield. Osswald *et al*. performed air activation on TiC-derived carbide-derived carbons (TiC-CDCs) and observed only a moderate (~10%) increase in surface area and pore volume with increasing activation time and temperature but this was accompanied by a large weight loss.[129] This was also followed by rapid broadening of micropores into mesopores. However, the highly reactive nature of O_2 allows lower temperatures to be used,[128] reducing the energy and cost compared to the use of steam or CO_2, due to its lower activation energy.

By contrast, CO_2 activation usually yields much higher surface areas and pore volumes for resultant carbons. Osswald *et al*. observed a 77% increase in surface area to ~3100 $m^2\ g^{-1}$ and doubling of pore volume to 1.3–1.4 $cm^3\ g^{-1}$ using TiC-CDCs with CO_2 activation at 950 °C for 2 hours.[129] For this reason, the milder oxidising agents, CO_2 and steam, are preferred to air as activating agents. Steam is generally known to be a more reactive oxidising agent than CO_2, thus lower carbonisation temperatures can be utilised.[130] Though the surface area, pore volume, and average pore diameter generally increases with the extent of the burn-off using CO_2 and steam, there is no defined type of porosity generated by each activating agent.[126] Nevertheless, physical activation is favourable in terms of the environment as readily available gases are used and harsh chemicals are avoided.

1.5.2.4 Chemical Activation

The chemical activation method is generally performed by mixing the precursor with a chemical activating agent (*e.g.*, KOH, H_3PO_4, $ZnCl_2$, $AlCl_3$, $MgCl_2$, NaOH), followed by carbonisation at 400–900 °C. The pore characteristics of the carbon depend on the concentration of the activating agent, the activation temperature, activation time, and the carbon source. An inert N_2 flow is most commonly used in this method. The chemical activation process can generate carbons with very high surface areas, commonly over 2000 $m^2\ g^{-1}$, and large pore volumes comprised primarily of micropores and some small mesopores.[131] There are many advantages of chemical activation over physical activation, such as:

1. Single-step reaction
2. Lower activation temperatures
3. Shorter activation time
4. Higher carbon yields
5. High surface areas and pore volumes
6. Micropores can be well developed and more narrow
7. Reduction of mineral matter content

However, the disadvantages are the corrosiveness of the activating agents and the requirement of a post-washing step to remove the chemical agents. Among the vast number of chemical activating agents, H_3PO_4, $ZnCl_2$, and KOH are most commonly used. H_3PO_4 and $ZnCl_2$ act as dehydrating agents, whereas KOH acts as an oxidising agent. H_3PO_4 produces a dehydrating effect at low temperatures, leading to bond weakening and crosslinking reactions (through cyclisation and condensation processes) are predominant. The structure at this point aids in reducing the release of volatile materials, restricts tar formation, and prevents loss of porosity.[132] Dehydration of the carbon precursor causes contraction in

the material, but this is partially counter-acted by the presence of the activating agent in the particle, which acts as a template to create microporosity.[126] H_3PO_4 is also able to combine with the organic precursor species to form phosphate and polyphosphate bridges which further reduces the volume reduction as the carbonisation proceeds. $ZnCl_2$ behaves as a similar dehydrating agent, but smaller micropores with more uniform sizes can be achieved due to the small size of $ZnCl_2$ and its hydrates.[133]

KOH activation is widely used, with the method known since 1978 and employed for the preparation of the commercially available activated carbons, AX21 and Maxsorb, which are prepared from fossil-based carbon sources.[134] Maxsorb has a very high surface area of over 3000 $m^2\ g^{-1}$ with a large pore volume (1.0–1.5 $cm^3\ g^{-1}$) primarily comprised of mesopores. However, unlike H_3PO_4 and $ZnCl_2$ which act as dehydrating agents, KOH is an oxidant.[135] Although KOH activation is well-known and thoroughly studied, the activation mechanism is not completely known due to the many variables in both the different reactivities of the precursors used and the experimental parameters. The overall activation process between KOH and C occurs by the following redox reaction:[135, 140]

$$6KOH + C \rightarrow 2K + 3H_2 + 2K_2CO_3 \quad (1.1)$$

The organic precursor framework is consumed to generate pores through the oxidation of carbon to K_2CO_3.[134, 140] This process comprises several simultaneous/consecutive reactions, shown in **Equation 1.2 to 1.5**.[134] At about 400 °C, KOH dehydrates to form K_2O (**Equation 1.2**). Carbon is then consumed through gasification with H_2O which generates pores and emits H_2 (**Equation 1.3**). CO_2 which was produced in **Equation 1.4** reacts with K_2O to form K_2CO_3 (**Equation 1.5**). By about 600 °C, all the KOH is consumed.[131]

$$2KOH \rightarrow K_2O + H_2O \quad (1.2)$$

$$C + H_2O \rightarrow CO + H_2 \quad (1.3)$$

$$CO + H_2O \rightarrow CO_2 + H_2 \quad (1.4)$$

$$CO_2 + K_2O \rightarrow K_2CO_3 \quad (1.5)$$

K_2CO_3 can be subsequently reduced to K_2O and CO_2 (**Equation 1.6**),[140] with the CO_2 further reduced by carbon to CO (**Equation 1.7**). CO and CO_2 evolution occurs at high temperatures of about >700 °C due to the decomposition of K_2CO_3, which can contribute additional porosity through further carbon gasification (**Equation 1.6, 1.8, and 1.9**).[136] Metallic K which can be produced from K_2CO_3 and K_2O

(**Equation 1.8 and 1.9**) is able to intercalate into the material and later removed during washing steps. The expanded separated layers formed from the intercalation process cannot return to their previous non-porous structure after washing but instead remain apart to create microporosity (**Figure 1.13**).[139, 141]

$$K_2CO_3 \rightarrow K_2O + CO_2 \quad (1.6)$$

$$CO_2 + C \rightarrow 2CO \quad (1.7)$$

$$K_2CO_3 + 2C \rightarrow 2K + 3CO \quad (1.8)$$

$$C + K_2O \rightarrow 2K + CO \quad (1.9)$$

Lower temperature gasification can also occur by using precursors with higher reactivity.[137] Additionally, higher degrees of gasification results in increased porosity development.[138] Although most alkaline metal carbonates melt before decomposing (891 °C for K_2CO_3), this can occur at temperatures below the melting point when heating carbonate-carbon mixtures.[144]

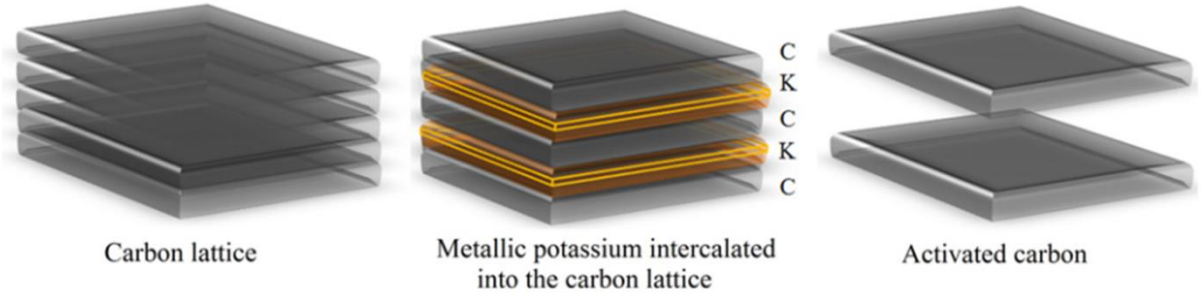

Figure 1.13 Activation mechanism by the intercalation of K into carbon lattices, expansion of the lattice by K, and the removal of intercalated K from the carbon structure. Figure reprinted from literature source.[141]

In summary, three main activation mechanisms are widely accepted for the use of KOH to generate porosity:[134, 140, 142]

- Etching of carbon network by redox reactions between various K compounds and C (**Equation 1.1, 1.8, and 1.9**)
- Gasification of carbon networks through formation of H_2O (**Equation 2**) and CO_2 (**Equation 1.4 and 1.6**)

- Expansion of carbon lattices by intercalation of as-prepared metallic K (**Equation 1.1, 1.8, and 1.9**) into the carbon matrix

The synergistic actions of these mechanisms result in the development of large surface area carbons with high porosity in KOH-activated carbons. The choice of gas flow is also an important consideration. Lillo-Rodenas *et al*. show that using a N_2 flow produces more porous carbons than performing the same activation under CO_2 (SA_{BET} of 2193 $m^2\ g^{-1}$ under N_2 vs. 36 $m^2\ g^{-1}$ under CO_2).[135] This is likely due to consumption of KOH by CO_2 through the following reaction:

$$4KOH + CO_2 \rightarrow 2K_2CO_3 + 2H_2O \quad (1.10)$$

Therefore, the presence of CO_2 should be avoided. CO_2 generated by the decomposition of K_2CO_3 at >700 °C (**Equation 6, 8, and 9**) will not interfere with this process as all the KOH is consumed by about 600 °C.[131]

In reality, the resultant carbon pore properties not only depend on the activation parameters (*i.e.*, KOH concentration, activation time, and activation temperature) but on the carbon source. Both these factors have a significant influence on the pore structure and surface chemistry, which overall affects the performance of KOH-activated carbons in many applications. Therefore, it is impossible to predict which activation procedure will work with a selected precursor to afford a carbon with the desired structure and property, or the exact reaction mechanism. However, these limitations do not limit research in this area but instead can bring new opportunities for the discovery of high performing carbons.

1.6 Applications for Porous Materials

Porous materials are advantageous compared to non-porous equivalents due to their large surface areas offering high levels of functionality *vs*. the amount of material required. The ability to tune their porosity, surface areas, microstructure, morphology, and heteroatom-doping make them excellent for energy storage applications. The following sections outline and review various areas of energy storage where POPs and porous carbons have been used, and discuss their superior properties in these applications.

1.6.1 Energy

There is a growing energy crisis. The world population is rising; alongside this, the number of power devices per person is also rising. Worldwide energy demand is therefore strongly increasing. Modern society has progressed rapidly, with the involvement of the industrial revolution, heavily relying on fossil fuels (**Figure 1.14**).[145]

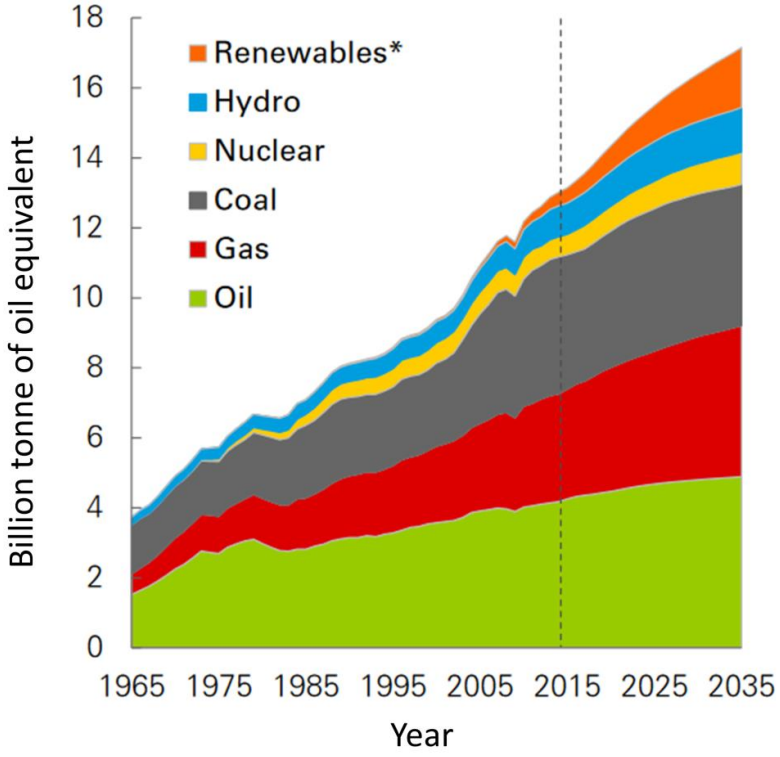

Figure 1.14 Primary energy consumption by fuel. *Renewables include wind, solar, geothermal, biomass, and biofuels. Figure reprinted from literature source.[145]

The use of fossil fuels has several heavy disadvantages:

- Combustion of this fuel or conversion into electricity results in significant CO_2 emissions to the environment and is a major contributor to climate change. Other harmful gases such as CH_4, N_2O, and fluorinated gases are also released.
- The use of petroleum fuels releases harmful, carcinogenic, and poisonous compounds to the atmosphere.
- Fossil fuels are non-renewable (the rate of formation is far outweighed by the rate of consumption).

These factors are driving society to move towards more sustainable and renewable energy resources. However, natural energy sources, such as solar, wind, and geothermal have limitations; there is no

sunlight at night, the wind does not always blow, and there is the potential for shifts in geothermal vents. All these natural sources also require the placement of a large array of solar panels, wind farms, or geothermal power stations which are not feasible to place everywhere, in addition to being relatively expensive.

Biofuels are a promising alternative to environmentally unsustainable fossil fuels. These energy sources have a large value heat of combustion (*e.g.*, biohydrogen, biodiesel, bioethanol, and biomethanol) and are obtained from biomass.[146] Biomass is abundant on earth, with many renewable sources such as wood, agricultural crops, water plants, forests, vegetable and animal remnants, and microbial cultures available.[147] Though this energy source has several advantages, production and utilisation of biofuel still has many disadvantages. There is a feedstock food/fuel competition,[146] which is increasingly demanding with a growing population, while the technology and processing methods are expensive and inefficient. The method demands a large amount of land and human labour to cultivate and burn the biomass. There can be poor control and productivity issues, in addition to being difficult to scale-up.[147] Moreover, biomass is commonly mixed with other fossil fuels due to its low efficiency.[148] This demands a larger amount of fuel overall for the same job and it does not tackle the original issue; also, biomass combustion is not entirely clean.[149]

Despite all the energy sources listed above being "sustainable", there are concerns for the reliability of output for the energy sources. We need to be able to store excess energy generated during periods of high power generation to cover periods of low power generation. This gives rise to the importance of energy storage devices.

1.6.2 Electrochemical Energy Storage

Energy storage is achieved with the use of devices which store energy from a variety of sources and can be used at any desired time. The performance characteristics of various energy storage devices can be compared by their power and energy densities (also known as specific power and specific energy, respectively), demonstrated in a simplified 'Ragone plot' shown in **Figure 1.15**.[150] Power density is the rate of energy transfer able to be delivered from and to the device, and energy density refers to the amount of energy able to be stored in a given system. The diagonal dashed lines represent the relative time to discharge and/or charge from the device.

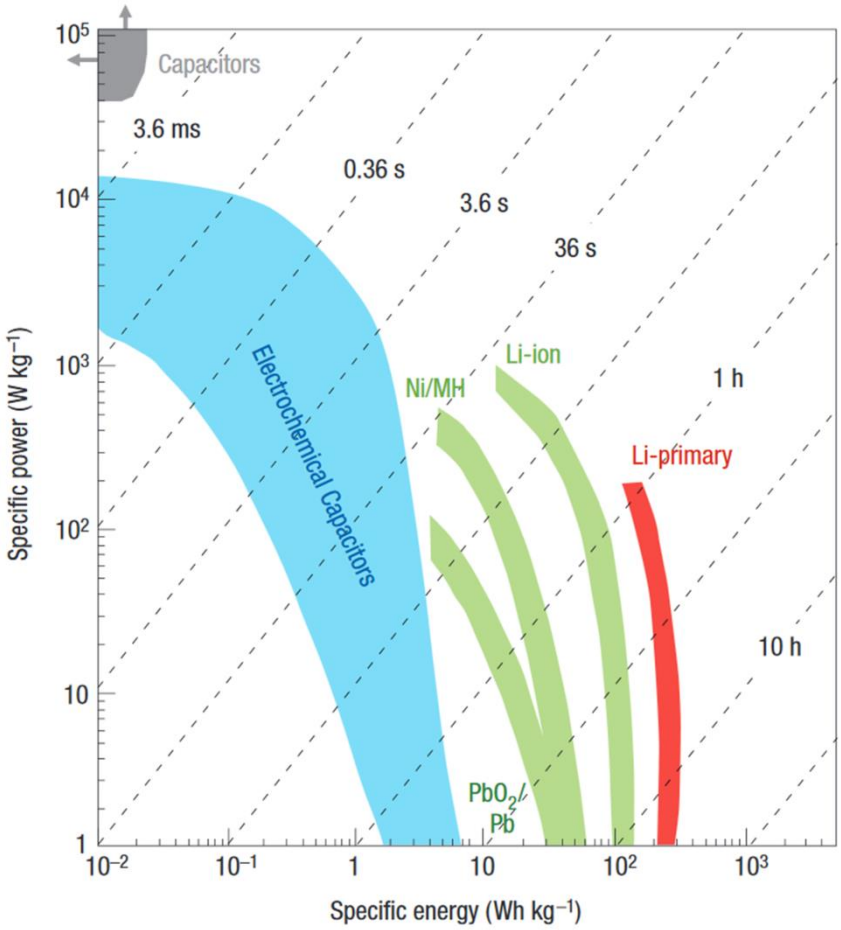

Figure 1.15 Ragone plot for various electrical energy output devices. Figure reprinted from literature source.[150]

1.6.2.1 Batteries

Batteries operate by redox reactions between their cathodes and anodes. Sony introduced lithium-ion batteries in 1990, following pioneering work by Whittingham, Scrosati, and Armand.[151] They are the current leading and commercial energy storage device,[152] as they can store large amounts of energy per mass/volume, and the level of power is suitable for many applications. Though being widely used in society, improvements need to be made.[151] As society moves away from a fossil fuel economy it will demand higher energy storage and more power for future electronics and transport systems. However, Li and some of the other transition metals currently used in batteries may one day become an issue.[153] Further problems are that batteries are limited in their power densities and more importantly, cycle lifetime,[154] as they are generally stable for fewer than 1000 charge-discharge cycles (**Table 1.1**).[155]

Table 1.1 Comparison of characteristics for batteries, traditional capacitors, and supercapacitors.[155]

Characteristic	Battery	Traditional capacitor	Carbon supercapacitor
Energy density (W h kg^{-1})	10-100	<0.1	1-10
Power density (W kg^{-1})	<1000	>>10000	500-10000
Discharge time	0.3-3 h	10^{-6} to 10^{-3} s	s to min
Charging time	1-5 h	10^{-6} to 10^{-3} s	s to min
Charge/discharge efficiency (%)	70-85	~100	85-98
Cycle life	~1000	Infinite	>500000
Max. voltage (V_{max}) determinants	Thermodynamics of phase reactions	Dielectric thickness and strength	Electrode and electrolyte stability window
Charge storage determinants	Active mass and thermodynamics	Electrode area and dielectric	Electrode Microstructure and electrolyte

1.6.2.2 Traditional Capacitors

Traditional parallel plate capacitors store charge by means of charge separation. These are constructed from two parallel plate electrodes separated by a polarisable insulator (a dielectric), where a potential difference (voltage) is applied across the electrodes which results in the build-up of positive and negative charges on the electrodes (**Figure 1.16**).

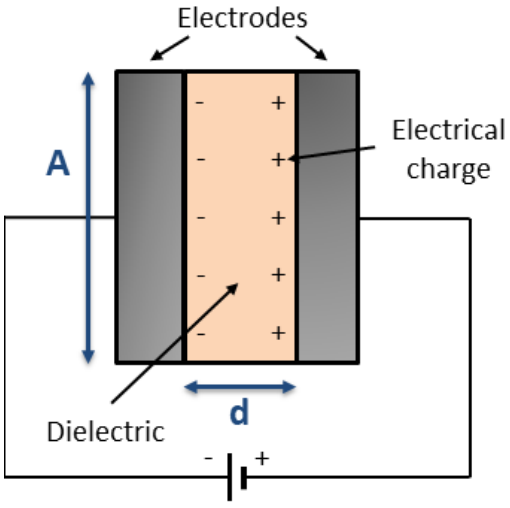

Figure 1.16 Diagram of traditional parallel plate capacitor.

The presence of a dielectric means that direct current (DC) cannot flow through the capacitor as it is blocked, and only voltage, *V*, exists across the electrodes in the form of electrical charge, *q*. The ratio of *q* to *V* will give the capacitance (*C*):

$$C = q / V \tag{1.11}$$

This charge is stored in an electrostatic field between the two electrodes. As electric current flows into the capacitor, this charges it up, with the electrostatic field becoming stronger (and potential difference increases) as it stores more energy. Similarly, as electric current flows out of the capacitor, this discharges it, and the potential difference decreases as energy is removed from the electrodes. In general, the ability of the electrodes to store charge in an electrostatic field is known as the capacitance of a capacitor. This charging mechanism allows fast charge-discharge of 10^{-6} to 10^{-3} s with very high power densities (**Table 1.1**). As traditional capacitors operate by purely electrostatic means, this gives them near infinite lifetime cyclability. However, the surface areas of traditional parallel plate capacitors are limited. Additionally, the dielectric thickness is limited by construction. These limitations have an impact of the capacitance, as it follows the **Equation 1.12**:

$$C = \varepsilon \frac{A}{d} \tag{1.12}$$

where ε is the permittivity, A is the surface area, and d is the dielectric thickness.

These parameters combined with the electrostatic charging mechanism results in low energy densities for traditional capacitors.

1.6.2.3 Supercapacitors

Supercapacitors, also known as ultracapacitors and electrochemical capacitors, bridge the gap between batteries and traditional capacitors. They can store hundreds or thousands of times more charge than traditional capacitors and have much higher power densities than batteries. They also retain the cycling stabilities of traditional capacitors, allowing them to be recharged many thousands of times without loss of performance. The structure of a symmetric supercapacitor consists of two porous electrodes on separate current collectors which are immersed in an electrolyte and are separated by a dielectric separator, which is permeable to ions (**Figure 1.17**). As a potential is applied across the current collectors the positively charged electrode attracts negative ions in the electrolyte while the negative electrode attracts positive ions.

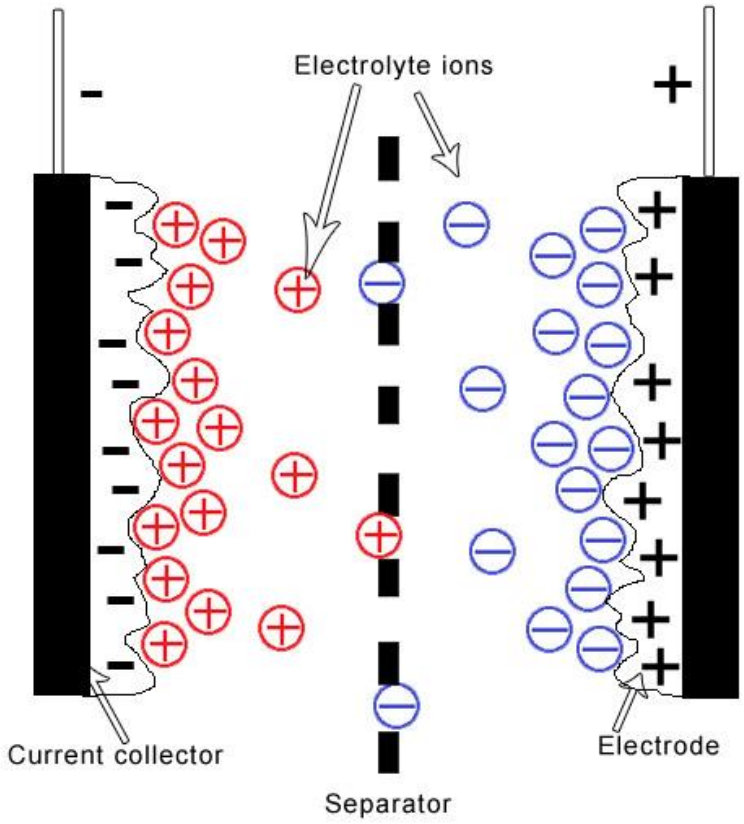

Figure 1.17 Diagram of a supercapacitor device in its charged state.

Charge is accumulated at the interface of both electrode/electrolyte surfaces which generates energy when the device discharges. Each electrode can be treated as a single capacitor of capacitance (C_1) or (C_2). The total capacitance takes both electrodes into account but is dominated by the electrode with the smallest capacitance:[156]

$$\frac{1}{C} = \frac{1}{C_1} + \frac{1}{C_2} \tag{1.13}$$

Technological advances in electronic devices and in transportation require high power densities which cannot be matched by batteries, making supercapacitors important. However, these developments will also require large energy densities, which supercapacitors currently lack. The low energy densities of supercapacitors mean that their optimal discharge time is usually less than a minute, making them currently unviable for many applications.[157] These energy storage demands make supercapacitors a viable alternative for development in future systems.[154]

There are two types of storage principles that contribute to capacitive behaviour: electric double-layer capacitance (EDLC) from pure charge separation at the electrode-electrolyte interface, and pseudocapacitance (PC) from fast and reversible surface Faradaic redox reactions that occur at

characteristic potentials.[158] These two storage mechanisms can often be independent in certain materials (*e.g.*, activated carbons, metal oxide); however, they can also be incorporated together to combine the advantages of both mechanisms in a supercapacitor material.

1.6.2.3.1 Electric Double-Layer Capacitance

Traditional parallel plate capacitors store very little energy compared to supercapacitors due to the inherent limitations in their charge storage areas and dielectric thickness (as physically, the charged plates can only be put so close together). Contrary to this, supercapacitors can store more energy through the EDLC mechanism because of their large surface areas and their atomically small charge separation distances.

EDLC is the storage of electrical energy by the electrical double-layer (EDL) effect, where ions attract to the electrodes with the opposite charge at the electrode-electrolyte interface (**Figure 1.18**).[159] The EDL effect was reported by Helmholtz in 1853 when he studied the distribution of charges at the interface of colloidal particles.[160] The concept of this interaction between a metal surface in contact with an electrolyte was then discussed in 1879.[161] The EDL model evolves from the Helmholtz model to the Gouy-Chapman model, to the Stern model, as illustrated from **Figure 1.18a to c**.

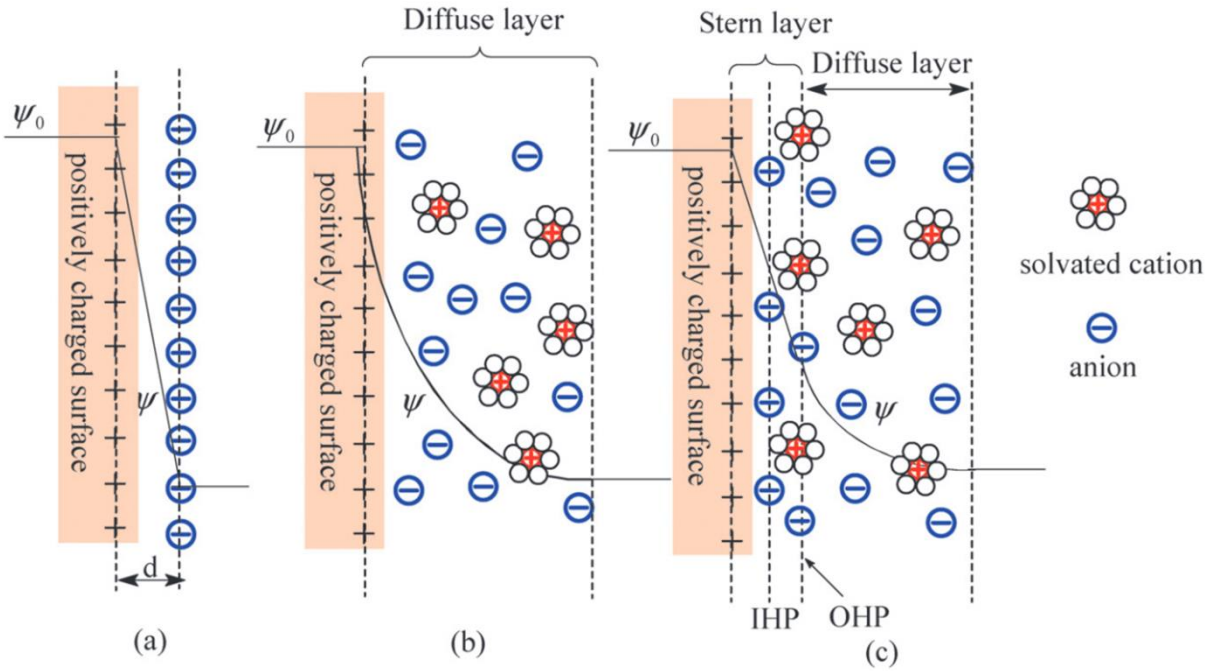

Figure 1.18 Development of models for the electrical double-layer effect. (a) Helmholtz model. (b) Gouy-Chapman model. (c) Stern model. The IHP refers to the distance of closest approach of specifically adsorbed ions (generally anions) and OHP refers to that of the non-specifically adsorbed

ions. The OHP is also the plane where the diffuse layer begins. *d* is the double layer distance described by the Helmholtz model. Ψ_0 and Ψ are the potentials at the electrode surface and the electrode-electrolyte interface, respectively. Figure reprinted from literature source.[162]

The Helmholtz EDL model states the presence of charged ions in contact with an electrode surface of opposite charge separated by an atomic distance, *d* (**Figure 1.18a**). The model is similar to that of traditional capacitors where both charges are represented by oppositely charged electrodes. The storage of charge is non-Faradaic, therefore there is no chemical or composition changes as no charge transfer occurs between the electrode and electrolyte. Because of this, the charge storage of EDLC electrodes is highly reversible, allowing them to achieve high stabilities over many thousands of charge-discharge cycles. As the phenomenon occurs via a surface interaction, common materials used for EDLC electrodes are activated carbons. The charge on the electrode is equally balanced in solution by a layer oppositely charged ions with an electro-neutral bulk solution parallel to this layer (**Figure 1.19**).

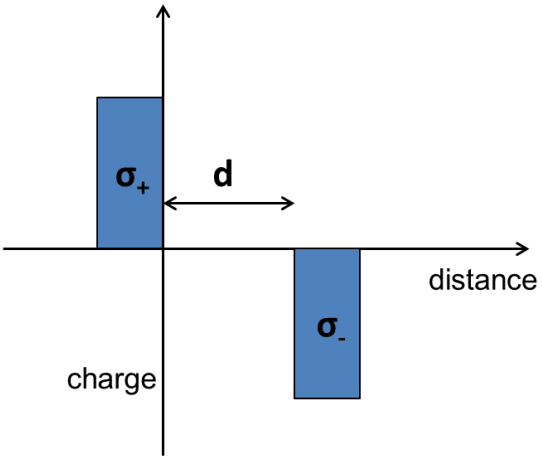

Figure 1.19 Charge distribution of ions in the Helmholtz model.

Charge originates from the rearrangement of electrolyte ions and/or the reorientation of dipoles in the solvent molecules. On the electrode-electrolyte interface there is a potential difference that exists which forms an electric field gradient across the charge separated layer. Ions are then either electrostatically attracted or repelled towards the charged electrode surface bringing about a high concentration of either cations or anions.

The Helmholtz model was further developed by Gouy (1910) and Chapman (1913). Their model adds the concept of a diffuse double-layer due to thermal motion; in which the excess of ions distribute themselves in a Boltzmann fashion extending some distance from the electrode surface (**Figure 1.18b**).[163] Gouy and Chapman showed that an excess of charged ions at the OHP does not exist, but instead suggests that the EDL must have a variable density of charge throughout the solution.

The Gouy-Chapman model considers that the electrostatic forces between the field and charge of the ions are opposed by Brownian motion which disperses the excess ions. This phenomenon leads towards a distribution of ion point charges contained in a single 'diffuse layer', illustrated in **Figure 1.20**. Most of the excess charge is close to the electrode but then gets progressively reduced further into the electrolyte. However, the Gouy-Chapman model results in an overestimation of EDLC as the two separated arrays of charges in a cell would increase and become more compact inversely with their separation distance, therefore large capacitance values would appear in the case of high charges close to the electrode surface.

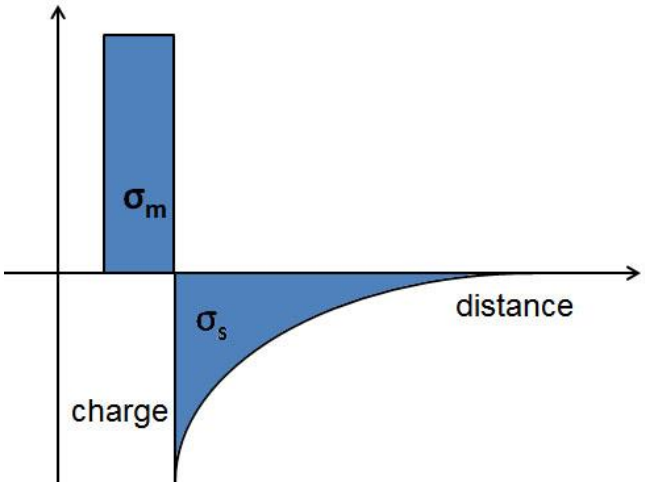

Figure 1.20 Charge distribution of solvent (σ_s) with charged electrode (σ_m).

In 1924, Stern suggested a model combining both the rigid Helmholtz layer and the diffuse layer of Gouy and Chapman.[164] This model recognises the existence of two regions of ion diffusion (**Figure 1.18c**)—the Stern layer (also known as the compact layer) and the diffuse layer. In the Stern layer, ions are strongly absorbed to the electrode. The Stern layer, which is based on the Helmholtz model, can be separated into two further layers based on the type of absorption: an inner Helmholtz plane (IHP) and an outer Helmholtz plane (OHP). The IHP exists between the surface of the electrode to a plane passing through the centre of ions which are in direct contact to the surface and are 'specifically absorbed'. The OHP passes through the centre of the hydrated ions at a distance of closest approach to the electrode. Beyond the OHP lies the diffuse layer which is what the Gouy-Chapman model defines.

The charge of the solution, q_S, resides partially in the Stern layer, q_H (Helmholtz), and the remainder in the diffuse region of the solution, q_G (Gouy-Chapman), *i.e.*, $q_S = q_H + q_G$. Thus, the EDLC can be treated as a combination of the capacitances arising from these two regions, C_H from the Stern type of

Helmholtz capacitance and C_G from the diffuse region capacitance. Thus the total capacitance, C_{DL}, can be expressed by the following equation:

$$\frac{1}{C_{DL}} = \frac{1}{C_H} + \frac{1}{C_G} \tag{1.14}$$

Multiple factors affect the EDLC at an electrode surface such as: the electrical field across the electrode, the types of electrolyte ions, the solvent the electrolyte is dissolved in, and the affinity between the absorbed ions with the electrode surface. Porous materials are commonly used for EDL capacitors; however, the behaviour at the pore surface of a porous electrode is more complex than that at an infinitely planar one. The ion transportation system of porous materials is confined and are drastically affected by multiple factors, such as the tortuous mass transfer path, the space constrain inside the pores, ohmic resistance associated with the electrolyte, and the wetting behaviour of the pore surface with the electrolyte.

The capacitance of a porous electrode for an EDL capacitor can be expressed by the following equation:

$$C = \frac{\varepsilon_r \varepsilon_0}{d} A \tag{1.15}$$

where ε_r is the electrolyte dielectric constant, ε_0 is the permittivity of a vacuum, A is the specific surface area of the electrode accessible to the electrolyte ions, and d is the effective thickness of the EDL (the Debye length). Based on **Equation 1.14**, there should be a linear relationship between the capacitance (C) and surface area (A). However, experimental results show that this simple linear relationship is not observed.[165]

It was long believed that the micropores of an electrode material do not participate in the formation of an EDL due to the small pores being inaccessible to large solvated ions.[162] However, in 2006, Raymundo-Piñero *et al*.[166] showed important contributions from micropores to the overall capacitance, and suggested that partial desolvation of hydrated ions occurred, therefore more ions can enter the pores, leading to enhanced EDLC. Simon and Gogotsi (2008) support contributions from sub-micropores, reporting a capacitance increase with pores less than 1 nm in carbon electrodes.[167] The EDLC was highest when the pore size was close to the ion diameter, therefore, confirming pores with sizes smaller than the solvated ion contributes towards capacitance.

While these findings are correct, they cannot be fully interpreted by the EDL theory as there is insufficient room in micropores to accommodate both the Stern layer and diffuse layer. Huang and co-workers (2008) proposed a heuristic approach to describe nanoporous carbon materials based on their

pore curvatures.[168] For mesoporous carbons, an electric double-cylinder capacitor (EDCC) model is proposed to describe the electrolyte distribution (**Figure 1.21a**), where mesopores are assumed to be cylindrical and that the solvated counter-ions enter the pores and accumulates at the pore wall to form an EDL. For microporous carbons, an electric wire-in-cylinder capacitor model is proposed (**Figure 1.21b**), where the pores are too small to allow formation of a double-cylinder. Partial or complete removal of the ion solvation shell allows access to the micropores.

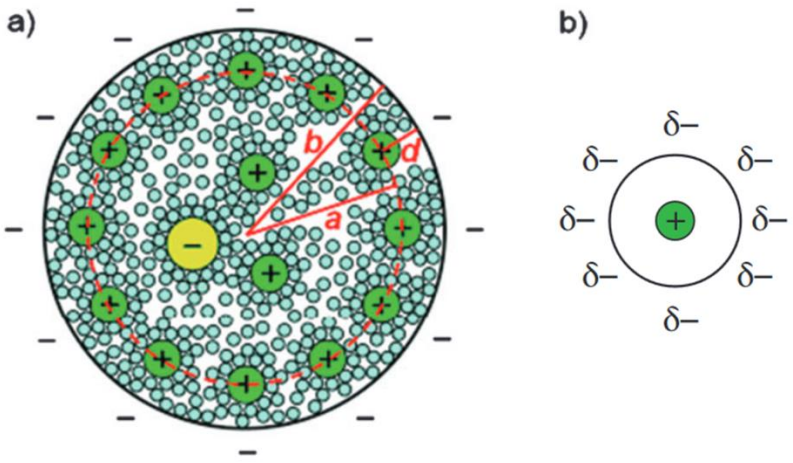

Figure 1.21 Schematic diagrams (top views) of (a) a negatively charged mesopore with solvated cations approaching the pore wall to form an electric double-cylinder capacitor and (b) a negatively charged micropore with cations lining up along the pore axis to form an electric wire-in-cylinder capacitor. Figure reprinted from literature sources.[167, 168]

When the pores are large enough so that the pore curvature is not significant, the EDCC model can be reduced back to the traditional planar EDL model, given in Equation **1.15**. The capacitance can be estimated for the EDCC model (**Equation 1.16**) and the EWCC model (**Equation 1.17**):[168]

$$C = \frac{\varepsilon_r \varepsilon_0}{b \ln[b/(b-d)]} A \tag{1.16}$$

$$C = \frac{\varepsilon_r \varepsilon_0}{b \ln(b/a_0)} A \tag{1.17}$$

where b is the pore radius, d is the distance of approaching ions to the surface of electrode, and a_0 is the effective size of the counter-ions.

Huang *et al*. were able to make good fits with experimental data using these models, regardless of the type of carbon material or electrolyte employed. The model shows an increase in capacitance with pore sizes smaller than 1 nm and a slightly increased capacitance with pore sizes larger than 2 nm, could be

explained using the EWCC and EDCC models, respectively. Additionally, the dielectric constant obtained when fitting the results with **Equation 1.17** is close to the value in vacuum, which indicates that ions desolvate before entering the micropores.[162]

1.6.2.3.2 Pseudocapacitance

Traditional parallel plate capacitors and pure EDL capacitors transfer charge into the double-layer with no Faradaic reactions occurring between the electrode and electrolyte. The capacitance is constant in this case and is independent of voltage.

Pseudocapacitance (PC) is Faradaic, involving fast and reversible redox reactions between the electrolyte and an electro-active species of the electrode. Most of the charge is transferred at or near surface of the electrode. In contrast to EDLC, charge transfer in PC is voltage dependent, arising from thermodynamics between the extent of charge acceptance (Δq) and the change of potential (ΔV).[169]

$$C = d(\Delta q)/d(\Delta V) \tag{1.18}$$

The derivative of this shown in **Equation 1.18** is more commonly used and corresponds to the calculation of capacitance:

$$C = q/V \tag{1.19}$$

PC can achieve higher energy density than EDLC but this is typically at the expense of power density and cycle life.[170] Metal oxides such as RuO_2,[171] MnO_2,[172] NiO,[173] and conducting polymers such as polyaniline and polypyrrole[174] are commonly studied as PC materials. Surface functional heteroatom-doped carbons also introduces PC contributions to the material.[175] The general specific capacitance values of these materials are briefly compared with each other in **Figure 1.22**.[176]

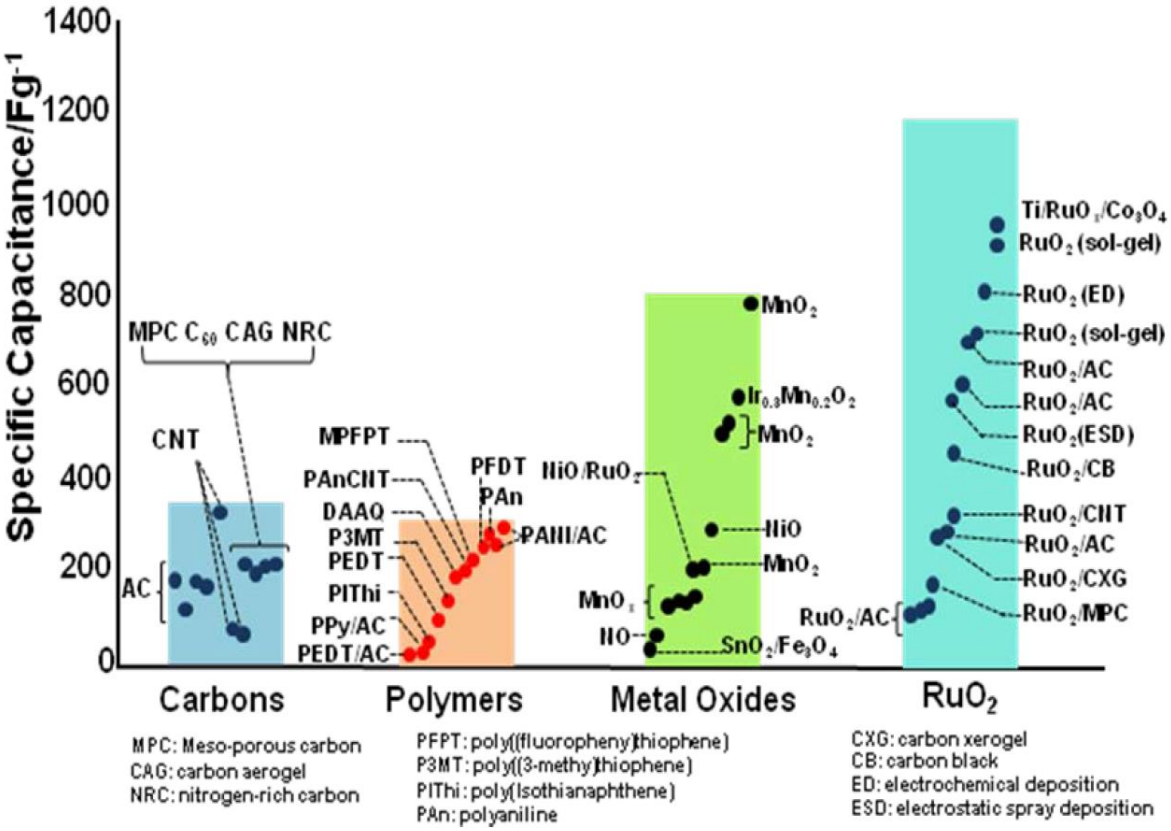

Figure 1.22 The reported specific capacitances of metal oxides, conducting polymers, and carbonaceous materials, in single or composite electrode materials. Figure reprinted from literature source.[176]

1.6.2.3.2.1 Metal Oxides

The cyclic voltammogram profile of metal oxides have a rectangular shape (**Figure 1.23**); not due to EDL charging but as a consequence of multiple redox reactions occurring in the metal oxide.

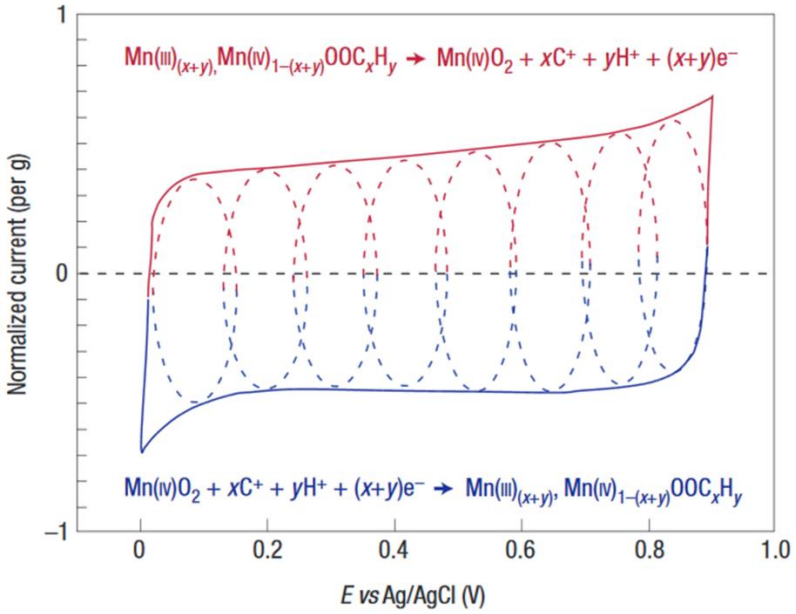

Figure 1.23 Cyclic voltammogram of MnO_2 in 0.1 M K_2SO_4, showing successive multiple surface redox reactions leading to the pseudocapacitive charge storage mechanism. The red (upper) part is related to the oxidation from Mn(III) to Mn(IV) and the blue (lower) part is related to the reduction from Mn(IV) to Mn(III). Figure reprinted from literature source.[167]

RuO_2 is one of the best known and best performing PC materials, due to its intrinsic reversibility of three distinct oxidation states within 1.2 V and high conductivity, with a capacitance as high as 720 F g^{-1} reported for an amorphous hydrous RuO_2 in 1995 by Zheng *et al*.[177] High capacitance from $RuO_2 \cdot xH_2O$ is achieved by the insertion and removal or intercalation of protons into its structure. During charge-discharging the surface is oxidised and reduced reversibly via proton exchange with the solution:[178]

$$RuO_x(OH)_y + \delta H^+ + \delta e^- \leftrightarrow RuO_{x-\delta}(OH)_{y+\delta} \quad (1.20)$$

where $RuO_x(OH)_y$ and $RuO_{x-\delta}(OH)_{y+\delta}$ represent the higher and lower oxidation states of the oxyruthenium species, respectively. The theoretical specific capacitance of $RuO_2 \cdot xH_2O$ was estimated to range between ~1300 to 2200 F g^{-1}.[179] Hu *et al*. (2006) tailored $RuO_2 \cdot xH_2O$ into a nanotubular array to achieve a very high capacitance of 1300 F g^{-1}.[180]

However, despite excelling in performance the use of RuO_2 is limited by its high cost and difficulties in large scale production. For this reason, research in metal oxides has shifted to the development of composite materials with RuO_2 to reduce costs, or towards other non-precious metal oxides and nitrides that can match this standard.[172, 181] However, it has been suggested that the cycling performance of metal oxide electrodes will tend to deteriorate because the electrode can rapidly dissolve in the concentrated electrolyte.[182]

1.6.2.3.2.2 Conducting Polymers

Incorporating a conjugated bond system into the polymer backbone can result in a conductive polymer. The polymers most commonly utilised as supercapacitor materials are polyaniline (PAni), polypyrrole (PPy), polythiophene (PTh), and derivatives of polythiophene.[183] The redox-active capabilities of heteroatom-containing conducting polymers allow high energy densities to be achieved through PC. They are generally attractive as they have high charge density and relatively low cost.

They can be considered as a bridge between metal oxides and porous carbon, with capacitances less than expensive metal oxides but higher than most carbon materials (**Table 1.2**).

Table 1.2 Theoretical and measured capacitances of conducting polymers.

Conducting polymer	M_w (g mol^{-1})	Dopant level	Potential range	Theoretical specific capacitance (F g^{-1})	Measured specific capacitance (F g^{-1})[a]
PAni	93	0.5	0.7	750	240
PPy	67	0.33	0.8	620	530
PTh	84	0.33	0.8	485	-
PEDOT	142	0.33	1.2	210	92

[a] Values from ref. [184]

The significant drawbacks of conducting polymers are their relatively low power due to the slow diffusion of ions within the bulk material and their low cycle life compared with carbon electrodes as the redox sites in polymer backbone are not sufficiently stable for many repeated redox processes. The PC of conducting polymers generally degrade in under a thousand cycles due to the continual doping/de-doping (intercalation/deintercalation) of ions, which causes volumetric changes in the physical structure.[185] For these reasons, the community have moved on to making composite structures with conducting polymers supported on stable, porous rigid materials (*e.g.*, porous carbon, carbon nanotubes (CNTs), carbon monoliths).[186]

1.6.2.3.2.3 Carbons

Carbon-based supercapacitors are based on EDLC. Various structures of carbon have been used in supercapacitor applications, such as carbon onions, CNTs, graphene, activated carbon, carbide-derived carbon, and templated carbon which have different properties (**Table 1.3**). Activated carbon not only has the lowest cost of the various carbon structures but also high volumetric capacitance (reaching 50–80 F cm^{-3}),[187] making functionalisation of these materials viable for commercialisation.

Table 1.3 Different carbon structures used in electric double-layer capacitors. Table reprinted from literature source.[187]

Material	Carbon onions	Carbon nanotubes	Graphene	Activated carbon	Carbide derived carbon	Templated carbon
Dimensionality	0-D	1-D	2-D	3-D	3-D	3-D
Conductivity	High	High	High	Low	Moderate	Low
Volumetric Capacitance	Low	Low	Moderate	High	High	Low
Cost	High	High	Moderate	Low	Moderate	High
Structure	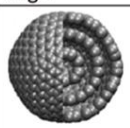	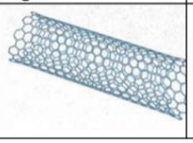	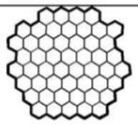	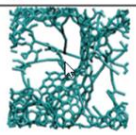	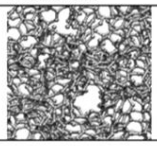	

Adding PC contributions to carbon materials is an efficient way to increase the capacitance that already exists from EDLC. In carbon materials, PC originates from fast redox reactions between heteroatom surface functionalities and the electrolyte. Electro-active heteroatoms on carbons can include oxygen,[188] nitrogen,[189] sulfur,[190] boron,[191] and phosphorus.[192] Heteroatom-doping into carbons cause structural distortions and changes of the charge densities due to their sizes and electronegativities being lower than carbon. The introduction of heteroatoms and their functional groups leads to many advantageous properties, not only extra capacitance, but with enhanced electric conductivity, improved electrochemical stability and better electrolyte wettability.[190]

Oxygen groups are nearly always present on the surface of carbons as a result of the carbonisation process or due to transfer from the carbon precursors. The main oxygen functionalities include lactone-, carbonyl-, carboxyl-, phenolic-, ether-, quinone-, etc (**Figure 1.24**).[193]

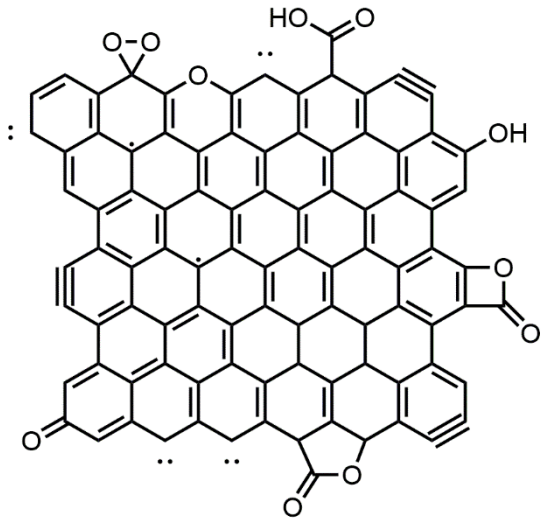

Figure 1.24 Main oxygen functionalities on a graphene sheet.

The oxygen groups are redox-active (**Figure 1.25**),[188] allowing contributions to PC.[194] Hydroquinone/quinone groups are the most commonly reported oxygen functionality for pseudocapacitors[195] and can also be used as additives in electrolytes.[196]

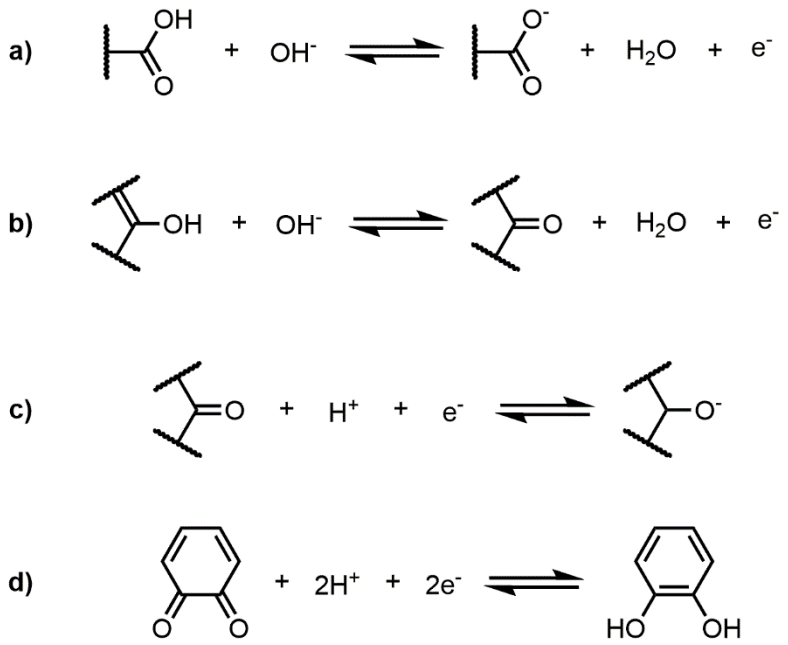

Figure 1.25 Faradaic redox reactions for (a) carboxyl- and (b) carbonyl-groups in base, and (c) carbonyl- and (d) quinone-groups in acid.

N-doped carbonaceous materials, such as N-doped porous carbons,[197] N-doped CNTs,[198] and N-doped graphene[199] are well established as redox-active, pseudocapacitive materials. However, as oxygen groups are nearly always present in these materials, it is difficult to definitively assign the direct contributions of nitrogen-containing groups. Thus, the exact pseudocapacitive mechanisms of N-doped materials has not been well elucidated.

N-atoms can be integrated within various parts of a graphitic structure, such as in the form of pyridinic (N-6), pyrrolic/pyridone (N-5), oxide (N-X), or inside the graphene as quaternary (N-Q) (**Figure 1.26**).[189] Pels *et al*. suggests pyridinic structures are more stable than pyrrolic ones, where there is a decreasing ratio of N-5 to N-6 with increasing temperature, and both are transformed to N-Q at high temperatures.[200]

N-doping in carbon materials can be performed by either carbonising N-containing precursors[111] or by reaction of the organic material with a nitrogenating component, such as a N-rich molecule (*e.g.*, urea,[201] melamine,[202] etc) or NH_3 gas.[203]

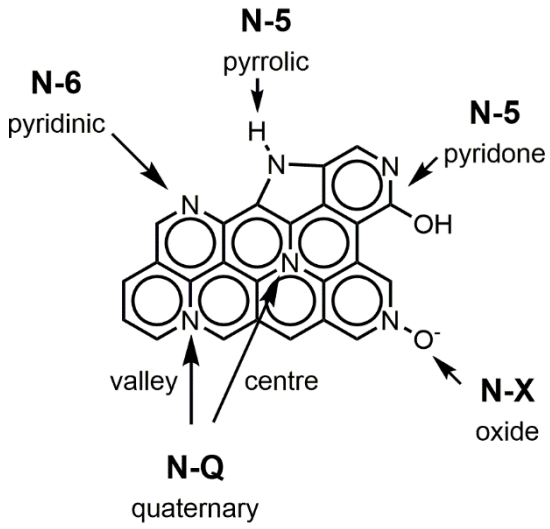

Figure 1.26 Various bonding configurations of N in a graphitic structure.

Seredych *et al*. showed that the capacitance of wood-derived activated carbon can be enhanced from 253 to 330 F g^{-1}, at a current density of 0.05 A g^{-1} in 1 M H_2SO_4, by further carbonisation with urea or melamine under an inert atmosphere.[175] The increased capacitance was observed even with a drop in BET surface area from 2176 $m^2 g^{-1}$ for the activated carbon to 1435 $m^2 g^{-1}$ for the N-doped form. The capacitance retention of the N-doped carbon was also improved to 86% from 0.05 to 1 A g^{-1} whereas the pristine activated carbon only retained 15% capacitance under the same conditions. The group suggests that N-6 and N-5 groups contribute to the PC interactions.

Gueon and Moon studied the effect of N-doping on CNTs packed in a spherical orientation.[204] They used melamine as a N-source and one doped sample with 11.2% N showed a specific capacitance of 215 F g^{-1} at 0.2 A g^{-1}, which is 3.1 times higher than that of the untreated sample. A second sample containing 8.8% N was also synthesised and they observed that as the N content increased, the oxygen content also slightly increased. Therefore, they suggest that N-doping is mediated by the presence of oxygen groups. The relative N-configurations of the particles were found to be N-6 ≈ N-5 > N-Q > N-X.

The redox mechanisms of N-6 and N-5 in acidic electrolyte are thought to follow **Figure 1.27**.[205]

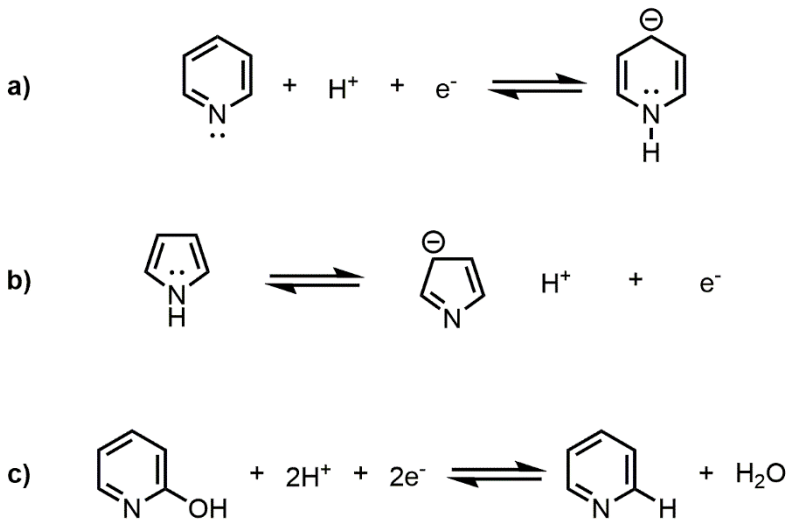

Figure 1.27 Faradaic redox couples for (a) pyridine, (b) pyrrole, and (c) pyridone.

Sulfur is similar to oxygen and nitrogen, in that it has lone-pair electrons and may be able to introduce PC contributions to carbon. S-based supercapacitors are less frequently reported in literature, with the first report made relatively recently by Hasegawa *et al*. (2011),[206] therefore the contributions of sulfur are not well established. The group synthesised a hierarchically porous carbon monolith doped with sulfur from poly(divinylbenzene) and achieved a capacitance of up to 206 F g^{-1} at 0.5 A g^{-1}. Small humps were observed in the CV which were attributed to the PC contributions of sulfur. Zhao *et al*. used resorcinol and thioldiphenol as carbon precursors, where S-doping took the form of sulfide, sulfoxide, and sulfone functional groups.[207] The materials showed improvement in specific capacitance by 38% compared with conventional ordered mesoporous carbon.

S-atoms can be integrated within various parts of a graphitic structure, such as in the form of thiophene, thioether, thiol, sulfoxide, sulfone, sulfonic acid, etc (**Figure 1.28**).[208]

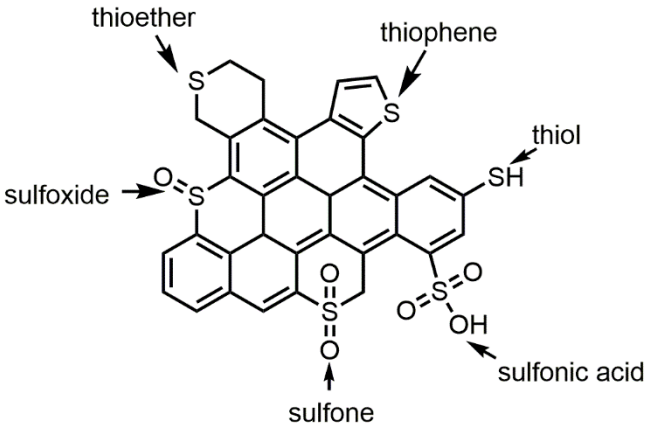

Figure 1.28 Various bonding configurations of S in a graphitic structure.

Co-doping of S and N has also garnered much interest recently with dual doped activated carbon,[209] carbon microspheres,[210] and graphene[211] reported for supercapacitor application.

1.6.3 Gas Storage

Perhaps the largest area of academic study for porous materials recently is the adsorption and storage of gases. The amount of gas absorbed is dependent on the surface area, pore size, and functionality of the materials. Thus, synthetic control over structure and composition of resultant materials offers strategies to heighten adsorption capacity and/or selectivity.

The storage of H_2, CH_4, and CO_2 are among the most widely studied areas. Interest in H_2 and CH_4 is driven by their potential use as a novel alternative and clean energy resource. For example, fuel cells which convert hydrogen and oxygen into electrical energy, have been regarded as a promising future technology due to their high efficiency (~60% *vs.* ~25% from combustion engines),[212] zero environmental pollution, and unlimited sources of reactants. Despite the advantages, H_2 is difficult to store as it naturally exists as a gas, making it particularly difficult to be used in mobile applications. Current methods include storing H_2 in high pressure or cryogenic tanks, however, this comes with various disadvantages and technical complexity. For high pressure tanks, there are safety concerns due to potential leaks, which can form explosive gas mixtures. In addition, full high pressure tanks only contain 4 wt% H_2 adding a large amount of excess mass to transportation vehicles.[212] Storing H_2 as a liquid is attractive as safety concerns regarding high pressure storage can be disregarded, in addition that this method has a higher volumetric density (70.8 kg m^{-3}) than the pressurised gas, improving energy efficiency for transport. Unfortunately however, H_2 liquefaction requires an extremely low temperature of 21.3 K at 1 bar which consumes ~20% of the recoverable energy, and the daily evaporation (to keep H_2 tanks cool) consumes another 2%.[213] For these reasons, materials-based storage which include metal hydrides as chemical H_2 storage materials, and sorbent materials are particularly attractive as they afford safer and more cost effective storage for use in on-board transportation and other sectors. Sorbent materials have an advantage over these due to the lower costs per unit mass and higher cyclability. Unfortunately, current efforts fall short of the Department of Energy (DOE) hydrogen storage targets of 0.045 kg H_2 kg^{-1} and 0.030 kg H_2 L^{-1} by 2020 (**Figure 1.29**),[214] thus, there is a large effort in the community to improve materials-based storage.

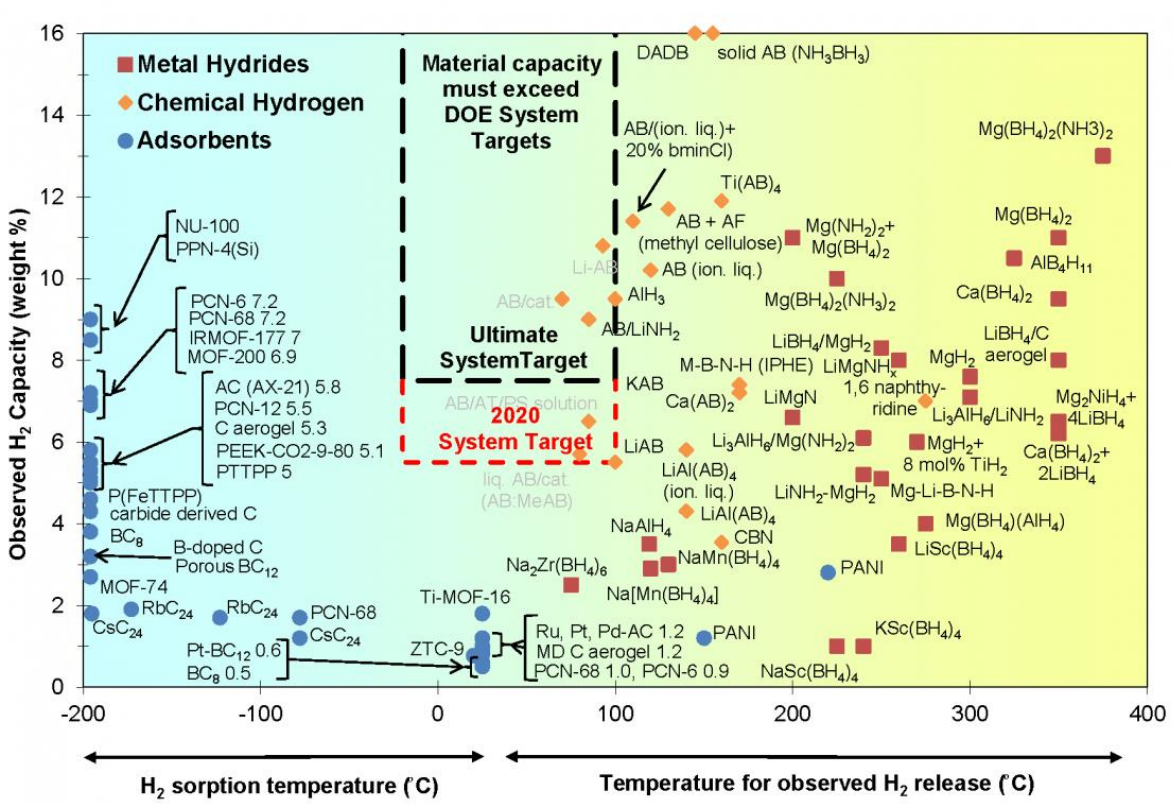

Figure 1.29 H_2 gravimetric capacity as a function of H_2 release temperature for various H_2 storage materials. Figure reprinted from literature source.[214]

CO_2 is the primary greenhouse which contributes towards global warming. The concentration of CO_2 in the atmosphere has increased rapidly in recent decades due to human activities such as burning fuel for energy generation, transportation, and industry (**Figure 1.30a**), which has led to the oceans absorbing ~30% of the emitted anthropogenic CO_2 causing acidification of the oceans (**Figure 1.30b**).[215] The 2013 Assessment Report of the Intergovernmental Panel on Climate Change (IPCC) reports that the increasing concentration of CO_2 in the Earth's atmosphere is the most significant contributor to positive drive in radiative forcing (the forcing agents affecting energy balance, thereby contributing to climate change).[215] The IPCC estimates that the amount of CO_2 in the atmosphere will reach 570 ppm by the year 2100—leading to a global temperature rise of 1.9 °C and a mean sea level of 3.8 m.[216]

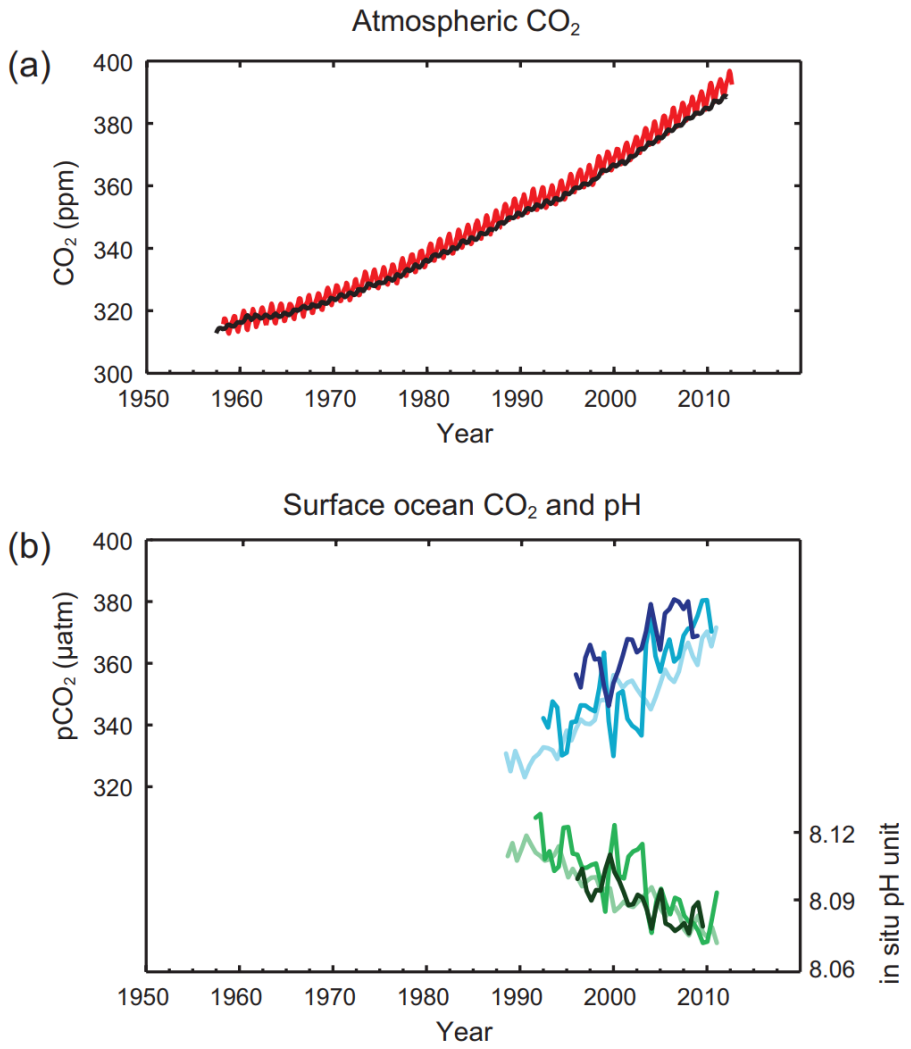

Figure 1.30 Multiple observed indicators of a changing global carbon cycle: (a) atmospheric concentrations of carbon dioxide (CO_2) from Mauna Loa (red) and South Pole (black) since 1958; (b) partial pressure of dissolved CO_2 at the ocean surface (blue curves) and in situ pH (green curves), a measure of the acidity of ocean water. Measurements are from three stations from the Atlantic (29°10'N, 15°30'W – dark blue/dark green; 31°40'N, 64°10'W – blue/green) and the Pacific Oceans (22°45'N, 158°00'W − light blue/light green). Figure reprinted from literature source.[215]

Carbon capture and storage (CCS) is an important technology that can capture up to 90% of CO_2 emissions produced from fossil fuels and preventing the CO_2 from entering the atmosphere.[217] The International Energy Agency (IEA) states that CCS technology is required to reduce the CO_2 contribution of global warming to 19% by 2050, which currently sits at 60%.[218] Current technologies developed include chemical absorption, membrane technology, and physical absorption. Among these technologies, chemical absorption using aqueous amine solutions are most applicable at present, however, they possess large drawbacks such as high equipment corrosion rate, high energy consumption for regeneration, and a large absorber volume is required. As a result, solid absorbents have been

suggested as a promising candidate to overcome the issues associated with chemical absorption. The use of highly porous or mesoporous materials have been suggested to promote effective mass transfer of CO_2 into the material and high capacity. The strategy of enhancing absorption and selectivity of CO_2 through the addition of some chemical absorption by grafting amine groups into the porous material has also been suggested as an effective strategy.[219] The use of porous solid sorbents holds many advantages, such as that they are easy to handle, have high adsorption capacity, can undergo many regeneration cycles, and require less energy for regeneration due to low regeneration temperatures of ~60 °C or pressure swings.[220]

When designing porous materials for the absorption of gases, it is important to focus both on their intrinsic absorption capacities and also their potential for practical applications, where particular sorbents may suit one particular application over another. For example, zeolites, such as 13X, shows a good CO_2 adsorption capacity of 5.5 mmol g^{-1} at 30 °C and 20 bar.[221] However, many zeolites and also MOFs are unstable to the presence of water vapour, which is present in flue feed streams (contains 4–14% CO_2, in addition to NO_x, CO_x, H_2O, and soot impurities),[219] and these materials can readily decompose under air. On the other hand, purely organic materials such as POPs and porous carbons are highly stable under humid conditions and are excellent candidates for gas storage materials.

The main criteria to access a porous material for practical application are:[220, 222]

1. Has high adsorption capacity, working capacity, and selectivity
2. Fast adsorption kinetics
3. Ease of synthesis and activation
4. Thermal and hydrothermal stability
5. Tolerance to feed gas impurities
6. Scalable
7. Cost associated with the synthesis, activation, and regeneration

1.7 Project Overview

This project aims to investigate the discovery and practical applications of new porous carbon-based materials for energy and environmental applications; specifically, in supercapacitive energy storage (Chapter 3 and 4), H_2 and CO_2 storage (Chapter 5), and heavy metal removal from waste water (Chapter 6).

Porous carbons have many advantages such as high surface areas and pore volumes, good thermal, chemical, and mechanical stability, high electrical conductivity, low cost, scalability, and ease of preparation from a variety of precursors which has all tried to be utilised in the applications within this thesis. In particular, the carbons could be tuned to specific applications by both the carbonisation technique and the choice of novel precursors (POPs and inverse vulcanised polymers). POPs can be specifically designed by the choice of monomer, allowing specific functionalisation into the carbon, and allows huge potential for future carbonaceous materials due to the diverse library of POPs. Inverse vulcanised polymers are very cheap materials that can be made from waste by-products and their properties can be improved by designing the correct carbonisation process.

Chapter 2, *Characterisation Methods*, discusses the characterisation techniques used in this thesis and gives a broad background on the technique.

Chapter 3, *Conjugated Microporous Polymer-Derived Carbons for Supercapacitive Energy Storage*, presents the use of the CMP, **CMP-1**, as a carbonisation precursor for supercapacitor application. Observing the effect of directly carbonising a standard CMP and improving its performance through the carbonisation method and the electrolyte used in the supercapacitor. This was one of the first reports for the use of CMPs as a carbonisation precursor.

Chapter 4, *Hypercrosslinked Polymer-Derived Carbons for Supercapacitive Energy Storage*, presents the use of various HCPs, **HCP-Ben**, **HCP-Py**, **HCP-Th**, and **HCP-Ani**, as carbonisation precursors for supercapacitor application. Understanding the role of heteroatom functionality and temperature control in performance. Structure-property relationships, distinguishing between the two supercapacitive mechanisms, EDLC and PC, and linking it to the functionality of each material. Two-electrode cells were also assembled to investigate more realistic supercapacitor performance. This is the first report that investigates the EDLC/PC-structure-property relationship using a large sample size (23 samples).

Chapter 5, *Hypercrosslinked Polymer-Derived Carbons for CO_2 and H_2 Storage*, presents the use of various HCPs, **HCP-Ben**, **HCP-Py**, and **HCP-Th**, as carbonisation precursors for CO_2 and H_2 gas storage application. The surface areas and pore volumes were maximised by chemically activated carbonisations under various temperatures. This reports carbonaceous materials with the highest surface area, and CO_2/H_2 sorption capacity under 298 K/10 bar, to date.

Chapter 6, *Inverse Vulcanised Polymer-Derived Carbons for Heavy Metal Capture*, presents the use of the inverse vulcanised polymer, sulfur dicyclopentadiene (**S-DCPD**), as a carbonisation precursor for Hg and Au capture from water. The surface areas and pore volumes were maximised by the chemical

activation amount and varying temperatures. These materials also showed very high CO_2 and H_2 sorption capacities. This reports the use of a material entirely comprised of low-cost industrial by-products with high performance.

1.8 References

[1] R. Smalley, *MRS Bull.* **2005**, *30*, 412.

[2] Y. Li, Z.-Y. Fu, B.-L. Su, *Adv. Funct. Mater.* **2012**, *22*, 4634.

[3] A. Züttel, *Mater. Today* **2003**, *6*, 24.

[4] Y.-S. Bae, R. Q. Snurr, *Angew. Chem., Int. Ed.* **2011**, *50*, 11586.

[5] M. A. Barakat, *Arab. J. Chem.* **2011**, *4*, 361.

[6] M. Thommes, K. Kaneko, V. Neimark Alexander, P. Olivier James, F. Rodriguez-Reinoso, J. Rouquerol, S. W. Sing Kenneth, in *Pure Appl. Chem.*, Vol. 87, 2015, 1051.

[7] B.-L. Su, C. Sanchez, X.-Y. Yang, in *Hierarchically Structured Porous Materials*, Wiley-VCH Verlag GmbH & Co. KGaA, **2011**, 1.

[8] S. Polarz, B. Smarsly, *J. Nanosci. Nanotechnol.* **2002**, *2*, 581.

[9] C. W. Jones, W. J. Koros, *Ind. Eng. Chem. Res.* **1995**, *34*, 158.

[10] R. Krishna, *Chem. Soc. Rev.* **2012**, *41*, 3099.

[11] K. Xia, Q. Gao, J. Jiang, J. Hu, *Carbon* **2008**, *46*, 1718.

[12] M. Kondo, T. Yoshitomi, H. Matsuzaka, S. Kitagawa, K. Seki, *Angew. Chem., Int. Ed. Engl.* **1997**, *36*, 1725; J. R. Long, O. M. Yaghi, *Chem. Soc. Rev.* **2009**, *38*, 1213; M. O'Keeffe, *Chem. Soc. Rev.* **2009**, *38*, 1215; H. Furukawa, K. E. Cordova, M. O'Keeffe, O. M. Yaghi, *Science* **2013**, *341*, 1230444.

[13] J. R. Holst, A. Trewin, A. I. Cooper, *Nat. Chem.* **2010**, *2*, 915; J. T. A. Jones, T. Hasell, X. Wu, J. Bacsa, K. E. Jelfs, M. Schmidtmann, S. Y. Chong, D. J. Adams, A. Trewin, F. Schiffman, F. Cora, B. Slater, A. Steiner, G. M. Day, A. I. Cooper, *Nature* **2011**, *474*, 367; T. Hasell, A. I. Cooper, *Nat. Rev. Mat.* **2016**, *1*, 16053.

[14] P. M. Budd, B. S. Ghanem, S. Makhseed, N. B. McKeown, K. J. Msayib, C. E. Tattershall, *Chem. Commun.* **2004**, *0*, 230; N. B. McKeown, P. M. Budd, *Chem. Soc. Rev*. **2006**, *35*, 675; N. B. McKeown, P. M. Budd, *Macromolecules* **2010**, *43*, 5163.

[15] A. P. Côté, A. I. Benin, N. W. Ockwig, M. Keeffe, A. J. Matzger, O. M. Yaghi, *Science* **2005**, *310*, 1166.

[16] S.-Y. Ding, W. Wang, *Chem. Soc. Rev*. **2013**, *42*, 548.

[17] N. Huang, P. Wang, D. Jiang, *Nat. Rev. Mat.* **2016**, *1*, 16068.

[18] M. P. Tsyurupa, V. A. Davankov, *React. Funct. Polym.* **2006**, *66*, 768; N. Fontanals, R. M. Marce, F. Borrull, P. A. G. Cormack, *Polym. Chem.* **2015**, *6*, 7231.

[19] S. Xu, Y. Luo, B. Tan, *Macromol. Rapid Commun.* **2013**, *34*, 471.

[20] C. D. Wood, B. Tan, A. Trewin, H. Niu, D. Bradshaw, M. J. Rosseinsky, Y. Z. Khimyak, N. L. Campbell, R. Kirk, E. Stöckel, A. I. Cooper, *Chem. Mater.* **2007**, *19*, 2034.

[21] P. Kuhn, M. Antonietti, A. Thomas, *Angew. Chem., Int. Ed.* **2008**, *47*, 3450.

[22] S. Ren, M. J. Bojdys, R. Dawson, A. Laybourn, Y. Z. Khimyak, D. J. Adams, A. I. Cooper, *Adv. Mater.* **2012**, *24*, 2357.

[23] P. Katekomol, J. Roeser, M. Bojdys, J. Weber, A. Thomas, *Chem. Mater.* **2013**, *25*, 1542.

[24] T. Ben, H. Ren, S. Ma, D. Cao, J. Lan, X. Jing, W. Wang, J. Xu, F. Deng, J. M. Simmons, S. Qiu, G. Zhu, *Angew. Chem., Int. Ed.* **2009**, *48*, 9457.

[25] T. Ben, S. Qiu, *CrystEngComm* **2013**, *15*, 17.

[26] K. Konstas, J. W. Taylor, A. W. Thornton, C. M. Doherty, W. X. Lim, T. J. Bastow, D. F. Kennedy, C. D. Wood, B. J. Cox, J. M. Hill, A. J. Hill, M. R. Hill, *Angew. Chem., Int. Ed.* **2012**, *51*, 6639.

[27] J.-X. Jiang, F. Su, A. Trewin, C. D. Wood, N. L. Campbell, H. Niu, C. Dickinson, A. Y. Ganin, M. J. Rosseinsky, Y. Z. Khimyak, A. I. Cooper, *Angew. Chem., Int. Ed.* **2007**, *46*, 8574.

[28] A. I. Cooper, *Adv. Mater.* **2009**, *21*, 1291.

[29] Y. Xu, S. Jin, H. Xu, A. Nagai, D. Jiang, *Chem. Soc. Rev.* **2013**, *42*, 8012.

[30] S. V. Rogozhin, V. A. Davankov, M. P. Tsyurupa, *USSR Patent 299165*, **1969**.

[31] J. A. Patterson, *Preparation of crosslinked polystyrene and their derivatives for use as solid support or insoluble reagents, in Biochemical Aspects of Reaction on Solid Supports*, Academic Press, New York **1971**.

[32] V. A. Davankov, S. V. Rogoshin, M. P. Tsyurupa, *J. Polym. Sci., Polym. Symp.* **1974**, *47*, 95.

[33] V. A. Davankov, M. M. Ilyin, M. P. Tsyurupa, G. I. Timofeeva, L. V. Dubrovina, *Macromolecules* **1996**, *29*, 8398.

[34] R. Joseph, W. T. Ford, S. Zhang, M. P. Tsyurupa, A. V. Pastukhov, V. A. Davankov, *J. Polym. Sci., Part A: Polym. Chem.* **1997**, *35*, 695.

[35] V. A. Davankov, M. P. Tsyurupa, *React. Polym.* **1990**, *13*, 27.

[36] S. Wang, C. Zhang, Y. Shu, S. Jiang, Q. Xia, L. Chen, S. Jin, I. Hussain, A. I. Cooper, B. Tan, *Sci. Adv.* **2017**, *3*, e1602610.

[37] O. W. Webster, F. P. Gentry, R. D. Farlee, B. E. Smart, *Makromol. Chem.-M. Symp.* **1992**, *54-55*, 477.

[38] N. B. McKeown, S. Makhseed, P. M. Budd, *Chem. Commun.* **2002**, *0*, 2780.

[39] H. M. El-Kaderi, J. R. Hunt, J. L. Mendoza-Cortés, A. P. Côté, R. E. Taylor, M. Keeffe, O. M. Yaghi, *Science* **2007**, *316*, 268.

[40] E. Jin, M. Asada, Q. Xu, S. Dalapati, M. A. Addicoat, M. A. Brady, H. Xu, T. Nakamura, T. Heine, Q. Chen, D. Jiang, *Science* **2017**, *357*, 673.

[41] W. Lu, D. Yuan, D. Zhao, C. I. Schilling, O. Plietzsch, T. Muller, S. Bräse, J. Guenther, J. Blümel, R. Krishna, Z. Li, H.-C. Zhou, *Chem. Mater*. **2010**, *22*, 5964.

[42] M. Rose, W. Bohlmann, M. Sabo, S. Kaskel, *Chem. Commun.* **2008**, *0*, 2462.

[43] Y. Zhao, K. X. Yao, B. Teng, T. Zhang, Y. Han, *Energy Environ. Sci.* **2013**, *6*, 3684; P. Lindemann, M. Tsotsalas, S. Shishatskiy, V. Abetz, P. Krolla-Sidenstein, C. Azucena, L. Monnereau, A. Beyer, A. Gölzhäuser, V. Mugnaini, H. Gliemann, S. Bräse, C. Wöll, *Chem. Mater*. **2014**, *26*, 7189; S. N. Talapaneni, D. Kim, G. Barin, O. Buyukcakir, S. H. Je, A. Coskun, *Chem. Mater.* **2016**, *28*, 4460.

[44] R. Dawson, A. Laybourn, R. Clowes, Y. Z. Khimyak, D. J. Adams, A. I. Cooper, *Macromolecules* **2009**, *42*, 8809; K. V. Rao, S. Mohapatra, T. K. Maji, S. J. George, *Chem. Eur. J* 2012, *18*, 4505; X.-S. Wang, J. Liu, J. M. Bonefont, D.-Q. Yuan, P. K. Thallapally, S. Ma, *Chem. Commun.* **2013**, *49*, 1533; K. Venkata Rao, R. Haldar, T. K. Maji, S. J. George, *Phys. Chem. Chem. Phys.* **2016**, *18*, 156.

[45] L. Chen, Y. Yang, D. Jiang, *J. Am. Chem. Soc.* **2010**, *132*, 9138; Y. Xie, T.-T. Wang, X.-H. Liu, K. Zou, W.-Q. Deng, *Nat. Comm.* **2013**, *4*, 1960; Z.-S. Wu, L. Chen, J. Liu, K. Parvez, H. Liang, J. Shu, H. Sachdev, R. Graf, X. Feng, K. Müllen, *Adv. Mater.* **2014**, *26*, 1450; S. Cui, M. Qian, X. Liu, Z. Sun, P. Du, *ChemSusChem* **2016**, *9*, 2365; Y. He, D. Gehrig, F. Zhang, C. Lu, C. Zhang, M. Cai, Y. Wang, F. Laquai, X. Zhuang, X. Feng, *Adv. Funct. Mater.* **2016**, *26*, 8255.

[46] J.-X. Jiang, Y. Li, X. Wu, J. Xiao, D. J. Adams, A. I. Cooper, *Macromolecules* **2013**, *46*, 8779; N. Kang, J. H. Park, K. C. Ko, J. Chun, E. Kim, H.-W. Shin, S. M. Lee, H. J. Kim, T. K. Ahn, J. Y. Lee, S. U. Son, *Angew. Chem., Int. Ed.* **2013**, *52*, 6228; K. Zhang, D. Kopetzki, P. H. Seeberger, M. Antonietti, F. Vilela, *Angew. Chem., Int. Ed.* **2013**, *52*, 1432; Z. J. Wang, S. Ghasimi, K. Landfester, K. A. I. Zhang, *Chem. Commun.* **2014**, *50*, 8177; Z. J. Wang, S. Ghasimi, K. Landfester, K. A. I. Zhang, *Chem. Mater.* **2015**, *27*, 1921; M. Liras, M. Iglesias, F. Sánchez, *Macromolecules* **2016**, *49*, 1666; Z. J. Wang, S. Ghasimi, K. Landfester, K. A. I. Zhang, *Adv. Synth. Catal.* **2016**, *358*, 2576; C.-A. Wang, Y.-W. Li, X.-L. Cheng, J.-P. Zhang, Y.-F. Han, *RSC Adv*. **2017**, *7*, 408.

[47] J.-X. Jiang, A. Trewin, D. J. Adams, A. I. Cooper, *Chem. Sci.* **2011**, *2*, 1777.

[48] Y. Xu, L. Chen, Z. Guo, A. Nagai, D. Jiang, *J. Am. Chem. Soc*. **2011**, *133*, 17622; X. Liu, Y. Zhang, H. Li, S. A, H. Xia, Y. Mu, *RSC Adv.* 2013, *3*, 21267; Y. Xu, A. Nagai, D. Jiang, *Chem. Commun.* 2013, *49*, 1591; P. Zhang, K. Wu, J. Guo, C. Wang, *ACS Macro Lett.* **2014**, *3*, 1139; B. Bonillo, R. S. Sprick, A. I. Cooper, *Chem. Mater*. **2016**, *28*, 3469.

[49] X. Liu, Y. Xu, D. Jiang, *J. Am. Chem. Soc*. **2012**, *134*, 8738; J. L. Novotney, W. R. Dichtel, *ACS Macro Lett.* **2013**, *2*, 423; Z. Li, H. Li, H. Xia, X. Ding, X. Luo, X. Liu, Y. Mu, *Chem. Eur. J* **2015**, *21*, 17355; T.-M. Geng, H. Zhu, W. Song, F. Zhu, Y. Wang, *J. Mater. Sci.* **2016**, *51*, 4104.

[50] L. Sun, Z. Liang, J. Yu, R. Xu, *Polym. Chem*. **2013**, *4*, 1932.

[51] L. Sun, Y. Zou, Z. Liang, J. Yu, R. Xu, *Polym. Chem.* **2014**, *5*, 471.

[52] Y. Kou, Y. Xu, Z. Guo, D. Jiang, *Angew. Chem., Int. Ed.* **2011**, *50*, 8753.

[53] X. Zhuang, F. Zhang, D. Wu, N. Forler, H. Liang, M. Wagner, D. Gehrig, M. R. Hansen, F. Laquai, X. Feng, *Angew. Chem., Int. Ed.* **2013**, *52*, 9668; F. Xu, X. Chen, Z. Tang, D. Wu, R. Fu, D. Jiang, *Chem. Commun.* **2014**, *50*, 4788; Q. Zhang, S. Ge, X. Wang, H. Sun, Z. Zhu, W. Liang, A. Li, *RSC Adv*. **2014**, *4*, 41649; S. Zhang, W. Huang, P. Hu, C. Huang, C. Shang, C. Zhang, R. Yang, G. Cui, *J. Mater. Chem. A* **2015**, *3*, 1896; S. Chai, N. Hu, Y. Han, X. Zhang, Z. Yang, L. Wei, L. Wang, H. Wei, *RSC Adv.* **2016**, *6*, 49425; J.-S. M. Lee, T.-H. Wu, B. M. Alston, M. E. Briggs, T. Hasell, C.-C. Hu, A. I. Cooper, *J. Mater. Chem. A* **2016**, *4*, 7665; Q. Zhang, Q. Dai, M. Li, X. Wang, A. Li, *J. Mater. Chem. A* **2016**, *4*, 19132; X.-C. Li, Y. Zhang, C.-Y. Wang, Y. Wan, W.-Y. Lai, H. Pang, W. Huang, *Chem. Sci.* **2017**, *8*, 2959.

[54] H. Zhang, Y. Zhang, C. Gu, Y. Ma, *Adv. Energy Mater*. **2015**, *5*, 1402175.

[55] R. S. Sprick, J.-X. Jiang, B. Bonillo, S. Ren, T. Ratvijitvech, P. Guiglion, M. A. Zwijnenburg, D. J. Adams, A. I. Cooper, *J. Am. Chem. Soc*. **2015**, *137*, 3265; V. S. Vyas, F. Haase, L. Stegbauer, G. Savasci, F. Podjaski, C. Ochsenfeld, B. V. Lotsch, *Nat. Comm.* **2015**, *6*, 8508; A. Bhunia, D. Esquivel, S. Dey, R. Fernandez-Teran, Y. Goto, S. Inagaki, P. Van Der Voort, C. Janiak, *J. Mater. Chem. A* **2016**, *4*, 13450; L. Li, Z. Cai, Q. Wu, W.-Y. Lo, N. Zhang, L. X. Chen, L. Yu, *J. Am. Chem. Soc.* **2016**, *138*, 7681; L. Li, W.-y. Lo, Z. Cai, N. Zhang, L. Yu, *Macromolecules* **2016**, *49*, 6903; R. S. Sprick, B. Bonillo, M. Sachs, R. Clowes, J. R. Durrant, D. J. Adams, A. I. Cooper, *Chem. Commun.* **2016**, *52*, 10008; C. Yang, B. C. Ma, L. Zhang, S. Lin, S. Ghasimi, K. Landfester, K. A. I. Zhang, X. Wang, *Angew. Chem., Int. Ed.* **2016**, *55*, 9202.

[56] J. Weber, A. Thomas, *J. Am. Chem. Soc*. **2008**, *130*, 6334; J.-X. Jiang, A. Laybourn, R. Clowes, Y. Z. Khimyak, J. Bacsa, S. J. Higgins, D. J. Adams, A. I. Cooper, *Macromolecules* **2010**, *43*, 7577; Q. Chen, J.-X. Wang, Q. Wang, N. Bian, Z.-H. Li, C.-G. Yan, B.-H. Han, *Macromolecules* **2011**, *44*, 7987.

[57] B. Kiskan, J. Weber, *ACS Macro Lett.* 2012, *1*, 37; T. Ratvijitvech, R. Dawson, A. Laybourn, Y. Z. Khimyak, D. J. Adams, A. I. Cooper, *Polymer* **2014**, *55*, 321.

[58] M. Trunk, A. Herrmann, H. Bildirir, A. Yassin, J. Schmidt, A. Thomas, *Chem. Eur. J* **2016**, *22*, 7179.

[59] R. Dawson, A. Laybourn, Y. Z. Khimyak, D. J. Adams, A. I. Cooper, *Macromolecules* **2010**, *43*, 8524.

[60] J.-X. Jiang, F. Su, H. Niu, C. D. Wood, N. L. Campbell, Y. Z. Khimyak, A. I. Cooper, *Chem. Commun.* **2008**, *0*, 486.

[61] L. Chen, Y. Honsho, S. Seki, D. Jiang, *J. Am. Chem. Soc.* **2010**, *132*, 6742.

[62] J. Schmidt, M. Werner, A. Thomas, *Macromolecules* **2009**, *42*, 4426.

[63] S. Yuan, B. Dorney, D. White, S. Kirklin, P. Zapol, L. Yu, D.-J. Liu, *Chem. Commun.* **2010**, *46*, 4547.

[64] L. Hao, B. Luo, X. Li, M. Jin, Y. Fang, Z. Tang, Y. Jia, M. Liang, A. Thomas, J. Yang, L. Zhi, *Energy Environ. Sci.* **2012**, *5*, 9747.

[65] P. Pandey, A. P. Katsoulidis, I. Eryazici, Y. Wu, M. G. Kanatzidis, S. T. Nguyen, *Chem. Mater.* **2010**, *22*, 4974.

[66] M. G. Rabbani, A. K. Sekizkardes, O. M. El-Kadri, B. R. Kaafarani, H. M. El-Kaderi, *J. Mater. Chem.* **2012**, *22*, 25409; C. Xu, N. Hedin, *J. Mater. Chem. A* **2013**, *1*, 3406.

[67] G. Lu, H. Yang, Y. Zhu, T. Huggins, Z. J. Ren, Z. Liu, W. Zhang, *J. Mater. Chem. A* **2015**, *3*, 4954.

[68] B. Li, Z. Guan, X. Yang, W. D. Wang, W. Wang, I. Hussain, K. Song, B. Tan, T. Li, *J. Mater. Chem. A* **2014**, *2*, 11930; Y. Zhang, S. A, Y. Zou, X. Luo, Z. Li, H. Xia, X. Liu, Y. Mu, *J. Mater. Chem. A* **2014**, *2*, 13422.

[69] C. Gu, Y. Chen, Z. Zhang, S. Xue, S. Sun, K. Zhang, C. Zhong, H. Zhang, Y. Pan, Y. Lv, Y. Yang, F. Li, S. Zhang, F. Huang, Y. Ma, *Adv. Mater.* **2013**, *25*, 3443.

[70] C. Gu, N. Huang, J. Gao, F. Xu, Y. Xu, D. Jiang, *Angew. Chem., Int. Ed*. **2014**, *53*, 4850; C. Gu, N. Huang, Y. Chen, L. Qin, H. Xu, S. Zhang, F. Li, Y. Ma, D. Jiang, *Angew. Chem., Int. Ed.* **2015**, *54*, 13594.

[71] J. Germain, J. M. J. Frechet, F. Svec, *J. Mater. Chem.* 2007, *17*, 4989; J. Germain, J. M. J. Frechet, F. Svec, *Chem. Commun.* **2009**, *0*, 1526.

[72] R. Chinchilla, C. Nájera, *Chem. Rev.* **2007**, *107*, 874.

[73] R. Chinchilla, C. Najera, *Chem. Soc. Rev.* **2011**, *40*, 5084.

[74] H. Doucet, J.-C. Hierso, *Angew. Chem., Int. Ed.* **2007**, *46*, 834.

[75] S. Thorand, N. Krause, *J. Org. Chem.* **1998**, *63*, 8551.

[76] N. Miyaura, K. Yamada, A. Suzuki, *Tetrahedron Lett.* **1979**, *20*, 3437; N. Miyaura, A. Suzuki, J. Chem. Soc., *Chem. Commun.* **1979**, *0*, 866.

[77] Q. Liu, Z. Tang, M. Wu, Z. Zhou, *Polym. Int.* **2014**, *63*, 381.

[78] K. Wang, L.-M. Yang, X. Wang, L. Guo, G. Cheng, C. Zhang, S. Jin, B. Tan, A. Cooper, *Angew. Chem., Int. Ed.* **2017**, *56*, 14149.

[79] J. K. Stille, E. Mainen, *J. Polym. Sci., Part B: Polym. Lett.* **1966**, *4*, 39; J. K. Stille, E. L. Mainen, *Macromolecules* **1968**, *1*, 36.

[80] A. B. Marco, D. Cortizo-Lacalle, I. Perez-Miqueo, G. Valenti, A. Boni, J. Plas, K. Strutyński, S. De Feyter, F. Paolucci, M. Montes, A. N. Khlobystov, M. Melle-Franco, A. Mateo-Alonso, *Angew. Chem.* **2017**, *56*, 6946.

[81] F. Pennella, R. L. Banks, G. C. Bailey, *Chem. Commun.* **1968**, *0*, 1548.

[82] F. A. Vingiello, J. Yanez, J. A. Campbell, *J. Org. Chem.* **1971**, *36*, 2053.

[83] W. Li, A. Zhang, H. Gao, M. Chen, A. Liu, H. Bai, L. Li, *Chem. Commun*. **2016**, *52*, 2780.

[84] L. Tan, B. Tan, *Chem. Soc. Rev.* **2017**, *46*, 3322.

[85] V. A. Davankov, M. P. Tsyurupa, *Hypercrosslinked Polymeric Networks and Adsorbing Materials: Synthesis, Properties, Structure, and Applications*, Elsevier, Oxford, UK **2011**.

[86] R. T. Woodward, L. A. Stevens, R. Dawson, M. Vijayaraghavan, T. Hasell, I. P. Silverwood, A. V. Ewing, T. Ratvijitvech, J. D. Exley, S. Y. Chong, F. Blanc, D. J. Adams, S. G. Kazarian, C. E. Snape, T. C. Drage, A. I. Cooper, *J. Am. Chem. Soc.* **2014**, *136*, 9028.

[87] C. Wilson, M. J. Main, N. J. Cooper, M. E. Briggs, A. I. Cooper, D. J. Adams, *Polym. Chem.* **2017**, *8*, 1914.

[88] D. Chen, S. Gu, Y. Fu, Y. Zhu, C. Liu, G. Li, G. Yu, C. Pan, *Polym. Chem.* **2016**, *7*, 3416; M. G. Schwab, A. Lennert, J. Pahnke, G. Jonschker, M. Koch, I. Senkovska, M. Rehahn, S. Kaskel, *J. Mater. Chem.* **2011**, *21*, 2131.

[89] B. Li, R. Gong, W. Wang, X. Huang, W. Zhang, H. Li, C. Hu, B. Tan, *Macromolecules* **2011**, *44*, 2410.

[90] Y. Luo, B. Li, W. Wang, K. Wu, B. Tan, *Adv. Mater.* **2012**, *24*, 5703.

[91] Z. Ren, Y. Lan, Y. Wang, *Aligned Carbon Nanotubes: Introduction to Carbon*, Springer-Verlag, Heidelberg **2013**.

[92] K. E. Spear, J. P. Dismukes, *Synthetic Diamond: Emerging CVD Science and Technology*, John Wiley & Sons, **1994**.

[93] J. Emsley, *Nature's Building Blocks: An A-Z Guide to the Elements*, OUP Oxford, **2011**.

[94] M. Inagaki, F. Kang, in *Materials Science and Engineering of Carbon*, Butterworth-Heinemann, **2016**, 1.

[95] M. Inagaki, K. Feiyu, *Carbon Materials Science and Engineering: From Fundamentals to Applications*, Tsinghua University Press 清华大学出版社有限公司, **2006**.

[96] E. Frank, L. M. Steudle, D. Ingildeev, J. M. Spörl, M. R. Buchmeiser, *Angew. Chem., Int. Ed.* **2014**, *53*, 5262.

[97] E. Fitzer, K.-H. Kochling, H. P. Boehm, H. Marsh, *Pure Appl. Chem.* **1995**, *67*, 473.

[98] H. Sugisawa, H. Edo, *J. Food Sci.* **1966**, *31*, 561.

[99] I. Karacan, T. Soy, *J. Mater. Sci.* **2013**, *48*, 2009.

[100] S. Subramoney, *Adv. Mater.* **1998**, *10*, 1157.

[101] A. F. Ismail, L. I. B. David, *J. Membr. Sci.* **2001**, *193*, 1.

[102] M. A. Shannon, P. W. Bohn, M. Elimelech, J. G. Georgiadis, B. J. Marinas, A. M. Mayes, *Nature* **2008**, *452*, 301.

[103] J.-S. Yu, S. Kang, S. B. Yoon, G. Chai, *J. Am. Chem. Soc.* **2002**, *124*, 9382.

[104] D. D. L. Chung, *Carbon* **2001**, *39*, 279.

[105] A. D. Roberts, X. Li, H. Zhang, *Chem. Soc. Rev.* **2014**, *43*, 4341.

[106] L. Qie, W. Chen, H. Xu, X. Xiong, Y. Jiang, F. Zou, X. Hu, Y. Xin, Z. Zhang, Y. Huang, *Energy Environ. Sci.* **2013**, *6*, 2497.

[107] B. Fang, J. H. Kim, M. Kim, J.-S. Yu, *Chem. Mater*. **2009**, *21*, 789.

[108] A. Stein, Z. Wang, M. A. Fierke, *Adv. Mater.* **2009**, *21*, 265.

[109] W. M. A. W. Daud, W. S. W. Ali, M. Z. Sulaiman, *Carbon* **2000**, *38*, 1925; W. Li, K. Yang, J. Peng, L. Zhang, S. Guo, H. Xia, *Ind. Crop. Prod.* **2008**, *28*, 190.

[110] P. K. Singla, S. Miura, R. R. Hudgins, P. L. Silveston, *Fuel* **1983**, *62*, 645.

[111] D. Hulicova, J. Yamashita, Y. Soneda, H. Hatori, M. Kodama, *Chem. Mater*. **2005**, *17*, 1241.

[112] Z. Rozlívková, M. Trchová, M. Exnerová, J. Stejskal, *Synth. Met.* **2011**, *161*, 1122.

[113] Y. Hou, T. Huang, Z. Wen, S. Mao, S. Cui, J. Chen, *Adv. Energy Mater.* **2014**, *4*, 1400337; K. Shen, X. Chen, J. Chen, Y. Li, *ACS Catal.* **2016**, *6*, 5887.

[114] H. Nishihara, T. Kyotani, *Adv. Mater.* **2012**, *24*, 4473.

[115] J. H. Knox, B. Kaur, G. R. Millward, *J. Chromatogr., A* **1986**, *352*, 3.

[116] T. Kyotani, L.-f. Tsai, A. Tomita, *Chem. Mater.* **1995**, *7*, 1427.

[117] T. Kyotani, T. Nagai, S. Inoue, A. Tomita, *Chem. Mater*. **1997**, *9*, 609.

[118] B. Liu, H. Shioyama, T. Akita, Q. Xu, *J. Am. Chem. Soc.* **2008**, *130*, 5390.

[119] J. Lee, S. Yoon, T. Hyeon, S. M. Oh, K. Bum Kim, *Chem. Commun.* **1999**, *0*, 2177.

[120] T. F. Baumann, J. H. Satcher, *Chem. Mater*. **2003**, *15*, 3745.

[121] R. Ryoo, S. H. Joo, S. Jun, *J. Phys. Chem. B* **1999**, *103*, 7743; S. Jun, S. H. Joo, R. Ryoo, M. Kruk, M. Jaroniec, Z. Liu, T. Ohsuna, O. Terasaki, *J. Am. Chem. Soc*. **2000**, *122*, 10712.

[122] C. Liang, K. Hong, G. A. Guiochon, J. W. Mays, S. Dai, *Angew. Chem., Int. Ed.* **2004**, *43*, 5785.

[123] C. Liang, S. Dai, *J. Am. Chem. Soc.* **2006**, *128*, 5316.

[124] H. Kosonen, S. Valkama, A. Nykänen, M. Toivanen, G. ten Brinke, J. Ruokolainen, O. Ikkala, *Adv. Mater*. **2006**, *18*, 201.

[125] L. Chuenchom, R. Kraehnert, B. M. Smarsly, *Soft Matter* **2012**, *8*, 10801.

[126] M. Sevilla, R. Mokaya, *Energy Environ. Sci.* **2014**, *7*, 1250.

[127] C. Bouchelta, M. S. Medjram, O. Bertrand, J.-P. Bellat, *J. Anal. Appl. Pyrolysis* **2008**, *82*, 70.

[128] E. A. Dawson, G. M. B. Parkes, P. A. Barnes, M. J. Chinn, *Carbon* **2003**, *41*, 571.

[129] S. Osswald, C. Portet, Y. Gogotsi, G. Laudisio, J. P. Singer, J. E. Fischer, V. V. Sokolov, J. A. Kukushkina, A. E. Kravchik, *J. Solid State Chem.* **2009**, *182*, 1733.

[130] S. K. Ryu, H. Jin, D. Gondy, N. Pusset, P. Ehrburger, *Carbon* **1993**, *31*, 841; F. Rodríguez-Reinoso, M. Molina-Sabio, M. T. González, *Carbon* **1995**, *33*, 15.

[131] J. Wang, S. Kaskel, *J. Mater. Chem.* **2012**, *22*, 23710.

[132] B. Jibril, O. Houache, R. Al-Maamari, B. Al-Rashidi, *J. Anal. Appl. Pyrolysis* **2008**, *83*, 151.

[133] M. Molina-Sabio, F. Rodríguez-Reinoso, *Colloids Surf. A* **2004**, *241*, 15.

[134] T. Otowa, R. Tanibata, M. Itoh, *Gas Sep. Purif.* **1993**, *7*, 241.

[135] M. A. Lillo-Ródenas, D. Cazorla-Amorós, A. Linares-Solano, *Carbon* **2003**, *41*, 267.

[136] H. Teng, L.-Y. Hsu, Ind. Eng. *Chem. Res.* **1999**, *38*, 2947.

[137] M. J. Bleda-Martínez, J. A. Maciá-Agulló, D. Lozano-Castelló, E. Morallón, D. Cazorla-Amorós, A. Linares-Solano, *Carbon* **2005**, *43*, 2677.

[138] M. A. Lillo-Ródenas, J. Juan-Juan, D. Cazorla-Amorós, A. Linares-Solano, *Carbon* **2004**, *42*, 1371.

[139] H. Marsh, D. S. Yan, T. M. O'Grady, A. Wennerberg, *Carbon* **1984**, *22*, 603.

[140] D. Lozano-Castelló, J. M. Calo, D. Cazorla-Amorós, A. Linares-Solano, *Carbon* **2007**, *45*, 2529.

[141] J. Romanos, M. Beckner, T. Rash, L. Firlej, B. Kuchta, P. Yu, G. Suppes, C. Wexler, P. Pfeifer, *Nanotechnology* **2012**, *23*, 015401.

[142] W. Qiao, S.-H. Yoon, I. Mochida, Energy Fuels **2006**, 20, 1680; H. Wang, Q. Gao, J. Hu, *J. Am. Chem. Soc*. **2009**, *131*, 7016.

[143] T. Kyotani, *Bull. Chem. Soc. Jpn.* 2**006**, *79*, 1322.

[144] F. Kapteijn, G. Abbel, J. A. Moulijn, *Fuel* **1984**, *63*, 1036.

[145] BP Energy Outlook 2017 Edition, BP p.l.c. 2017. Retrieved from http://www.bp.com/content/dam/bp/pdf/energy-economics/energy-outlook-2017/bp-energy-outlook-2017.pdf

[146] P. S. Nigam, A. Singh, *Progr. Energy Combust. Sci.* **2011**, *37*, 52.

[147] R. A. Voloshin, M. V. Rodionova, S. K. Zharmukhamedov, T. Nejat Veziroglu, S. I. Allakhverdiev, *Int. J. Hydrogen Energy* **2016**, *41*, 17257.

[148] Co-utilisation of Biomass with Fossil Fuels, IEA Bioenergy. Retrieved from http://www.ieabioenergy.com/wp-content/uploads/2013/09/5267.pdf

[149] What is Biomass Energy?, Conserve Energy Future. Retrieved from http://www.conserve-energy-future.com/Advantages_Disadvantages_BiomassEnergy.php

[150] P. Simon, Y. Gogotsi, *Nat. Mater*. **2008**, *7*, 845.

[151] J. M. Tarascon, M. Armand, *Nature* **2001**, *414*, 359.

[152] J. W. Choi, D. Aurbach, *Nat. Rev. Mat.* **2016**, *1*, 16013.

[153] H. Vikström, S. Davidsson, M. Höök, *Appl. Energy* **2013**, *110*, 252.

[154] J. R. Miller, P. Simon, *Science* **2008**, *321*, 651.

[155] A. G. Pandolfo, A. F. Hollenkamp, *J. Power Sources* **2006**, *157*, 11.

[156] E. Frackowiak, *Phys. Chem. Chem. Phys*. **2007**, 9, 1774.

[157] R. Kötz, M. Carlen, *Electrochim. Acta* **2000**, *45*, 2483.

[158] M. S. Halper, J. C. Ellenbogen, *Supercapacitors: A Brief Overview*, Mc Lean, Virginia **2006**; Y. M. Volfkovich, A. A. Mikhailin, D. A. Bograchev, V. E. Sosenkin, V. S. Bagotsky, *Studies of Supercapacitor Carbon Electrodes with High Pseudocapacitance*, **2012**.

[159] Z. Stojek, *The Electrical Double Layer and Its Structure*, **2010**.

[160] H. Helmholtz, *Ann. Phys.* **1853**, *165*, 211.

[161] H. Helmholtz, *Ann. Phys.* **1879**, *243*, 337.

[162] L. L. Zhang, X. S. Zhao, *Chem. Soc. Rev.* **2009**, *38*, 2520.

[163] G. Gouy, *J. Phys. Radium* **1910**, *9*, 457; G. Gouy, *Compt. Rend.* **1910**, *149*, 654; D. L. Chapman, *Phil. Mag.* **1913**, *25*, 475.

[164] O. Stern, Z. *Electrochem.* **1924**, *30*, 508.

[165] D. Qu, H. Shi, *J. Power Sources* **1998**, *74*, 99; M. Endo, T. Maeda, T. Takeda, Y. J. Kim, K. Koshiba, H. Hara, M. S. Dresselhaus, *J. Electrochem. Soc.* **2001**, *148*, A910.

[166] E. Raymundo-Piñero, K. Kierzek, J. Machnikowski, F. Béguin, *Carbon* **2006**, *44*, 2498.

[167] P. Simon, Y. Gogotsi, *Nat. Mater.* **2008**, *7*, 845.

[168] J. Huang, B. G. Sumpter, V. Meunier, *Chem. Eur. J* **2008**, *14*, 6614.

[169] B. E. Conway, *Electrochemical Supercapacitors: Scientific Fundamentals and Technological Applications*, Kluwer Academic/Plenum Publisher, New York **1999**.

[170] B. You, L. Wang, L. Yao, J. Yang, *Chem. Commun.* **2013**, *49*, 5016.

[171] V. Subramanian, S. C. Hall, P. H. Smith, B. Rambabu, *Solid State Ion.* **2004**, *175*, 511.

[172] M. Ghaemi, F. Ataherian, A. Zolfaghari, S. M. Jafari, *Electrochim. Acta* **2008**, *53*, 4607.

[173] Q. Lu, M. W. Lattanzi, Y. Chen, X. Kou, W. Li, X. Fan, K. M. Unruh, J. G. Chen, J. Q. Xiao, *Angew. Chem., Int. Ed.* **2011**, *50*, 6847.

[174] L. Li, E. Liu, J. Li, Y. Yang, H. Shen, Z. Huang, X. Xiang, W. Li, *J. Power Sources* **2010**, *195*, 1516; L. Z. Fan, Y. S. Hu, J. Maier, P. Adelhelm, B. Smarsly, M. Antonietti, *Adv. Funct. Mater.* **2007**, *17*, 3083.

[175] M. Seredych, D. Hulicova-Jurcakova, G. Q. Lu, T. J. Bandosz, *Carbon* **2008**, *46*, 1475.

[176] K. Naoi, P. Simon, *J. Electrochem. Soc.* **2008**, *17*, 34.

[177] J. P. Zheng, P. J. Cygan, T. R. Jow, *J. Electrochem. Soc.* **1995**, *142*, 2699.

[178] S. Ardizzone, G. Fregonara, S. Trasatti, *Electrochim. Acta* **1990**, *35*, 263; S. Trasatti, G. Buzzanca, *J. Electroanal. Chem.* **1971**, *29*, App. 1.

[179] C.-C. Hu, W.-C. Chen, K.-H. Chang *J. Electrochem. Soc.* **2004**, *151*, A281.

[180] C.-C. Hu, K.-H. Chang, M.-C. Lin, Y.-T. Wu, *Nano Lett.* **2006**, *6*, 2690.

[181] A. Burke, *J. Power Sources* **2000**, *91*, 37; R. Kötz, M. Carlen, *Electrochim. Acta* **2000**, *45*, 2483; D. Choi, G. E. Blomgren, P. N. Kumta, *Adv. Mater.* **2006**, *18*, 1178.

[182] Y. Wang, A. Yuan, X. Wang, *J. Solid State Electrochem.* **2008**, *12*, 1101.

[183] G. A. Snook, P. Kao, A. S. Best, *J. Power Sources* **2011**, *196*, 1.

[184] G. A. Snook, G. Z. Chen, *J. Electroanal. Chem.* **2008**, *612*, 140.

[185] H. Talbi, P.-E. Just, L. H. Dao, *J. Appl. Electrochem.* **2003**, *33*, 465.

[186] J. Yang, Y. Liu, S. Liu, L. Li, C. Zhang, T. Liu, *Mater. Chem. Front.* **2017**, *1*, 251; C. Peng, S. Zhang, D. Jewell, G. Z. Chen, *Prog. Nat. Sci.* **2008**, *18*, 777.

[187] P. Simon, Y. Gogotsi, *Acc. Chem. Res.* **2013**, *46*, 1094.

[188] Y. J. Oh, J. J. Yoo, Y. I. Kim, J. K. Yoon, H. N. Yoon, J.-H. Kim, S. B. Park, *Electrochim. Acta* **2014**, *116*, 118.

[189] Y. Deng, Y. Xie, K. Zou, X. Ji, *J. Mater. Chem. A* **2016**, *4*, 1144.

[190] J. P. Paraknowitsch, A. Thomas, *Energy Environ. Sci.* **2013**, *6*, 2839.

[191] N. Shcherban, S. Filonenko, P. Yaremov, V. Dyadyun, I. Bezverkhyy, V. Ilyin, *J. Mater. Sci.* **2017**, *52*, 1523.

[192] D. Hulicova-Jurcakova, A. M. Puziy, O. I. Poddubnaya, F. Suárez-García, J. M. D. Tascón, G. Q. Lu, *J. Am. Chem. Soc.* **2009**, *131*, 5026.

[193] L. R. Radovic, B. Bockrath, *J. Am. Chem. Soc.* **2005**, *127*, 5917.

[194] L.-x. Li, F. Li, *New Carbon Mater.* **2011**, *26*, 224.

[195] K. Okajima, K. Ohta, M. Sudoh, *Electrochim. Acta* **2005**, *50*, 2227; M. Latifatu, H. S. Lee, C. S. Yoon, J. Oh, J. H. Park, J. W. Park, J. M. Ko, *Int. J. Electrochem. Sci.* **2016**, *11*, 5353.

[196] D. Vonlanthen, P. Lazarev, K. A. See, F. Wudl, A. J. Heeger, *Adv. Mater.* **2014**, *26*, 5095; E. Frackowiak, M. Meller, J. Menzel, D. Gastol, K. Fic, *Faraday Discuss.* **2014**, *172*, 179.

[197] X. Y. Chen, C. Chen, Z. J. Zhang, D. H. Xie, X. Deng, J. W. Liu, *J. Power Sources* **2013**, *230*, 50.

[198] A. R. John, P. Arumugam, *J. Power Sources* **2015**, *277*, 387.

[199] H. M. Jeong, J. W. Lee, W. H. Shin, Y. J. Choi, H. J. Shin, J. K. Kang, J. W. Choi, *Nano Lett.* **2011**, *11*, 2472.

[200] J. R. Pels, F. Kapteijn, J. A. Moulijn, Q. Zhu, K. M. Thomas, *Carbon* **1995**, *33*, 1641.

[201] S. Ratha, A. K. Samantara, K. K. Singha, A. S. Gangan, B. Chakraborty, B. K. Jena, C. S. Rout, *ACS Appl. Mater. Interfaces* **2017**, *9*, 9640.

[202] L.-B. Xing, S.-F. Hou, J. Zhou, J.-L. Zhang, W. Si, Y. Dong, S. Zhuo, *J. Solid State Chem.* **2015**, *230*, 224.

[203] A. S. Jalilov, G. Ruan, C.-C. Hwang, D. E. Schipper, J. J. Tour, Y. Li, H. Fei, E. L. G. Samuel, J. M. Tour, *ACS Appl. Mater. Interfaces* **2015**, *7*, 1376.

[204] D. Gueon, J. H. Moon, *ACS Appl. Mater. Interfaces* **2015**, *7*, 20083.

[205] Y.-H. Lee, K.-H. Chang, C.-C. Hu, *J. Power Sources* **2013**, *227*, 300.

[206] G. Hasegawa, M. Aoki, K. Kanamori, K. Nakanishi, T. Hanada, K. Tadanaga, *J. Mater. Chem.* **2011**, *21*, 2060.

[207] X. Zhao, Q. Zhang, C.-M. Chen, B. Zhang, S. Reiche, A. Wang, T. Zhang, R. Schlögl, D. Sheng Su, *Nano Energy* **2012**, *1*, 624.

[208] G. Hasegawa, T. Deguchi, K. Kanamori, Y. Kobayashi, H. Kageyama, T. Abe, K. Nakanishi, *Chem. Mater.* **2015**, *27*, 4703.

[209] C. Chang, X. Yang, S. Xiang, X. Lin, H. Que, M. Li, *J. Electrochem. Soc.* **2017**, *164*, A1601.

[210] W. Lei, J. Guo, Z. Wu, C. Xuan, W. Xiao, D. Wang, *Sci. Bull.* **2017**, *62*, 1011.

[211] T. Wang, L.-X. Wang, D.-L. Wu, W. Xia, D.-Z. Jia, *Sci. Rep.* **2015**, *5*, 9591.

[212] L. Schlapbach, A. Züttel, *Nature* **2001**, *414*, 353.

[213] A. W. C. van den Berg, C. O. Arean, *Chem. Commun*. **2008**, *0*, 668.

[214] Materials-Based Hydrogen Storage, Department of Energy. Retrieved from https://energy.gov/eere/fuelcells/materials-based-hydrogen-storage

[215] Climate Change 2013: The Physical Science Basis, Intergovernmental Panel on Climate Change. Retrieved from https://www.ipcc.ch/report/ar5/wg1/

[216] M. K. Mondal, H. K. Balsora, P. Varshney, *Energy* **2012**, *46*, 431; J. Hansen, M. Sato, P. Kharecha, D. Beerling, R. Berner, V. Masson-Delmotte, M. Pagani, M. Raymo, D. L. Royer, J. C. Zachos, *Open Atmos. Sci. J.* **2008**, *2*, 217.

[217] What is CCS?, Carbon Capture & Storage Association. Retrieved from http://www.ccsassociation.org/what-is-ccs/

[218] C.-H. Yu, C.-H. Huang, C.-S. Tan, *Aerosol Air Qual. Res.* **2012**, *12*, 745.

[219] D. Y. C. Leung, G. Caramanna, M. M. Maroto-Valer, *Renew. Sus. Energ. Rev.* **2014**, *39*, 426.

[220] R. Sabouni, H. Kazemian, S. Rohani, *Environ. Sci. Pollut. R.* **2014**, *21*, 5427.

[221] B. Danielle, K. Mourad, N. Patrick, M. Murielle, H. Robert, *Sci. Technol. Adv. Mater* **2008**, *9*, 013007.

[222] O. K. Farha, J. T. Hupp, *Acc. Chem. Res.* **2010**, *43*, 1166.

Chapter 2

Characterisation Methods

2.1 Introduction

The characterisation methods in this chapter are arranged based on their relative usage throughout the thesis. The chapter begins with an explanation about gas adsorption theory due to its heavy usage in the field of porous materials. Electrochemistry and supercapacitor theory were introduced in Chapter 1 but the methods for quantifying performances are discussed here in this chapter. Other characterisation methods are discussed more briefly.

2.2 Gas Sorption

Adsorption is defined as the enrichment of molecules, atoms, or ions in the vicinity of an interface.[1] There are two types of adsorption: physical (physisorption) and chemical (chemisorption). *Physisorption* is a general phenomenon where a gas is brought into contact with a surface of a solid through attractive intermolecular forces (van der Waals). Specific molecular interactions, such as polarisation, can also occur as a result of geometric and electronic properties of the gas and the surface. *Chemisorption* is when intermolecular forces are involved which lead to the formation of chemical bonds between the gas and surface.

Gas adsorption measurements are used to characterise the porosity of materials. The characterisation method is used to monitor the adsorption of various subcritical fluids (*e.g.*, N_2 at 77 K, CO_2 at 298 K, H_2 at 77 K) and can also be used for organic vapours and supercritical gases. Various modelling techniques have been developed, such as density functional theory and molecular simulations (*e.g.*, Monte-Carlo simulations), which allows more accurate and comprehensive porosity structural analysis from the obtained adsorption data. The relationship between the amount of gas adsorbed and the equilibrium pressure of the gas at constant temperature is known as the *adsorption isotherm*.[1]

The solid surface can be defined by three individual different levels (**Figure 2.1**). A van der Waals surface which is formed by the outer surface of the solid (**Figure 2.1, 1**). A probe-accessible surface (known as the Connolly surface in simulation studies) which is the surface assigned by the physisorbed gas probe rolling over the van der Waals surface (**Figure 2.1, 2**). A *r*-distance surface (**Figure 2.1, 3**) which is located at distance *r* from the probe-accessible surface. Therefore, smaller gas probes will give more accurate information about the pore size of solids as large probes may not be able to access very small pores.

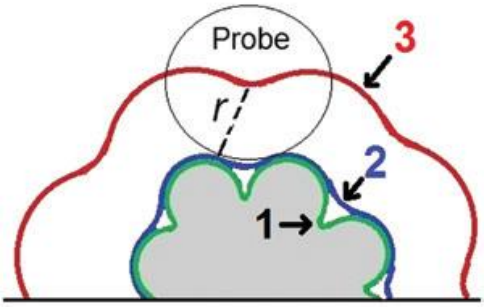

Figure 2.1 Schematic representation of several surfaces of an adsorbent, 1: van der Waals; 2: probe-accessible; 3: *r*-distance. Figure reprinted from literature source.[1]

In the context of physisorption, there are three classifications of pores depending on the size:[2]

1. Macropores: pores with widths exceeding 50 nm
2. Mesopores: pores of widths between 2 and 50 nm
3. Micropores: pores with widths less than 2 nm

Physisorption filling of micropores always occurs at low relative pressures, where the range is dependent on the shape and dimensions of the micropores, the size of the gas molecule, and their interactions with each other. Physisorption in mesopores happens in multiple stages. Monolayer adsorption initially occurs where all the gas molecules are in contact with the surface. Multilayer adsorption then occurs where the gas accommodates more than one layer so that not all of the gas molecules are in contact with the surface. This is followed by pore condensation, where the gas condenses to a liquid-like phase in the pore at a pressure less than the saturation pressure of the bulk liquid, generally at a partial pressure (P/P_0) of around 0.5.

The analysis of pore sizes over the complete micropore and mesopore range requires experiments that span over a broad range of pressures starting below 1 Pa. Thus, gas sorption is usually performed within the relative pressure range $10^{-7} \leq P/P_0 \leq 1$ with special instruments which ensures the sample cell and manifold can be evacuated to very low pressures. It is also important to ensure that the purity of the absorptive gas is not less than 99.999%.[1] The amount of remaining un-adsorbed gas in the effective void volume (dead space) should also be calculated. This is performed using a non-adsorbing gas such as helium to measure the dead space under operational conditions. Prior to measurements, the sample should be outgassed at elevated temperature to remove all physisorbed species from the surface to avoid false results.

In 1985, IUPAC originally recommended physisorption isotherms to be grouped into six types.[2] However, due to the rise of new characteristic types of isotherms, the 2015 IUPAC document has refined the classifications to take these into account, shown in **Figure 2.2**.[1]

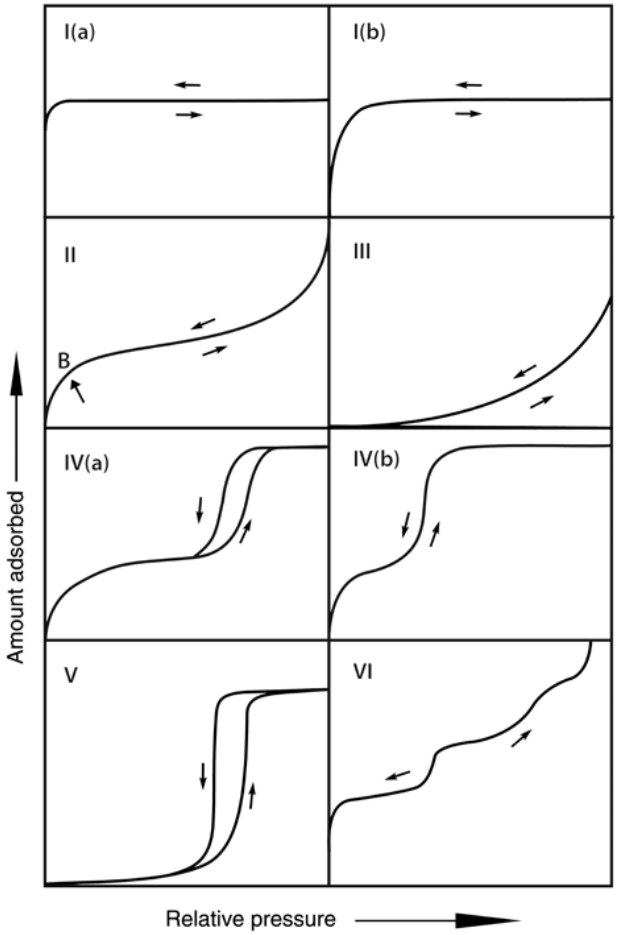

Figure 2.2 Classification of physisorption isotherms. Figure reprinted from literature source.[1]

As a general rule of thumb, uptakes at very low pressures are associated with micropores, uptakes at around $P/P_0 = 0.5$ are associated with mesopores, and uptakes associated at high pressures are associated with macropores. Steep uptakes at particular regions are associated with narrow pore sizes in that area, *e.g.*, the Type Ia isotherm has a steep uptake at very low pressures due to enhanced adsorbent-adsorptive interactions in the narrow micropores. Thus, the broad uptake in a Type Ib isotherm is due to the material having a broader pore size distribution in the micropore range. Materials with Type I isotherms have small external surfaces areas relative to the internal surface areas within the material. The Type II isotherm is associated with macroporous or non-porous materials. Adsorption at high P/P_0 is a result of unrestricted monolayer-multilayer absorption. The sharp knee in the beginning of the isotherm at point B indicates completion of monolayer coverage. If this point is more gradual, this corresponds to an overlap of the monolayer coverage and the onset of multilayer adsorption in the isotherm. In a Type III isotherm, there is no point B due to no identifiable monolayer formation as the interactions between the

gas and the surface are relatively weak and the absorbed gas molecules occupy more favoured sites on the surface of the macroporous or non-porous solid. Type IV isotherms are given by hierarchical structures with both micropores and mesopores. Mesopore absorption behaviour is determined by both gas-surface interactions and also by interactions between the molecules in the condensed state. Capillary condensation in the mesopores result in a hysteresis loop in Type IVa isotherms. This occurs when the pore width exceeds a certain critical width dependent on the absorption system and temperature; with it occurring with measurements under N_2 for pores wider than ~4 nm.[3] Thus, Type IVb isotherms are observed with mesopores of smaller width. A Type V isotherm has no adsorption in the low pressure region due to weak absorbent-absorbate interactions but a rise in higher pressure attributed to molecular clustering followed by pore filling. Stepwise increases in a Type VI isotherm is attributed to layer-by-layer adsorption on a highly uniform non-porous surface. The step height represents the capacity of the absorbed layer whilst the sharpness is dependent on the system and temperature.

There are two major models used to describe the adsorption of gases onto a surface, the Langmuir model[4] and the Brunauer-Emmett-Teller (BET) model.[5]

2.2.1 Langmuir Model

The Langmuir model is the simpler of the two which explains adsorption by assuming the adsorbate behaves as an ideal gas under isothermal conditions. The following assumptions are made in the model:[6]

1. The surface is a perfectly flat plane and homogeneous
2. The absorbing gas absorbs onto an immobile state
3. All sites are equivalent
4. Each site can only hold one molecule (monolayer)
5. Adsorbed molecules do not interact with each other

An adsorbate gas (A_g) adsorbs onto a solid surface (S) to yield an adsorbed complex (A_{ad}):

$$A_g + S \rightleftarrows A_{ad} \tag{2.1}$$

The adsorption is associated with an equilibrium constant, K, which is a function of the rate constants for adsorption (k_a) and desorption (k_d):

$$K = \frac{k_a}{k_d} \tag{2.2}$$

The fractional occupancy of adsorption sites, θ, is the fraction of the number of sites occupied by an adsorbate (N_s) over the total number of adsorption sites (N). This can also be expressed in terms of relative amounts or volumes:

$$\theta = \frac{N_s}{N} = \frac{n_a}{n_m} = \frac{V_a}{V_m} \tag{2.3}$$

where n_a is the amount in moles adsorbed, n_m is the total amount that can be absorbed on the monolayer, V_a is the volume of gas absorbed, and V_m is the total volume that can be absorbed on the monolayer.

The rate of adsorption (r_{ad}) is dependent on k_a, P/P_0, and the non-occupied adsorption sites (1–θ). The rate of desorption (r_d) is dependent on k_d and θ. Thus:

$$r_{ad} = k_a P/P_0(1-\theta) \tag{2.4}$$

$$r_d = k_d\theta \tag{2.5}$$

Therefore, at equilibrium:

$$k_a P/P_0(1-\theta) = k_d\theta \tag{2.6}$$

This can be rearranged to give the fractional occupancy as a function of pressure which yields the Langmuir adsorption isotherm:

$$\theta = \frac{KP/P_0}{(1+KP/P_0)} \tag{2.7}$$

The equation can be rewritten by substituting **Equation 2.3** into **Equation 2.7** to give the following:

$$\frac{P/P_0}{n_a} = \frac{1}{n_m K} + \frac{P/P_0}{n_m} \tag{2.8}$$

Where $(P/P_0)/n_a$ *vs.* P/P_0 will yield a straight line plot of gradient $1/n_m$. The Langmuir surface area (SA_{Lang}) can therefore be calculated using n_m, the cross-section of the adsorbate gas (a_m), and Avagadro's number (N_A):

$$SA_{Lang} = n_m N_A a_m \tag{2.9}$$

The specific SA_{Lang} can be calculated by normalising it against the mass of solid.

2.2.2 Brunauer-Emmett-Teller (BET) Model

The BET model is an extension of the Langmuir model which takes into account multilayer adsorption. The following assumptions are made in the model:

1. The gas molecules can adsorb onto the surface in infinite layers
2. The gas molecules only interact with adjacent layers
3. Langmuir theory can be applied to each layer

The BET equation in linear form is:

$$\frac{P/P_0}{n_a(1-P/P_0)} = \frac{1}{n_m c} + \frac{c-1}{n_m c} \times (P/P_0) \tag{2.10}$$

where c is the BET constant, defined as:

$$c = \exp(\frac{E_1 - E_L}{RT}) \tag{2.11}$$

where E_1 is the heat of adsorption for the first layer and E_L is the heat of adsorption for the second layer and beyond.

n_m can thus be derived from the intercept of the BET equation by plotting $(P/P_0)/n_a(1- P/P_0)$ *vs.* P/P_0. Using n_m derived from the BET model, SA_{BET} can thus be derived:

$$SA_{BET} = n_m N_A a_m \tag{2.9}$$

The BET method is the most widely used procedure for evaluating the surface areas of solids, despite some weaknesses in its theoretical foundations. For example, as BET theory assumes the surface is homogeneous, thus differences between the surface and lateral adsorbate-adsorbate interactions are ignored.[7] Therefore, high energy sites will be occupied at lower relative pressures, resulting in nonlinearity of BET plots at $P/P_0 < 0.5$. There are also difficulties in differentiating mono-multilayer adsorption from pore filling. Thus, the measured surface area reflects an "apparent" BET surface area and not a real internal surface, which can be an overestimation.

The gas sorption analyses presented in this thesis were performed as follows.

2.2.3 Nitrogen Adsorption Isotherms

Nitrogen adsorption and desorption isotherms were obtained using an ASAP2420 or ASAP2020 volumetric adsorption analyser (Micromeritics Instrument Corporation) with approximately 100 mg samples at 77.3 K with an equilibration interval of 30 s. All samples were degassed at 120 °C for 15 h under dynamic vacuum (10^{-5} bar) before analysis.
Brunauer-Emmett-Teller (BET) surface area was obtained in the relative pressure (P/P_0) range of 0.05–0.20, and total pore volume (V_t) was determined from the amount of nitrogen adsorbed at P/P_0 = *ca.* 0.99.

2.2.4 Pore Size Analysis

Pore structure properties of the samples were determined via nitrogen adsorption and desorption at 77.3 K using a volumetric technique on an ASAP2420 or ASAP2020 adsorption analyser (Micromeritics Instrument Corporation). Before analysis, the samples were degassed at 120 °C for 15 h under dynamic vacuum (10^{-5} bar). The cylindrical pore - pillared clay surface model was used. The isotherms of this model are calculated using a combination of NL-DFT calculations and experimental isotherms for reference samples of montmorillionite.[8] The model reports pore widths from 3.8 to 387 Å.

2.2.5 Carbon Dioxide and Hydrogen Adsorption Isotherms

1 bar carbon dioxide and hydrogen isotherms were collected on a Micromeritics ASAP2020 at 298 K and 77.3 K, respectively with approximately 100 mg samples. 10 bar carbon dioxide and hydrogen isotherms were collected using a Micromeritics ASAP2050 at 298 K and 77.3 K, respectively with approximately 100 mg samples. Carbon dioxide saturation isotherms were performed using a Micromeritics 3Flex Surface Characterization Analyser equipped with a cryostat at 195 K with approximately 100 mg samples. All samples were degassed at 120 °C for 15 h under vacuum (10^{-5} bar) before analysis

2.3 Electrochemistry

2.3.1 Evaluating Supercapacitor Performance

CV, also known as *I-V* plots, can aid the understanding of charge transfer mechanisms. The CV profiles depends on a variety of parameters such as electrode, scan rate, temperature, and electrolyte composition (*i.e.*, solvent, salt, pH).

CV is an important experimental criterion for quantifying the capacitive performance of a material. A quasi-rectangular CV profile is characteristic of good reversible supercapacitor behaviour (**Figure 2.3**).[9]

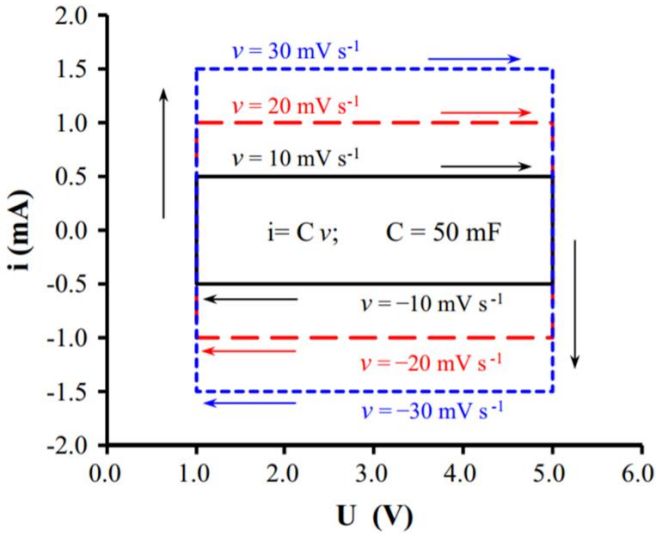

Figure 2.3 Cyclic voltammetry showing quasi-rectangular profiles at various scan rates. Figure reprinted from literature source.[9]

Potential windows are chosen to avoid irreversible electrode and electrolyte reactions, such as solvent decomposition and irreversible redox reactions on the electrodes. This avoids over-oxidation and/or over-reduction so that we only record current from the "capacitive potential range" of the material.[10] **Figure 2.4** shows an activated carbon electrode in 3 M KOH run towards overly negative potentials,[11] resulting in a steep negative current due to irreversible hydrogen evolution from the electrolyte and hydrogen storage on the electrode surface denoted by the additional current response upon positive sweep.

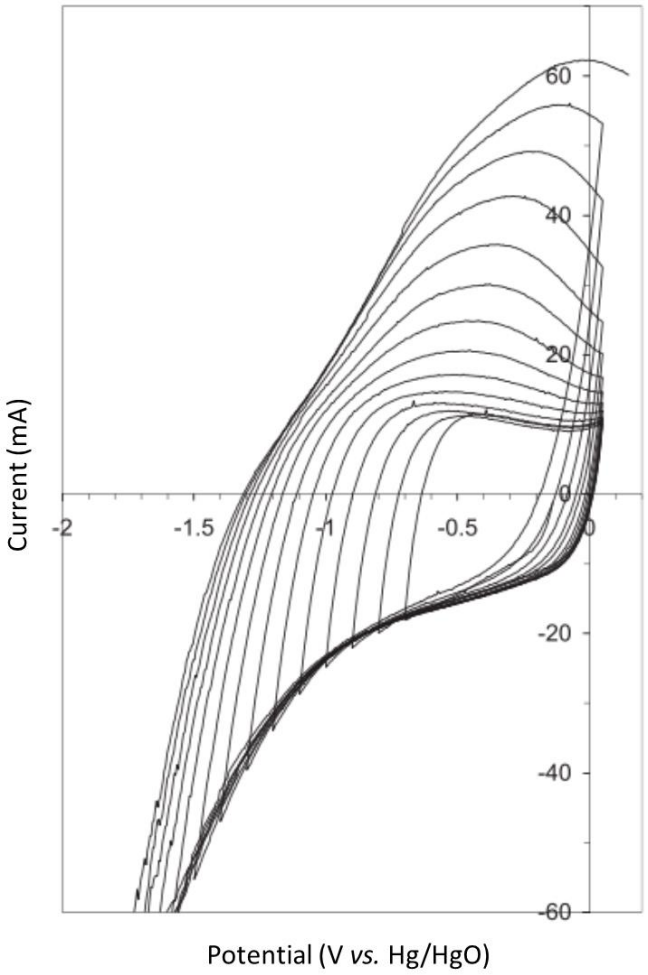

Figure 2.4 Cyclic voltammogram profile of activated carbon towards negative potentials in 3 M KOH at a scan rate of 100 mV s^{-1}. Figure reprinted from literature source.[11]

The specific capacitance (C_{sv}) of a material can be calculated by CV using the following equation:[12]

$$C_{sv} = \frac{q_a + q_c}{2ms \times \Delta V} \tag{2.10}$$

where q_a and q_c represents the anodic and cathodic charge integrated from the positive and negative sweeps of the CV, m is the mass loading of active material, s is the potential scan speed and ΔV corresponds to the potential window of the CV.

Galvanostatic charge-discharge (GCD), also known as constant current charge-discharge, applies a constant current to charge (positive current) or discharge (negative current) to evaluate the rate of potential increase (charging) or decrease (discharging). A triangular charge-discharge shape (**Figure 2.5**),[9]is typical behaviour for constant charge and discharge of supercapacitive materials with good reversibility.[13]

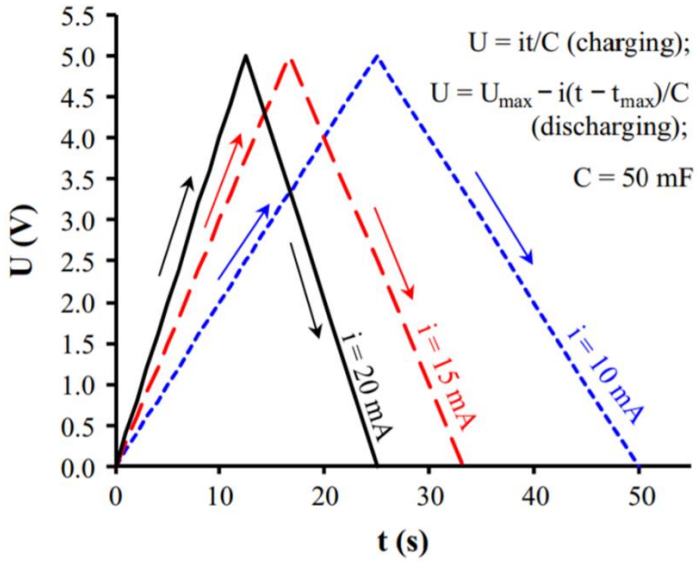

Figure 2.5 Galvanostatic charge-discharge showing triangular profiles at various current densities. Figure reprinted from literature source.[9]

The specific capacitance (C_{sc}) of a material can be calculated by GCD using the following equation:[14]

$$C_{sc} = \frac{I \times t}{V \times m} \tag{2.11}$$

where I is the discharge current, t is discharge time, V is the discharge voltage, and m is the mass loading of active material.

Coulombic efficiency (η, also known as Faradaic efficiency, Faradaic yield, or current efficiency) is the efficiency with which charge, which has been transferred into a system through a electrochemical reaction, can come back out of the system. Coulombic efficiency decreases when undesirable side reactions occur, causing heat and/or chemical by-products. The coulombic efficiency of a system can be calculated from GCD using the following equation:

$$\eta = \frac{t_d}{t_c} \times 100\% \tag{2.12}$$

where t_d is the discharge time and t_c is the charge time.

Energy and power densities are two important parameters for evaluating the electrochemical performance of supercapacitors. The maximum energy (E in W h kg^{-1}) can be calculated using **Equation 2.13**:[15]

$$E = \frac{1}{2\times3600} CV^2 \quad (2.13)$$

where C is the specific capacitance and V is the maximum cell voltage.

The maximum power (P in W kg^{-1}) can be obtained using **Equation 2.14**:[16]

$$P = \frac{V^2}{4R} \quad (2.14)$$

where V is the maximum cell voltage and R is the equivalent series resistance (ESR).

Factors which affect the overall ESR in supercapacitors are the electric conductivity of the electrode material, the contact resistance between the electrode and the current collector, the resistance of the electrolyte, and the resistance from ionic diffusion within the pores and by the separator. The ESR in EDL capacitors is lower than that of pseudocapacitors as the charge storage mechanism is purely electrostatic and does not involve any resistance from charge transfer; therefore, the power densities of pseudocapacitors are generally lower. However, the ESR can be reduced by using an additive, such as carbon black, which improves the conductivity of the electrode material and the electrical contact between the electrode and current collector.[17]

The power density can also be calculated using the energy density from **Equation 2.13** and the discharge time from GCD:

$$P = \frac{\mathrm{E}}{t/3600} \quad (2.15)$$

Electrochemical impedance spectroscopy (EIS) uses an alternating current electrode processes by applying a small amplitude alternating signal then observing how the electrode returns to the stationary state.[18] The real part of the impedance at a given frequency gives information about the ESR which includes several contributions such as the electrolyte (including the separator) resistance, the resistance of the active material, and the active material/current collector interface resistance.[19] A Nyquist plot of a cell typically contains a semi-circle and then a vertical step towards Z' (**Figure 2.6**).[20] The plot gives information about the solution resistance (R_s) and the charge transfer resistance (R_{ct}). R_s is related to the bulk solution resistance which depends on the conductivity of the electrolyte and the thickness of the separator. R_{ct} can be separated into electronic and ionic resistance components.[19] The electronic resistance is a combination of the intrinsic electronic conductivity of the carbon particles, the electronic

contact between particles, and the contact between the active material and the current collector. The ionic resistance is the resistance of the electrolyte in the pores of the electrode, which is dependent on the electrolyte conductivity, the porous structure of the material, and the thickness of the active material. If the semicircle is small, incomplete, or does not appear, this indicates that the interfacial charge-transfer resistance and distributed capacitance are very small, indicating excellent capacitive responses.[21] The internal resistance (R_{int}) of the cell can be estimated from the intersection between the low frequency section crossing the X-axis and the region (if any) immediately after the semicircle.[22] The imaginary part of the Nyquist plot approaching vertical (phase angle towards 90°) in the low frequency region indicates a typical and ideal capacitive behaviour.[23]

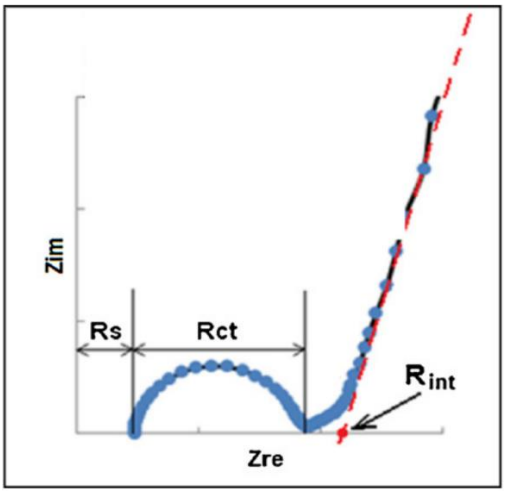

Figure 2.6 A typical Nyquist plot for an EDLC cell. Figure modified from literature source.[20]

The specific capacitance (C_{si}) from EIS can be calculated using the following equation:[20]

$$C_{si} = -1/(2\pi f Z'' m) \quad (2.16)$$

where f is frequency, Z'' is the imaginary part of impedance, and m is the mass of active material.

2.3.2 Electrolytes

The performance of supercapacitors can also be affected by the choice of electrolyte. Supercapacitors can utilise either an aqueous, organic, or an ionic liquid electrolyte. Aqueous electrolytes, such as acids (*e.g.*, H_2SO_4), neutral-based (*e.g.*, Na_2SO_4), and alkalis (*e.g.*, KOH), have various advantages over that of organic electrolytes such as low cost, better safety, high ionic conductivity (up to ~1 S cm^{-1}), lower ESR, and possess lower minimum pore size requirements. The capacitance of high surface area carbons in aqueous electrolytes tend to be higher than when using organic electrolytes, due to the higher

dielectric constants of aqueous systems.[24] However, aqueous electrolytes have lower decomposition voltages compared to organic electrolytes, of ~1.23 V.[25]

Organic electrolytes have been developed that allow for cell operating voltages of above 2.5 V.[25, 26] Organic electrolytes, such as acetonitrile or propylene carbonate containing dissolved quaternary alkyl ammonium salts, are already employed in commercial supercapacitors, which target high energy applications.[27] However, the main disadvantage of organic electrolytes are that the ESR is significantly higher than that of aqueous electrolytes, typically by a factor of 50. This leads to a higher internal resistance in the capacitor and therefore a lower maximum power density. Additionally, to avoid electrolyte depletion during the supercapacitor charging process, electrolyte concentration must be high. If the volume of electrolyte is too low compared to the surface area of the electrode, the supercapacitor performance is reduced. This problem is predominant in organic electrolytes where the solubility of the salts may be low. Therefore, trade-offs exist between aqueous and organic electrolytes in terms of capacitance, cost, resistance, and voltage, which one must balance with the intended application of the supercapacitor.

Ionic liquids are salts that possess a melting point lower than the operation temperature. They have replaced organic electrolytes in a wide range of applications.[28] Their advantages include a large liquid phase range, wider potential window, and better safety profiles than organic electrolytes, making them viable for many types of electrochemical systems. However, ionic liquids are extremely expensive and have shown very limited capacitance when used with various materials (*e.g.*, less than 25 F g^{-1} in CNTs).[29]

When weighing the properties of the different electrolyte types against each other, aqueous electrolytes are an ideal choice for screening many new materials; primarily due to their low cost, better safety profiles, and ease of use. Supercapacitive materials developed under the aqueous electrolyte system can be optimised through the electrochemical setup in a later stage.

The decomposition of water into oxygen and hydrogen at standard temperature (298 K) and pressure (1 atm), at pH 0, are based on the following two half reactions *vs.* the standard hydrogen electrode (SHE):

$$\text{Oxidation: } 2H_2O \rightarrow 4H^+ + 4e^- + O_2;\ E°_{1/2} = 1.23\ \text{V} \tag{2.17}$$

$$\text{Reduction: } 4H^+ + 4e^- \rightarrow 2H_2;\ E°_{1/2} = 0\ \text{V} \tag{2.18}$$

Thus, according the **Equation 2.19**, the standard potential of water electrolysis is 1.23 V, shown by **Equation 2.20**.

$$E°_{cell} = E°_{cathode} - E°_{anode} \quad (2.19)$$

$$\text{Overall: } 2H_2O \rightarrow H_2 + O_2;\ E°_{cell} = 1.23\ V \quad (2.20)$$

Under basic conditions, oxygen and hydrogen evolution occurs by the **Equation 2.21 and 2.22**, respectively. The overall reaction is the same as **Equation 2.20**.

$$\text{Oxidation: } 4OH^- \rightarrow O_2 + 2H_2O + 4e^- \quad (2.21)$$

$$\text{Reduction: } 2H_2O + 2e^- \rightarrow H_2 + 2OH^- \quad (2.22)$$

Although the potential remains unchanged at various pHs, the position of the potential window is dependent of pH. Acidic electrolytes are positioned at more positive potentials, whereas, basic electrolytes are positioned at more negative potentials. The potentials can be obtained from the Nernst equation,[30] which is derived from the Gibbs free energy. Gibbs free energy is related to the cell potential by the following equation:

$$\Delta G = -nFE \quad (2.23)$$

where n is the number of moles of electrons transferred and F is the Faraday constant. Under standard state conditions, this can be rewritten as:

$$\Delta G° = -nFE° \quad (2.24)$$

From thermodynamics, the Gibbs free energy under non-standard conditions is related to the Gibbs free energy under standard conditions by the equation:

$$\Delta G = \Delta G° + RT\ln Q \quad (2.25)$$

where R is the ideal gas constant, T is the temperature (in K), and Q is the concentration ratio of products over reactants. **Equation 2.23 and 2.24** can be substituted into **Equation 2.25** to yield the following equation:

$$-nFE = -nFE° + RT\ln Q \quad (2.26)$$

And this both sides of the above can be divided by $-nF$ to yield the Nernst equation:[30]

$$E = E^0 - \frac{RT}{nF}\ln Q \quad (2.27)$$

where R is the ideal gas constant, T is the temperature (in K), n is the number of moles of electrons transferred, F is the Faraday constant, and Q is the concentration ratio of products over reactants. At 298 K, **Equation 2.27** can be rewritten as:

$$E = E^0 - \frac{0.0592}{n}\log Q \quad (2.28)$$

Thus, at pH 14, the potential for the hydrogen evolution reaction can be calculated by the following:

$$E = E^0 - \frac{0.0592}{2}\log\frac{P_{H_2}}{(H^+)^2} = 0 - \frac{0.0592}{2}\log(10^{14})^2 = 0 - \frac{0.0592}{2}(28) = -0.8288\,V \quad (2.29)$$

$[H^+]$ obtained from the pH from the following equation:

$$pH = -\log [H^+] \quad (2.30)$$

The stability of water at various pHs can be expressed by a potential/pH relationship, known as a "Pourbaix diagram" (**Figure 2.7**). Thus, E_{cell} does not change with pH as both redox couples shift -59.2 mV/pH, according to the Nernst equation.

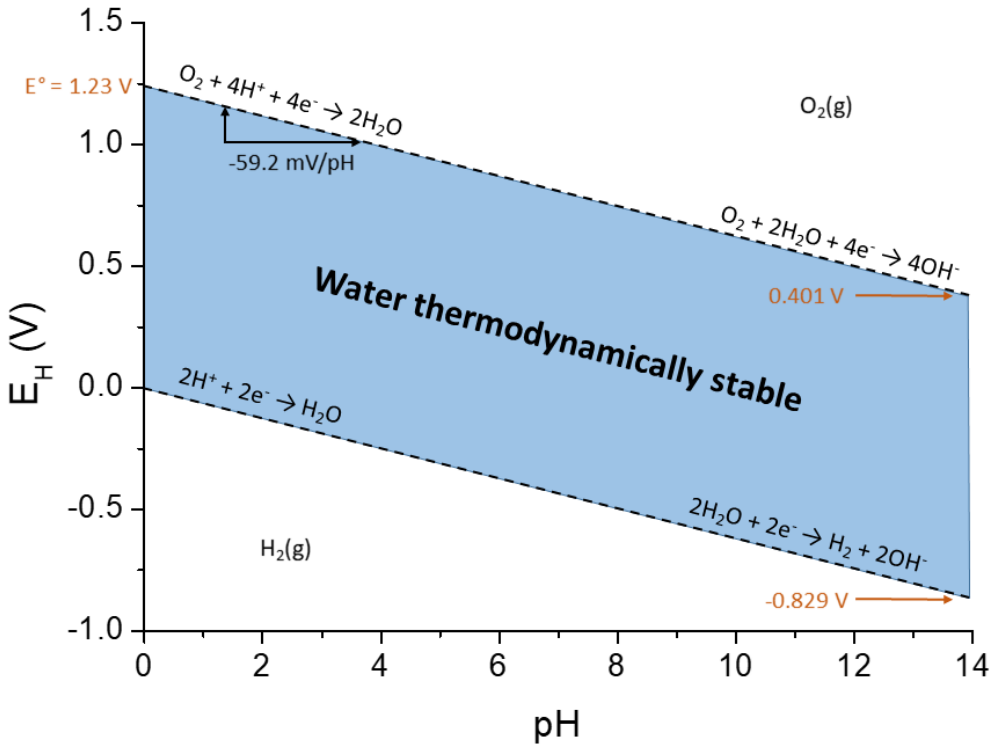

Figure 2.7 Pourbaix diagram for water under standard temperature and pressure. The x-axis shows the potential against the SHE and the y-axis is the pH of the electrolyte. Assuming no overpotential, at E_H and pH outside the shaded area, O_2 or H_2 evolution will occur from the electrode until equilibrium is reached due to the decomposition of water.

Using the Nernst equation, the upper stability limit (**Equation 2.31**) and lower stability limit (**Equation 2.32**) of an aqueous electrolyte at various pH can be easily written as:

$$E = 1.23\ V - 0.592 * \text{pH}(V) \tag{2.31}$$

$$E = 0\ V - 0.592 * \text{pH}(V) \tag{2.32}$$

However, the potential window of aqueous electrolytes can vary from the theoretical value for the breakdown of water of 1.23 V, due to higher or lower overpotentials for oxygen and/or hydrogen evolution.[31] The overpotential of a cell (which is directly related to a cell's voltage efficiency) can vary by the cell design (*e.g.*, type of current collector used) and the active material stability window. Decreased overpotentials (lower V) have a negative impact on the overall energy density of a cell according to **Equation 2.13**.

The ionic strength of an electrolyte solution is a measure of the concentration of ions in that solution, regardless of the dissociation strength or activity. The molar ionic strength (I) of all ions in a solution can be calculated by the following equation:

$$I = \frac{1}{2}\sum_i c_i z_i^2 \tag{2.33}$$

where c_i is the molar concentration of the ion, z_i is the charge number of the ion, and the sum is taken over all ions in the solution.

Properties of the ions in the electrolytes used in this thesis are shown in **Table 2.1**. *B*-coefficients of the Jones-Dole empirical expression of the relative viscosities of electrolyte solutions are used due to several advantages; *i.e.*, it is an excellent source of primary data, provides information concerning the solvation of the ions and their effects, and correlations can be made with the coefficients and other ion-additive properties.[32]

Table 2.1 Properties of electrolyte ions at 25 °C.

Ion	Diameter (nm)[33]	Viscosity *B*-coefficient[a] ($dm^3\ mol^{-1}$)[32]	Conductivity[b] ($S\ m^2\ mol^{-1}$)[34]
H_3O^+	0.2755	0.068	349.8
Na^+	0.2356	0.085	50.1
K^+	0.2798	-0.009	73.5
SO_4^{2-}	0.3815	0.206	159.6
OH^-	0.2660	0.122	198.0

[a] *B*-coefficients of ions in aqueous solution. [b] At infinite dilution.

2.3.3 Two-Electrode Systems

Full cell supercapacitors consist of a two-electrode configuration rather than three-electrode configuration. The advantage of the three-electrode configuration is that the exact potential can be controlled and that the potential will be kept constant should any changes to the active materials occur during operation. In the two-electrode configuration, only the voltage can be controlled but not the exact potentials where the voltage lies. However, it is known that overestimations of capacitance may occur in the three-electrode configuration,[21] so studying supercapacitor performance in a two-electrode set-up can give more realistic results and minimise any errors.

Full cell supercapacitors can be constructed in a symmetric or asymmetric configuration (**Figure 2.8**).[35] Symmetric supercapacitors uses two identical electrodes separated by an electrolyte. The symmetric system is simpler, thus commonly used commercially, and is good for evaluating an active material alone. Asymmetric supercapacitors (also known as hybrid capacitors) uses two dissimilar electrodes, such as a porous carbon and a battery-type electrode. The advantage is that higher energy and power densities can be utilised due to the non-identical potentials of the electrodes. However, as one of the electrodes is entirely pseudocapacitive, the stability of the cell is usually lower.

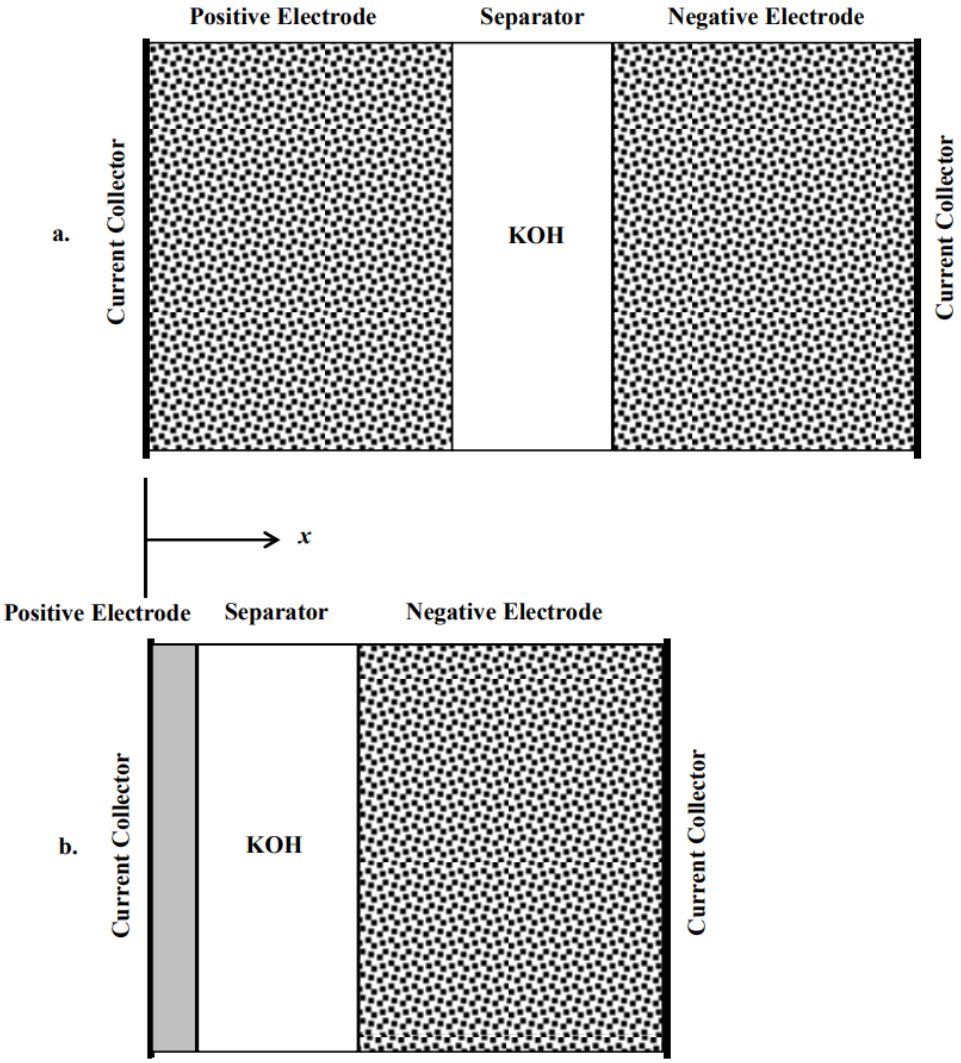

Figure 2.8 Schematic representations of a) symmetric capacitor and b) asymmetric capacitor. Figure modified from literature source.[35]

For the two-electrode symmetric cell, the specific capacitance (C_{s2}) of a single electrode can be calculated. The specific capacitance (C_{sv2}) from CV in the two-electrode configuration can calculated using the following equation:[36]

$$C_{sv2} = 2(q_a + q_c)/(m_t s \Delta V) \quad (2.34)$$

where m_t is the total mass of active material in both electrodes.

The specific capacitance (C_{sc2}) from charge-discharge profiles in the two-electrode configuration can be calculated using the following equation:[22]

$$C_{sc2} = 4(I \times t)/(V \times m_t) \quad (2.35)$$

The capacitance from impedance spectroscopy (C_{si2}) in the two-electrode configuration can be calculated using the following equation:[22]

$$C_{si2} = -2/(\pi f Z'' m_t) \quad (2.36)$$

Electrochemical analyses presented in this thesis were performed as follows.

2.3.4 Electrode Preparation

Graphite substrates (10 x 10 x 5 mm, Well Hand Industrial Corp.) were polished using fine sand paper and sonicated with DI water in an ultrasonic bath for 10 min, then with 0.5 M H_2SO_4 for 10 min, and finally with deionised water for 30 min. The substrates were then dried in an oven at 80 °C overnight. The mass of the electrodes were then measured. Active material (8 mg, 80 wt%) was mixed with Super C65 carbon black (1 mg, 10 wt%) and poly(vinylidine difluoride) (PVDF, 1 mg, 10 wt%) in *N*-methylpyrrolidinone (NMP, 1 mL) solvent. The resulting slurry was homogenised by ultrasonication and a total of 1 mg of the active material mass was coated onto an exposed surface of 10 x 10 mm of the substrate by pipette. The substrate was dried at 80 °C overnight in an oven. Mass loading of the substrate was then measured. The samples were weighed on a 5 decimal place balance.

2.3.5 Electrochemical Measurements

The electrochemical responses were investigated using a EC-Lab SP-200 (Bio-Logic Science Instruments SAS, France) in a two- or three-electrode configuration in a jacketed cell at 25 °C. In the three-electrode configuration, a Ag/AgCl electrode (Argenthal, 3 M KCl, 0.207 V *vs.* standard hydrogen electrode at 25 °C) was used as the reference electrode and a platinum wire was employed as the counter electrode. A Luggin capillary was used to minimise errors due to ohmic potential (iR) drop in the electrolyte. In the two-electrode configuration, graphite-based working electrodes without

separator were used in the same jacketed cell. Electrolyte solution was degassed for at least 30 min with N_2. 1 M H_2SO_4, 1 M Na_2SO_4, or 3 M KOH was used as the electrolyte solution for evaluating the capacitive performances.

2.4 Thermogravimetric Analysis (TGA)

TGA measures the mass of a sample over time with varying temperature. The measurement can provide information about phase transitions, absorption and desorption, decomposition, and solid-gas reactions. A variety of gases can be used, such as N_2 and air. TGA can be useful to estimate yields from carbonisations at distinct temperatures or to observe the inorganic content of a material.

The TGA analyses presented in this thesis were performed as follows. TGA was carried out in platinum pans using a Q5000IR analyser (TA instruments) with an automated vertical overhead thermobalance. The samples were heated on a high temperature platinum pan at 5 °C min^{-1} to 1000 °C under nitrogen.

2.5 Powder X-Ray Diffraction (PXRD)

PXRD is a method used to determine the crystalline or semi-crystalline structure of materials through the use of X-rays. The sample is irradiated with X-rays and scatters in a specular fashion if the radiating wavelength is comparable to the interatomic spacings of the crystalline system. The waves which are scattered from the crystalline material can interfere constructively and remain in phase; occurring when the angle of incidence is equal to the angle of scattering, and the path lengths of the two waves is equal to an integer number of the wavelengths (**Figure 2.9**). A detector in the instrument measures the intensity and angles of diffracted beams.

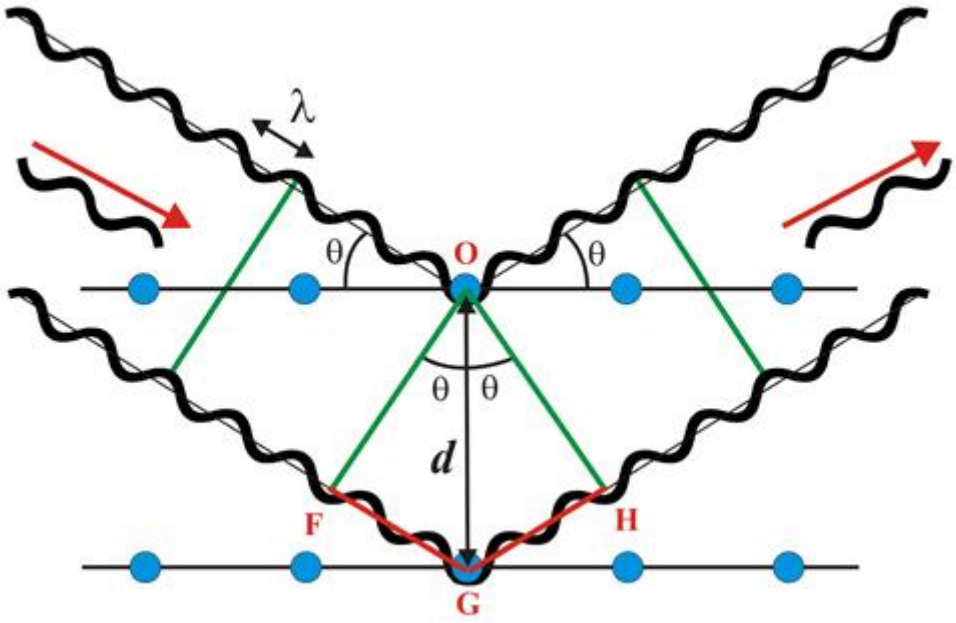

Figure 2.9 Schematic representation of the Bragg model of diffraction. Figure reprinted from the Spanish National Research Council.

Bragg's Law describes the condition on the scattering angle (θ) for constructive interference to be at its strongest:[37]

$$2d\,sin\theta = n\lambda \tag{2.37}$$

where d is distance, n is a positive integer, and λ is the wavelength of the incident wave.

In PXRD, this results in a one-dimensional dataset as the random orientation of bulk particles—due to being a powdered sample rather than a single crystal—resulting in an averaging of the crystallite orientation. This yields less information than single crystal X-ray diffraction which uses a two-dimensional detector, however, powder samples are usually easier to obtain as they do not require one to grow single crystals.[38] For this reason, PXRD is routinely used to characterise materials. As amorphous carbons are made throughout the thesis, one expects to only see broad diffraction peaks. However, the method can be used to check for trace metal impurities which will be observed as sharp peaks, as is the case in Chapter 4 and 6.

PXRD analyses presented in this thesis were performed as follows. PXRD data were collected in transmission mode on loose powder samples held on thin Mylar film in Stainless steel well plates on a Panalytical X'Pert PRO MPD equipped with an high throughput screening (HTS) XYZ stage, X-ray focusing mirror, 1/2 degree divergence slit, 0.04 degree soller slits, 4 mm beam mask and PIXcel

detector, using Cu Kα radiation. Data were measured over the range 5-50° 2Θ in 0.013° steps over 60 minutes.

2.6 Raman Spectroscopy

Raman spectroscopy provides structural information of materials by observing the vibrational, rotational, and other low-frequency modes in the system.[39] This is performed by illuminating a sample with a laser beam in the visible, near infrared, or near ultraviolet range. The laser light interacts with the various nodes in the system, resulting in the energy of the laser photons being shifted up or down. This shift in energy gives information about the vibrational modes (Raman shifts) in the system, which are typically reported in wavenumbers. For carbon, the disordered (*D*) and graphitic (*G*) bands are of the most interest and can be monitored at ~1350 cm^{-1} and ~1590 cm^{-1}, respectively. A *2D* band (also known as *G*') can also be monitored at ~2650 cm^{-1}, however, this is usually observed in single layer or highly ordered carbons.[40]

Ramen spectroscopy analyses presented in this thesis were performed as follows. Raman spectra were recorded with a Raman microscope (Renishaw inVia), using a 785 nm wavelength laser focused through an inverted microscope (Leica), *via* a 50x objective (Leica). Loose powders were mounted on pyrex glass slides for measurement.

2.7 Elemental Analysis

Elemental analysis quantitively determines the elemental composition of a sample. The most common form of elemental analysis determines the level of carbon, hydrogen, nitrogen, and sulfur elements by combustion analysis. This is performed by burning the sample in an excess of oxygen and collecting the combustion products: CO_2, H_2O, NO_x, and SO_2, with the masses used to calculate the composition of the sample. The method is useful for quantifying changes in the material after carbonisation reactions as the elemental composition cannot be theoretically calculated like in traditional chemistry reactions.

Elemental analyses presented in this thesis were performed as follows. CHN elemental analysis was conducted on a Thermo FlashEA 1112. CHNS elemental analysis was conducted on an Elementar vario MICRO cube. This was performed by the Chemistry Department Service at the University of Liverpool.

2.8 X-ray Photoelectron Spectroscopy (XPS)

XPS is a quantitative technique that measures the surface elemental composition, empirical formula, chemical state, and electronic state of the elements in a material. This is performed by irradiating a material with X-rays and simultaneously measuring the kinetic energy and number of electrons that escape from the 0 to 10 nm range of the material. Peaks from a single element can then be quantified and partitioned into different bonding states using a table of binding energies, allowing the environment of the element to be probed within the material. XPS is complimentary to elemental analysis; as XPS is a surface technique, elemental analysis is a bulk technique. XPS also has advantages of quantifying O and metal contents.

XPS analyses presented in this thesis were performed as follows. XPS spectra were obtained using two systems. The first system used a standard ultrahigh vacuum surface science chamber consisting of a PSP Vacuum Technology electron energy analyser (angle integrating ±10◦) and a dual anode X-ray source. The base pressure of the system was less than 2×10^{-10} mbar, with hydrogen as the main residual gas in the chamber. These XPS measurements were carried out with a Mg K-alpha source (1253.6 eV). The spectrometer was calibrated using Au 4f7/2 at 83.9 eV. The samples were corrected for charging using the adventitious carbon 1s peak to 284.6 eV. The peaks were deconvoluted using the CASA XPS software. These were performed by Dr David Hesp and Thomas Whittles. The second system used a Thermo Scientific K-Alpha spectrometer with a microfocused monochromatic Al Kα X-ray source at an energy, voltage, current, and power of 1486.6 eV, 12 kV, 3 mA, and 36 W, respectively. These were performed by the National EPSRC XPS Users' Service (NEXUS) at Newcastle University.

2.9 Inductively Coupled Plasma Optical Emission Spectrometry (ICP-OES)

ICP-OES is used to detect chemical elements, namely heavy metals. A sample (if solid) is initially digested in strong acid to form a solution. An inductively coupled plasma is then used to produce excited atoms and ions from the sample that emits electromagnetic radiation at characteristic wavelengths to a particular element. The concentration of the element can also be determined by the intensity of the emissions. This is particularly useful to determine the metal content of bulk solid samples (*e.g.*, insoluble polymers and carbons), as XPS can only quantify the surface content.

ICP-OES analyses presented in this thesis were performed as follows. ICP-OES was performed on a Perkin Elmer 7300DV ICP-OES through microwave digestion of samples in conc. nitric acid. This was performed by Butterworth Laboratories Ltd.

2.10 Field Emission Scanning Electron Microscopy (FE-SEM)

FE-SEM is used to study the surface structures of materials using a focused beam of electrons. An electron beam is accelerated and focused onto a sample which produces secondary electrons that are detected. The number of these detected electrons depends on the variations on the surface of the sample. By scanning the electron beam and detecting the variation of the number of emitted electrons, a surface topography can be constructed. The measurement requires the sample to be conductive (at least on the surface) otherwise the non-conductive sample collects charge from the electron beam which causes image artefacts to appear. This can be solved by coating the sample with an ultrathin layer of an electrically conductive metal by low-vacuum sputter coating.

FE-SEM analyses presented in this thesis were performed as follows. Powdered samples were mounted onto carbon tape. Non-conducting materials were sputter coated with gold. High resolution imaging of the material morphology was obtained using a Hitachi S-4800 cold FE-SEM.

2.11 High-resolution transmission electron microscopy (HR-TEM)

HR-TEM is used to study the structure within a sample by transmitting a beam of electrons through the sample. The electron beam passes through the sample and the interaction of the electrons with the sample as it transmits through forms an image. The image is then magnified by other lenses and detected

HR-TEM analyses presented in this thesis were performed as follows. TEM specimens were produced by ultrasonically dispersing powder in analytical grade methanol, the suspension was then dropped onto copper mesh grids with holey carbon support films and allowed to dry. HR-TEM was performed using a JEOL 2100FCS microscope, equipped with a Schottky field emission gun, operating at 200 kV. Bright field images were recorded in conventional TEM illumination mode. Chemical analyses were performed by energy dispersive x-ray spectroscopy using a windowless EDAX spectrometer. This was performed by Dr Karl Dawson.

2.12 Swelling Experiments

HCPs are known to swell in variety of sorbents due to their flexible crosslinking (as discussed in Chapter 1). This experiment was performed on carbonised HCPs to show the absence of swelling after conversion to porous carbon (Chapter 5).

Material swelling analyses presented in this thesis were performed as follows. A variable-volume view cell containing optically transparent sapphire windows was used, developed by Licence *et al*.[41] A sample of material (roughly 0.5 cm^3) was ground into a coarse powder using a pestle and mortar and added into a 1 mL glass vial. The vial was then placed, open, in the view cell, and fixed into position using a small piece of adhesive. Images of the samples were taken at ambient pressure and at higher pressures under a CO_2 atmosphere using a digital camera (Nikon Coolpix P6000). This was performed by Dr Meera Vijayaraghavan.

2.13 Metal Uptake Experiments

Porosity in materials not only allows the uptake of liquids and gases, but also metals. This allows for applications such as water desalination. In Chapter 6, S-doped carbons were synthesised to target the uptake of metal ions.

Metal uptake analyses presented in this thesis were performed as follows. In brief, carbon samples were placed into vials containing aqueous metal solutions of varying concentrations and placed on a roller at room temperature for 1 h. After this time, the solutions were filtered and analysed by ICP-OES. Full details of this procedure can be found in Chapter 6. This was performed by Douglas Parker.

2.14 References

[1] M. Thommes, K. Kaneko, A. V. Neimark, J. P. Olivier, F. Rodriguez-Reinoso, J. Rouquerol, K. S. W. Sing, *Pure Appl. Chem.* **2015**, *87*, 1051.

[2] K. S. W. Sing, D. H. Everett, R. A. W. Haul, L. Moscou, R. A. Pierotti, J. Rouquerol, T. Siemieniewska, *Pure Appl. Chem*. **1985**, *57*, 603.

[3] M. Thommes, K. A. Cychosz, *Adsorption* **2014**, *20*, 233.

[4] I. Langmuir, *J. Am. Chem. Soc.* **1916**, *38*, 2221.

[5] S. Brunauer, P. H. Emmett, E. Teller, *J. Am. Chem. Soc*. **1938**, *60*, 309.

[6] R. I. Masel, *Principles of Adsorption and Reaction on Solid Surfaces*, John Wiley & Sons, 1996.

[7] S. Lowell, J. E. Shields, M. A. Thomas, M. Thommes, *Characterization of Porous Solids and Powders: Surface Area, Pore Size and Density*, **2004**.

[8] J. P. Olivier, M. L. Occelli, *J. Phys. Chem. B* **2001**, *105*, 623.

[9] G. Z. Chen, *Prog. Nat. Sci. Mater*. **2013**, *23*, 245.

[10] Z. Dai, C. Peng, J. H. Chae, K. C. Ng, G. Z. Chen, Sci. Rep. **2015**, 5, 9854.

[11] K. Jurewicz, E. Frackowiak, F. Béguin, *Appl. Phys. A* **2004**, *78*, 981.

[12] C.-C. Hu, T.-W. Tsou, *Electrochem. Commun.* **2002**, *4*, 105; I. L. Chen, Y.-C. Wei, T.-Y. Chen, C.-C. Hu, T.-L. Lin, *J. Power Sources* **2014**, *268*, 430; N. L. Torad, R. R. Salunkhe, Y. Li, H. Hamoudi, M. Imura, Y. Sakka, C.-C. Hu, Y. Yamauchi, *Chem. Eur. J*. **2014**, *20*, 7895.

[13] J.-S. M. Lee, T.-H. Wu, B. M. Alston, M. E. Briggs, T. Hasell, C.-C. Hu, A. I. Cooper, *J. Mater. Chem. A* **2016**, *4*, 7665.

[14] N. L. Torad, R. R. Salunkhe, Y. Li, H. Hamoudi, M. Imura, Y. Sakka, C.-C. Hu, Y. Yamauchi, *Chem. Eur. J*. **2014**, *20*, 7895.

[15] P. Simon, Y. Gogotsi, *Acc. Chem. Res.* 2**013**, *46*, 1094.

[16] E. Frackowiak, *Phys. Chem. Chem. Phys*. **2007**, *9*, 1774

[17] N. L. Wu, S. Y. Wang, *J. Power Sources* **2002**, *110*, 233.

[18] R. Negroiu, P. Svasta, C. Pirvu, A. Vasile, C. Marghescu, "Electrochemical impedance spectroscopy for different types of supercapacitors", presented at *2017 40th International Spring Seminar on Electronics Technology (ISSE)*, 10-14 May 2017, **2017**.

[19] P. L. Taberna, C. Portet, P. Simon, *Appl. Phys. A* **2006**, *82*, 639.

[20] C. Lei, F. Markoulidis, Z. Ashitaka, C. Lekakou, *Electrochim. Acta* **2013**, *92*, 183.

[21] S.-C. Lin, Y.-T. Lu, Y.-A. Chien, J.-A. Wang, T.-H. You, Y.-S. Wang, C.-W. Lin, C.-C. M. Ma, C.-C. Hu, *J. Power Sources* **2017**, *362*, 258.

[22] M. D. Stoller, R. S. Ruoff, *Energy Environ. Sci*. **2010**, *3*, 1294.

[23] P. L. Taberna, P. Simon, J. F. Fauvarque *J. Electrochem. Soc.* **2003**, *150*, A292.

[24] B. E. Conway, W. G. Pell, *J. Solid State Electrochem.* **2003**, *7*, 637.

[25] O. Haas, E. J. Cairns, *Annu. Rep. Prog. Chem., Sect. C: Phys. Chem*. **1999**, *95*, 163.

[26] M. Frank Rose, C. Johnson, T. Owens, B. Stephens, *J. Power Sources* **1994**, *47*, 303.

[27] A. G. Pandolfo, A. F. Hollenkamp, *J. Power Sources* **2006**, *157*, 11.

[28] Y. Chen, X. Zhang, D. Zhang, P. Yu, Y. Ma, *Carbon* **2011**, *49*, 573.

[29] J. N. Barisci, G. G. Wallace, D. R. MacFarlane, R. H. Baughman, *Electrochem. Commun*. **2004**, *6*, 22.

[30] F. J. Vidal-Iglesias, J. Solla-Gullón, A. Rodes, E. Herrero, A. Aldaz, *J. Chem. Educ*. **2012**, *89*, 936.

[31] A. J. Bard, L. R. Faulkner, *Electrochemical Methods: Fundamentals and Applications, 2nd Edition*, Wiley, **2000**.

[32] H. D. B. Jenkins, Y. Marcus, *Chem. Rev.* **1995**, *95*, 2695.

[33] Y. Marcus, *Chem. Rev*. **1988**, *88*, 1475; H. D. B. Jenkins, K. P. Thakur, *J. Chem. Educ.* **1979**, *56*, 576.

[34] A. W. Adamson, *Textbook of Physical Chemistry.*, Academic Press Inc., London **1973**.

[35] J. A. Staser, J. W. Weidner, *J. Electrochem. Soc.* **2014**, *161*, E3267.

[36] B. Anothumakkool, A. Torris A. T, S. N. Bhange, M. V. Badiger, S. Kurungot, *Nanoscale* **2014**, *6*, 5944.

[37] H. P. Meyers, *Introductory Solid State Physics*, Taylor & Francis, London **2014**.

[38] K. D. M. Harris, M. Tremayne, B. M. Kariuki, *Angew. Chem., Int. Ed.* **2001**, *40*, 1626.

[39] P. Vandenabeele, in *Practical Raman Spectroscopy – An Introduction*, John Wiley & Sons, Ltd, **2013**, 1.

[40] J. Hodkiewicz, Characterizing Carbon Materials with Raman Spectroscopy, Thermo Fisher Scientific.

[41] P. Licence, M. P. Dellar, R. G. M. Wilson, P. A. Fields, D. Litchfield, H. M. Woods, M. Poliakoff, S. M. Howdle, *Rev. Sci. Instrum.* **2004**, *75*, 3233.

Chapter 3

Conjugated Microporous Polymer-Derived Carbons for Supercapacitive Energy Storage

Some of the contents in this chapter are taken from **Paper II**.

J.-S. M. Lee, T.-H. Wu, B. Alston, M. E. Briggs, T. Hasell, C.-C. Hu, A. I. Cooper, "Porosity-Engineered Carbons for Supercapacitive Energy Storage Using Conjugated Microporous Polymer Precursors" *J. Mater. Chem. A* **2016**, *4*, 7665–7673.

3.1 Background and Context

Supercapacitive materials require a well-developed and controlled pore structure to allow the efficient diffusion of electrolytes during charging and discharging. However, many of the materials reported show ill-defined and diagonal CV curves associated with potentially poor electrolyte diffusion, therefore high resistance in their materials. An advantage of CMPs is the ease with which their pore size can be tuned, simply by changing the length of the monomer. CMPs are also very stable during the carbonisation process, due to their highly conjugated, cross-linked structure, and it was found that the pore sizes present in the CMP could be transferred to the carbon, albeit with a slight decrease after carbonisation. By optimising the carbonisation procedure and supercapacitor system, we were able to obtain CMP-derived carbons that show high capacitance with characteristics of typical supercapacitors.

3.2 Introduction

Supercapacitors are energy-storage devices characterised by high-power density, long cycle life, and rapid charge/discharge capability.[1] The demand for new supercapacitive materials is driven by technological advances in electronic devices and in transportation requiring high power and large energy density. Supercapacitive energy storage operates either by the EDLC mechanism, which favours high surface area materials, or by the PC mechanism which is due to redox active groups in the material. PC generally provides a higher energy density than EDLC, but typically at the expense of power density and cycle life.[2] One strategy for achieving high energy densities while simultaneously keeping a high power density and cycle life is to combine principles from both EDLC and PC.

In developing supercapacitive electrode materials, it is important to consider the kinetics of ion and electron transport in electrodes and at the electrode-electrolyte interface. Thus, an electrode material with fine control over pore structure and good electrical conductivity is required.[3] Activated carbons have been studied extensively but a major challenge with these materials is the poor control that exists over pore size distribution and pore structure. The process by which carbons are produced using activating agents generally results in a broad pore size distribution.[4] Templating methods have been employed to assist in the control of pore size distribution, but this still results in large pore lengths (0.5–1 μm), which make ion diffusion inefficient.

CMPs are a class of materials that combine extended π-conjugation within a microporous framework. CMPs have emerged as useful materials for applications such as catalysis,[5] light harvesting,[6] carbon dioxide capture,[7] superhydrophobic separations,[8] luminescence,[9] sensing,[10] and fluorescence

enhancement.[11] In 2011, Kou *et al.* reported interesting specific capacitance results for an aza-CMP material (**Figure 3.1a**).[12] However, the CV profiles did not show the rectangular-like *i-E* curve traditionally observed for supercapacitors. Instead the current proportionately increased with the shift in electrode potential in both the positive and negative sweeps over the whole potential range (**Figure 3.1b**), which can be associated with high electric resistance and is undesirable for supercapacitor applications.[13] The resistance was predominant at faster scan rates, likely due to low electrical conductivity or slow electrolyte diffusion through the pore structure.

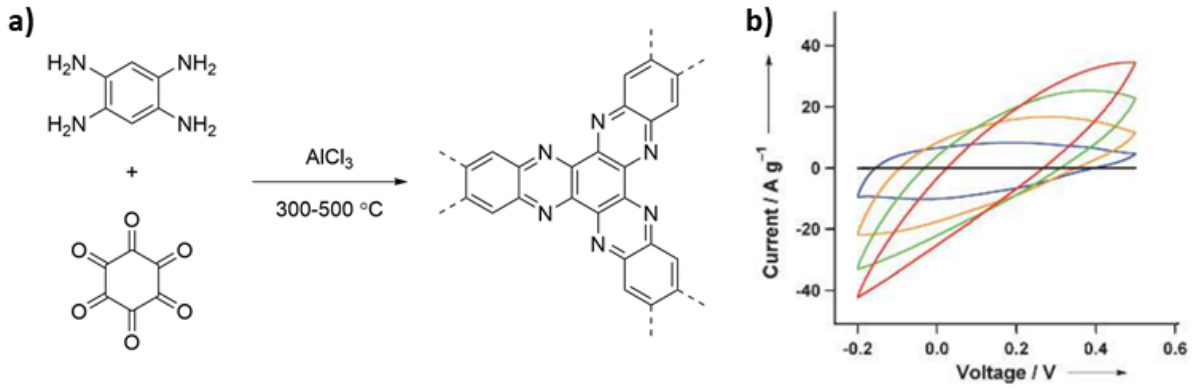

Figure 3.1 a) Synthesis of Aza-CMPs. b) Cyclic voltammograms of Aza-CMP:@350 at scan rates of 25 (blue), 50 (orange), 100 (green), and 200 mV s^{-1} (red), and hexaazatriphenylene at a scan rate of 100 mV s^{-1} (black). Figure modified from literature source.[12]

Most CMPs, though conjugated in nature, are not often electrically conductive due to the poor orbital overlap of the twisted benzene rings (*e.g.*, in polyarylene ethynylenes), the meta-substitution pattern often present in CMPs, and inefficient packing within the amorphous 3-D structure. The combination of these three factors makes many if not most CMPs reported so far unsuitable for electrochemical applications. Thus, a traditional strategy to enhance conductivity in carbon-based materials is to graphitise the structure through high temperature carbonisation.[14] CMPs have previously been used as carbonisation precursors for gas sorption and related applications but they have not yet been thoroughly investigated as supercapacitors.[15]

In this chapter, we explore the effects of carbonisation on the capacitive behaviour of CMPs in aqueous electrolytes using voltammetric and galvanostatic charge-discharge techniques. This work overcomes the resistivity issues observed by Kou *et al.* by incorporating high electric conductivity into CMPs through graphitising the structure with carbonisation, in addition to allowing pore size control in the resultant material. The first reported CMP, 'CMP-1'[16] was used as an example to demonstrate the flexibility of this approach (**Scheme 3.1**).

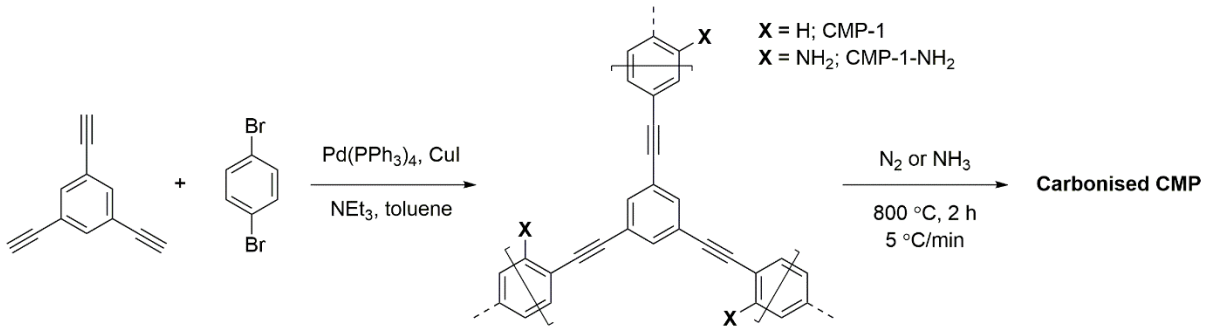

Scheme 3.1 Synthesis of CMP-1 and subsequent carbonisation method.

3.3 Experimental

3.3.1 Chemical Reagents

1,4-Diiodobenzene, 2,5-dibromoaniline, tetrakis(triphenylphosphine)palladium(0), copper(I) iodide, triethylamine, sulphuric acid, sodium sulphate, and potassium hydroxide were purchased from Sigma Aldrich. 1,3,5-Triethynylbenzene was purchased from TCI America. DMF and toluene were purchased from Fisher Scientific. High purity nitrogen and NH_3 were purchased from BOC. All chemicals were used as received without any further purification. Triply distilled water was used in all experiments.

3.3.2 Synthesis

Preparation of CMP-1

CMP-1 was synthesised following a previously reported literature methods.[16] To a flame-dried 2-necked round bottomed flask under N_2 was added 1,3,5-triethynylbenzene (2.25 g, 15 mmol), 1,4-diiodobenzene (4.95 g, 15 mmol), tetrakis(triphenylphosphine)palladium(0) (693.5 mg, 0.6 mmol, 4 mol%) and copper(I) iodide (228.5 mg, 1.2 mmol, 8 mol%). The contents were evacuated and purged with N_2 three times and to this was added DMF (25 mL) and triethylamine (25 mL). The dark brown mixture was allowed to stir at 80 °C for 3 d. The resultant brown mixture was allowed to cool, filtered and washed with methanol. The product was further purified by Soxhlet extraction with methanol overnight. The contents were then dried in a vacuum oven at 80 °C overnight to yield a dark brown solid (4.37 g, >100% yield). Elemental analysis expected: C: 96.53%, H: 3.47%. Elemental analysis measured: C: 81.92%, H: 3.65%.

Preparation of CMP-1-NH_2

To a flame-dried 2-necked round bottomed flask under N_2 was added 1,3,5-triethynylbenzene (200 mg, 1.33 mmol), 2,5-dibromoaniline (334 mg, 1.33 mmol), tetrakis(triphenylphosphine)palladium(0) (61.5 mg, 0.05 mmol, 4 mol%) and copper(I) iodide (20.3 mg, 0.1 mmol, 8 mol%). The contents were evacuated and purged with N_2 three times and to this was added toluene (3.3 mL) and triethylamine (2 mL). The dark brown mixture was allowed to stir at 80 °C for 3 d. The resultant rusty brown mixture was allowed to cool, filtered and washed with methanol. The product was further purified by Soxhlet extraction with methanol overnight. The contents were then dried overnight in a vacuum oven at 80 °C to yield a light brown solid (351.3 mg, 93% yield). Elemental analysis expected: C: 88.87%, H: 3.73%, N: 7.40%. Elemental analysis measured: C: 67.18%, H: 3.34%, N: 2.02%.

Preparation of C1-CMP-1

CMP-1 (300 mg) was homogeneously dispersed onto a ceramic boat. The ceramic boat was then put into a tube furnace and exposed to a flow of N_2 at room temperature for 30 min, heated to 800 °C with a heating rate of 5 °C min^{-1}, then held at 800 °C for 2 hours before cooling to room temperature. The resultant black powder was used as obtained.

Preparation of C2-CMP-1

This follows the preparation of C1-CMP-1 but the set point was held for 6 h.

Preparation of N1-CMP-1

This follows the preparation of C1-CMP-1 but CMP-1-NH_2 was used as the precursor.

Preparation of N2-CMP-1

This follows the preparation of C1-CMP-1 but NH_3 was initially used in place of N_2 until the heating at set point was complete, then the gas flow was switched with a N_2 flow.

Preparation of N3-CMP-1

This follows the general preparation of N2-CMP-1 but C1-CMP-1 was used as the precursor.

3.4 Results and Discussion

3.4.1 Methodology of Conjugated Microporous Polymers-Derived Carbons

Using a heating ramp rate of 5 °C min^{-1}, CMP-1 was carbonised at 800 °C for either 2 h or 6 h under a N_2 atmosphere. The resultant carbons, without post-treatment, were labelled as C1-CMP-1 and C2-CMP-1, respectively. A set point hold time of 6 h is relatively long compared to what is often used for other carbonisation precursors, which typically require heating at set point of around 2 h.[17, 18] This was used due to the thermally stable nature of CMP-1 (**Figure 3.2**), which is already highly conjugated and has fewer hydrogens to remove than most other carbon precursors. An advantage of this is the relatively high carbonisation yields obtained when using CMPs as precursors (**Table 3.1**). The longer set point hold time for C2-CMP-1 results in a slightly more carbonised material, which can be seen by comparing the C, H, N elemental analysis for C1-CMP-1 and C2-CMP-1.

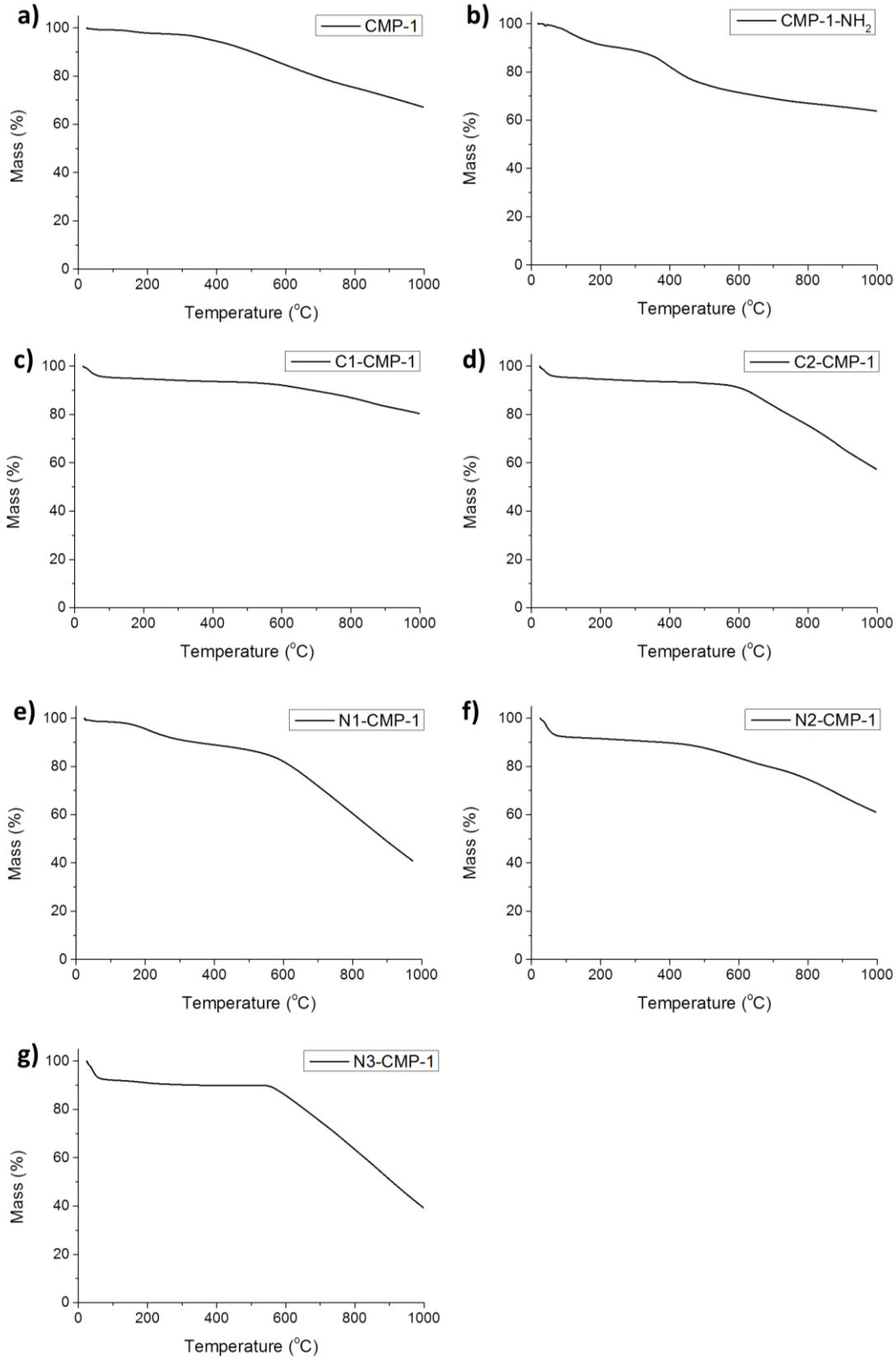

Figure 3.2 TGA analysis of (a) CMP-1, (b) CMP-1-NH_2, (c) C1-CMP-1, (d) C2-CMP-1, (e) N1-CMP-1, (f) N2-CMP-1, and (g) N3-CMP-1 measured at a heating rate of 20 °C min^{-1} under nitrogen flow.

Table 3.1 Physical properties of pre- and post-carbonised CMPs.

Sample	Surface area (m^2 g^{-1})[a]	Pore volume (cm^3 g^{-1})		Yield (%)[d]	Elemental analysis (%)		
		Total pore volume[b]	Micropore volume[c]		C	H	N
CMP-1	737	0.41	0.18	-	81.92	3.65	-
CMP-1-NH_2	522	1.07	0.04	-	67.18	3.34	2.02
C1-CMP-1	608	0.33	0.22	80	87.92	0.62	-
C2-CMP-1[e]	577	0.31	0.21	70	88.51	0.56	-
N1-CMP-1	791	1.15	0.18	73	85.00	0.59	1.89
N2-CMP-1[f]	1139	0.64	0.40	49	75.98	0.87	9.07
N3-CMP-1[f]	1436	0.76	0.51	60	80.79	0.70	7.14

[a] Apparent BET surface area. [b] Calculated by single point pore volume at $P/P_0 = 0.99$. [c] Determined by DFT method. [d] Yield calculated from final mass against the starting precursor mass. [e] Held at set point for 6 h. [f] NH_3 gas was used during the carbonisation.

Nitrogen-doping is known to be beneficial for supercapacitive materials because it enables easier dipolar attraction with the electrolyte cations,[19] gives rise to additional pseudocapacitive contributions,[20] and enhances electrical conductivity.[21] An amine-functionalised CMP-1 (CMP-1-NH_2), similar to one previously synthesised in our group,[22] was carbonised in the same way as C1-CMP-1 to produce N1-CMP-1. Replacement of the N_2 gas flow with NH_3 in the carbonisation process of CMP-1 allowed incorporation of additional nitrogen content into the graphitised polymer, N2-CMP-1. Further carbonisation of C1-CMP-1 in the presence of ammonia afforded a third nitrogen-doped carbon, N3-CMP-1 (**Table 3.1**).

TGA curves of some representative samples indicated residual masses of 5–7% (**Figure 3.3**) and indicated slightly higher thermal stabilities of N2-CMP-1 and N3-CMP-1 which both use a pre-carbonised sample as a precursor (C1-CMP-1).

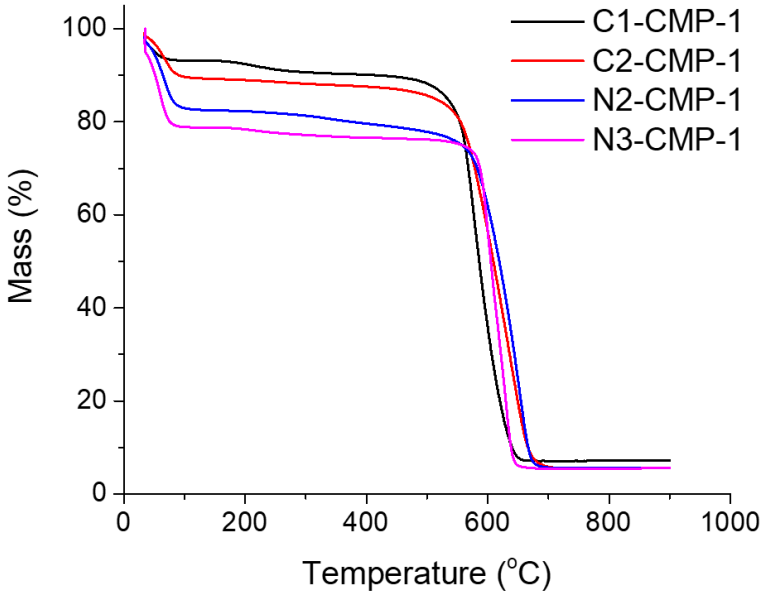

Figure 3.3 TGA analysis of CMP-derived carbons heated in air.

3.4.2 Structure and Properties of Conjugated Microporous Polymer-Based Materials

Heating of pristine or carbonised CMP-1 in the presence of NH_3 resulted in a dramatic increase in porosity, concomitant with increased N-doping, as observed by XPS. XPS of N1-CMP-1 shows a primary C 1s peak at 285 eV, a small O 1s peak at 533.3 eV, and a weak N 1s peak at 401.2 eV (**Figure 3.4a**).[23] N2-CMP-1 and N3-CMP-1 has a dominant C 1s peak at 285 eV, a smaller signal for the O 1s peak at 533.2 eV, and a N 1s peak at 400.1 eV (**Figure 3.4b,c**). Analysis of the C 1s peak for all the samples suggests the presence of C=C at 284.7 eV,[24] sp^2 bonded C=N at 285.5 eV, and sp^3 bonded C-N at 286.9 eV.[25] These peaks verify the integration of N atoms into the carbonised CMP-1 samples (1.9% N/C atomic ratio in N1-CMP-1; 10.4% N/C atomic ratio in N2-CMP-1; 5.3% N/C atomic ratio in N3-CMP-1). Further investigation of the high-resolution N 1s spectrum of these samples confirms the presence of pyridinic (398.3 ± 0.2 eV), pyrrolic (399.9 ± 0.2 eV), quaternary (401.1 ± 0.2 eV), and oxidised (402.8 ± 0.2 eV) nitrogen (**Figure 3.4d,e,f**).[18, 23, 26] The pyridinic and pyrrolic peaks at lower binding energies contribute to the π-conjugated system with a pair of *p*-electrons. Substitution of carbon atoms with nitrogen in the form of "graphitic" nitrogen results in higher N 1s binding energies. The highest energy peak in this environment is commonly associated with highly electronegative oxidised nitrogen.[27] Discounting quaternary nitrogen, all other nitrogen functional groups are situated at the edges of the layers. The different methods of N-doping results in different ratios of pyridinic, pyrrolic, quaternary, and oxidised nitrogen in the material (**Table 3.2**) The main conclusion of the nitrogen peak deconvolution analysis is that all samples contain a small amount of oxidised nitrogen. The pyridinic, pyrrolic, and quaternary functionalities are mostly present in identical

quantities in N1-CMP-1, whereas pyridinic and pyrrolic nitrogen are dominant in the N2-CMP-1 and N3-CMP-1 samples, with N3-CMP-1 containing the largest amount of pyrrolic nitrogen groups.

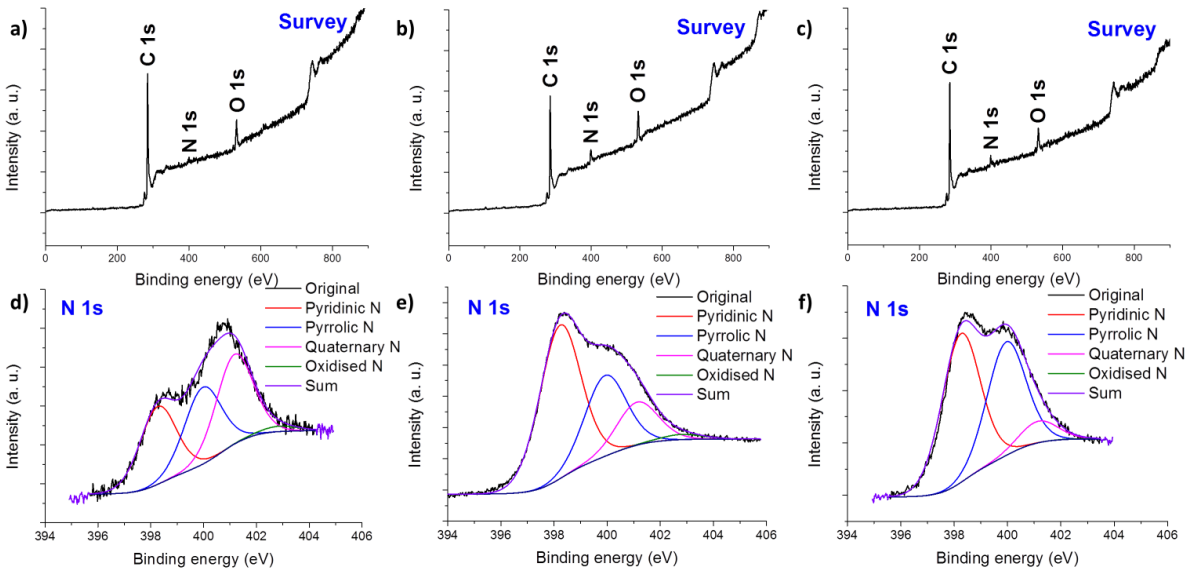

Figure 3.4 XPS spectra for the (a-c) survey scans of (a) N1-CMP-1, (b) N2-CMP-1, (c) N3-CMP-1, and the (d-f) N 1s core-level spectra of (d) N1-CMP-1, (e) N2-CMP-1, (f) N3-CMP-1.

Table 3.2 Distribution of N groups from XPS of N 1s.

	Amount (%)			
Sample	Pyridinic	Pyrrolic	Quaternary	Oxidised
N1-CMP-1	31.15	30.75	35.91	2.19
N2-CMP-1	54.34	28.59	15.21	1.86
N3-CMP-1	52.32	39.90	7.59	0.20

The surface area and pore structure of the CMPs and carbonised materials were investigated by nitrogen sorption measurements at 77.3 K. Both CMP-1 and the carbonised materials produced from this precursor show predominantly Type I isotherms, or Type I with some Type IVa isotherm character: there is steep adsorption at low relative pressure, indicating microporosity, and a hysteresis loop around $P/P_0 = 0.5$, indicating mesoporosity (**Figure 3.5a**). CMP-1-NH_2 and its carbonised sample, N1-CMP-1, show Type II isotherms with the adsorption curve increasing steeply at higher relative pressure, which can be ascribed to macroporosity. **Figure 3.5b** shows the pore size distribution curves for these materials derived using nonlocal density functional theory (NL-DFT). After carbonisation, the pore size decreases by about 2.5 Å compared to the pristine CMP and no additional peaks are observed. This is likely due to further micropore development of the porous carbonised materials from their CMP precursors, as seen in **Table 3.1**. The result shows that it is possible to produce carbonised CMP materials with fine-tuned pore sizes that are related to the pore structure of the CMP precursor. This is

a significant advantage, particularly when engineering pore sizes for efficient electrolyte ion diffusion in supercapacitors. Both CMP precursors seem to give better control than a previous study that uses a different porous polymer, PAF-1, as the carbon source.[28]

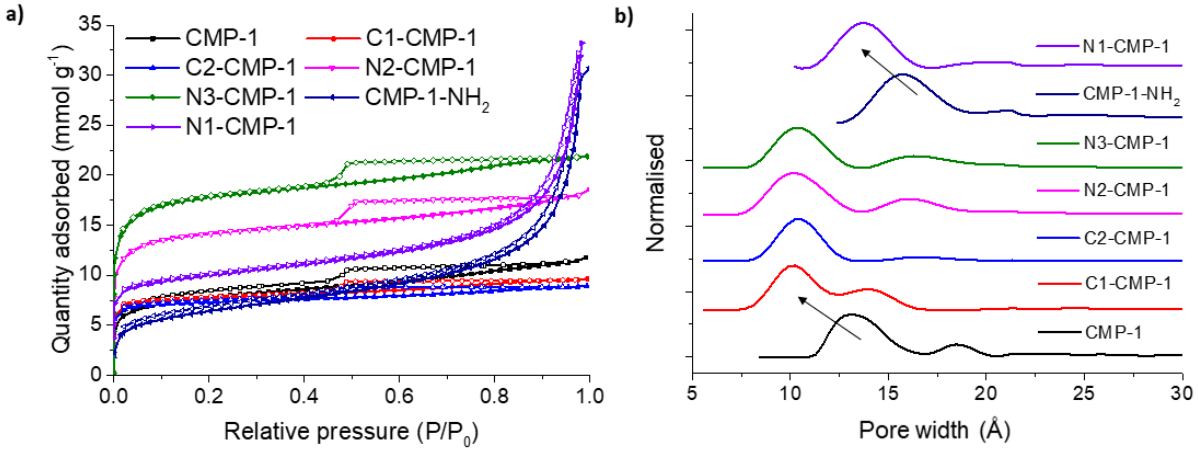

Figure 3.5 (a) Nitrogen adsorption-desorption isotherms of carbonised CMPs at 77.3 K (the adsorption and desorption branches are labelled with filled and empty symbols, respectively) and (b) pore size distribution calculated by NL-DFT.

FE-SEM was used to study the morphology of CMP-1 and the carbonised samples. The carbonised samples (**Figure 3.6**) all show similar morphologies to those of the parent polymer, CMP-1. This shows that the morphology of CMP-1 is retained during carbonisation, and the enhanced electrochemical properties are unlikely due to a morphology change.

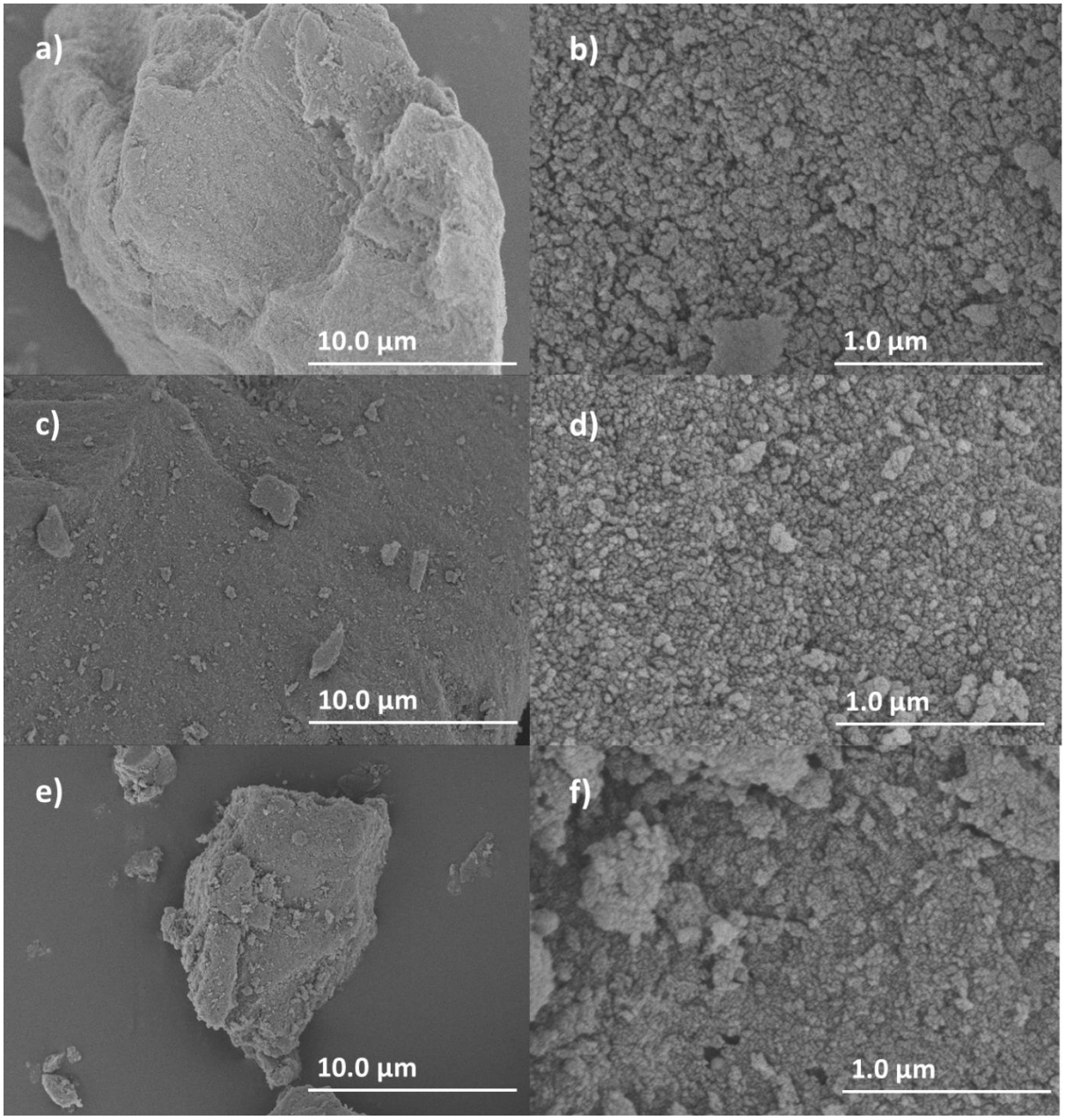

Figure 3.6 FE-SEM images of (a, b) CMP-1, (c, d) C1-CMP-1, and (e, f) C2-CMP-1 at low and high magnifications, respectively.

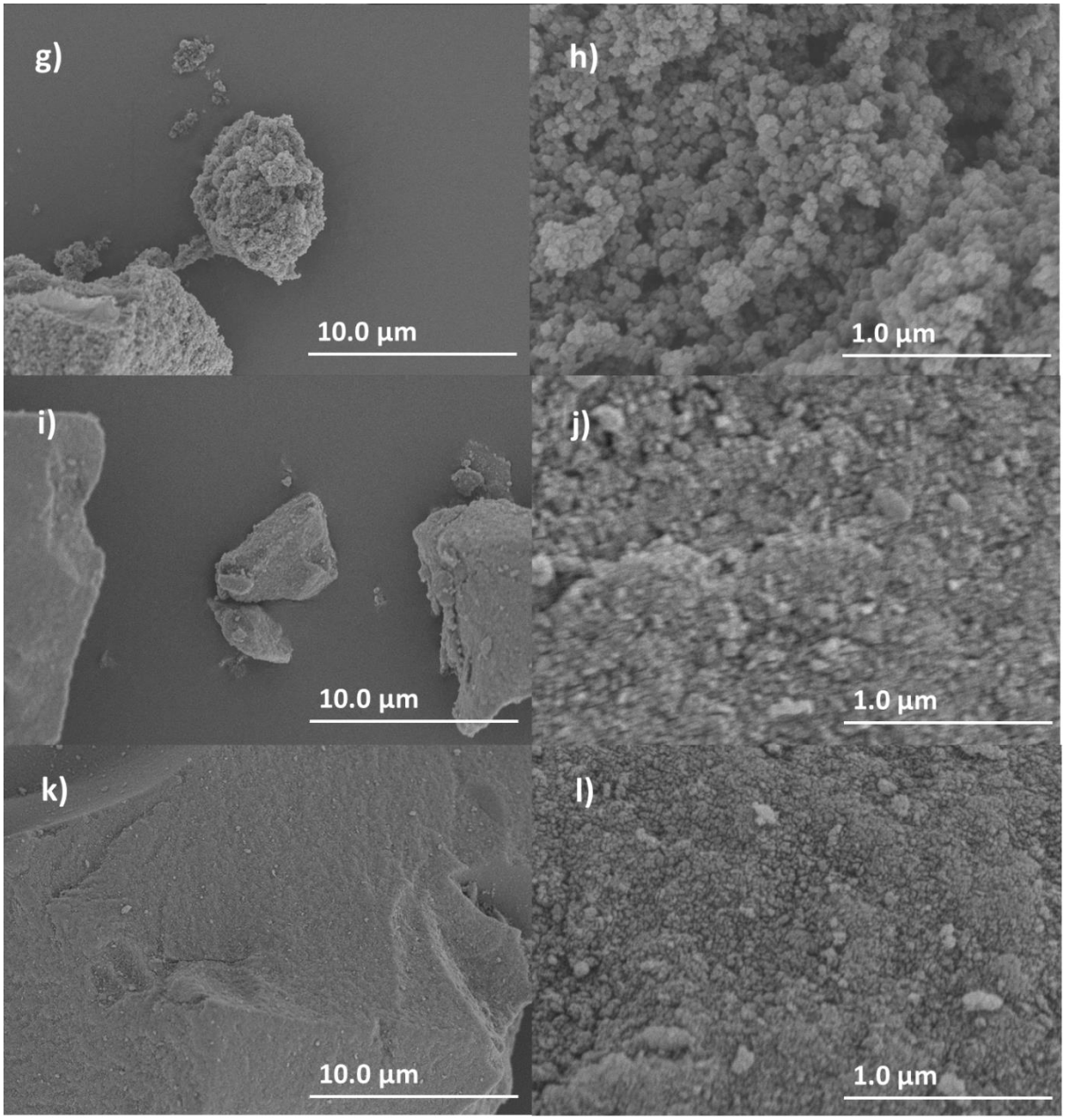

Figure 3.6 FE-SEM images of (g, h) N1-CMP-1, (i, j) N2-CMP-1, and (k, l) N3-CMP-1 at low and high magnifications, respectively.

Raman spectroscopy was used to investigate the graphitic structures in the carbonised CMPs (**Figure 3.7**). Two first-order Raman bands are present between 1100 and 1800 cm^{-1}; namely the *D* band at ~1350 cm^{-1} and the *G* band at ~1590 cm^{-1} attributed to the breathing mode of *K*-point phonons of A_{1g} symmetry and the in-plane stretching motion of symmetric sp^2 C-C bonds respectively.[29]

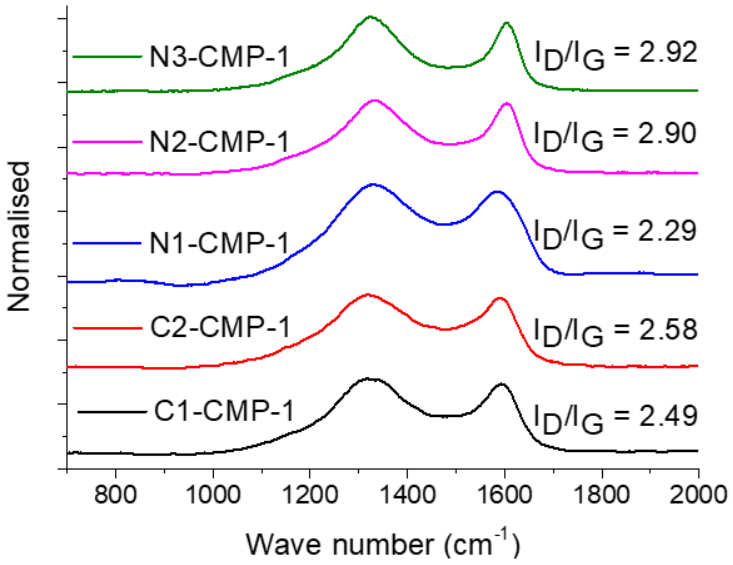

Figure 3.7 Raman spectra of carbonised CMPs with peaks at 1350 cm^{-1} and 1596 cm^{-1} assigned to the *D* band and *G* bands, respectively.

Reports demonstrate that the intensity ratio I_D/I_G of the *D* and *G* bands in Raman can be used to roughly estimate the average in-plane crystallite size (L_a) of the graphene sp^2 domains (**Equation 3.1**):[30]

$$L_a(nm) = (2.4 \times 10^{-10})\lambda_l^4 \left(\frac{I_D}{I_G}\right)^{-1} \quad (3.1)$$

where λ_l is the wavelength of laser in nanometer units and I_D/I_G is the ratio between the *D* band and *G* band from Raman spectroscopy.

The I_D/I_G ratio varied from 2.29 to 2.92, which would suggest a range of crystalline domains between 31 and 40 nm within the structure. HR-TEM also supports some increase in ordering, with aligned features observed in the carbonised material and none in the as-made CMPs (**Figure 3.8**). The materials thus show evidence for enhanced long-range structure ordering after the carbonisation treatment.

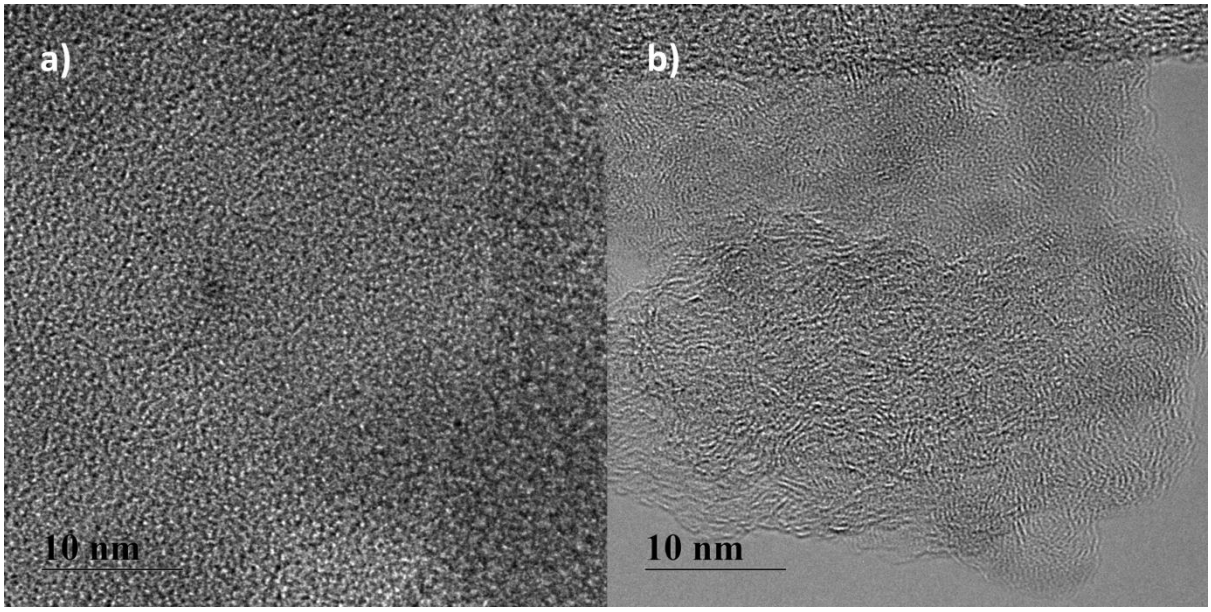

Figure 3.8 HR-TEM of (a) CMP-1 and (b) N1-CMP-1.

3.4.3 Supercapacitive Performances of CMP-Based Carbons

The electrochemical performance of the resulting samples was initially evaluated by CV measurements in a 1 M H_2SO_4 aqueous electrolyte using a three-electrode cell. **Figure 3.9a** shows the CVs of the carbonised CMP-1 samples at a scan rate of 20 mV s^{-1}. The current response from C1-CMP-1 is increased compared with CMP-1, yielding a specific capacitance of 31.0 F g^{-1} for C1-CMP-1 compared with 1.8 F g^{-1} for CMP-1. This demonstrates carbonised CMP-1 has enhanced electrochemical conductivity compared to its precursor. C2-CMP-1 shows an increase in current density from the CV and achieves a higher specific capacitance of 66.1 F g^{-1} at 20 mV s^{-1}. The CV curve of C2-CMP-1 also shows a more quasi-rectangular shape, which typically characterises good reversible supercapacitor behaviour.[31]

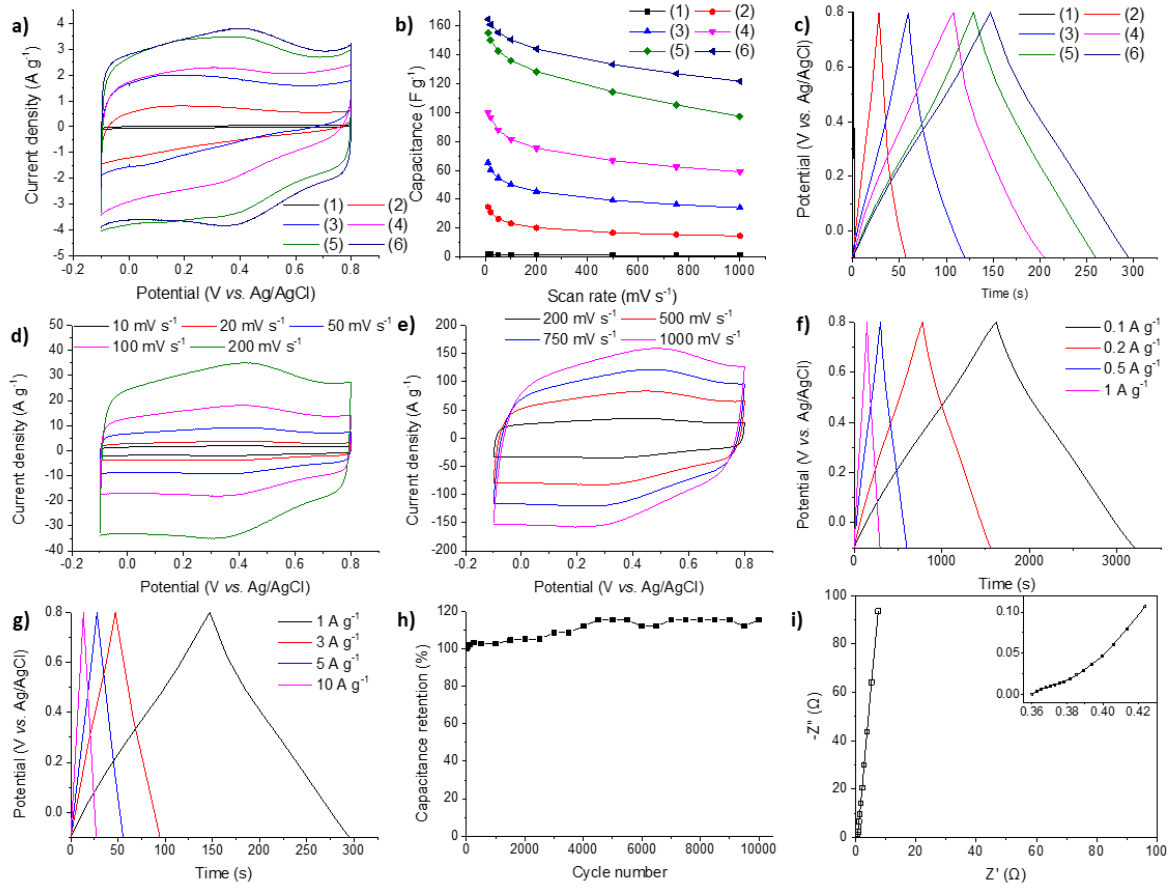

Figure 3.9 (a) Cyclic voltammograms of CMP-1 and carbonised CMPs at a scan rate of 20 mV s^{-1}: CMP-1 (1), C1-CMP-1 (2), C2-CMP-1 (3), N1-CMP-1 (4), N2-CMP-1 (5) and N3-CMP-1 (6). (b) Specific capacitance at varying scan rates. (c) Galvanostatic charge-discharge curves of CMP-1 and carbonised CMPs at a current density of 1 A g^{-1}. (d) Cyclic voltammograms of N3-CMP-1 at varying scan rates between 10 mV s^{-1} and 200 mV s^{-1}. (e) Cyclic voltammograms of N3-CMP-1 at varying scan rates between 200 mV s^{-1} and 1000 mV s^{-1}. (f) Galvanostatic charge discharge curves of N3-CMP-1 at current densities between 0.1 A g^{-1} and 1 A g^{-1}. (g) Galvanostatic charge discharge curves of N3-CMP-1 at current densities between 1 A g^{-1} and 10 A g^{-1}. (h) Cycling stability of N3-CMP-1 at a current density of 5 A g^{-1}. (i) Nyquist impedance spectrum of N3-CMP-1 measured at 350 mV *vs.* Ag/AgCl in 1 M H_2SO_4.

Nitrogen containing carbonised CMPs showed increased performances, with capacitances of 96.5 F g^{-1} for N1-CMP-1, 150.1 F g^{-1} for N2-CMP-1, and 160.9 F g^{-1} for N3-CMP-1 at 20 mV s^{-1}. However, the CV curve of N1-CMP-1 shows a more inclined shape compared with the other samples, which may be due to limited ion diffusion.[32] This would explain why the capacitance decreases rapidly as the scan rate increases and the transport time decreases (**Figure 3.9b**). The ammonia-treated CMPs, N2-CMP-1 and N3-CMP-1, showed high current responses and therefore better capacitive performance. The better performance of N3-CMP-1 is likely due to its higher surface area and greater volume of micropores,

which contribute to the quasi-rectangular symmetrical shape that denotes a highly reversible supercapacitor. The GCD times (**Figure 3.9c**) are consistent with the charge densities of the CV results. All the carbonised CMP materials showed a triangular GCD shape, which is typical behaviour for constant charge and discharge for supercapacitive materials. The N-doped CMPs' superior function can be compared with N-doped carbonised PAF-1,[33] which showed non-triangular GCD profiles. This was particularly pronounced at lower current densities, and may indicate poor reversibility, as was also indicated by the non-rectangular CV profiles produced for the PAF-1 derived materials at higher scan rates, possibly due to unideal resistance.

N3-CMP-1 shows high capacitance and possesses nearly identical voltammetric charges when integrating from both the positive and negative sweeps, indicating excellent reversibility. The electrochemical behaviour of this sample was studied further, and CV responses of N3-CMP-1 at scan rates from 10 mV s^{-1} to 200 mV s^{-1} are shown in **Figure 3.9d**. The CV retains a quasi-rectangular shape when the scan rate is increased, with the capacitance only reducing from 164.6 F g^{-1} at 10 mV s^{-1} to 144.0 F g^{-1} at 200 mV s^{-1}, demonstrating excellent capacitance rate-retention. Moreover, a specific capacitance of 121.6 F g^{-1} was measured at the extremely fast scan rate of 1000 mV s^{-1}. Voltammetric currents of the material also swiftly reach their respective plateau when the direction of the potential sweep is changed; even with scan rates as fast as 1000 mV s^{-1} (**Figure 3.9e**). This indicates a low ESR for the material, arising from its high electronic conductivity and the low ionic resistance of the electrolyte within the pores during charging and discharge.[34] The GCD profile (**Figure 3.9f,g**) also show a consistent triangular shape with varying current densities from 0.1 A g^{-1} to 10 A g^{-1}, leading to capacitances of 175.3 F g^{-1} at 0.1 A g^{-1}, 164.0 F g^{-1} at 1.0 A g^{-1}, and 148.6 F g^{-1} at 10 A g^{-1}, highlighting this material's notable capacitance retention and Coulombic efficiencies of 97%, 100%, and 100%, respectively. Even after 10000 GCD cycles at a current density of 5 A g^{-1}, the material did not show any loss in capacitance suggesting excellent stability (**Figure 3.9h**). In fact, a slight increase in capacitance was observed which is likely due to progressive wetting of a small fraction of less accessible and therefore previously occluded pores during extended cycling. A Nyquist plot of N3-CMP-1 in the low frequency region shows the impedance of the imaginary part approaches vertical, indicative of typical ideal capacitive behaviour (**Figure 3.9i**).[35]

The respective contributions of EDLC and PC of N3-CMP-1 can be compared against each other due to the relatively slower electrochemical kinetics that arise from Faradaic redox reactions participating in the PC mechanism,[20] originating from the same procedure in estimating the outer electroactive sites of metal oxides.[36] The total maximum specific capacitance, $C_{S,T,M}$, is partitioned from EDLC and PC. In this procedure, the total voltammetric charge, q_T, is calculated by estimating the charge to $v = 0$ from the plot of $1/q$ *vs.* $v^{1/2}$ (**Figure 3.10a**). The specific capacitance associated with EDLC, $C_{S,DL}$, is

calculated from the double-layer charge, q_{DL}, which is estimated from the charge to $v = \infty$ from the plot of q *vs.* $v^{-1/2}$ (**Figure 3.10b**). The PC charge can be obtained by the difference between q_T and q_{DL}. Thus, $C_{S,T,M}$, $C_{S,DL}$, and $C_{S,P}$, is calculated by dividing the corresponding charge with its respective potential window of the CV, *i.e.*, 0.9 V and 1.1 V for 1 M H_2SO_4 and 3 M KOH respectively (**Table 3.3**). The presence of N-containing functional groups in the material gives rise to 14% pseudocapacitance associated with $C_{S,T,M}$. Therefore the material possesses both EDLC and PC mechanisms which can be seen from the redox peaks in **Figure 3.9d**.

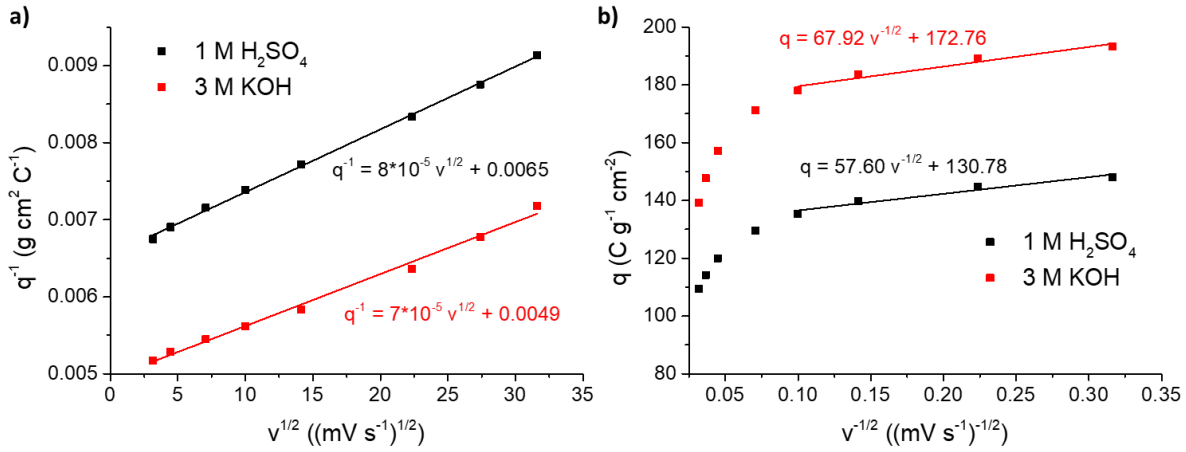

Figure 3.10 (a) Dependence of $1/q$ on $v^{1/2}$ and (b) dependence of q on $v^{-1/2}$ for N3-CMP-1 in acidic and basic electrolytes.

Table 3.3 Summary of maximum total specific capacitance ($C_{S,T,M}$), double-layer capacitance (C_{DL}) and pseudocapacitance (C_P) of N3-CMP-1 in acidic and basic electrolyte.

Electrolyte	$C_{S,T,M}$ (F g^{-1})	C_{DL} (F g^{-1})	C_P (F g^{-1})	$C_P/C_{S,T,M}$ (F g^{-1})
1 M H_2SO_4	169.5	145.3	24.2	14.3
3 M KOH	185.2	157.1	28.1	15.2

3.4.4 Electrolyte Optimisation

N3-CMP-1 was further investigated using different aqueous electrolytes of varying pH. The ionic strength was kept constant to correspond to the 1 M H_2SO_4 that was used previously. **Figure 3.11a** shows the CVs of N3-CMP-1 in 1 M Na_2SO_4 at scan speeds from 10 mV s^{-1} to 200 mV s^{-1}. The CV profile of 1 M Na_2SO_4 shows a quasi-rectangular shape with good capacitances of 116.9 F g^{-1} at 10 mV s^{-1} and 100.3 F g^{-1} at 200 mV s^{-1}. The voltammetric currents when using 1 M Na_2SO_4 aqueous electrolyte are slightly lower than when using 1 M H_2SO_4, which is a known phenomenon due to better conductivity of acidic electrolyte arising from the proton hopping mechanism in aqueous media.[37] This electrolyte also yielded symmetrical triangular GCD profiles (**Figure 3.11b**), with a specific

capacitance of 145.4 F g^{-1} at 0.1 A g^{-1}. The use of 3 M KOH for N3-CMP-1 gave rise to a fair quasi-rectangular CV profile, showing capacitances of 175.7 F g^{-1} at 10 mV s^{-1}, 155.7 F g^{-1} at 200 mV s^{-1} and 127.9 F g^{-1} at 1000 mV s^{-1} (**Figure 3.11c**). Unusually, and in contrast to the previous proton hopping argument, the specific capacitance values were higher with 3 M KOH than with 1 M H_2SO_4. The GCD tests on N3-CMP-1 emphasise this and show a large capacitance of 260.0 F g^{-1} at a current density of 0.1 A g^{-1} (**Figure 3.11d**). This is not conventional for supercapacitors, although the shape of the CV was less symmetrical when using basic media, which suggests that there may be increased redox activity seen from the addition peaks. This is supported by a larger PC contribution, of 15%, towards $C_{S,T,M}$ when compared to acidic electrolyte (**Table 3.3**).

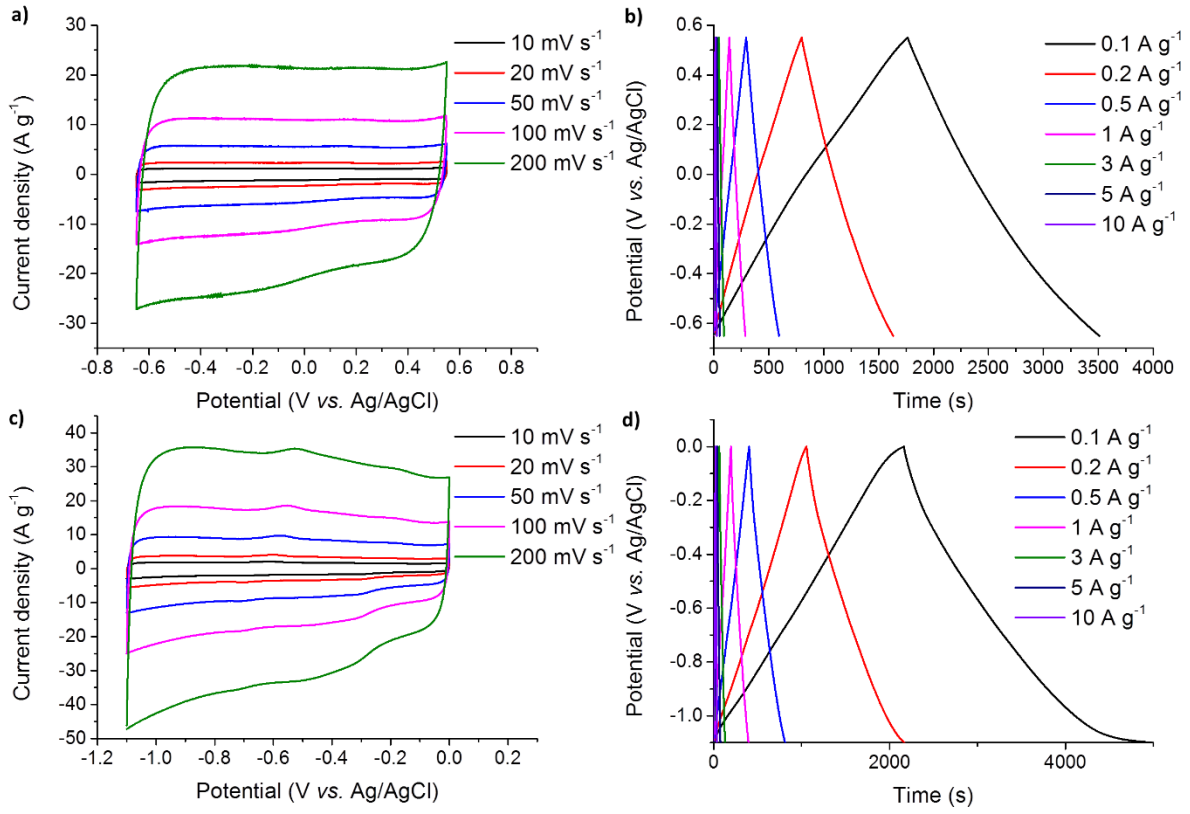

Figure 3.11 (a) Cyclic voltammograms of N3-CMP-1 at varying scan rates in 1 M Na_2SO_4. (b) Galvanostatic charge-discharge curves of N3-CMP-1 at varying current densities in 1 M Na_2SO_4. (c) Cyclic voltammograms of N3-CMP-1 at varying scan rates in 3 M KOH. (d) Galvanostatic charge-discharge curves of N3-CMP-1 at varying current densities in 3 M KOH.

N3-CMP-1 also retains a quasi-rectangular shape at very high scan rates in both 1 M Na_2SO_4 and 3 M KOH (**Figure 3.12**) and good capacitance retention (**Figure 3.13**), which shows the material has a pore structure suitable for efficient diffusion of these electrolytes.

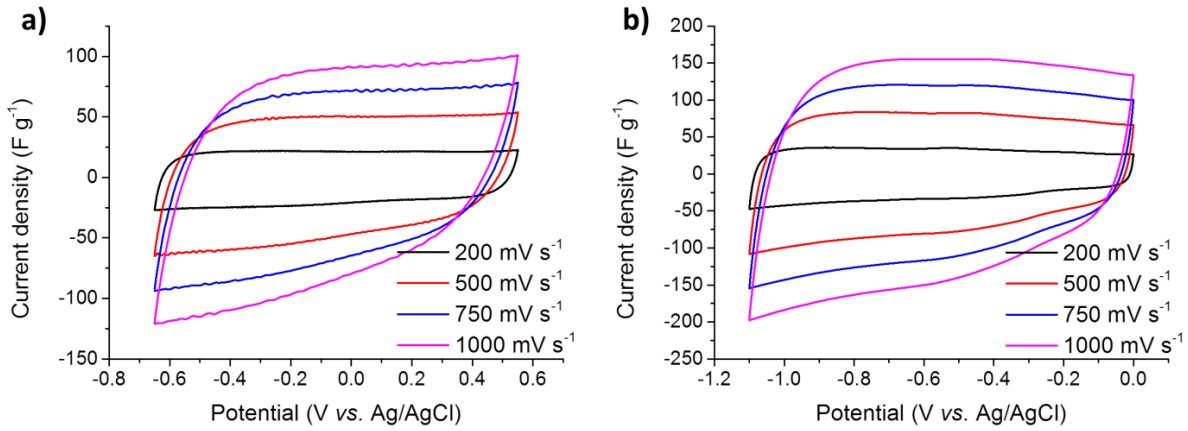

Figure 3.12 Cyclic voltammograms of N3-CMP-1 in (a) 1 M Na_2SO_4 and (b) 3 M KOH at high scan rates.

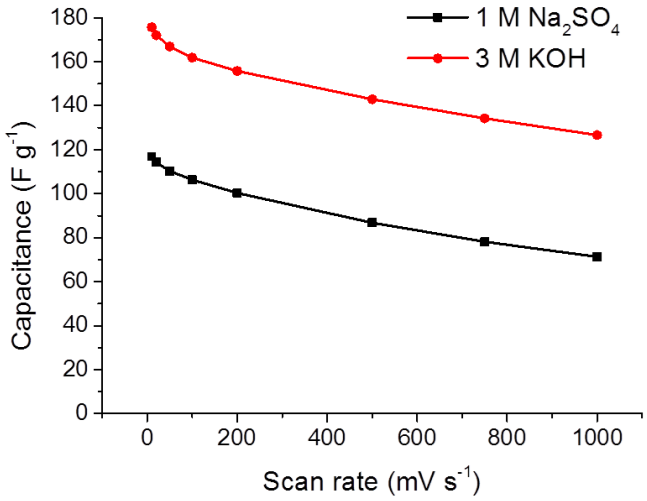

Figure 3.13 Specific capacitance of N3-CMP-1 at varying scan rates in 1 M Na_2SO_4 and 3 M KOH.

In addition to the larger pseudocapacitive contributions when using KOH, the ion sizes are also smaller than for H_2SO_4.[38] As N3-CMP-1 retains its microporosity during carbonisation, the relatively small pore diameter of ~10 Å may also allow better diffusion of KOH, resulting in higher capacitances.

Ragone plots of N3-CMP-1 show that in KOH, the material exhibits maximum energy and power densities of 43.7 W h kg^{-1} and 5.5 kW kg^{-1}, respectively (**Figure 3.14a**). The material reaches the energy regimes of Li-ion batteries whilst retaining power densities of supercapacitors (**Figure 3.14b**), therefore, showing promise in using CMP-derived materials for supercapacitors.

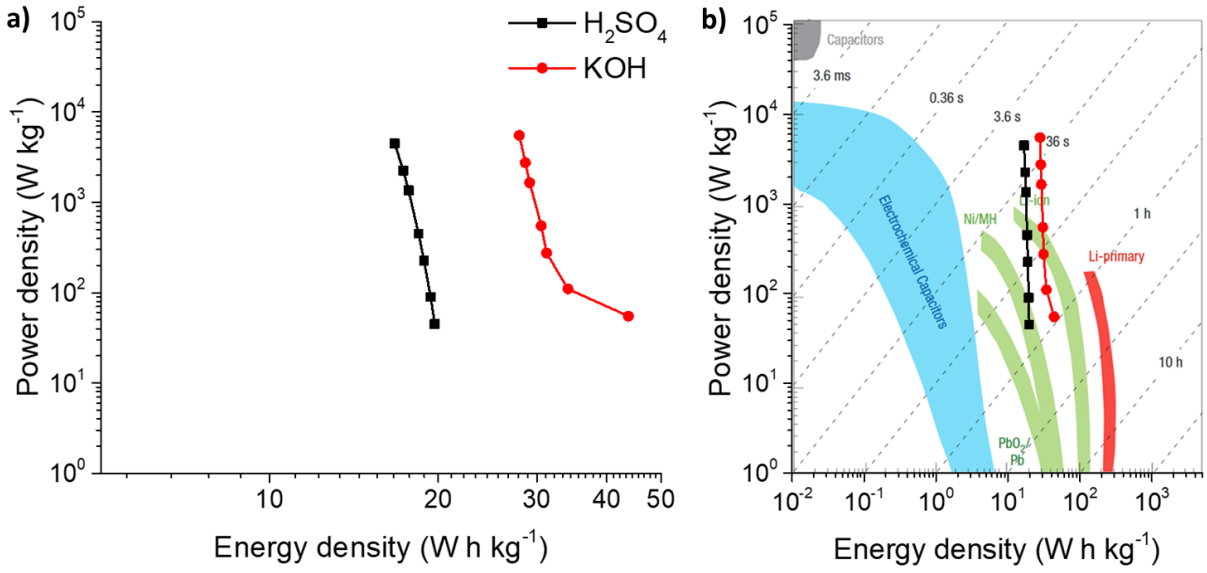

Figure 3.14 (a) Ragone plots of N3-CMP-1 in 1 M H_2SO_4 and 3 M KOH. (b) Overlay of results with other energy storage devices, adapted from literature source.[39]

3.5 Conclusions and Outlook

In summary, conductive CMP-type materials were prepared by carbonisation of CMPs using various methods. Our best performing material, N3-CMP-1, shows ideal supercapacitive behaviour, with a high capacitance of 175 F g^{-1} and no signs of degradation after 10000 cycles with an acidic electrolyte. It was also shown that more ideal capacitor behaviour can be achieved with a neutral electrolyte and that an even higher capacitance of 260 F g^{-1} can be obtained with a basic electrolyte. These promising initial results open up a new method to access electro-active properties from CMPs.

The application of carbonised CMPs to supercapacitors offers exciting opportunities, and indeed three further works on this topic were published during the undergoing of this project. Yuan *et al.* initially produced a pillared porous graphene framework through the Yamamoto coupling of functionalised reduced graphene oxide possessing a capacitance of 286 F g^{-1} at 10 mV s^{-1}.[40] They developed this further with a composite material composed of a CMP and graphene.[41] Our results demonstrate a simpler, more direct approach that can be used for a whole library of CMPs. The approach reported by Bhosale *et al*. requires a specific N- and S- containing CMP precursor; however this yielded a non-rectangular CV profile, which suggests a more resistive material.[42] At the time of writing this thesis, there has been numerous reports on CMP-derived supercapacitors which have built upon the work presented in this chapter.[43] There has also been a few recent reports that utilises CMPs as supercapacitors without high temperature synthesis or carbonisation.[44] This remains a challenge as CMPs are generally not electronically conductive, so supercapacitor performance is only derived from

the PC mechanism with relatively poor performance characteristics (CV and GCD shapes) compared to traditional supercapacitors. Until conductive CMPs are discovered, carbonisation remains a viable and efficient option to impart electric conductivity in these types of materials.

3.6 References

[1] Y. Zhu, S. Murali, M. D. Stoller, K. J. Ganesh, W. Cai, P. J. Ferreira, A. Pirkle, R. M. Wallace, K. A. Cychosz, M. Thommes, D. Su, E. A. Stach, R. S. Ruoff, *Science* **2011**, *332*, 1537.

[2] B. You, L. Wang, L. Yao, J. Yang, *Chem. Commun.* **2013**, *49*, 5016.

[3] C. Liu, F. Li, L.-P. Ma, H.-M. Cheng, *Adv. Mater*. **2010**, *22*, E28.

[4] J. Yan, T. Wei, W. Qiao, Z. Fan, L. Zhang, T. Li, Q. Zhao, *Electrochem. Commun*. **2010**, *12*, 1279.

[5] L. Chen, Y. Yang, D. Jiang, *J. Am. Chem. Soc*. **2010**, *132*, 9138; J.-X. Jiang, C. Wang, A. Laybourn, T. Hasell, R. Clowes, Y. Z. Khimyak, J. Xiao, S. J. Higgins, D. J. Adams, A. I. Cooper, *Angew. Chem., Int. Ed.* **2011**, *123*, 1104; Z. Xie, C. Wang, K. E. deKrafft, W. Lin, *J. Am. Chem. Soc.* **2011**, *133*, 2056; R. S. Sprick, J.-X. Jiang, B. Bonillo, S. Ren, T. Ratvijitvech, P. Guiglion, M. A. Zwijnenburg, D. J. Adams, A. I. Cooper, *J. Am. Chem. Soc*. **2015**, *137*, 3265.

[6] L. Chen, Y. Honsho, S. Seki, D. Jiang, *J. Am. Chem. Soc.* **2010**, *132*, 6742.

[7] R. Dawson, D. J. Adams, A. I. Cooper, *Chem. Sci.* **2011**, *2*, 1173; W. Lu, J. P. Sculley, D. Yuan, R. Krishna, Z. Wei, H.-C. Zhou, *Angew. Chem., Int. Ed.* **2012**, 51, 7480.

[8] A. Li, H.-X. Sun, D.-Z. Tan, W.-J. Fan, S.-H. Wen, X.-J. Qing, G.-X. Li, S.-Y. Li, W.-Q. Deng, *Energy Environ. Sci.* **2011**, *4*, 2062.

[9] Y. Xu, L. Chen, Z. Guo, A. Nagai, D. Jiang, *J. Am. Chem. Soc*. **2011**, *133*, 17622.

[10] X. Liu, Y. Xu, D. Jiang, *J. Am. Chem. Soc.* **2012**, *134*, 8738.

[11] J.-X. Jiang, A. Trewin, D. J. Adams, A. I. Cooper, *Chem. Sci.* **2011**, *2*, 1777.

[12] Y. Kou, Y. Xu, Z. Guo, D. Jiang, *Angew. Chem., Int. Ed.* **2011**, *50*, 8753.

[13] C.-C. Hu, C.-C. Wang, *J. Power Sources* **2004**, *125*, 299.

[14] I. C. Lewis, Carbon 1982, 20, 519; L. Wang, C. Schutz, G. Salazar-Alvarez, M.-M. Titirici, *RSC Adv*. **2014**, *4*, 17549; Y. Li, H. Zhu, F. Shen, J. Wan, X. Han, J. Dai, H. Dai, L. Hu, *Adv. Funct. Mater*. **2014**, *24*, 7366.

[15] B. Ashourirad, A. K. Sekizkardes, S. Altarawneh, H. M. El-Kaderi, *Chem. Mater*. **2015**, *27*, 1349; X. Zhuang, F. Zhang, D. Wu, N. Forler, H. Liang, M. Wagner, D. Gehrig, M. R. Hansen, F. Laquai, X. Feng, *Angew. Chem. Int. Ed*. **2013**, *52*, 9668; X. Zhuang, D. Gehrig, N. Forler, H. Liang, M. Wagner, M. R. Hansen, F. Laquai, F. Zhang, X. Feng, *Adv. Mater*. **2015**, *27*, 3789.

[16] J.-X. Jiang, F. Su, A. Trewin, C. D. Wood, N. L. Campbell, H. Niu, C. Dickinson, A. Y. Ganin, M. J. Rosseinsky, Y. Z. Khimyak, A. I. Cooper, *Angew. Chem. Int. Ed.* **2007**, *46*, 8574.

[17] L.-M. Li, E.-H. Liu, J. Li, Y.-J. Yang, H.-J. Shen, Z.-Z. Huang, X.-X. Xiang, *Acta Phys. Chim. Sin*. **2010**, *26*, 1521; Z. Rozlívková, M. Trchová, M. Exnerová, J. Stejskal, *Synth. Met*. **2011**, *161*, 1122.

[18] L. Li, E. Liu, J. Li, Y. Yang, H. Shen, Z. Huang, X. Xiang, W. Li, *J. Power Sources* **2010**, *195*, 1516.

[19] Y. Kou, Y. Xu, Z. Guo, D. Jiang, *Angew. Chem., Int. Ed.* **2011**, *123*, 8912.

[20] Y.-H. Lee, K.-H. Chang, C.-C. Hu, *J. Power Sources* **2013**, *227*, 300.

[21] Y. Qiu, X. Zhang, S. Yang, *Phys. Chem. Chem. Phys.* **2011**, *13*, 12554.

[22] R. Dawson, A. Laybourn, R. Clowes, Y. Z. Khimyak, D. J. Adams, A. I. Cooper, *Macromolecules* **2009**, *42*, 8809.

[23] Z.-H. Sheng, L. Shao, J.-J. Chen, W.-J. Bao, F.-B. Wang, X.-H. Xia, *ACS Nano* **2011**, *5*, 4350.

[24] B. You, N. Li, H. Zhu, X. Zhu, J. Yang, *ChemSusChem* **2013**, *6*, 474.

[25] K. J. Boyd, D. Marton, S. S. Todorov, A. H. Al-Bayati, J. Kulik, R. A. Zuhr, J. W. Rabalais, *J. Vac. Sci. Technol. A* **1995**, *13*, 2110.

[26] T. Fuller, C. Hartnig, V. Ramani, H. Uchida, H. A. Gasteiger, S. Cleghorn, P. Strasser, T. Zawodzinski, D. Jones, P. Shirvanian, T. Jarvi, P. Zelenay, P. B. C. Lamy, *Proton Exchange Membrane Fuel Cells 9*, Vol. 25, Vienna, Austria **2009**.

[27] F. Xu, M. Minniti, P. Barone, A. Sindona, A. Bonanno, A. Oliva, *Carbon* **2008**, *46*, 1489.

[28] Y. Li, S. Roy, T. Ben, S. Xu, S. Qiu, *Phys. Chem. Chem. Phys.* **2014**, *16*, 12909.

[29] N. J. Bell, Y. H. Ng, A. Du, H. Coster, S. C. Smith, R. Amal, *J. Phys. Chem. C* **2011**, *115*, 6004; D. Mhamane, W. Ramadan, M. Fawzy, A. Rana, M. Dubey, C. Rode, B. Lefez, B. Hannoyer, S. Ogale, *Green Chem*. **2011**, *13*, 1990.

[30] F. Tuinstra, J. L. Koenig, *J. Chem. Phys.* **1970**, *53*, 1126; L. G. Cançado, K. Takai, T. Enoki, M. Endo, Y. A. Kim, H. Mizusaki, A. Jorio, L. N. Coelho, R. Magalhães-Paniago, M. A. Pimenta, *Appl. Phys. Lett.* **2006**, *88*, 163106.

[31] E. Raymundo-Piñero, M. Cadek, F. Béguin, *Adv. Funct. Mater*. **2009**, *19*, 1032.

[32] J. Hu, H. Wang, Q. Gao, H. Guo, *Carbon* **2010**, *48*, 3599.

[33] Z. Xiang, D. Wang, Y. Xue, L. Dai, J.-F. Chen, D. Cao, *Sci. Rep*. **2015**, *5*, 8307.

[34] F.-C. Wu, R.-L. Tseng, C.-C. Hu, C.-C. Wang, *J. Power Sources* **2006**, *159*, 1532.

[35] P. L. Taberna, P. Simon, J. F. Fauvarque *J. Electrochem. Soc.* **2003**, *150*, A292.

[36] S. Ardizzone, G. Fregonara, S. Trasatti, *Electrochim. Acta* **1990**, *35*, 263; D. Baronetto, N. Krstajić, S. Trasatti, *Electrochim. Acta* **1994**, *39*, 2359; K.-H. Chang, C.-C. Hu, C.-Y. Chou, *Chem. Mater*. **2007**, *19*, 2112.

[37] A. Bard, L. R. Faulkner, *Electrochemical Methods: Fundamentals and Applications*, Wiley, New York **1980**.

[38] R. J. Podolsky, *Circulation* **1960**, *21*, 818.

[39] P. Simon, Y. Gogotsi, *Nat. Mater.* **2008**, *7*, 845.

[40] K. Yuan, Y. Xu, J. Uihlein, G. Brunklaus, L. Shi, R. Heiderhoff, M. Que, M. Forster, T. Chassé, T. Pichler, T. Riedl, Y. Chen, U. Scherf, *Adv. Mater.* **2015**, *27*, 6714.

[41] K. Yuan, P. Guo-Wang, T. Hu, L. Shi, R. Zeng, M. Forster, T. Pichler, Y. Chen, U. Scherf, *Chem. Mater*. **2015**, *27*, 7403; K. Yuan, T. Hu, Y. Xu, R. Graf, G. Brunklaus, M. Forster, Y. Chen, U. Scherf, *ChemElectroChem* **2016**, *3*, 822.

[42] M. E. Bhosale, R. Illathvalappil, S. Kurungot, K. Krishnamoorthy, *Chem. Commun.* **2016**, *52*, 316.

[43] Y. Zhao, F. Xie, C. Zhang, R. Kong, S. Feng, J.-X. Jiang, *Microporous Mesoporous Mater.* **2017**, *240*, 73; Y. Xu, S. Wu, S. Ren, J. Ji, Y. Yue, J. Shen, *RSC Adv*. **2017**, *7*, 32496; Q. Xu, Y. Tang, L. Zhai, Q. Chen, D. Jiang, *Chem. Commun.* **2017**, *53*, 11690; A. C. Lim, H. S. Jadhav, J. G. Seo, *Dalton Trans.* **2018**, *47*, 852.

[44] X.-C. Li, Y. Zhang, C.-Y. Wang, Y. Wan, W.-Y. Lai, H. Pang, W. Huang, *Chem. Sci.* **2017**, *8*, 2959; Y. Liao, H. Wang, M. Zhu, A. Thomas, *Adv. Mater.* **2018**, 1705710.

Chapter 4

Hypercrosslinked Polymer-Derived Carbons for Supercapacitive Energy Storage

Some of the contents in this chapter are taken from **Paper III**.

J.-S. M. Lee, M. E. Briggs, C.-C. Hu, A. I. Cooper, "Controlling Electric Double-Layer Capacitance and Pseudocapacitance in Heteroatom-Doped Carbons from Hypercrosslinked Polymers". *Nano Energy* **2018**, *46*, 277–289.

4.1 Background and Context

Working towards cheaper and more sustainable materials, HCPs are good candidates as they can be synthesised from low-cost precursors via scalable reactions. In addition to this, the synthetic diversity of HCPs is large, thus their properties can be tuned towards specific applications. This strategy was utilised by synthesising a range of HCPs which do and do not contain various heteroatoms, applying electrical conductivity through various carbonisation temperatures, and observing their performances as supercapacitors. Through this method, it was found that one could control which of the two supercapacitive mechanisms were dominant. Through optimisation, two materials were produced—one EDLC dominant and one PC dominant—which show different characteristics from each other, but both outperform many top performing materials in literature.

4.2 Introduction

As society moves away from fossil fuels, there is a need for higher energy storage capacities and higher power densities in energy storage devices such as batteries[1] and supercapacitors.[2] Supercapacitors, are characterised by high power densities, rapid charge/discharge speeds, and exceptional cycle lifetimes.[3] Activated carbon materials are commonly used as EDLC electrodes, with the first patent by Becker awarded in 1957.[4] There are no Faradic redox reactions in these EDLC electrodes, meaning that the charge storage kinetics are fast and reversible, which allows fast energy uptake and delivery, and hence good power performance. EDLC electrodes are generally very stable because the storage mechanism is purely electrostatic, but this means that EDLC devices also suffer from limited energy densities.[5] Pseudocapacitors operate by fast, reversible, Faradaic redox reactions at the surface of the electrode and they can achieve higher energy densities than the EDLC devices, but this is typically at the expense of power density and cycle life.[6] Transition metal oxides are commonly studied as pseudocapacitor electrodes due to high capacitance contributions from their change in oxidation states. However, because pseudocapacitors can only store charge in the first few nanometres from the surface, this limits these materials being thin films or small particles.[5]

Redox-active porous carbons[7, 8] can combine the advantages of high power density and cycle life from EDLC with the high energy density from PC. Porous carbon-based supercapacitors have been produced by carbonisation of precursors such as biomass,[9] linear polymers,[10] graphene oxide,[11, 12] and a variety of porous organic polymers.[7, 13, 14] Such routes avoid the use of expensive transition metals, although the performance of organic-based supercapacitors is generally lower;[5, 15, 16] as such, there is a need for performance improvements in carbon-based supercapacitors. While biomass is a cheap precursor, its

limited chemistry, coupled with the natural variability between sources of biomass, is a major drawback.[17] Microporous solids have been used as precursors for carbonaceous materials, leading to enhanced properties where the choice of porous precursor affects the functionality of the resultant carbons. Examples of porous precursors include MOFs,[18-20] PAFs,[13, 21] and CMPs.[7, 14, 22] Although these materials can show excellent performance as supercapacitor electrodes, these precursor networks involve costly starting materials (*e.g.*, PAFs, CMPs, and many MOFs) and they often require expensive catalysts for their synthesis (*e.g.*, PAFs and CMPs). In addition, some of these precursor networks require preparation under rigorous anhydrous and anaerobic conditions (*e.g.*, PAFs), which further increases the cost of scale-up and reduces potential benefit over transition metal-based supercapacitors.

HCPs are microporous materials synthesised from cheap organic monomers using non-rigorous reaction conditions that nonetheless possess potential for synthetic diversification.[23] Permanent porosity in HCPs is a result of extensive crosslinking, which creates a rigid structure that is incapable of complete collapse into a dense, non-porous state upon desolvation. HCPs have been known for many years and are scalable,[24] with Purolite International Ltd marketing Hypersol-Macronet® polymer resins since the 1990s.[25] HCPs can be prepared from a one-step Friedel-Crafts "knitting" procedure using formaldehyde dimethyl ether as a crosslinker with a very wide range of aromatic molecules, giving access to a large library of functional porous polymers.[26] The surface areas, pore-size distributions, and surface functionalities of HCPs can be tuned by simply changing the aromatic monomer, the reaction stoichiometry, or by the inclusion of functionalised aromatic co-monomers. HCPs have been used extensively in gas storage applications,[27, 28] separations,[29] and heterogeneous catalysis.[30] However, unmodified HCPs have not been used in electrochemical applications due to their non-conducting nature.

The aim of the project was to find a simple procedure to induce electrical conductivity in HCPs, while allowing transfer of heteroatom functionality, and hence to introduce pseudocapacitance into the resulting carbonaceous material. This chapter describes how a simple carbonisation process can be applied to a range of HCPs to induce electrical conductivity for use as a supercapacitor electrode. By transferring parent heteroatoms or by applying doping during carbonisation, this allowed the HCP-based carbonaceous material to exhibit both EDLC and PC properties, thus yielding high performance supercapacitors.

4.3 Experimental

4.3.1 Chemical Reagents

Benzene, pyrrole, thiophene, aniline, FDA, iron(III) chloride, 1,2-dichloroethane, and poly(vinylidine difluoride) were purchased from Sigma Aldrich. Methanol and NMP were purchased from Fisher Scientific. Super C65 carbon black was purchased from Timical. High purity nitrogen and NH_3 were purchased from BOC. All chemicals were used as received without any further purification. Deionised (DI) water was used in purifications.

4.3.2 Synthesis

Preparation of Hypercrosslinked Polymers

The HCPs were synthesised using a previously reported literature method.[26] The monomer (either benzene, pyrrole, thiophene, or aniline; 50 mmol) was added to 1,2-dichloroethane (100 mL) under nitrogen in a 250 mL two-necked Radley's flask equipped with a reflux condenser. FDA (8.8 mL, 100 mmol) was added and the mixture was stirred for 10 min. Iron(III) chloride (16.2 g, 100 mmol) was then added and the mixture was heated under reflux at 80 °C overnight. After cooling the dark brown/black precipitate was filtered and washed with methanol. The solids were further purified by Soxhlet extraction with methanol for 1 day then dried under vacuum at 70 °C for 1 day. Gravimetric yields for all polymers were >90%. Elemental analysis: HCP-Ben, C: 85.50%, H: 5.45%; HCP-Py, C: 58.80%, H: 5.10%, N: 11.02%; HCP-Th, C: 52.79%, H: 3.20%, S: 23.40%; HCP-Ani, C: 60.56%, H: 3.20%, N: 9.86%.

Preparation of C-HCP-Δ

In a typical procedure, hypercrosslinked polymer (300 mg) was homogeneously dispersed into a ceramic boat and inserted within a tube furnace. The furnace was purged with N_2 (100 mL min^{-1}) at room temperature for 30 min, heated to the specified temperature at a rate of 5 °C min^{-1}, held at the set point for 2 h, and finally cooled naturally to room temperature. The resultant black powder was used as obtained.

Preparation of N-HCP-Δ

In a typical procedure, hypercrosslinked polymer (800 mg) was homogeneously dispersed into a ceramic boat and inserted within a tube furnace. The furnace was purged with NH_3 (100 mL min^{-1}) at room temperature for 30 min, heated to the specified temperature at a rate of 5 °C min^{-1}, and held at the

set point for 2 h. The gas flow was then switched to N_2 and the furnace was allowed to cool naturally to room temperature. The resultant black powder was used as obtained.

Preparation of P-N-HCP-Δ

This follows the general preparation of N-HCP-Δ but C-HCP-800 was used as a precursor.

4.4 Results and Discussion

4.4.1 Methodology of Hypercrosslinked Polymers and HCP-Based Carbons

Benzene, pyrrole, thiophene, and aniline were crosslinked according to known literature methods;[26] the resulting polymer networks were referred to as HCP-Ben, HCP-Py, HCP-Th, and HCP-Ani, respectively (**Scheme 4.1**).

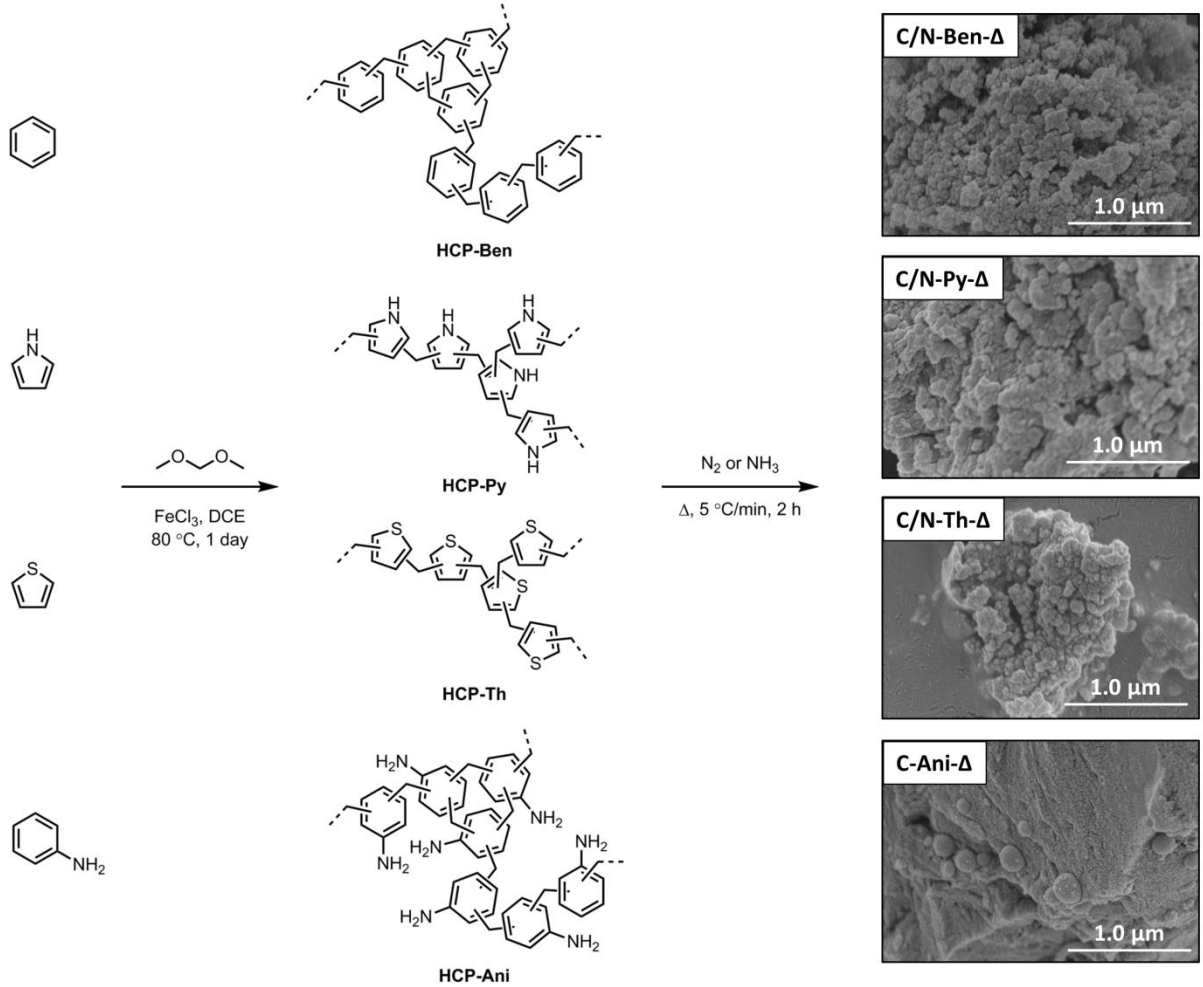

Scheme 4.1 Synthesis of the hypercrosslinked polymers and subsequent carbonisation methods.

These monomers were chosen to produce a variety of HCPs containing either no heteroatoms (benzene), N-atoms (pyrrole and aniline), or S-atoms (thiophene). TGA under nitrogen was performed to determine the thermal stability of the HCPs, mimicking the conditions to be used for carbonisation (**Figure 4.1**). HCP-Py, HCP-Th, and HCP-Ani all show some mass loss below 100 °C due to the evaporation of physisorbed atmospheric water;[28] this is because the N and S atoms present in these polymers have strong affinities for water. HCP-Ben shows the highest thermal stability, with only 30% mass loss at up to 1000 °C, whereas HCP-Py, HCP-Th, and HCP-Ani show greater mass losses up to this temperature. This was ascribed to the loss of heteroatoms, which are prone to removal during high temperature carbonisations. A good mass recovery was retained after heating the HCPs at high temperatures; hence, these HCPs are suitable candidates for carbonisation.

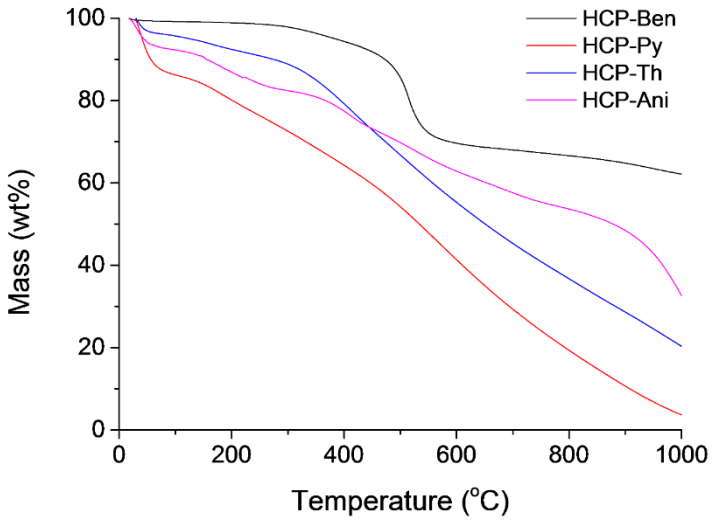

Figure 4.1 TGA curves of HCPs at a ramp rate of 5 °C min^{-1} under N_2.

Carbonised HCPs were obtained by direct carbonisation under a N_2 atmosphere; the samples were heated at a ramp rate of 5 °C min^{-1} to the set point then held at the set-point for 2 h, before cooling. These carbons are referred to as C-Ben-Δ, C-Py-Δ, C-Th-Δ, and C-Ani-Δ, with Δ signifying the carbonisation temperature.

Doping carbons with heteroatoms, such as nitrogen, is known to enhance supercapacitive energy storage due to better dipolar attraction to the electrolyte cations,[31] increased electrical conductivity,[12] and the introduction of PC contributions.[7, 32] C-Py-Δ, C-Th-Δ, and C-Ani-Δ carbons (but not C-Ben-Δ) possess 'native' heteroatoms that are retained from their respective precursors (**Table 4.1**). Replacement of the N_2 gas flow with NH_3 for the carbonisation process of HCPs allowed the incorporation of additional N groups into the carbons. This process was performed on HCP-Ben, HCP-Py, and HCP-Th, to produce

N-doped carbons, which are referred to as N-Ben-Δ, N-Py-Δ, and N-Th-Δ, respectively, with Δ again signifying the carbonisation temperature. The post-synthesis treatment of carbons with NH_3 at high temperature also allows the incorporation of nitrogen groups, which has been shown previously to be advantageous for supercapacitive carbon materials.[7] Further studies using C-Ben-800 and C-Py-800 as precursors for the NH_3 post-treatment process produced P-N-Ben-Δ and P-N-Py-Δ, respectively, with Δ signifying the post-treatment temperature.

Table 4.1 Physical properties of HCPs and carbonised products, and their supercapacitive properties.

		Pore volume[a] ($cm^3\ g^{-1}$)			Elemental analysis (%)				Capacitance ($F\ g^{-1}$)	
Sample	Surface area ($m^2\ g^{-1}$)[b]	Total pore volume	Micropore volume	Yield (%)[c]	C	H	N	S	CV[d]	GCD[e]
HCP-Ben	1382	1.52	0.40	-	85.50	5.45	0.00	0.00	-	-
C-Ben-800	539	0.47	0.21	69	93.40	0.75	0.00	0.00	33	30
C-Ben-900	511	0.42	0.20	64	86.16	0.54	0.00	0.00	34	49
C-Ben-1000	737	0.64	0.28	59	94.32	0.41	0.00	0.00	114	116
N-Ben-600	425	0.36	0.19	71	84.49	1.91	2.16	0.00	100	126
N-Ben-700	458	0.41	0.17	62	83.52	1.20	1.60	0.00	115	130
N-Ben-800	1252	0.96	0.45	40	80.26	1.28	7.50	0.00	267	283
N-Ben-1000	655	0.64	0.24	26	92.43	0.57	1.08	0.00	129	136
P-N-Ben-600[f]	369	0.34	0.16	89	85.15	0.50	1.40	0.00	51	48
P-N-Ben-800[f]	697	0.67	0.28	80	66.50	1.39	5.17	0.00	158	190
HCP-Py	322	0.25	0.14	-	58.80	5.10	11.02	0.00	-	-
C-Py-700	305	0.22	0.14	59	76.35	1.49	9.42	0.00	96	107
C-Py-800	387	0.22	0.16	49	75.20	1.38	8.86	0.00	126	134
C-Py-900	388	0.24	0.15	50	76.85	1.20	6.41	0.00	132	159
C-Py-1000	557	0.35	0.22	39	78.18	1.73	3.24	0.00	108	113
N-Py-600	320	0.23	0.15	54	72.98	2.05	12.73	0.00	58	70
N-Py-700	329	0.47	0.31	53	73.05	1.97	13.44	0.00	284	317
N-Py-800	1484	0.83	0.47	11	72.21	2.13	9.79	0.00	183	237
P-N-Py-600[g]	418	0.29	0.20	95	76.33	1.14	11.52	0.00	135	173
P-N-Py-700[g]	443	0.30	0.21	45	80.45	1.24	8.51	0.00	162	231
HCP-Th	484	0.33	0.22	-	52.79	3.20	0.00	23.40	-	-
C-Th-800	616	0.34	0.25	50	79.32	0.38	0.00	13.58	52	49
N-Th-600	464	0.31	0.21	56	71.80	1.63	7.93	12.38	24	23
N-Th-700	760	0.49	0.34	33	73.95	1.55	13.03	0.94	220	226
N-Th-800	508	0.35	0.22	17	55.50	2.12	7.33	0.00	166	196
HCP-Ani	7	0.01	0.00	-	58.69	5.05	8.54	0.00	-	-
C-Ani-800	376	0.30	0.13	47	88.26	0.35	1.34	0.00	66	66

[a] Calculated by single point pore volume. [b]Apparent BET surface area. [c] Carbonisation yield by mass. [d] Specific capacitance measured by cyclic voltammetry at a scan rate of 10 mV s^{-1} in 1 M H_2SO_4. [e] Specific capacitance measured by galvanostatic charge-discharge at a current density of 1 A g^{-1} in 1 M H_2SO_4. [f] Post-synthesis treatment with NH_3 carried out on C-Ben-800. [g] Post-synthesis treatment with NH_3 carried out on C-Py-800.

TGA curves of some representative samples indicated residual masses of 5–9% (**Figure 4.2**). The variances in thermal stability are thought to be due to the choice of carbon precursor.

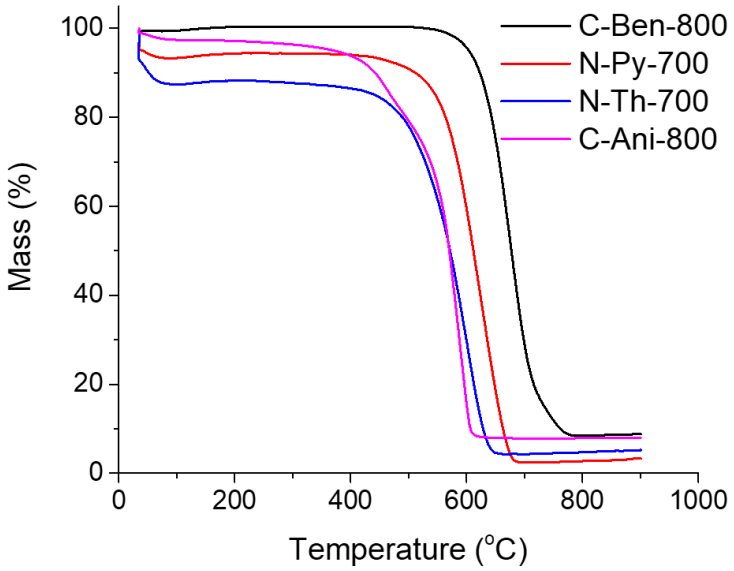

Figure 4.2 TGA analysis of HCP-derived carbons heated in air.

4.4.2 Structure and Properties of Hypercrosslinked Polymer-Based Materials

The apparent BET surface areas and pore structures of the HCPs and synthesised carbons were investigated by N_2 sorption measurements at 77.3 K (**Table 4.1**). The HCPs have surface areas and total pore volumes of 1382 $m^2\ g^{-1}$ and 1.52 $cm^3\ g^{-1}$ for HCP-Ben, 322 $m^2\ g^{-1}$ and 0.25 $cm^3\ g^{-1}$ for HCP-Py, 484 $m^2\ g^{-1}$ and 0.33 $cm^3\ g^{-1}$ for HCP-Th, and 7 $m^2\ g^{-1}$ and 0.01 $cm^3\ g^{-1}$ for HCP-Ani, respectively. HCP-Ben, HCP-Py, and HCP-Th all exhibit Type II isotherms (**Figure 4.3**), suggesting the presence of macropores within their hierarchical pore structure,[33] although it should be stressed that these materials can also swell in N_2, even at low temperatures,[34] which might also affect the isotherm shape at higher relative pressures. HCP-Ani exhibits a Type III isotherm due to relatively weak absorbent-absorbate interactions and absorbed N_2 molecules clustering around the most favourable sites on the surface of the non-porous solid. The surface area matches previously reported HCP-Ani,[35] which was used for gas separations of CO_2 and N_2 at 300 K.

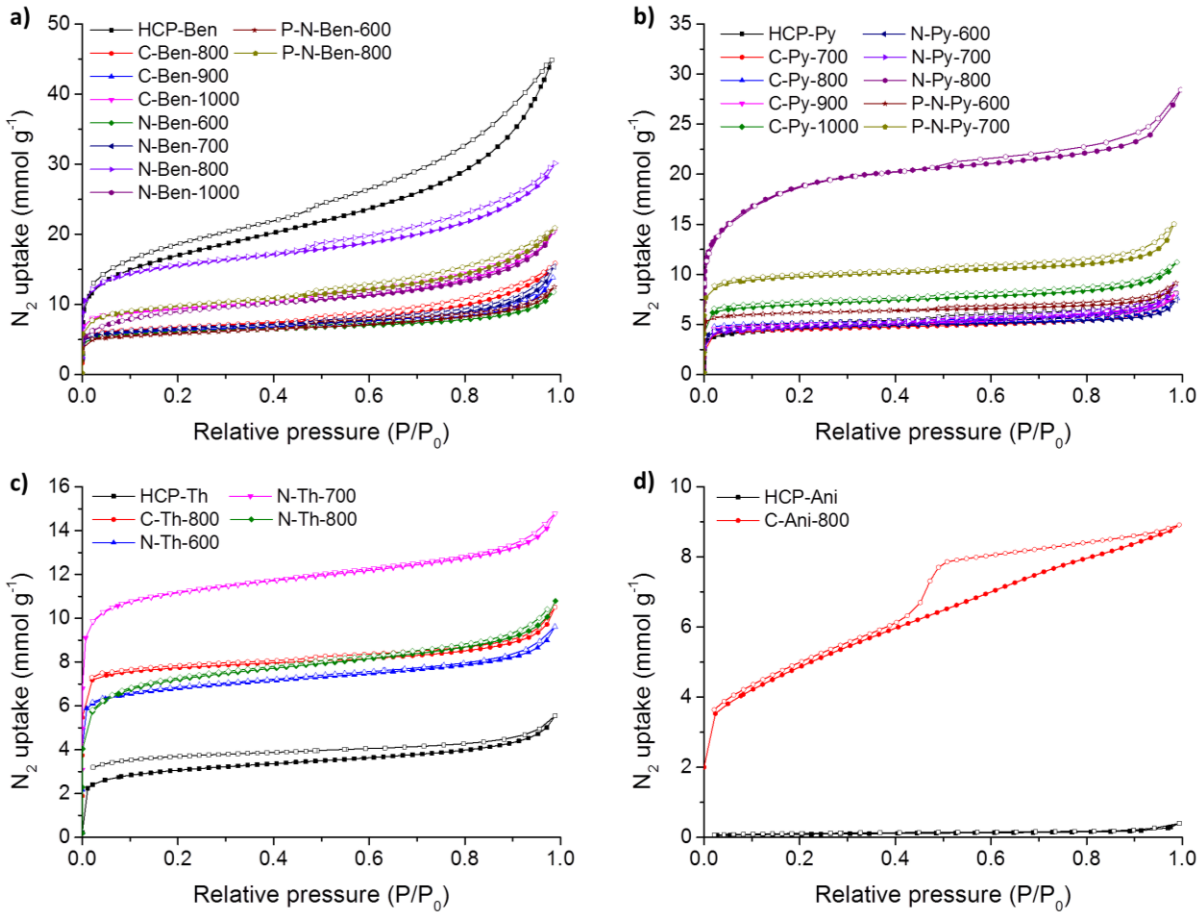

Figure 4.3 Nitrogen adsorption–desorption isotherms of (a) HCP-Ben and x-Ben-Δ, (b) HCP-Py and x-Py-Δ, (c) HCP-Th and x-Th-Δ, and (d) HCP-Ani and C-Ani-800 at 77.3 K (the adsorption and desorption branches are labelled with filled and empty symbols, respectively).

Nearly all carbonised products display Type I isotherms with a steep uptake at low P/P_0, and additional Type IVa characteristics of a hysteresis loop appearing at P/P_0 = 0.5, indicative of a hierarchical structure with high levels of micropores and additional mesopores (**Figure 4.3**). In general, carbonisations in a N_2 atmosphere afford carbons with a more microporous structure than the parent polymer, as demonstrated by the narrowing of the micropore-size distributions (**Figure 4.4**), a sharper increase in the gas sorption isotherms at low P/P_0, and decreased level of mesopores in the overall pore-size distributions. This was also observed for the low temperature carbonisations in NH_3; however, when high temperatures were used (800–1000 °C) increases in the mesopore content were observed. Carbonisations of HCP-Ben and HCP-Py under N_2 resulted in porous carbons with similar surface areas between 700 and 900 °C (539 and 511 $m^2\ g^{-1}$ for C-Ben-800 and C-Ben-900, respectively, and 305, 387, and 388 $m^2\ g^{-1}$ for C-P-700, C-Py800, and C-Py-900, respectively, **Table 4.1**). However, an increase in surface area was observed at 1000 °C (737 $m^2\ g^{-1}$ for C-Ben-1000 and 557 $m^2\ g^{-1}$ for C-Py-1000). C-Th-800 had a relatively high surface area of 616 $m^2\ g^{-1}$ and C-Ani-800 had a surface area of 376 $m^2\ g^{-1}$. Similarly, carbonisations under an NH_3 atmosphere resulted in broadly equivalent surface areas for

HCP-Ben and HCP-Py at 600 and 700 °C, but an increase was observed at a higher temperature of 800 °C. N-Py-800 yielded the highest surface area of 1484 m^2 g^{-1}, closely followed by N-Ben-800 (1252 m^2 g^{-1}), which was due to the additional etching effects from NH_3. Though N-Py-800 yielded the highest surface area carbon from the materials synthesised here, N-Py-700 possessed the highest N-content of 13.44% (9.79% for N-Py-800); both surface area and N-content are important factors for supercapacitor electrodes. Of the carbonised HCP-Th samples, N-Th-700 had the highest surface area of 760 m^2 g^{-1}; unlike N-Ben-800 and N-Py-800, carbonisation at 800 °C reduced the surface area to 508 m^2 g^{-1} due to a decrease in the microporous structure (69% micropore content for N-Th-700 *vs.* 63% for N-Th-800) and probable pore collapse. High temperature carbonisation of HCP-Ben at 1000 °C under NH_3 also yielded a lower surface area of 655 m^2 g^{-1} due to pore collapse (47% micropore content from N-Ben-800 *vs.* 38% from N-Ben-1000). The other HCPs could not be carbonised to 1000 °C due to their lower thermal stabilities, and hence low mass recovery.

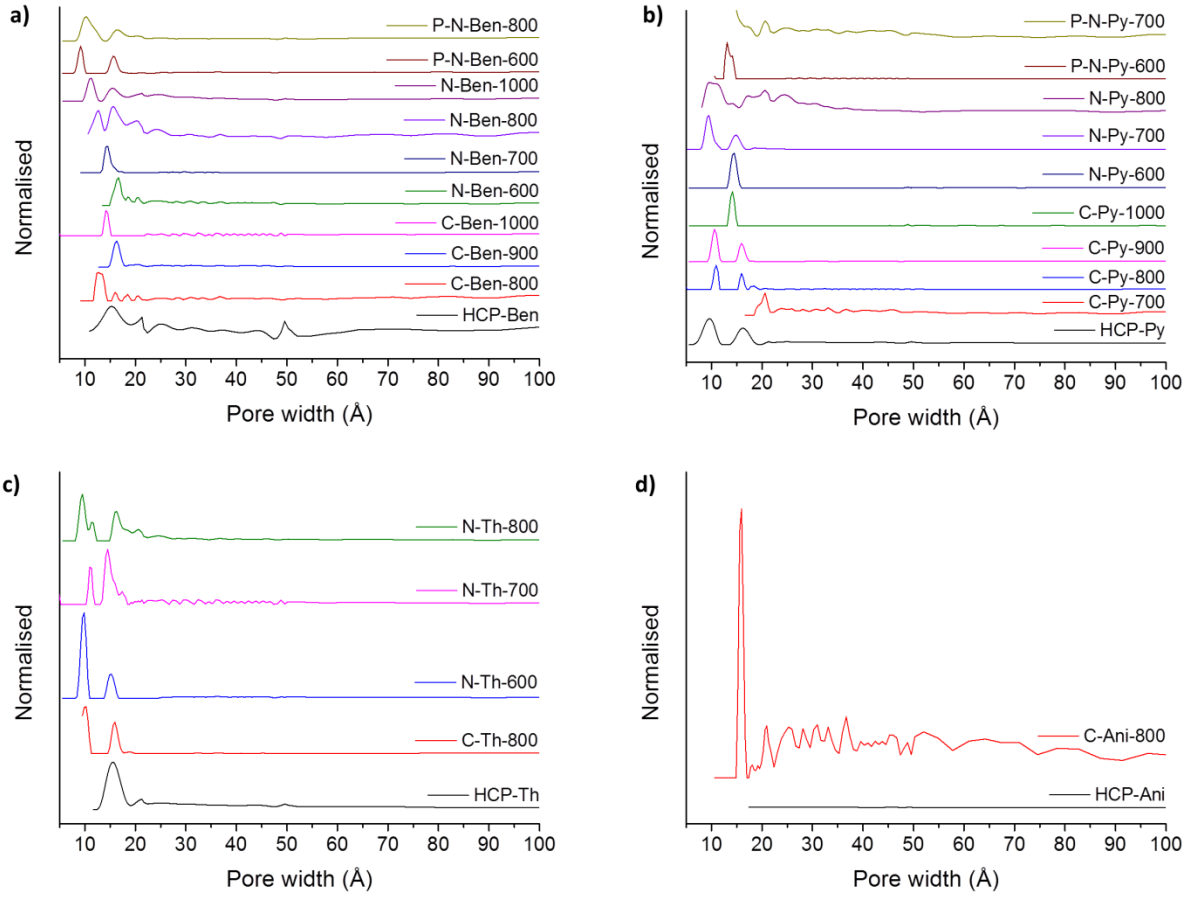

Figure 4.4 Pore size distributions of (a) HCP-Ben and x-Ben-Δ, (b) HCP-Py and x-Py-Δ, (c) HCP-Th and x-Th-Δ, and (d) HCP-Ani and C-Ani-800, calculated by NL-DFT.

Carbonisations of heteroatom-containing HCPs (HCP-Py, HCP-Th, and HCP-Ani) under N_2 resulted in the gradual loss of heteroatom content with increasing carbonisation temperature (**Table 4.1**). Though

C-Ani-800 and C-Py-800 had similar surface areas, C-Ani-800 possessed a lower N-content (1.34%) compared with C-Py-800 (8.86%). This was likely due to the lower initial N-content of HCP-Ani (8.54%) compared with HCP-Py (11.02%) and that the heterocyclic N in HCP-Py may be more thermally stable than the primary aryl amines of HCP-Ani, which allows higher incorporation of N atoms into the carbonised product. For this reason, carbonisation of HCP-Ani was not studied further at other temperatures.

An optimal carbonisation temperature for incorporating N into the carbonised HCPs under an NH_3 flow was found. N-Ben-800, formed by the carbonisation of HCP-Ben at 800 °C under NH_3, yielded the highest N-content in its series (7.50%) whereas carbonisation of HCP-Py and HCP-Th under NH_3 at 700 °C yielded the highest N-content (13.44% for N-Py-800 and 13.03% for N-Th-800) in their respective series. During high temperature carbonisations, heteroatoms tend to be more easily removed than carbon;[36] it therefore makes sense that less NH_3 is incorporated into the carbon at very high temperatures. Likewise, if the temperature is too low, carbonisation will not fully occur; therefore, intermediate temperatures are required to ensure the formation of a graphitic structure that incorporates the maximum amount of N from NH_3. Interestingly, N-Th-600 contains both high levels of N (7.93%) *and* S (12.38%) atoms. However, when the NH_3 carbonisation was increased to 700 °C in the synthesis of N-Th-700, the N content remained high while the S content dropped to 0.94%; further increasing the temperature to 800 °C resulted in total loss of S atoms. It is possible that removal of the S atoms provides space within the structure for integration of additional N as the N-content of N-Th-700 closely matches that of N-Py-700, while N-Th-800 closely matches N-Py-800.

C-Ben-800 and C-Py-800 were N-doped post-synthesised by treatment with NH_3 at various temperatures, which had previously shown positive results with CMP-derived carbons (Chapter 3).[7] Post-synthesis doping of C-Ben-800 at 600 °C (P-N-Ben-600) only showed moderate N incorporation of 1.40%. However, using a higher temperature of 800 °C allowed the incorporation of a higher N-content of 5.17% in P-N-Ben-800. The temperature trend is similar for directly carbonised HCPs under NH_3; N-Ben-800 has a much higher N-content than N-Ben-600 (7.50% *vs.* 2.16%). P-N-Py-600 showed a N-content of 11.52%, which was higher than its precursor, C-Py-800, which had a N-content of 8.86%. However, P-N-Py-700 contained 8.51% N, so it can be assumed that no further N-doping occurred at 700 °C. Rather, increase in apparent surface area from 387 to 443 $m^2\ g^{-1}$ is likely due to NH_3 etching further pores within the material, resulting in a 47% mass recovery. Interestingly, although post synthesis N-doping affords carbons with lower N-contents than the direct NH_3 carbonisation method—in line with previous studies[7]— the surface area of the P-N-HCP-Δ materials were lower than the N-HCP-Δ series in this study.

FE-SEM was used to study the morphology of the HCPs and the resulting carbons (**Figure 4.5**). The images show similar morphologies for the HCPs and their carbonised products, irrespective of whether they were carbonised under N_2 or NH_3 gas. Therefore, it can be concluded that morphology is well retained when using HCPs as carbonisation precursors, which could be advantageous when designing surfaces on HCPs that need to be translated into porous carbons.

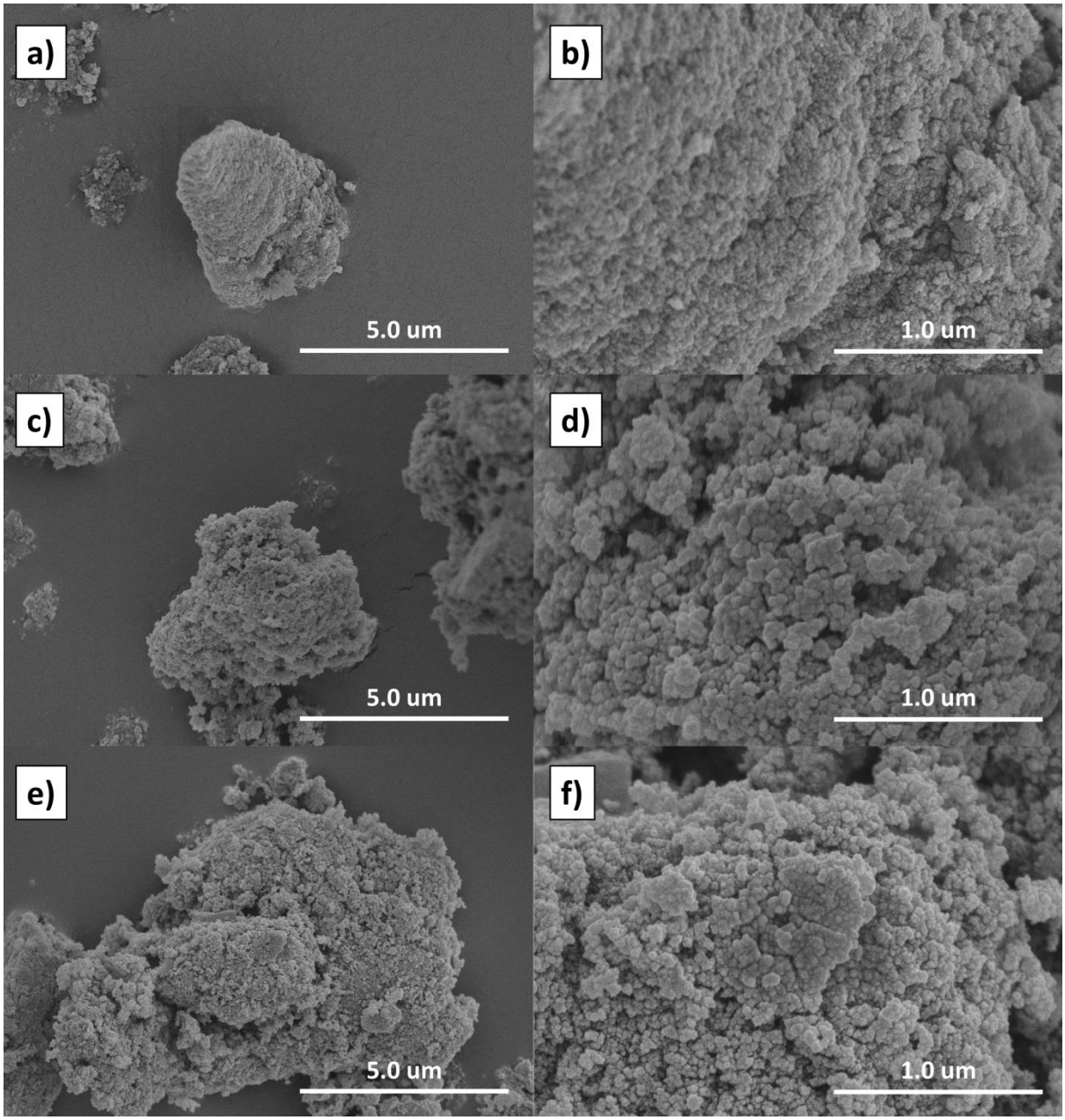

Figure 4.5 FE-SEM images of (a, b) HCP-Ben, (c, d) C-Ben-800, and (e, f) N-Ben-800 at low and high magnification, respectively.

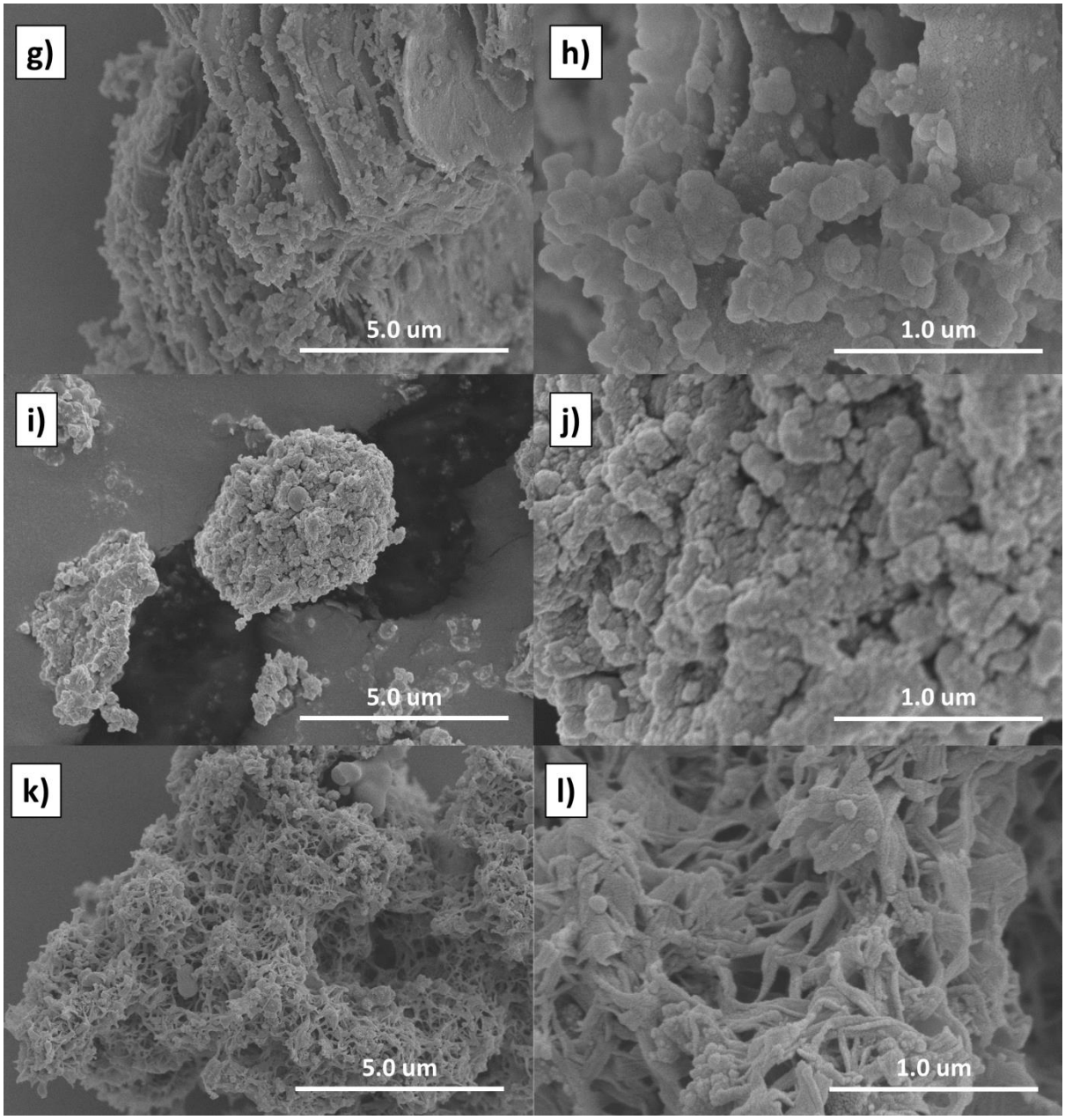

Figure 4.5 FE-SEM images of (g, h) HCP-Py, (i, j) C-Py-800, (k, l) N-Py-700 at low and high magnification, respectively.

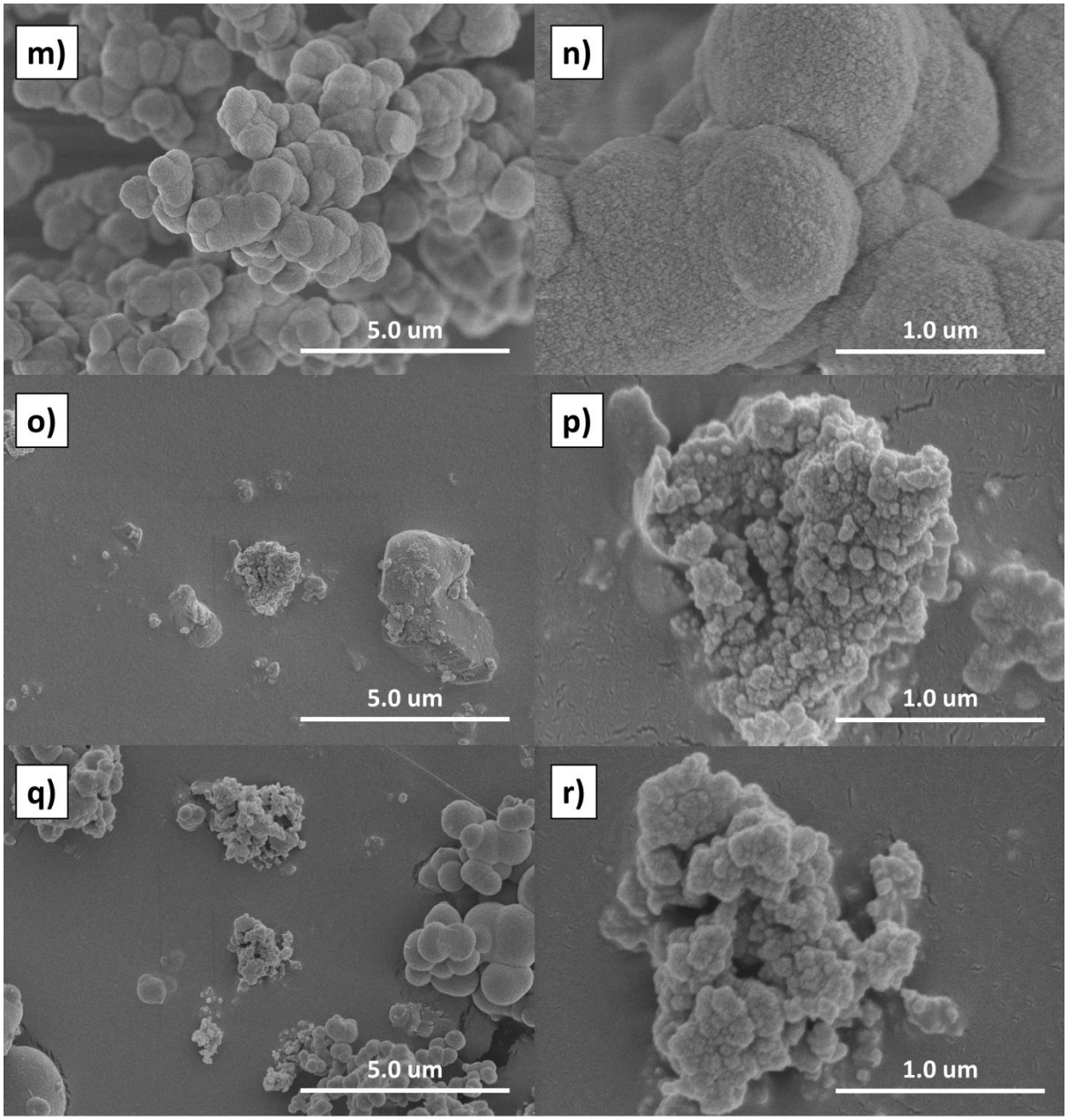

Figure 4.5 FE-SEM images of (m, n) HCP-Th, (o, p) C-Th-800, (q, r) N-Th-700 at low and high magnification, respectively.

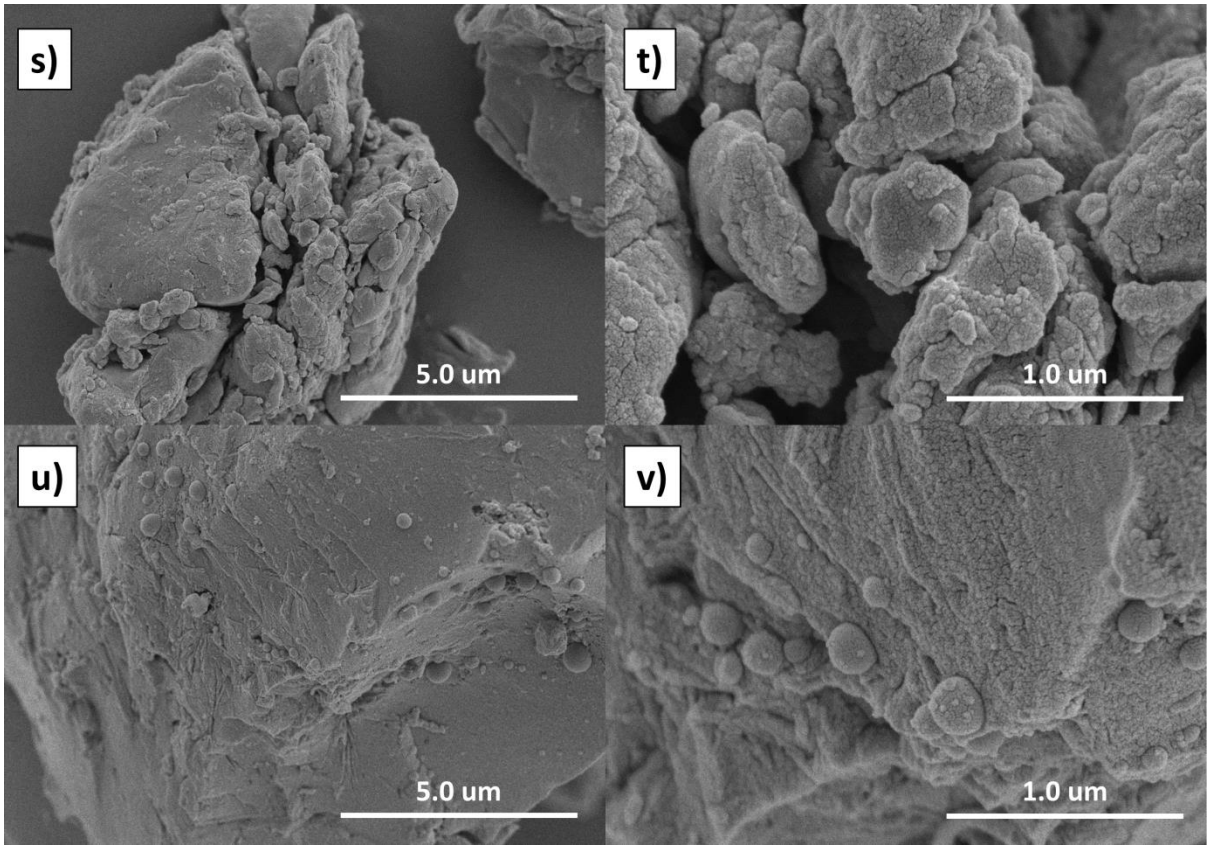

Figure 4.5 FE-SEM images of (s, t) HCP-Ani and (u, v) C-Ani-800 at low and high magnification, respectively.

PXRD of the HCPs and carbons are shown in **Figure 4.6a–d**. All HCPs and carbonised products show characteristic peaks at $2\theta \approx 26$ and 44° corresponding to the (002) and (101) planes of hexagonal graphite (JCPDS Card no. 41-1487), respectively.[37] The relatively broad peaks suggest that the materials possess a low degree of graphitisation and are predominately amorphous.[28, 38] Some additional crystalline peaks appeared in various samples that are attributed to small levels of alumina contamination from either the tube used in the furnace or the boat which carried the sample (**Figure 4.6e**). Repeat syntheses were attempted but failed to yield an uncontaminated sample. However, the small levels of alumina did not affect the other characterisation methods and supercapacitance analysis.

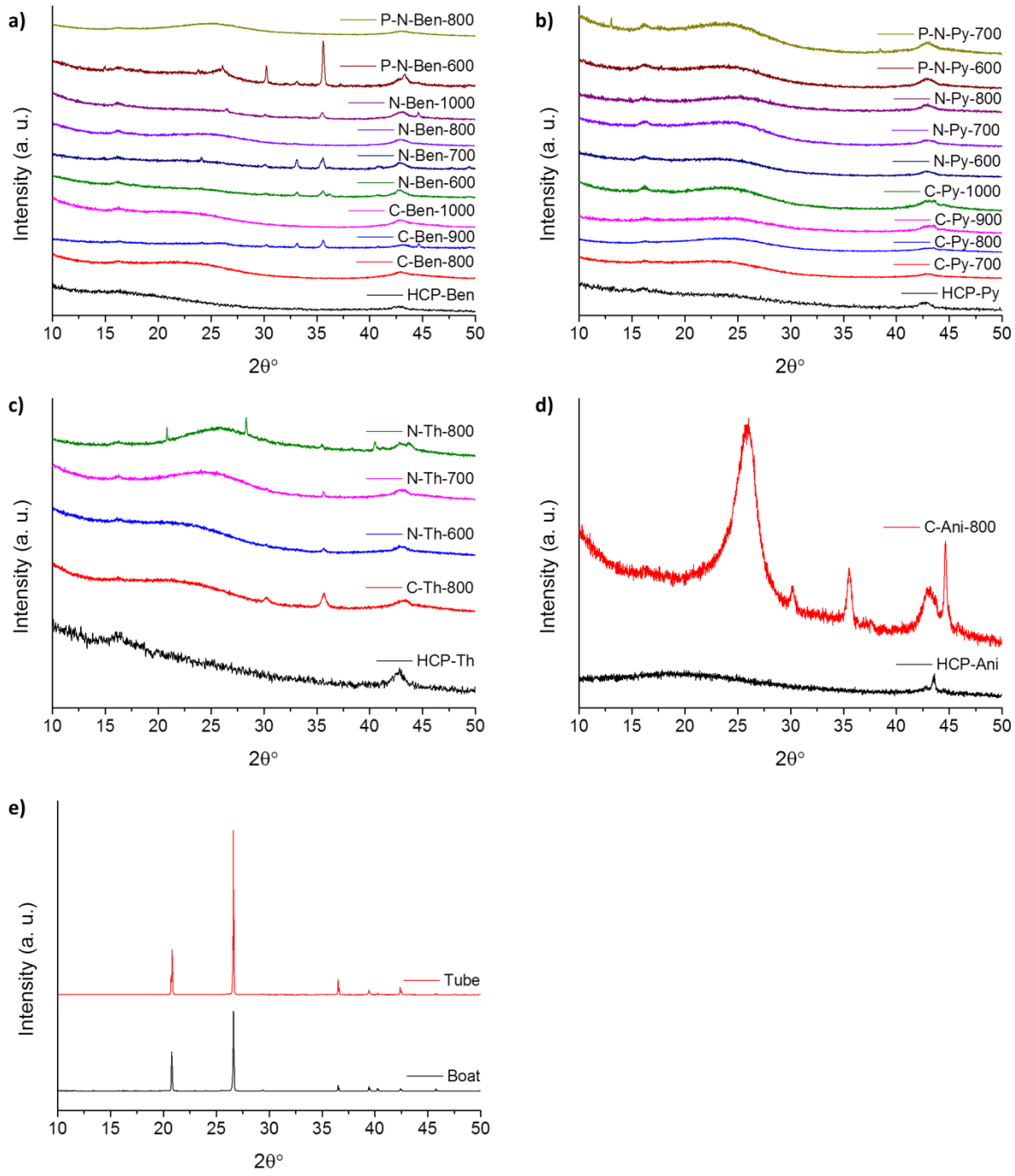

Figure 4.6 PXRD of (a) HCP-Ben and x-Ben-Δ, (b) HCP-Py and x-Py-Δ, (c) HCP-Th and x-Th-Δ, (d) HCP-Ani and C-Ani-800, and (e) alumina tube and boat samples.

Raman spectra of the porous carbons show two first-order Raman shifts of carbon present between 1100 and 1800 cm^{-1} (**Figure 4.7**). The *D* band at ≈ 1350 cm^{-1} and *G* band at ≈ 1590 cm^{-1} are attributed to the breathing mode of *k*-point phonons of A_{1g} symmetry and the in-plane stretching motion of symmetric sp^2 C-C bonds, respectively.[7, 39] Carbonisations between 600 and 1000 °C did not lead to a large change between the intensity ratio, I_D/I_G, of the *D* and *G* bands, as it is known that very high temperatures (~2000–3000 °C) are required to form highly ordered graphitic carbon.[40] However, it was noted that

the I_D/I_G ratio was largely dependent on the carbonisation precursor, with an I_D/I_G ratio for x-Ben-Δ of 2.08–2.49, x-Py-Δ of 2.41–3.01, x-Th-Δ of 2.35–2.80, and C-Ani-800 of 1.78. It was also observed that the I_D/I_G of N-HCP-Δ and P-N-HCP-Δ was generally higher than C-HCP-Δ, likely due to the addition of N atoms increasing defects in the graphitic carbon structure.

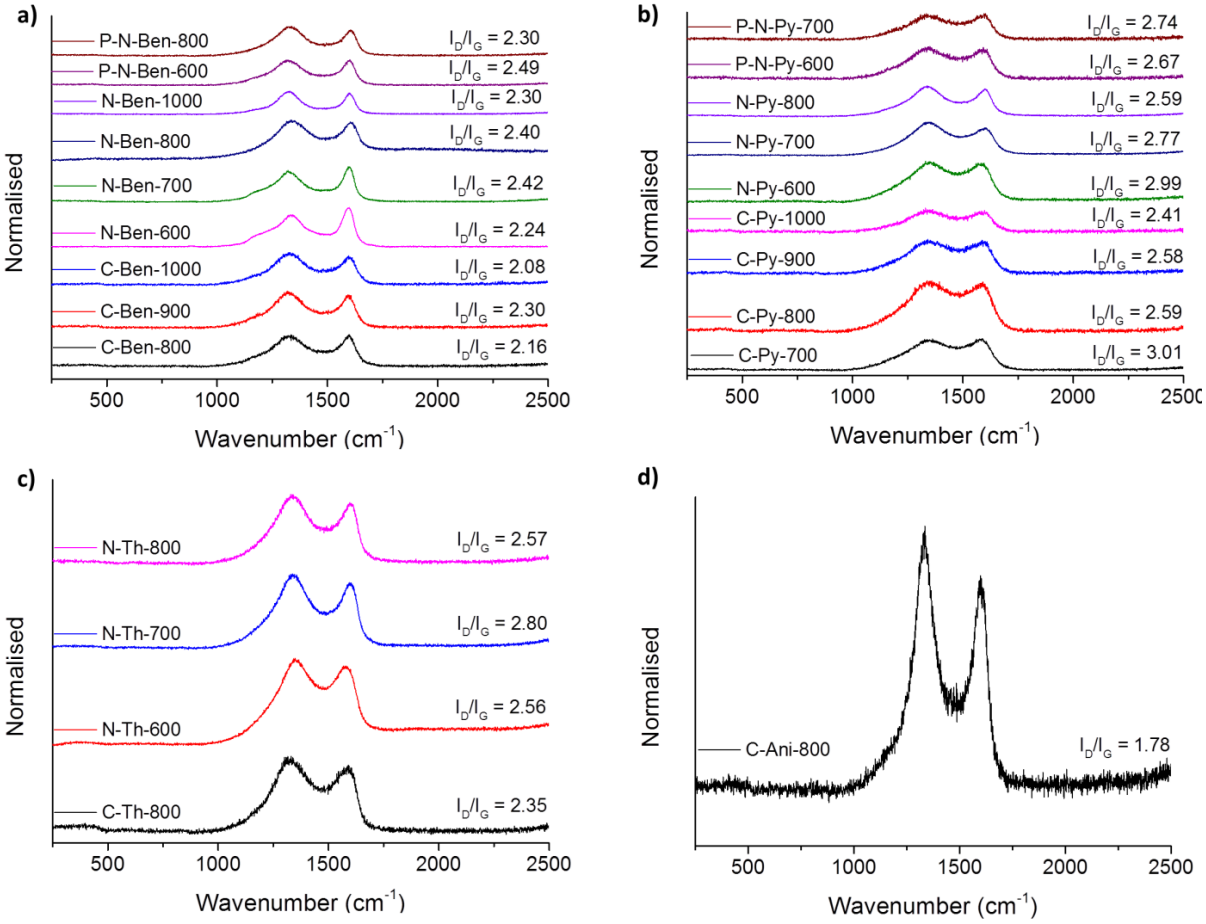

Figure 4.7 Raman spectra of (a) x-Ben-Δ, (b) x-Py-Δ, (c) x-Th-Δ, and C-Ani-800, with peaks at 1350 cm^{-1} and 1596 cm^{-1} assigned to the *D* band and *G* band, respectively.

4.4.3 Supercapacitive Performances of HCP-Derived Carbons

The electrochemical performances of the HCP-derived porous carbons were first evaluated using a three-electrode cell in 1 M H_2SO_4 aqueous electrolyte. The HCPs directly carbonised under N_2, C-HCP-Δ, were initially studied by CV at a scan rate of 10 mV s^{-1} (**Figure 4.8a**). The large range of materials tested required various potential windows to be employed to avoid irreversible electrode reactions, such as solvent decomposition and irreversible redox reactions on the electrodes. This avoids over-oxidation and/or over-reduction so that we only record current from the "capacitive potential range" of the material.[41] C-Ben-800, C-Ben-900, and C-Ben-1000 have a specific capacitance of 33, 34, and

114 F g^{-1}, respectively, at a scan rate of 10 mV s^{-1} (**Table 4.2**). The increase in capacitance of C-Ben-1000 is likely due to its higher degree of carbonisation, observed by the high carbon to hydrogen ratio of C-Ben-1000 (**Table 4.1**), and higher graphitic carbon content (**Figure 4.7**). These materials show quasi-rectangular CV curves, which are characteristic of good reversible supercapacitor behaviour.[42] As expected, C-Py-Δ, C-Th-800, and C-Py-800 show larger current densities due to the presence of heteroatoms contributing to PC. C-Th-800, which contains 13.58% S, shows a moderate specific capacitance of 52 F g^{-1}, whereas C-Ani-800 exhibits a higher capacitance of 66 F g^{-1} with only 1.34% N. This is likely due to N groups providing larger PC than S groups, which is reflected in the literature by the popularity of N-containing carbonaceous supercapacitors.[43] C-Py-700, C-Py-800, C-Py-900, and C-Py-1000 show high capacitances of 101, 126, 134, and 108 F g^{-1}, respectively, due to the high N-content of the carbons transferred from HCP-Py precursor. The increase in capacitance on going from C-Py-700 to C-Py-900 is due to the higher levels of carbonisation and resultant graphitisation. Though C-Py-1000 had the highest degree of graphitisation from its series (I_D/I_G = 2.41), the decrease in capacitance was likely due to lower N-content of 3.24%. Therefore, a balance exists between higher capacitance resulting from higher degrees of carbonisation at higher temperatures and a reduction in capacitance due to the concomitant decrease in heteroatom content. When comparing the carbons synthesised at 800 °C from the four HCPs, the precursors are ranked: HCP-Py > HCP-Ani > HCP-Th > HCP-Ben. The capacitance of C-Py-800 rapidly decays at higher scan rates, which is common for PC electrodes; however, it is still higher than the other C-HCP-800 materials (**Figure 4.8b**). The materials were tested with GCD experiments, with the charge-discharge times (**Figure 4.8c**) consistent with the current densities obtained from the CV results. Thus specific capacitances calculated by GCD experiments follow the same trend as for the specific capacitances calculated by CV (**Table 4.3**). All the C-HCP-Δ carbons showed a triangular charge-discharge shape, which is typical behaviour for constant charge and discharge of supercapacitive materials with good reversibility.[7]

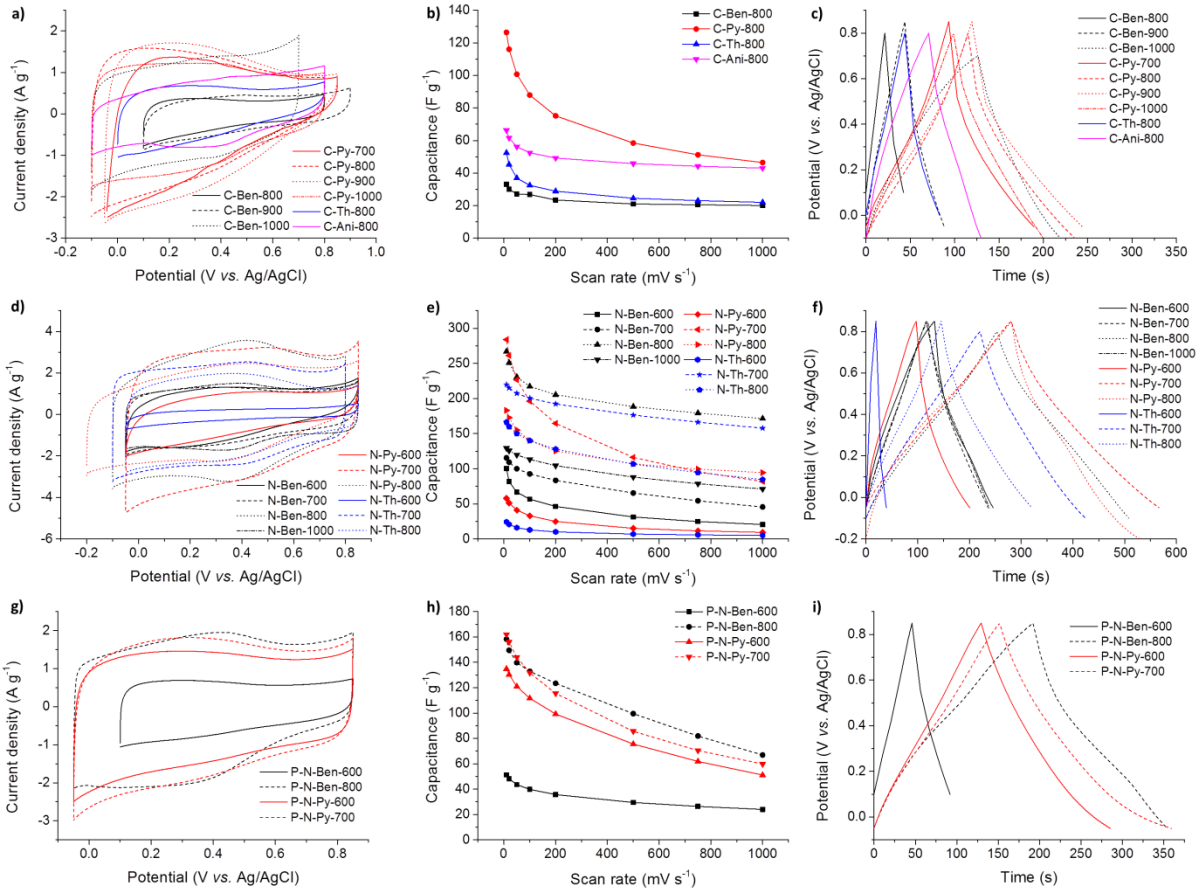

Figure 4.8 Electrochemical analysis of all carbonised materials in a three-electrode system in 1 M H_2SO_4. (a) Cyclic voltammograms of C-HCP-Δ at a scan rate of 10 mV s^{-1}. (b) Specific capacitance of C-HCP-800 at varying scan rates. (c) Galvanostatic charge-discharge curves of C-HCP-Δ at a current density of 1 A g^{-1}. (d) Cyclic voltammograms of N-HCP-Δ at a scan rate of 10 mV s^{-1}. (e) Specific capacitance of N-HCP-Δ at varying scan rates. (f) Galvanostatic charge-discharge curves of N-HCP-Δ at a current density of 1 A g^{-1}. (g) Cyclic voltammograms of P-N-HCP-Δ at a scan rate of 10 mV s^{-1}. (h) Specific capacitance of P-N-HCP-Δ at varying scan rates. (i) Galvanostatic charge-discharge curves of P-N-HCP-Δ at a current density of 1 A g^{-1}.

Table 4.2 Specific capacitance (F g^{-1}) of HCP-based porous carbons at various scan rates.

Scan rate (mV s^{-1})	10	20	50	100	200	500	750	1000
C-Ben-800	33	30	27	27	23	21	21	20
C-Ben-900	34	30	25	22	19	16	15	14
C-Ben-1000	114	109	102	97	92	84	80	77
N-Ben-600	100	82	67	57	46	31	25	21
N-Ben-700	115	109	100	93	83	65	54	46
N-Ben-800	267	251	231	217	205	188	179	171
N-Ben-1000	129	126	120	113	104	88	79	71
P-N-Ben-600	51	48	44	40	36	29	26	24
P-N-Ben-800	158	149	140	133	123	99	82	67
C-Py-700	96	81	65	53	44	33	29	27
C-Py-800	126	116	101	88	75	58	51	46
C-Py-900	134	123	104	88	69	45	37	32
C-Py-1000	108	102	93	85	78	68	64	60
N-Py-600	58	51	41	33	25	15	12	9
N-Py-700	284	261	227	196	164	116	96	82
N-Py-800	183	173	155	140	125	107	100	94
P-N-Py-600	135	130	121	112	99	76	62	51
P-N-Py-700	162	156	144	132	115	86	70	60
C-Th-800	52	45	37	32	29	24	23	22
N-Th-600	24	21	16	13	10	7	6	5
N-Th-700	220	215	207	201	192	176	166	158
N-Th-800	166	160	150	140	128	107	94	85
C-Ani-800	66	62	56	52	49	46	44	43

Table 4.3 Specific capacitance (F g^{-1}) of HCP-based porous carbons at various current densities.

Current density (A g^{-1})	1	3	5	10
C-Ben-800	30	20	19	17
C-Ben-900	49	37	33	28
C-Ben-1000	116	106	103	98
N-Ben-600	126	91	78	64
N-Ben-700	130	122	115	106
N-Ben-800	283	263	252	239
N-Ben-1000	136	120	116	110
P-N-Ben-600	48	41	38	34
P-N-Ben-800	180	164	157	149
C-Py-700	107	81	70	55
C-Py-800	134	110	101	87
C-Py-900	139	114	101	82
C-Py-1000	113	99	94	86
N-Py-600	70	46	37	25
N-Py-700	317	276	256	225
N-Py-800	237	180	167	150
P-N-Py-600	173	141	132	121
P-N-Py-700	231	186	173	158
C-Th-800	49	37	32	28
N-Th-600	23	14	11	7
N-Th-700	226	224	221	216
N-Th-800	196	175	166	155
C-Ani-800	66	64	60	56

The N-doped HCP-based carbons show much larger current responses than the HCPs carbonised under N_2, as observed by CV at a scan rate of 10 mV s^{-1} (**Figure 4.8d**). All N-HCP-Δ samples show quasi-rectangular CV curves. N-Ben-600 and N-Ben-700 have similar specific capacitances of 100 and 115 F g^{-1}, respectively. However, the CV curve for N-Ben-700 exhibits a more symmetrical quasi-rectangular shape denoting higher reversibility, which is likely developed by the harsher carbonisation conditions. N-Ben-800 also exhibits a highly symmetrical CV curve but with much larger current responses, yielding the highest capacitance of 267 F g^{-1} from the HCP-Ben precursor. N-Ben-1000 has a decreased capacitance of 129 F g^{-1} due to a lower N-content in the carbon from the high temperature carbonisation. However, the higher temperature yields a highly symmetrical and reversible CV curve, which can be compared with N-Ben-600 and N-Ben-700 due to the similar current responses. N-Py-600 has a capacitance of 58 F g^{-1}, while with N-Py-700 the capacitance dramatically increases to 284 F g^{-1},

even though the surface areas and N-content of N-Py-600 (320 m^2 g^{-1} and 12.73%, respectively) and N-Py-700 (329 m^2 g^{-1} and 13.44%, respectively) are similar. A Nyquist plot in the low frequency region shows the impedance of the imaginary part approaches vertical with N-Py-700, indicative of typical ideal capacitive behaviour (**Figure 4.9**),[44] whereas the low frequency capacitive behaviour of N-Py-600 is shifted along the real axis towards more resistive values.[44] Therefore, the low capacitance of N-Py-600 was ascribed to the low electric conductivity of this material when carbonised at the relatively low temperature of 600 °C. N-Py-800 has a lower capacitance of 183 F g^{-1} due to a decrease in N-content to 9.79%, despite possessing a very high surface area (1484 m^2 g^{-1}). Higher levels of porosity can aid electrolyte ion diffusion and afford higher levels of EDLC. These benefits can be seen with the capacitance retention of N-Py-800 at higher scan rates (**Figure 4.8e**) with 51% capacitance retention at extremely high scan rates of 1000 mV s^{-1}, whereas N-Py-700 only retains 29% capacitance at this rapid scan rate (**Table 4.2**). The weak capacitance retention of N-Py-700 is due to the electrode being largely PC-based rather than EDLC-based, which is known to have slower kinetics and lower power density.[6] Interestingly, even though N-Py-800 has a higher surface area and N-content than N-Ben-800, the capacitance is lower. We suggest that the greater hierarchical structure of N-Ben-800 (47% microporous) supports more efficient electrolyte diffusion than N-Py-800 (57% microporous), as it is known that micropores alone are not favourable for quick electrolyte ion diffusion and result in low capacitances.[45] The quicker electrolyte ion diffusion of N-Ben-800 allows higher capacitance retention at 1000 mV s^{-1} of 64%. N-Th-600 has a low capacitance of 24 F g^{-1} due to the same reason as N-Py-600 of low electric conductivity, combined with a lower N-content 7.93%. The 12.38% S in this material was thought to not play a large role, as previously discussed with C-Th-800. N-Th-700 showed a much higher capacitance of 220 F g^{-1} due to its higher conductivity, higher N-content of 13.03%, and a higher surface area of 760 m^2 g^{-1}. Its CV shape is highly symmetrical with a sharp quasi-rectangular shape, which is reflected by its high capacitance retention at 1000 mV s^{-1} of 72%. The combination of a lower N-content (7.33%) and surface area (508 m^2 g^{-1}) for N-Th-800 resulted in a lower capacitance of 166 F g^{-1}. The GCD curves reflect the same trend in capacitive results from CV (**Figure 4.8f**). All N-HCP-Δ materials show typical supercapacitor behaviour displayed by the triangular charge-discharge profiles. N-Py-700 exhibited the highest specific capacitance at 1 A g^{-1} of 317 F g^{-1} closely followed by N-Ben-800 of 283 F g^{-1} (**Table 4.3**).

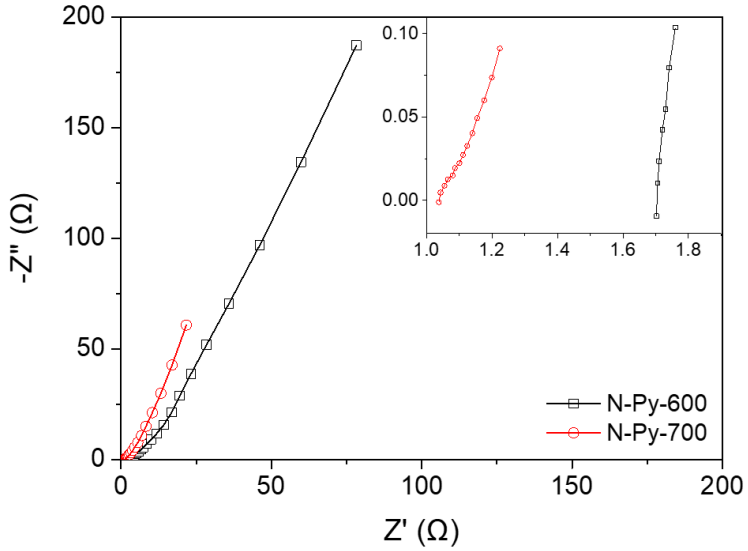

Figure 4.9 Nyquist impedance spectrum of N-Py-600 and N-Py-700 measured at 400 mV *vs.* Ag/AgCl in 1 M H_2SO_4. Inset shows the results at the high frequency region.

CV studies of P-N-HCP-Δ materials at a scan rate of 10 mV s^{-1} are shown in **Figure 4.8g**. P-N-Ben-600 shows relatively low current response, yielding a capacitance of 51 F g^{-1}. This is attributed to the low levels of N-doping (1.40%) at 600 °C and the decrease in surface area from 538 m^2 g^{-1} for C-Ben-800 to 425 m^2 g^{-1}. Nevertheless, the post NH_3 carbonisation increased its supercapacitive behaviour from its precursor, which had a capacitance of 33 F g^{-1} at the same scan rate. Using a higher post-synthesis NH_3 carbonisation temperature of 800 °C resulted in a higher surface area (697 m^2 g^{-1}) and N-content (5.17%) in P-N-Ben-800, which yields a higher specific capacity of 158 F g^{-1}. P-N-Py-600 displayed a capacitance of 135 F g^{-1}, close to its precursor of 126 F g^{-1}, despite having a higher surface area and N-content. Interestingly, P-N-Py-700 yields a higher capacitance of 162 F g^{-1} despite its surface area being close to that of P-N-Py-600 and having a lower N-content (8.51% for P-N-Py-700 *vs.* 11.52% for P-N-Py-600). This is thought to be due to the better conductivity of P-N-Py-700 as higher post-carbonisation temperatures are used, as evidenced by a more vertical low frequency region of P-N-Py-700 in the Nyquist plot which is shifted away from the real axis along lower resistive values (**Figure 4.10**).[44] P-N-Py-700 exhibits a slightly higher capacitance than P-N-Ben-800, likely due to the higher N-content thus PC contribution from P-N-Py-700. However, as P-N-Ben-800 has a larger surface area, and thus a higher EDLC contribution, it retains more capacitance at higher scan rates than P-N-Py-700 (**Figure 4.8h**). GCD of P-N-HCP-Δ materials at a current density of 1 A g^{-1} show that they retain a triangular charge-discharge shape (**Figure 4.8i**). Though high capacitances of up to 231 F g^{-1} were obtained for P-N-Py-700 at a current density of 1 A g^{-1}, the N-Ben-800 and N-Py-700 displayed superior supercapacitive behaviour compared to the post NH_3 carbonised materials.

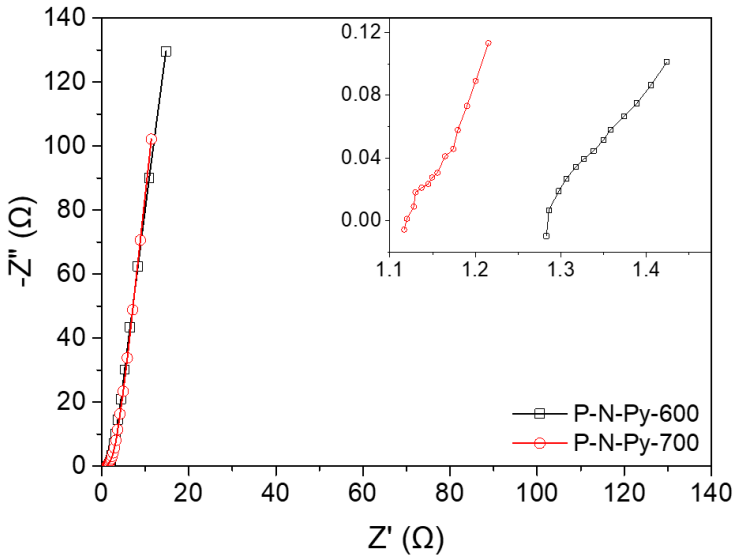

Figure 4.10 Nyquist impedance spectrum of P-N-Py-600 and P-N-Py-700 measured at 400 mV *vs.* Ag/AgCl in 1 M H_2SO_4. Inset shows the results at the high frequency region.

N-Ben-800 and N-Py-700 showed excellent supercapacitive behaviour; N-Ben-800 has a higher surface area and a good N-content, whereas N-Py-700 has a lower surface area but higher N-content. The CV results of N-Ben-800 at scan rates between 10 and 200 mV s^{-1} are shown in **Figure 4.11a**. The CV retains a highly symmetric quasi-rectangular shape when the scan rate was increased, with the capacitance only reducing from 267 F g^{-1} at 10 mV s^{-1} to 205 F g^{-1} at 200 mV s^{-1}, demonstrating excellent capacitance retention of 77%. Moreover, a specific capacitance of 171 F g^{-1} was observed at an extremely high scan rate of 1000 mV s^{-1}. Voltammetric currents of the material also swiftly reach their respective plateau when the direction of the potential sweep is changed; even with scan rates as fast as 1000 mV s^{-1} (**Figure 4.11b**). N-Ben-800 possesses a low ESR which is due to its high electric conductivity and low ionic resistance of the electrolyte in the pores during charging and discharging.[46] GCD curves between 0.1 and 10 A g^{-1} retains a consistent symmetrical triangular shape with the varying current densities (**Figure 4.11c&d**), exhibiting excellent capacitances of 295 F g^{-1} at 0.1 A g^{-1}, 283 F g^{-1} at 1 A g^{-1} and 239 F g^{-1} at 10 A g^{-1}, a capacitance retention of 81% between 0.1 to 10 A g^{-1}. The Nyquist plot of N-Ben-800 in the low frequency region shows the impedance of the imaginary part approaches vertical, demonstrating ideal capacitive behaviour (**Figure 4.11e**). The capacitances of N-Ben-800 can be calculated from the imaginary part of the impedance spectrum which shows increasing capacitance with lower applied frequencies (**Figure 4.11f**). The capacitance behaviour is visible at frequencies below 10 Hz,[47] with the curve in the low frequency range (10 to 0.01 Hz) approaching almost horizontal to ~300 F g^{-1}. Interestingly, though capacitance increases with lower applied frequencies for N-Py-700, the curve does not plateau at the lower frequency range. This is thought to be due to the slower kinetics of N-Py-700 which is more pseudocapacitive than N-Ben-800, therefore, may require even lower applied frequencies to begin plateauing (*i.e.*, full utilisation of PC).

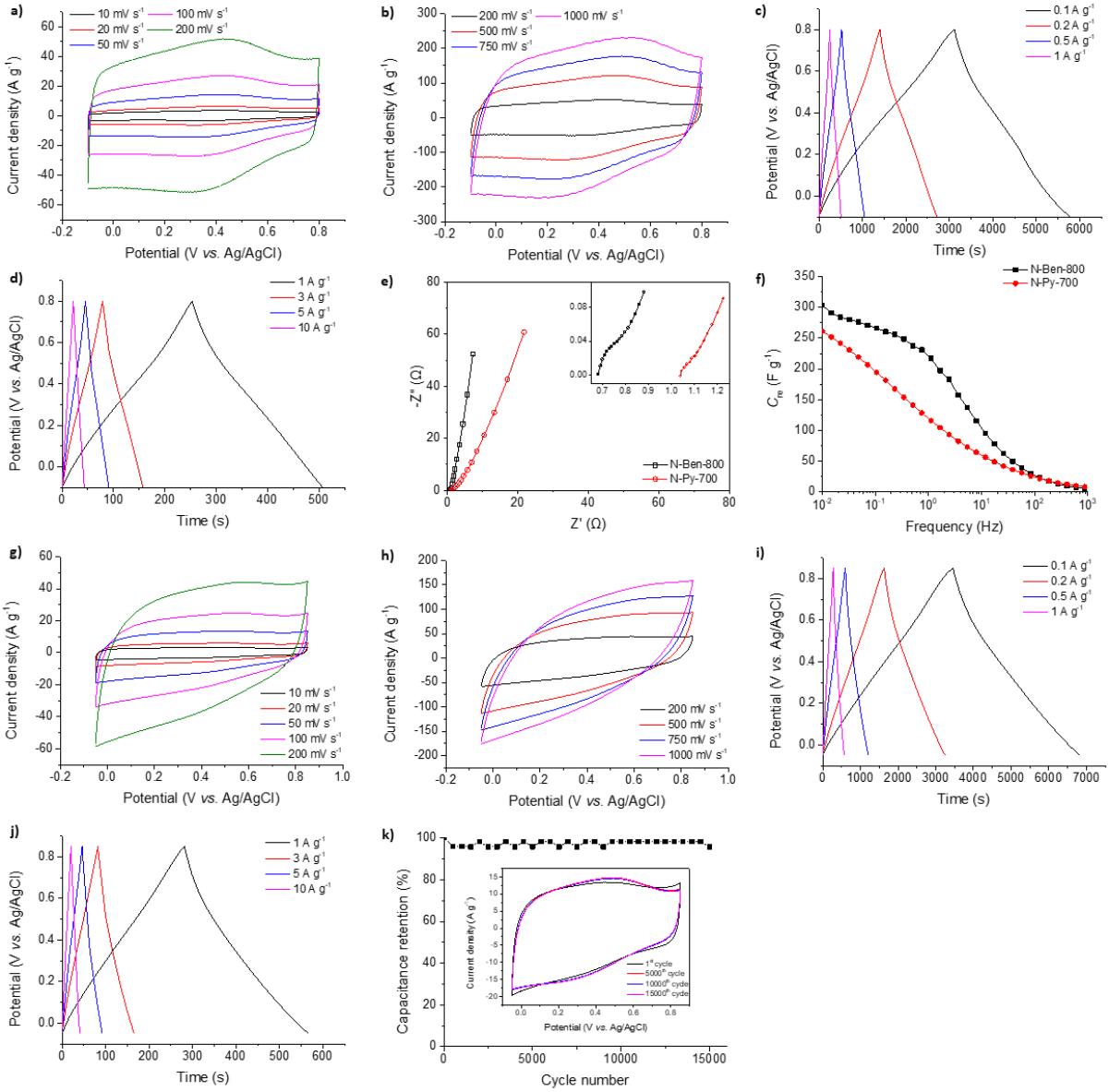

Figure 4.11 Electrochemical analysis of the optimised carbonised materials in a three-electrode system in 1 M H_2SO_4. (a) Cyclic voltammograms of N-Ben-800 at varying scan rates between 10 and 200 mV s^{-1}. (b) Cyclic voltammograms of N-Ben-800 at varying scan rates between 200 and 1000 mV s^{-1}. (c) Galvanostatic charge-discharge curves of N-Ben-800 at current densities between 0.1 and 1 A g^{-1}. (d) Galvanostatic charge-discharge curves of N-Ben-800 at current densities between 1 and 10 A g^{-1}. (e) Nyquist impedance spectrum of N-Ben-800 and N-Py-700 measured at 400 mV *vs.* Ag/AgCl. Inset shows the results in the high frequency region. (f) Frequency dependence of specific capacitance for N-Ben-800 and N-Py-700 at 400 mV *vs.* Ag/AgCl. (g) Cyclic voltammograms of N-Py-700 at varying scan rates between 10 and 200 mV s^{-1}. (h) Cyclic voltammograms of N-Py-700 at varying scan rates between 200 and 1000 mV s^{-1}. (i) Galvanostatic charge-discharge curves of N-Py-700 at current densities between 0.1 and 1 A g^{-1}. (j) Galvanostatic charge-discharge curves of

N-Py-700 at current densities between 1 and 10 A g^{-1}. (k) Cycling stability test of N-Py-700 at a current density of 5 A g^{-1}. Inset shows the CV of N-Py-700 at a scan rate of 50 mV s^{-1} after the 1st, 5000th, 10000th, and 15000th cycle.

N-Py-700 is highly symmetrical between scan rates of 10 and 200 mV s^{-1} (**Figure 4.11g**) which confirms its good electrochemical stability and capacitance,[15, 48] with high specific capacitances of 284 F g^{-1} at 10 mV s^{-1} and 164 F g^{-1} at 200 mV s^{-1}, a capacitance retention of 58%. The capacitance retention is lower than N-Ben-800 because N-Ben-800 has a larger surface area, and hence its capacitance is mainly attributed to the EDLC mechanism, which has fast electrochemical kinetics.[5] By contrast, N-Py-700 has a relatively low surface area but higher N-content, hence its capacitance is mainly attributed to the PC mechanism, which is known to give lower power densities.[6] This is more evident at very high scan rates (*e.g.*, 1000 mV s^{-1}) which yields a capacitance of 82 F g^{-1}. Although the capacitance at 1000 mV s^{-1} is relatively low, its CV shape retains high symmetry and possesses a more quasi-rectangular profile than other expensive and optimised materials (**Figure 4.11h**),[13, 21, 31] even when they are run at lower scan rates. GCD experiments of N-Py-700 between current densities of 0.1 and 10 A g^{-1} all display symmetrical triangular profiles (**Figure 4.11i&j**), indicating the material has typical supercapacitor behaviour. Exceptionally, the material exhibits an extremely high capacitance of 374 F g^{-1} at 0.1 A g^{-1}. This is higher than some of the best performing organic materials (**Table 4.4**) such as N-doped carbons,[49-51] B/N-co-doped porous carbon (BNC-9),[52] N-doped carbon nanotubes (PNCNTs),[53] N-doped graphene,[54] N-doped microspheres (A-PNCM),[55] and more costly networks such as CTF-,[56, 57] CMP-,[7, 14, 58] PAF-,[13] and MOF-derived carbonaceous materials.[18, 20] N-Py-700 also outperforms carbons with surface areas >3000 m^2 g^{-1},[59] exemplifying the importance of heteroatom doping in porous carbons to produce high performing supercapacitive materials. Moreover, N-Py-700 shows excellent stability, with 95.8% capacitance retention after 15,000 charge-discharge cycles at a current density of 5 A g^{-1} (**Figure 4.11k**). The CV shape shifts to a more quasi-rectangular shape from the 1st to 5000th cycle, presumably due to the initial activation period that allows progressive wetting of the pores during cycling (**Figure 4.11k, inset**). The 5000th, 10000th, and 15000th CV cycle shows very little change, indicating minimum degradation of N-Py-700 after cycling.

Table 4.4 Specific capacitances of a selection of top performing organic materials reported in the literature.

Sample	Capacitance ($F\ g^{-1}$)	Current density ($A\ g^{-1}$)	Potential window (V)	Electrolyte	Reference
N-Py-700	374	0.1	0.9	1 M H_2SO_4	This work
Porous N-doped carbon (CA-GA-2)	300	0.1	1.0	1 M H_2SO_4	[49]
N-doped carbon from PANI	235	1.0	1.0	1 M H_2SO_4	[50]
N-doped mesoporous carbon (H-NMC-2.5)	262	0.2	0.9	1 M H_2SO_4	[51]
B/N-co-doped porous carbon (BNC-9)	268	0.1	1.0	6 M KOH	[52]
Porous N-doped carbon nanotubes (PNCNTs)	210	0.5	1.0	6 M KOH	[53]
N-doped graphene	282	< 1	0.8	6 M KOH	[54]
Porous N-doped carbon microspheres (A-PNCM)	282	0.5	1.0	6 M KOH	[55]
2-D Covalent triazine framework	151	0.1	3.0	$EMIMBF_4$	[57]
Terephthalonitrile-derived N-rich network (TNNs-550)	298	0.2	1.0	1 M H_2SO_4	[56]
N-doped carbon from CMP (N3-CMP-1)	260	0.1	1.1	3 M KOH	[7]
Carbon from pyrene-based CMP (SDBPy-800)	301	1.0	0.9	6 M KOH	[14]
Triazatruxene-based CMP (TAT-CMP-2)	183	1.0	1.0	1 M Na_2SO_4	[58]
Carbon from PAF (K-PAF-1)	280	1.0	0.8	6 M KOH	[13]
Carbon from MOF (MAC-A)	274	0.25	1.0	6 M KOH	[18]
Core-shell nanoporous carbon from MOF and PANI (carbon-PANI core-shell)	236	1.0	0.8	1 M H_2SO_4	[20]

Both N-Ben-800 and N-Py-700 were also tested at extremely high current densities of up to 100 $A\ g^{-1}$ (**Figure 4.12**) and showed capacitances of 162 and 88 $F\ g^{-1}$, respectively (**Figure 4.13**). This represents a 68% and 39% capacitance retention for N-Ben-800 and N-Py-700, respectively, upon increasing the current density from 10 to 100 $A\ g^{-1}$. N-Ben-800 performs better at faster rates due to its higher proportion of EDLC.

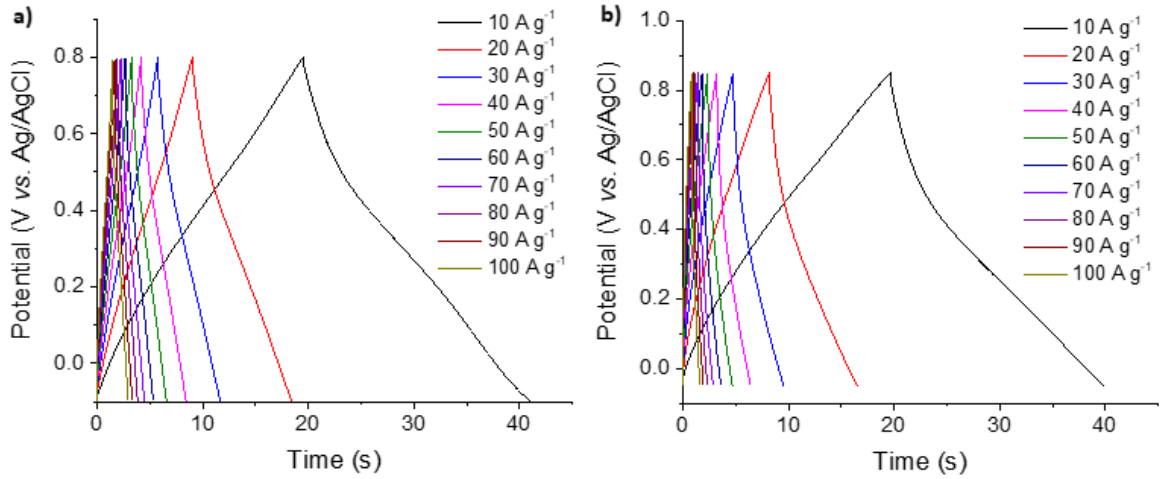

Figure 4.12 (a) Galvanostatic charge-discharge curves of N-Ben-800 at current densities between 10 and 100 A g^{-1}. (b) Galvanostatic charge-discharge curves of N-Py-700 at current densities between 10 and 100 A g^{-1}.

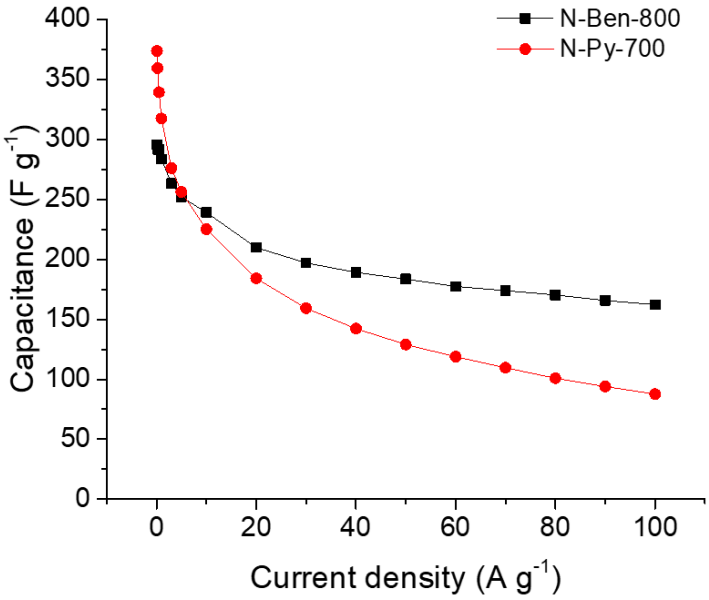

Figure 4.13 Specific capacitance of N-Ben-800 and N-Py-700 at varying current densities.

Ragone plots show that the N-Ben-800 and N-Py-700 exhibit maximum energy and power densities of 42 W h kg^{-1} and 45 kW kg^{-1}, respectively (**Figure 4.14a**). The energy densities of the optimised materials reaches the regime of batteries such as Pb-acid, NiCd, and Li-ion (10–150 W h kg^{-1}), whilst being over one order of magnitude in power density than those of batteries (<0.3 kW kg^{-1}) (**Figure 4.14b**).[4]

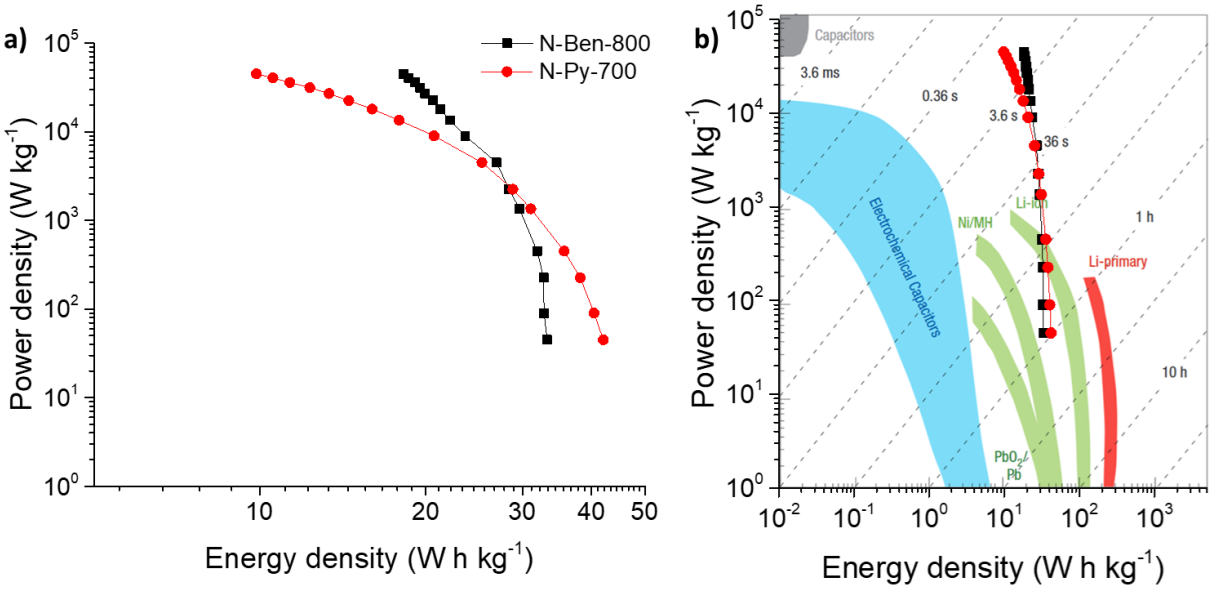

Figure 4.14 (a) Ragone plots of N-Ben-800 and N-Py-700. (b) Overlay of results with other energy storage devices, adapted from literature source.[5]

Full cell supercapacitors of N-Ben-800 and N-Py-700 were constructed in order to study the materials in a practical device and to minimise any errors which may cause overestimation of capacitance in the three-electrode method.[60] A symmetrical two-electrode set-up was used containing the charge balanced material in 1 M H_2SO_4 and showed results consistent with the three-electrode method (**Figure 4.15**). The CV shape of N-Ben-800 is highly quasi-rectangular at scan rates between 10 and 200 mV s^{-1} (**Figure 4.15a**)—even more so than during the three-electrode method (**Figure 4.11a**)—and retains this shape at scan rates up to 1000 mV s^{-1} (**Figure 4.15b**). The current response in the two-electrode configuration is slightly larger at 0 V as the open-circuit potential of N-Ben-800 in the three-electrode configuration was found to be 0.4 V—the middle of the redox couple in N-Ben-800. The capacitance was found to be 229 F g^{-1} at 10 mV s^{-1} and 163 F g^{-1} at the very high scan rate of 1000 mV s^{-1} (**Figure 4.15c**). The GCD curves of N-Ben-800 are symmetric and linear, with negligible voltage drop demonstrating low internal resistance and ideal capacitive behaviour in the full cell set-up with a high capacitance of 211 F g^{-1} at 1 A g^{-1} (**Figure 4.15d**). The Nyquist plot in the two-electrode set-up similarly shows phase angles close to 90° demonstrating ideal capacitive behaviour, with a slight deviation at very low frequencies due to the pseudocapacitive contributions of N-Ben-800 readily occurring at these low frequencies (**Figure 4.15e**). The capacitance from impedance spectroscopy is almost horizontal at the low frequency range (10 to 0.01 Hz), reaching a stable capacitance of 230 F g^{-1} (**Figure 4.15f**). The CV shape of N-Py-700 between 10 to 1000 mV s^{-1} are all quasi-rectangular (**Figure 4.15g&h**), indicating ideal capacitive performance, more so than during the three-electrode configuration (**Figure 4.11g&h**), thus these materials are suitable for practical devices. Interestingly, the capacitance of N-Py-700 in the two-electrode configuration at 10 mV s^{-1} was similar to N-Ben-800 (222 *vs*. 229 F g^{-1}) but the capacitance retention was lower at higher scan rates due to its pseudocapacitive nature

(**Figure 4.15c**). The GCD curves of N-Py-700 in the two-electrode configuration also retained its symmetric triangular shape, demonstrating its ideality as a supercapacitor material, with a capacitance of 199 F g^{-1} at 1 A g^{-1} (**Figure 4.15i**). The Nyquist plot of N-Py-700 approaches vertical with a phase angle of 83°—higher than in the three-electrode configuration—showing ideal capacitive behaviour (**Figure 4.15e**). Additionally, the Bode plot of the two-electrode configuration also shows a plateau towards 83° at lower frequencies compared against the three-electrode configuration, supporting the material as an ideal capacitor for practical applications (**Figure 4.16**).

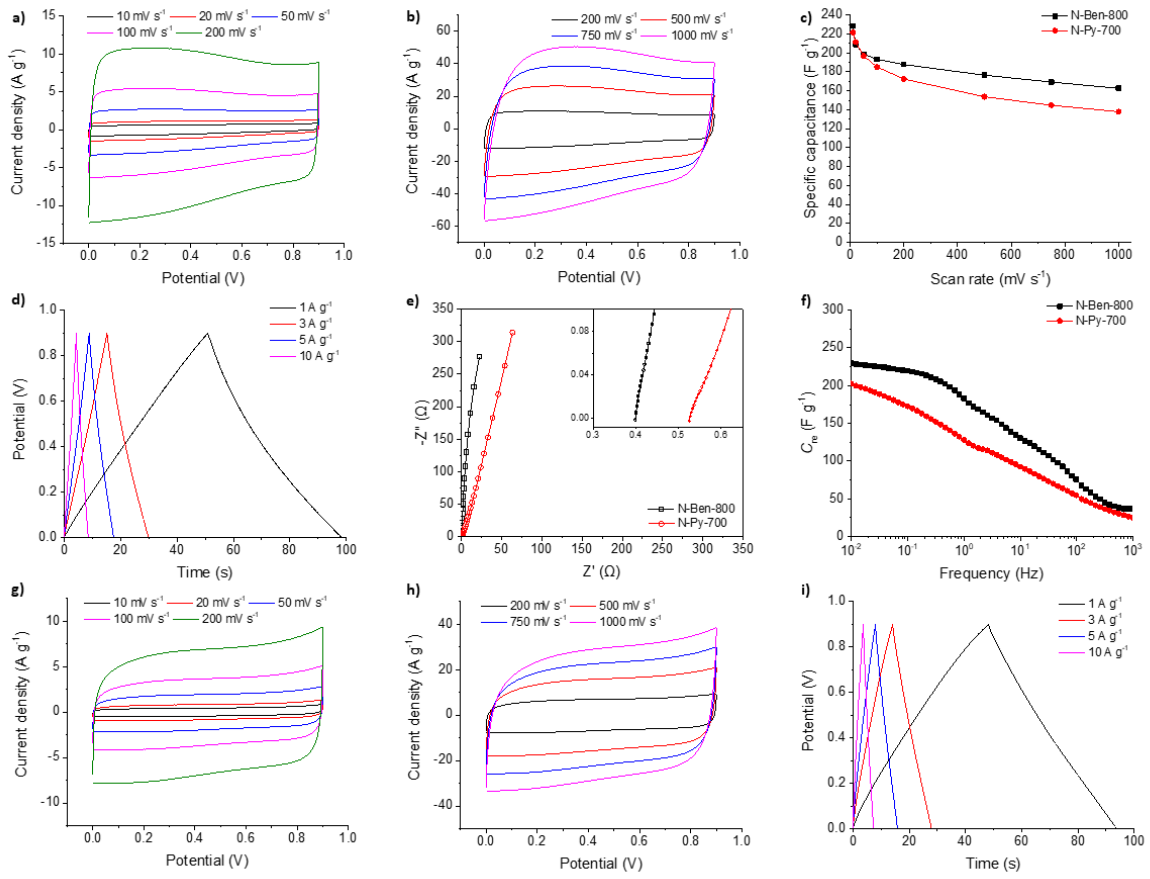

Figure 4.15 Electrochemical analysis of the optimised carbonised materials in a two-electrode system in 1 M H_2SO_4. (a) Cyclic voltammograms of N-Ben-800 at varying scan rates between 10 and 200 mV s^{-1}. (b) Cyclic voltammograms of N-Ben-800 at varying scan rates between 200 and 1000 mV s^{-1}. (c) Specific capacitance of N-Ben-800 and N-Py-700 at varying scan rates. (d) Galvanostatic charge-discharge curves of N-Ben-800 at current densities between 1 and 10 A g^{-1}. (e) Nyquist impedance spectrum of N-Ben-800 and N-Py-700 measured at 0 V. Inset shows the results in the high frequency region. (f) Frequency dependence of specific capacitance for N-Ben-800 and N-Py-700 at 0 V. (g) Cyclic voltammograms of N-Py-700 at varying scan rates between 10 and 200 mV s^{-1}. (h) Cyclic voltammograms of N-Py-700 at varying scan rates between 200 and 1000 mV s^{-1}. (i) Galvanostatic charge-discharge curves of N-Py-700 at current densities between 1 and 10 A g^{-1}.

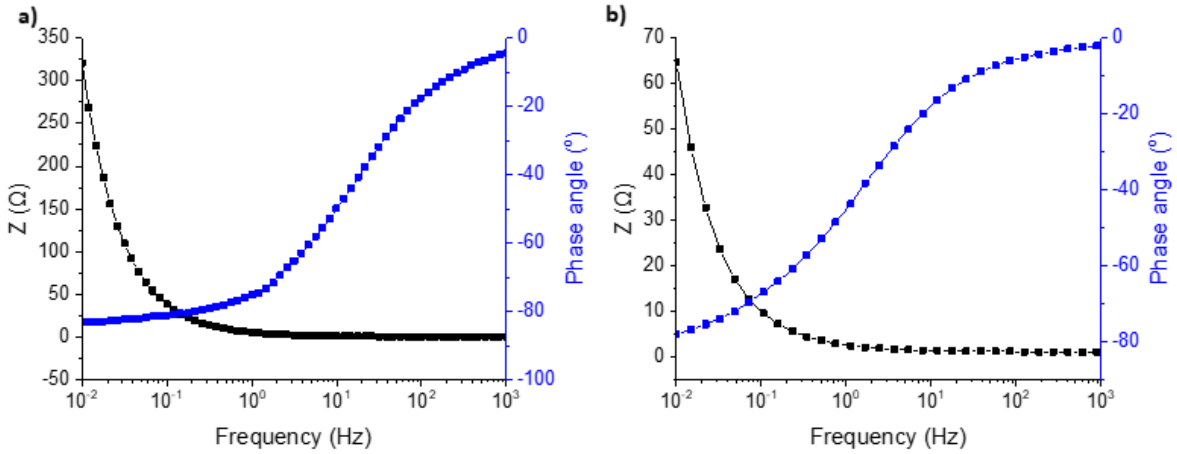

Figure 4.16 Bode plots of N-Py-700 measured in (a) two-electrode and (b) three-electrode configurations.

4.4.4 Differentiating Between EDLC and PC Mechanisms

In order to better understand the supercapacitive contributions from the surface area and from the heteroatom-doping, it is valuable to quantify the relative contributions from EDLC and PC. The respective EDLC and PC contributions from the heteroatom-doped carbons can be compared against each other due to the relatively slower electrochemical kinetics from Faradaic redox reactions of N- and S-containing functional groups in the PC mechanism compared to the faster EDLC process.[32] The maximum total specific capacitance, $C_{S,T,M}$, can be partitioned into EDLC contributions, C_{DL}, and PC contributions, C_P, by using the same procedure developed to estimate the outer electroactive sites of metal oxides.[61, 62] In this partition procedure, the total voltammetric charge, q_T, is calculated by extrapolation of voltammetric charge to $v = 0$ from the plot of $1/q$ *vs.* $v^{1/2}$ (**Figure 4.17a,c,e,g**). Charge associated with the double-layer, q_{DL}, is calculated by the extrapolation of voltammetric charge to $v = \infty$ from the plot of q *vs.* $v^{-1/2}$ (**Figure 4.17b,d,f,h**). Therefore, charge associated with PC, q_P, can be obtained by the difference between q_T and q_{DL}. Thus, specific capacitance from the maximum total ($C_{S,T,M}$), EDLC (C_{DL}), and PC (C_P), contributions can be calculated by dividing the corresponding charge with their respective potential windows used in CV (**Table 4.5**).

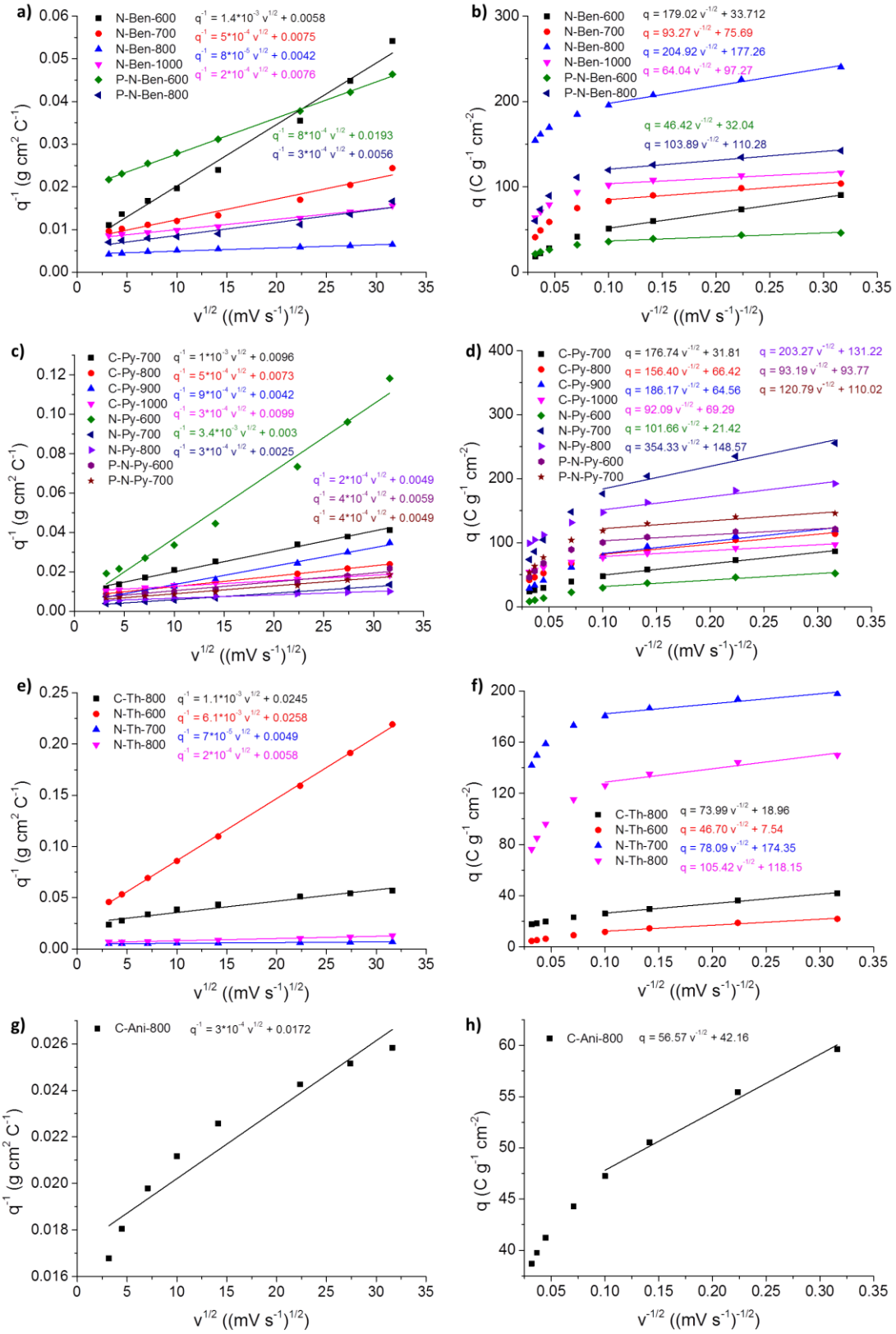

Figure 4.17 (a, c, e, g) Dependence of $1/q$ *vs.* $v^{1/2}$ and (b, d, f, h) dependence of q *vs.* $v^{-1/2}$ for heteroatom doped HCP-based carbons in 1 M H_2SO_4.

Table 4.5 Summary of maximum total specific capacitance ($C_{S,T,M}$), double-layer capacitance (C_{DL}), and pseudocapacitance (C_P) of heteroatom doped HCP-based carbons in 1 M H_2SO_4.

Sample	$C_{S,T,M}$ (F g^{-1})	C_{DL} (F g^{-1})	C_P(F g^{-1})	$C_P/C_{S,T,M}$ (%)
N-Ben-600	192	37	154	80.4
N-Ben-700	148	84	64	43.2
N-Ben-800	264	197	67	25.5
N-Ben-1000	147	108	39	26.3
P-N-Ben-600	58	36	22	38.1
P-N-Ben-800	198	123	76	38.2
C-Py-700	116	35	80	69.4
C-Py-800	152	76	78	51.5
C-Py-900	265	72	193	72.8
C-Py-1000	112	77	65	31.4
N-Py-600	370	24	347	93.6
N-Py-700	444	165	279	62.9
N-Py-800	194	125	69	35.7
P-N-Py-600	188	104	84	44.7
P-N-Py-700	227	111	116	50.1
C-Th-800	51	24	27	53.6
N-Th-600	43	8	35	80.5
N-Th-700	227	194	33	14.6
N-Th-800	192	131	60	31.4
C-Ani-800	65	47	18	27.5

All of the heteroatom-doped carbons possess both EDLC and PC contributions. As expected, higher overall PC contributions, $C_P/C_{S,T,M}$, are obtained where there are high levels of heteroatoms combined with relatively low surface areas, the latter of which decreases the EDLC contribution. The low temperature carbonisations materials prepared at 600 °C (N-Ben-600, N-Py-600, and N-Th-600) generally have very high $C_P/C_{S,T,M}$ as low electric conductivity result in lower EDLC contributions. N-Ben-700 has a slightly higher surface area and lower N-content than N-Ben-600, resulting in a lower $C_P/C_{S,T,M}$ (43.2% *vs*. 80.4%). N-Ben-800, which is the best supercapacitive material in its series, has the highest C_{DL} of 197 F g^{-1} attributed to its high surface area of 1252 m^2 g^{-1}, and it results in a $C_P/C_{S,T,M}$ of 25.5%; it is therefore a strongly EDLC-biased material. Even though the N-content of N-Ben-1000 is lower than N-Ben-800, the $C_P/C_{S,T,M}$ is higher due to the reduction of surface area in the material, and thus the C_{DL} contribution. The $C_P/C_{S,T,M}$ of P-N-Ben-600 and P-N-Ben-800 is very similar (38.1% and 38.2%, respectively), as the increase in surface area and N-content in P-N-Ben-800 increases both C_{DL} and C_P. As expected, N-Py-700 has the highest $C_{S,T,M}$ of 444 F g^{-1}, which is in line with yielding the

highest capacitance of all materials at a scan rate of 10 mV s^{-1}. This is largely attributed to the high C_P of 279 F g^{-1} from its high N-content of 13.44%, resulting in a $C_P/C_{S,T,M}$ of 62.9%. N-Py-800, which has a higher surface area than N-Ben-800, has a lower C_{DL}, in line with the pore structure of N-Ben-800 facilitating better electrolyte ion diffusion kinetics and, hence, EDLC. However, the N-content and C_P of N-Py-800 is higher than N-Ben-800, leading to a larger $C_P/C_{S,T,M}$ of 35.7%. C-Th-800 has a relatively low $C_P/C_{S,T,M}$ of 53.6%, despite possessing a high S-content of 13.58% (*c.f.*, C-Py-700: N-content = 9.42%, $C_P/C_{S,T,M}$ = 69.4%; N-Py-700: N-content = 13.44%, $C_P/C_{S,T,M}$ = 62.9%), which may be due to S-groups providing lower PC contributions than N-groups, as discussed previously. This is further supported by comparing N-Th-600 with N-Th-800, which have similar N-contents but the C_P of N-Th-800 (60 F g^{-1}) is higher than N-Th-600 (35 F g^{-1}), despite containing no S-atoms; this is likely due to increased electric conductivity from the higher carbonisation temperatures. Surprisingly, although N-Th-700 has a high N-content, it has a low $C_P/C_{S,T,M}$ of 14.6% compared with others in its series, and thus a high EDLC contribution. This could be due to N-groups in N-Th-700 increasing electrical conductivity[12] and increased dipolar attraction to the electrolyte cations[31] in the relatively high surface area carbon, aiding the EDLC mechanism. XPS was also measured for various samples to check the O-content of the materials (**Table 4.6**). The carbonisations integrated a similar amount of O species into the materials (8.16 to 10.83%) so it was assumed that the O-content does not greatly affect this study due to the consistent levels across samples. The XPS and CHNS values of C and N vary slightly due to differences of the surface and overall composition, however the N-content of XPS follows the same trend as CHNS.

Table 4.6 Elemental compositions of various carbonised materials calculated from the XPS survey scan.

Sample	C (%)	N (%)	O (%)	S (%)
N-Ben-800	87.46	2.78	9.76	-
P-N-Ben-800	85.84	3.33	10.83	-
C-Py-800	86.20	4.44	9.36	-
N-Py-600	84.25	7.30	8.45	-
N-Py-700	83.58	7.13	9.29	-
P-N-Py-700	86.19	4.13	9.68	-
N-Th-700	83.52	6.78	9.29	0.41
C-Ani-800	90.28	1.56	8.16	-

This partition capacitance model has generally been used for either comparing very similar materials,[32, 62] or for comparing a single material in different electrolytes,[7, 61] where perhaps 2 or 3 samples are compared. Hence, factors that may affect the partitioning, such as electric conductivity, pore structure, wettability, and morphology, are assumed to be the same. Due to the large sample size of this study (20 samples), there are some small deviations against the line of best fit shown in **Fig. 4.17a,c,g**. The

$C_P/C_{S,T,M}$ contributions of these materials can also be plotted against the normalised heteroatom to surface area ratio (**Figure 4.18**).

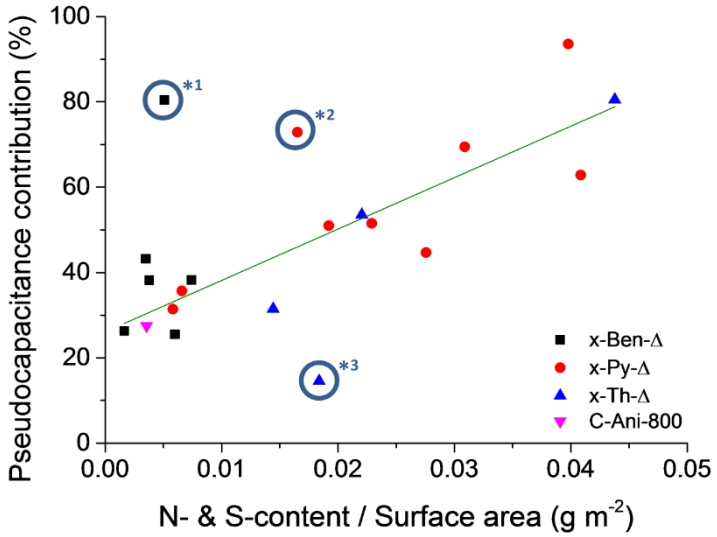

Figure 4.18 Correlation of overall pseudocapacitance contributions against N- & S-content to surface area ratio. *[1] = N-Ben-600. *[2] = N-Py-600. *[3] = N-Th-700. Heteroatom-content is taken from CHNS.

In general we found that $C_P/C_{S,T,M}$ in the HCP-based carbons is, approximately, linearly proportional to the ratio of heteroatom-doping to surface area, irrespective of the carbonisation precursor. The three outliers in the plot (blue circle) are a result of low electric conductivity in N-Ben-600 and N-Py-600, and the high EDLC contributions in N-Th-700, as discussed above. N-Th-600 could also be considered as an outlier due to its low electric conductivity if S-doping is not accounted for (**Figure 4.19**). A combination of EDLC and PC contributions is important for supercapacitive materials, with their ratio yielding different storage behaviour, as exhibited by the two best-performing carbons, N-Ben-800 and N-Py-700, which have a $C_P/C_{S,T,M}$ of 25.5% and 62.9%, respectively.

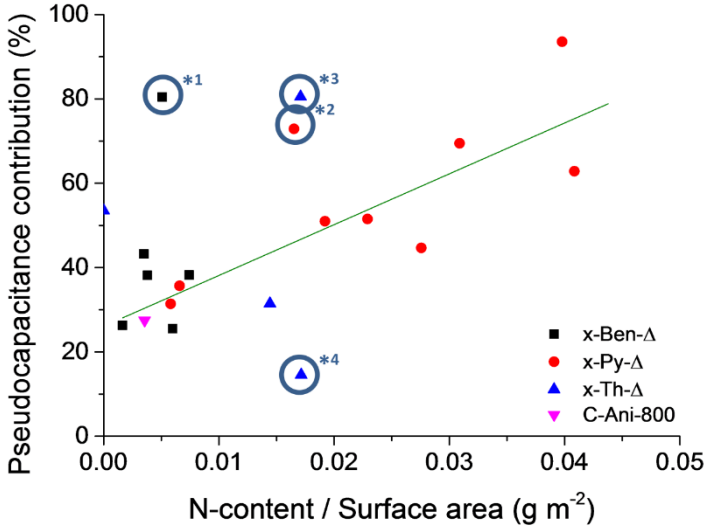

Figure 4.19 Correlation of overall pseudocapacitance contributions against N-content to surface area ratio. *[1] = N-Ben-600. *[2] = N-Py-600. *[3] = N-Th-600. *[4] = N-Th-700.

Though it is widely known that redox-active, heteroatom-doped carbons contribute to PC,[5, 7, 32, 43] this study uncovers the direct quantitative contribution that heteroatom-doping provides. To our knowledge, this is the first time that such a large range of materials has been studied and their EDLC and PC contributions compared.

4.5 Conclusions and Outlook

In summary, this chapter shows that the carbonisation of HCPs through various methods can be used to generate carbons with excellent supercapacitive properties. The method produces conductive carbons using low-cost precursors, while allowing heteroatoms to be incorporated by choice of feedstock and by changing the type of gas used in the carbonisation. A 63% PC-based material, N-Py-700, shows ideal supercapacitive behaviour, with a very high capacitance of 374 F g^{-1} at 0.1 A g^{-1}, and retains 96% capacitance after 15000 charge-discharge cycles. N-Ben-800, which shows 74% EDLC, exhibits a capacitance of 295 F g^{-1} at 0.1 A g^{-1} with an excellent capacitance retention of 81% at a very high current density of 10 A g^{-1}. The EDLC and PC contributions of the HCP-based carbons were quantified and compared against their properties, allowing synthetic control over the two supercapacitive mechanisms. There is a near endless synthetic diversity to form HCPs by this route, since more than 25 million aromatic molecules are susceptible to the Friedel-Crafts alkylation.[28] Hence, it is likely that further supercapacitive HCP-based carbons will be produced that exhibit improved energy storage properties over the promising materials presented here.

As with CMPs, electrically conducting HCPs have yet to be discovered. A Friedel-Crafts alkylation method which adds CH_2 bonds between aromatic molecules was chosen for this study. A Scholl coupling method which links two aromatic molecules directly in the presence of a Lewis acid is suggested for potentially producing conducting HCPs. However, the disorder and formation of a 3-D, non-crystalline polymer will likely prohibit electrical conduction. Through careful synthetic conditions, one may be able to Scholl couple adjacent benzene rings into small nanoribbons, although this may not constitute a conventional HCP anymore. To further study the carbonisation of HCPs synthesised through the "knitting" method, P- and B-containing HCPs could demonstrate interesting properties upon carbonisation since these elements have been shown to contribute towards supercapacitance.[63] Additionally, co-polymerisation of two different heteroatom-containing monomers may produce a homogenous distribution of these heteroatoms which may boost performance through a synergetic effect.

4.6 References

[1] J. W. Choi, D. Aurbach, *Nat. Rev. Mat.* **2016**, *1*, 16013; J. M. Tarascon, M. Armand, *Nature* **2001**, *414*, 359; H. Vikström, S. Davidsson, M. Höök, *Appl. Energy* **2013**, *110*, 252.

[2] J. R. Miller, P. Simon, *Science* **2008**, *321*, 651.

[3] Y. Zhu, S. Murali, M. D. Stoller, K. J. Ganesh, W. Cai, P. J. Ferreira, A. Pirkle, R. M. Wallace, K. A. Cychosz, M. Thommes, D. Su, E. A. Stach, R. S. Ruoff, *Science* **2011**, *332*, 1537.

[4] R. Kötz, M. Carlen, *Electrochim. Acta* **2000**, *45*, 2483.

[5] P. Simon, Y. Gogotsi, *Nat. Mater*. **2008**, *7*, 845.

[6] B. You, L. Wang, L. Yao, J. Yang, *Chem. Commun*. **2013**, *49*, 5016.

[7] J.-S. M. Lee, T.-H. Wu, B. M. Alston, M. E. Briggs, T. Hasell, C.-C. Hu, A. I. Cooper, *J. Mater. Chem. A* **2016**, *4*, 7665.

[8] W. Fan, Y.-Y. Xia, W. W. Tjiu, P. K. Pallathadka, C. He, T. Liu, *J. Power Sources* **2013**, *243*, 973; D.-W. Wang, F. Li, L.-C. Yin, X. Lu, Z.-G. Chen, I. R. Gentle, G. Q. Lu, H.-M. Cheng, *Chem. Eur. J* **2012**, *18*, 5345.

[9] L. Wang, G. Mu, C. Tian, L. Sun, W. Zhou, P. Yu, J. Yin, H. Fu, *ChemSusChem* **2013**, *6*, 880; E. Raymundo-Piñero, F. Leroux, F. Béguin, *Adv. Mater.* **2006**, *18*, 1877; J. Deng, M. Li, Y. Wang, *Green Chem.* **2016**, *18*, 4824.

[10] T. Zhu, J. Zhou, Z. Li, S. Li, W. Si, S. Zhuo, *J. Mater. Chem. A* **2014**, *2*, 12545; L. Wei, M. Sevilla, A. B. Fuertes, R. Mokaya, G. Yushin, *Adv. Funct. Mater.* **2012**, *22*, 827; Y. Li, X. Xu, Y. He, Y. Jiang, K. Lin, *Polymers* **2017**, *9*, 2.

[11] L. Zhang, F. Zhang, X. Yang, G. Long, Y. Wu, T. Zhang, K. Leng, Y. Huang, Y. Ma, A. Yu, Y. Chen, *Sci. Rep.* **2013**, *3*, 1408; M. Xue, D. Chen, X. Wang, J. Chen, G. F. Chen, *J. Mater. Chem. A* **2015**, *3*, 7715.

[12] Y. Qiu, X. Zhang, S. Yang, *Phys. Chem. Chem. Phys*. **2011**, *13*, 12554.

[13] Y. Li, S. Roy, T. Ben, S. Xu, S. Qiu, *Phys. Chem. Chem. Phys*. **2014**, *16*, 12909.

[14] Y. Zhao, F. Xie, C. Zhang, R. Kong, S. Feng, J.-X. Jiang, *Microporous Mesoporous Mater.* **2017**, *240*, 73.

[15] J. P. Zheng, P. J. Cygan, T. R. Jow, *J. Electrochem. Soc*. **1995**, *142*, 2699.

[16] W. Sugimoto, in *Encyclopedia of Applied Electrochemistry*, (Eds: G. Kreysa, K.-i. Ota, R. F. Savinell), Springer New York, New York, NY **2014**, 1813.

[17] A. Funke, F. Ziegler, *Bioresour. Technol.* **2011**, *102*, 7595.

[18] J. Hu, H. Wang, Q. Gao, H. Guo, *Carbon* **2010**, *48*, 3599.

[19] R. R. Salunkhe, Y. V. Kaneti, J. Kim, J. H. Kim, Y. Yamauchi, *Acc. Chem. Res*. **2016**, *49*, 2796.

[20] R. R. Salunkhe, J. Tang, N. Kobayashi, J. Kim, Y. Ide, S. Tominaka, J. H. Kim, Y. Yamauchi, *Chem. Sci*. **2016**, *7*, 5704.

[21] Z. Xiang, D. Wang, Y. Xue, L. Dai, J.-F. Chen, D. Cao, *Sci. Rep*. **2015**, *5*, 8307.

[22] K. Yuan, P. Guo-Wang, T. Hu, L. Shi, R. Zeng, M. Forster, T. Pichler, Y. Chen, U. Scherf, *Chem. Mater.* **2015**, *27*, 7403; H. Wang, Z. Cheng, Y. Liao, J. Li, J. Weber, A. Thomas, C. F. J. Faul, *Chem. Mater.* **2017**, *29*, 4885.

[23] L. Tan, B. Tan, *Chem. Soc. Rev.* **2017**, *46*, 3322.

[24] V. A. Davankov, M. P. Tsyurupa, *React. Polym*. **1990**, *13*, 27; W. Li, A. Zhang, H. Gao, M. Chen, A. Liu, H. Bai, L. Li, *Chem. Commun.* **2016**, *52*, 2780.

[25] M. P. Tsyurupa, L. A. Maslova, A. I. Andreeva, T. A. Mrachkovskaya, V. A. Davankov, *React. Polym.* **1995**, *25*, 69.

[26] B. Li, R. Gong, W. Wang, X. Huang, W. Zhang, H. Li, C. Hu, B. Tan, *Macromolecules* **2011**, *44*, 2410.

[27] R. Dawson, E. Stockel, J. R. Holst, D. J. Adams, A. I. Cooper, *Energy Environ. Sci*. **2011**, *4*, 4239; S. Wang, C. Zhang, Y. Shu, S. Jiang, Q. Xia, L. Chen, S. Jin, I. Hussain, A. I. Cooper, B. Tan, *Sci. Adv.* **2017**, *3*. 3.

[28] J.-S. M. Lee, M. E. Briggs, T. Hasell, A. I. Cooper, *Adv. Mater.* **2016**, *28*, 9804.

[29] T. Mitra, R. S. Bhavsar, D. J. Adams, P. M. Budd, A. I. Cooper, *Chem. Commun*. **2016**, *52*, 5581; C. H. Lau, X. Mulet, K. Konstas, C. M. Doherty, M.-A. Sani, F. Separovic, M. R. Hill, C. D. Wood, *Angew. Chem., Int. Ed.* **2016**, *55*, 1998; Z.-A. Qiao, S.-H. Chai, K. Nelson, Z. Bi, J. Chen, S. M. Mahurin, X. Zhu, S. Dai, *Nat. Comm.* **2014**, *5*, 3705.

[30] R. Dawson, A. I. Cooper, D. J. Adams, *Prog. Polym. Sci*. **2012**, *37*, 530; S. Xu, Y. Luo, B. Tan, *Macromol. Rapid Commun.* **2013**, *34*, 471; Z. Dou, L. Xu, Y. Zhi, Y. Zhang, H. Xia, Y. Mu, X. Liu, *Chem. Eur. J* **2016**, *22*, 9919.

[31] Y. Kou, Y. Xu, Z. Guo, D. Jiang, *Angew. Chem., Int. Ed*. **2011**, *50*, 8753.

[32] Y.-H. Lee, K.-H. Chang, C.-C. Hu, *J. Power Sources* **2013**, *227*, 300.

[33] M. Thommes, K. Kaneko, A. V. Neimark, J. P. Olivier, F. Rodriguez-Reinoso, J. Rouquerol, K. S. W. Sing, *Pure Appl. Chem.* **2015**, *87*, 1051.

[34] V. Davankov, M. Tsyurupa, in *Comprehensive Analytical Chemistry*, Vol. Volume 56 (Eds: A. D. Vadim, P. T. Maria), Elsevier, **2011**, 195.

[35] R. Dawson, T. Ratvijitvech, M. Corker, A. Laybourn, Y. Z. Khimyak, A. I. Cooper, D. J. Adams, *Polym. Chem.* **2012**, *3*, 2034.

[36] Z. Song-lin, G. Shang-yu, Y. Xi-gen, X. Bo-sen, *J. Forest. Res.* **2003**, *14*, 75.

[37] L. Qie, W.-M. Chen, Z.-H. Wang, Q.-G. Shao, X. Li, L.-X. Yuan, X.-L. Hu, W.-X. Zhang, Y.-H. Huang, *Adv. Mater*. **2012**, *24*, 2047; S. Gao, H. Fan, Y. Chen, L. Li, Y. Bando, D. Golberg, *Nano Energy* **2013**, *2*, 1261.

[38] C. Hu, Y. Xiao, Y. Zhao, N. Chen, Z. Zhang, M. Cao, L. Qu, *Nanoscale* **2013**, *5*, 2726.

[39] N. J. Bell, Y. H. Ng, A. Du, H. Coster, S. C. Smith, R. Amal, *J. Phys. Chem. C* **2011**, *115*, 6004.

[40] M. Inagaki, K. Feiyu, *Carbon Materials Science and Engineering: From Fundamentals to Applications*, Tsinghua University Press 清华大学出版社有限公司, **2006**.

[41] Z. Dai, C. Peng, J. H. Chae, K. C. Ng, G. Z. Chen, *Sci. Rep.* **2015**, *5*, 9854.

[42] E. Raymundo-Piñero, M. Cadek, F. Béguin, *Adv. Funct. Mater.* **2009**, *19*, 1032.

[43] X. Chen, R. Paul, L. Dai, *Natl. Sci. Rev.* **2017**, *4*, 453; A. Borenstein, O. Hanna, R. Attias, S. Luski, T. Brousse, D. Aurbach, *J. Mater. Chem. A* **2017**, *5*, 12653; M. Sevilla, R. Mokaya, *Energy Environ. Sci.* **2014**, *7*, 1250.

[44] P. L. Taberna, P. Simon, J. F. Fauvarque, *J. Electrochem. Soc*. **2003**, *150*, A292.

[45] K. Xia, Q. Gao, J. Jiang, J. Hu, *Carbon* **2008**, *46*, 1718.

[46] F.-C. Wu, R.-L. Tseng, C.-C. Hu, C.-C. Wang, *J. Power Sources* **2006**, *159*, 1532.

[47] T.-H. Wu, C.-T. Hsu, C.-C. Hu, L. J. Hardwick, *J. Power Sources* **2013**, *242*, 289.

[48] C. Largeot, C. Portet, J. Chmiola, P.-L. Taberna, Y. Gogotsi, P. Simon, *J. Am. Chem. Soc.* **2008**, *130*, 2730; X. Feng, Y. Liang, L. Zhi, A. Thomas, D. Wu, I. Lieberwirth, U. Kolb, K. Müllen, *Adv. Funct. Mater*. **2009**, *19*, 2125.

[49] L. Zhao, L.-Z. Fan, M.-Q. Zhou, H. Guan, S. Qiao, M. Antonietti, M.-M. Titirici, *Adv. Mater.* **2010**, *22*, 5202.

[50] L. Li, E. Liu, J. Li, Y. Yang, H. Shen, Z. Huang, X. Xiang, W. Li, *J. Power Sources* **2010**, *195*, 1516.

[51] J. Wei, D. Zhou, Z. Sun, Y. Deng, Y. Xia, D. Zhao, *Adv. Funct. Mater.* **2013**, *23*, 2322.

[52] H. Guo, Q. Gao, *J. Power Sources* **2009**, *186*, 551.

[53] G. Xu, B. Ding, P. Nie, L. Shen, J. Wang, X. Zhang, *Chem. Eur. J* **2013**, *19*, 12306.

[54] H. M. Jeong, J. W. Lee, W. H. Shin, Y. J. Choi, H. J. Shin, J. K. Kang, J. W. Choi, *Nano Lett.* **2011**, *11*, 2472.

[55] J. Han, G. Xu, H. Dou, D. R. MacFarlane, *Chem. - Eur. J.* **2015**, *21*, 2310.

[56] L. Hao, B. Luo, X. Li, M. Jin, Y. Fang, Z. Tang, Y. Jia, M. Liang, A. Thomas, J. Yang, L. Zhi, *Energy Environ. Sci.* **2012**, *5*, 9747.

[57] L. Hao, J. Ning, B. Luo, B. Wang, Y. Zhang, Z. Tang, J. Yang, A. Thomas, L. Zhi, *J. Am. Chem. Soc.* **2015**, *137*, 219.

[58] X.-C. Li, Y. Zhang, C.-Y. Wang, Y. Wan, W.-Y. Lai, H. Pang, W. Huang, *Chem. Sci*. **2017**, *8*, 2959.

[59] E. Raymundo-Piñero, K. Kierzek, J. Machnikowski, F. Béguin, *Carbon* **2006**, *44*, 2498.

[60] M. D. Stoller, R. S. Ruoff, *Energy Environ. Sci.* **2010**, *3*, 1294.

[61] S. Ardizzone, G. Fregonara, S. Trasatti, *Electrochim. Acta* **1990**, *35*, 263.

[62] D. Baronetto, N. Krstajić, S. Trasatti, *Electrochim. Acta* **1994**, *39*, 2359; K.-H. Chang, C.-C. Hu, C.-Y. Chou, *Chem. Mater.* **2007**, *19*, 2112.

[63] V. Thirumal, A. Pandurangan, R. Jayavel, R. Ilangovan, *Synth. Met.* **2016**, *220*, 524; Y. Wen, B. Wang, C. Huang, L. Wang, D. Hulicova-Jurcakova, *Chem. Eur. J* **2015**, *21*, 80.

Chapter 5

Hypercrosslinked Polymer-Derived Carbons for CO_2 and H_2 Storage

Some of the contents in this chapter are taken from **Paper IV**.

J.-S. M. Lee, M. E. Briggs, T. Hasell, A. I. Cooper, "Hyperporous Carbons from Hypercrosslinked Polymers". *Adv. Mater.* **2016**, *28*, 9804–9810.

5.1 Background and Context

There have been many recent reports of using porous materials as carbonisation precursors that show advantages to non-porous precursors. These reports primarily use MOFs, PAFs, and CMPs which can have various disadvantages in regard to cost and scalability. HCPs are advantageous as they overcome these problems. The strategy was utilised by synthesising a range of HCPs which do and do not contain various heteroatoms, and maximising their surface areas by chemically activating them with KOH for carbonisation. It was found that each precursor has a preferential carbonisation temperature to maximise porosity, whilst still retaining their parent heteroatoms. The best performing material, Py800, has the highest apparent BET surface area of an organic derived-carbon to date, and showed the highest CO_2 and H_2 uptakes, outperforming many high-performing and more expensive materials.

5.2 Introduction

Porous carbonaceous materials have been of interest for many years because of applications[1] such as gas separation,[2] water purification,[3] catalysis,[4] electromagnetic interface shielding,[5] and energy storage in batteries,[6] supercapacitors,[7] and fuel cells.[8] Porous carbons are appealing because of their relatively low cost and their ease of preparation from a variety of natural and synthetic precursors. Porous carbons are noted for their high surface areas (>1000 $m^2\ g^{-1}$) and pore volumes (>0.5 $cm^3\ g^{-1}$); they also have good chemical, thermal, and mechanical stability, high electrical conductivity, and they can be processed for various applications.[9] Porous carbonaceous materials are traditionally prepared by physical activation, chemical activation, or by a combination of the two.[10]

Highly porous carbons have been produced in the past with the use of KOH as a chemical activating agent, through precursors including linear polymers,[11, 12] carbon nanotubes,[13] and graphene oxide.[14] A number of microporous solids have been precursors for carbonaceous materials with advanced properties, including ZIFs,[15] MOFs,[16] PAFs,[17] CMPs,[18] and HCPs.[19] The choice of precursor material can affect the functionality in the resultant carbons. For instance, carbonised ZIFs have been used for supercapacitor electrodes,[20] carbonised MOFs as oxygen reduction catalysts and lithium sulphur batteries,[21] carbonised PAFs for gas storage,[22] carbonised CMPs as chemosensors, electrocatalysis, and supercapacitors,[23, 24] and carbonised HCPs for benzene/chlorobenzene vapour absorption and as a porous carbon support for oxygen reduction reactions.[25] While these materials show good performance for their respective applications, many of the microporous precursors involved costly starting materials (*e.g.*, PAFs, many MOFs, and CMPs) or expensive catalysts for their

preparation (*e.g.*, CMPs, PAFs). Also, some of these precursor porous materials are prepared under rigorous anhydrous and anaerobic conditions (*e.g.*, PAFs), which makes scale-up challenging.

HCPs are microporous materials synthesised from cheap organic monomers that show good stability and potential for synthetic diversification. Permanent porosity in HCPs is a result of extensive cross-linking, which prevents the polymer chains from collapsing into a dense, non-porous state. HCPs have been known for many years and are scalable.[26] They can be prepared using a FDA cross-linker through a simple one-step Friedel-Crafts reaction, which opens up this approach to a large library of polymers derived from simple aromatic monomers.[27] HCPs can exhibit a range of surface areas, pore-size distributions, and surface functionalities that can be tuned by changing the aromatic monomer, the reaction stoichiometry, or by the inclusion of functionalised aromatic co-monomers. Benzene-derived HCPs have received renewed interest due to their high uptake of CO_2 (15.3 mmol g^{-1} at 40 bar) and their potential application in the purification of syngas.[28, 29] However, this high CO_2 uptake is also associated with swelling of the polymer, which could cause limitations for some practical applications.

The aim of this project was to find a simple process that could be used to further improve the properties of HCPs. Ideally, the surface area of the materials would be increased while minimising the pronounced swelling that is observed with CO_2 or with other adsorbed species, such as organic liquids. This chapter discusses how a simple carbonisation process can be used to significantly enhance the surface areas of HCPs, whilst simultaneously preventing swelling of the material. These results are transferable across a family of three related HCPs, derived from three low-cost monomers; benzene, thiophene, and pyrrole.

5.3 Experimental

5.3.1 Chemical Reagents

Benzene, thiophene, pyrrole, FDA, iron(III) chloride, 1,2-dichloroethane, potassium hydroxide, and activated carbon were purchased from Sigma Aldrich. Methanol was purchased from Fisher Scientific. Zeolite 13X was purchased from Micromeritics. High purity nitrogen was purchased from BOC. All chemicals were used as received without any further purification. DI water was used in purifications.

5.3.2 Synthesis

Preparation of Hypercrosslinked Polymers

The hypercrosslinked polymers were synthesised using a previously reported literature method,[27] The monomer (either benzene, thiophene or pyrrole; 50 mmol) was added to 1,2-dichloroethane (100 mL) under nitrogen in a 250 mL two-necked Radley's flask equipped with a reflux condenser. Dimethoxymethane (8.8 mL, 100 mmol) was added and the mixture was stirred for 10 min. Iron(III) chloride (16.2 g, 100 mmol) was then added and the mixture was heated under reflux at 80 °C overnight. After cooling the dark brown/black precipitate was filtered and washed with methanol. The solids were further purified by Soxhlet extraction with methanol for 1 day then dried under vacuum at 70 °C for 1 day. Gravimetric yields for all polymers were >90%. Elemental analysis: HCP-Ben, C: 85.50%, H: 5.45%; HCP-Th, C: 52.79%, H: 3.20%, S: 23.40%; HCP-Py, C: 58.80%, H: 5.10%, N: 11.02%.

Preparation of Carbonised Materials

In a typical procedure, hypercrosslinked polymer (1.0 g) and KOH (4.0 g, 71.2 mmol) were thoroughly mixed using a pestle and mortar. The mixture was placed in a ceramic boat and inserted within a tube furnace. The furnace was purged with N_2 at room temperature for 30 min, heated to the specified temperature at a rate of 5 °C min^{-1}, held at the set temperature for 2 h and finally cooled to room temperature. The residue was washed thoroughly with DI water, 1 M HCl, and DI water until the filtrate attained pH 7. Further purification of the carbons was carried out by Soxhlet extraction with methanol overnight. The resultant carbons were dried under vacuum for 1 day at 70 °C.

5.4 Results and Discussion

5.4.1 Methodology of Hypercrosslinked Polymers and HCP-based Activated Carbons

Benzene, thiophene, and pyrrole were hypercrosslinked according to known literature methods,[27] and the resulting polymers are referred to as HCP-Ben, HCP-Th and HCP-Py (**Scheme 5.1**). These monomers were chosen to produce a variety of HCPs containing either no heteroatoms (benzene), N-atoms (pyrrole), or S-atoms (thiophene).

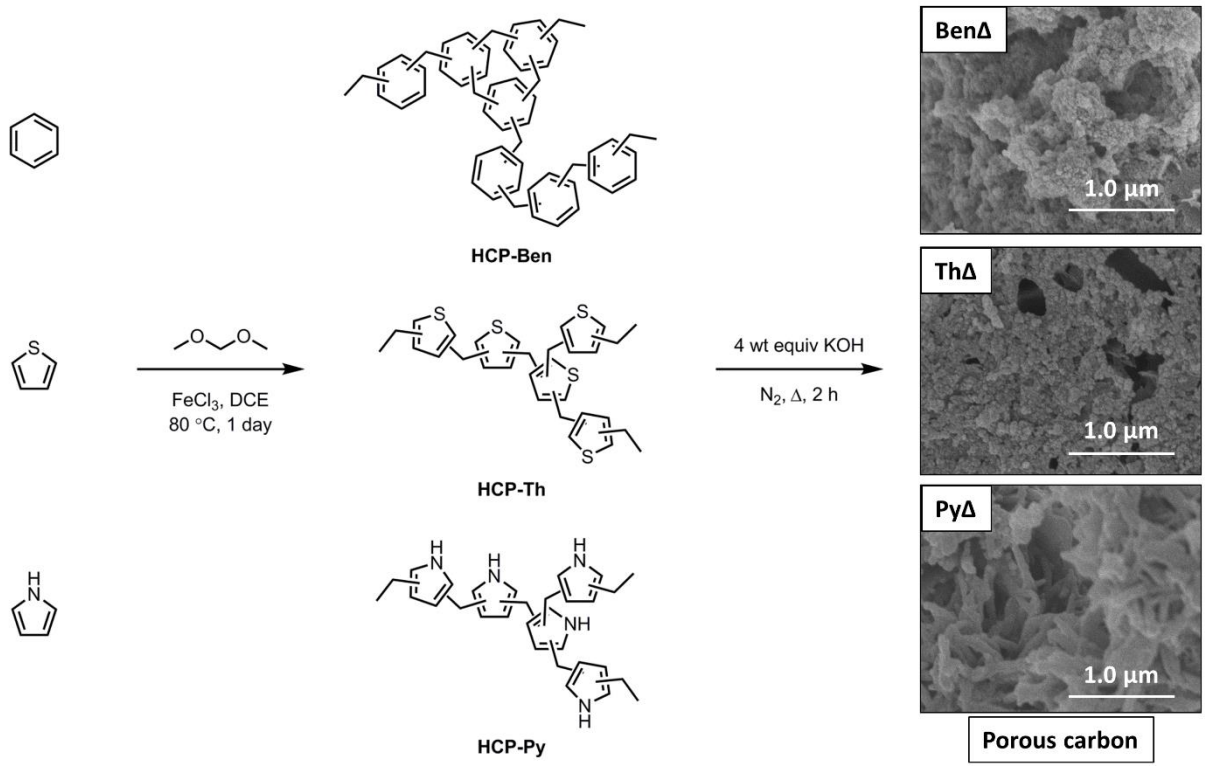

Scheme 5.1 Synthesis of the hypercrosslinked polymers and subsequent carbonisation method.

TGA in nitrogen was performed to determine the thermal stability of the HCPs, mimicking the conditions that would be used for the carbonisation (**Figure 5.1**). HCP-Th and HCP-Py show some mass loss below 100 °C; this was ascribed to evaporation of physisorbed atmospheric water since the S and N atoms present in these polymers are known to have a strong affinity for water. HCP-Ben shows high thermal stability with little mass loss below 500 °C and only 30% mass loss up to 1000 °C, whereas HCP-Th and HCP-Py show continuous mass loss up to 80% and 96%, respectively, at 1000 °C.

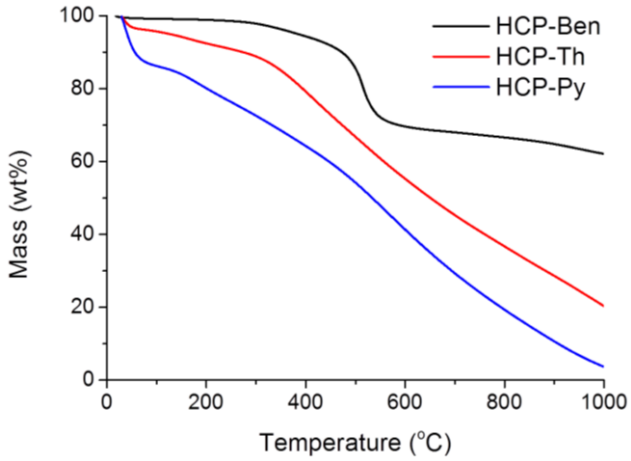

Figure 5.1 TGA curves of HCPs at a ramp rate of 5 °C min^{-1} under N_2.

Carbonised HCPs were obtained by mixing the HCPs with KOH in a 1:4 ratio and heating at various temperatures between 700 and 1000 °C, followed by extraction of residual salts and drying. The carbons are referred to as BenΔ, ThΔ and PyΔ, with Δ signifying the carbonisation temperature.

TGA curves of some representative samples indicated residual masses of 2–8% (**Figure 5.2**).

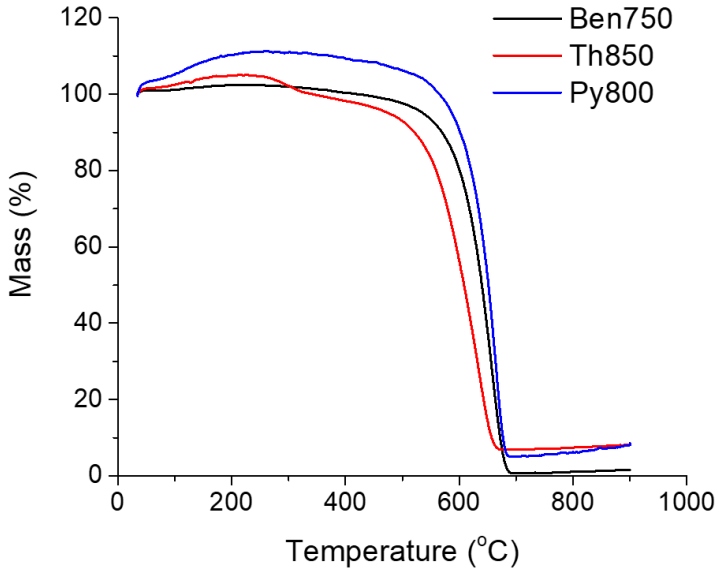

Figure 5.2 TGA analysis of HCP-derived activated carbons heated in air.

5.4.2 Structure and Properties of Hypercrosslinked Polymer-Derived Activated Carbons

The apparent BET surface areas of the synthesised carbons are shown in **Figure 5.3a**; Ben750, Th850, and Py800 were observed to have the highest BET surface areas of 3105 $m^2 g^{-1}$, 2682 $m^2 g^{-1}$, and 4334 $m^2 g^{-1}$, respectively, and these materials were therefore evaluated in more detail.

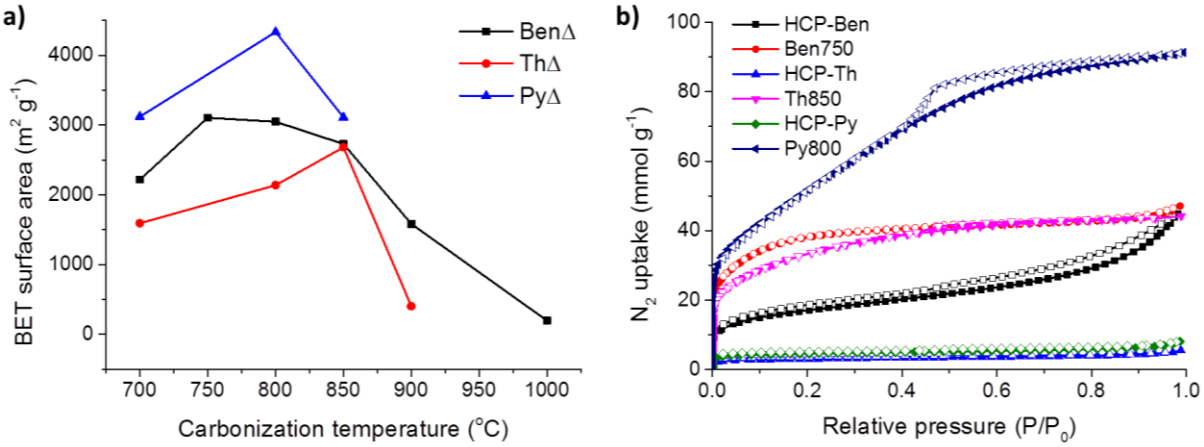

Figure 5.3 (a) BET surface areas of carbonised HCPs at various temperatures. (b) Nitrogen adsorption-desorption isotherms of HCPs and the porous carbons at 77.3 K (the adsorption and desorption branches are labelled with filled and empty symbols, respectively).

Nitrogen sorption isotherms for the HCPs Ben750, Th850, and Py800, are shown in **Figure 5.3b**. The physical properties of these carbons and their HCP precursors are summarised in **Table 5.1**. Following IUPAC classification,[30] these isotherm shapes include examples that are Type Ib (associated with a broad range of micropores), Type II (associated with the presence of macropores), and Type IVa (associated with mesoporous characteristics). The isotherms of the carbonisation precursors (HCP-Ben, HCP-Th and HCP-Py) are all Type II signifying the presence of macropores within the HCPs, though it should also be stressed that these materials can swell in liquid nitrogen.[31] The HCPs have surface areas and total pore volumes of 1382 $m^2\ g^{-1}$ and 1.52 $cm^3\ g^{-1}$ for HCP-Ben, 484 $m^2\ g^{-1}$ and 0.33 $cm^3\ g^{-1}$ for HCP-Th, and 322 $m^2\ g^{-1}$ and 0.25 $cm^3\ g^{-1}$ for HCP-Py. Carbonisation with KOH resulted in increased microporosity for Ben750, Th850, and Py800, while Py800 also showed a large increase in mesoporosity. The N_2 isotherms of Ben750 and Th850 are Type Ib; most of the nitrogen uptake occurs at $P/P_0 < 0.02$, indicating a mostly microporous structure, which is also apparent from comparison of the micropore volume with the total pore volume (**Table 5.1**). Py800 shows a Type IVa isotherm associated with a mesoporous material with a relatively small portion (33%) of its total pore volume derived from micropores, as seen in the pore size distribution of the material (**Figure 5.4**). Py800 also shows an extremely high surface area of 4334 $m^2\ g^{-1}$ which, to our knowledge, is the highest reported to date for an organic derived activated carbonaceous material.[12, 13, 32]

Table 5.1 Physical properties of hypercrosslinked polymers and optimised carbons.

		Pore volume ($cm^3\ g^{-1}$)[b]		
Sample	Surface area[a]	Total pore volume	Micropore volume	Pore size (Å)[c]
HCP-Ben	1382	1.52	0.40	12/15
HCP-Th	484	0.33	0.22	15
HCP-Py	322	0.25	0.14	9
Ben750	3105	1.58	1.00	11
Th850	2682	1.51	0.70	12
Py800	4334	3.14	1.05	13/22-47

[a] BET surface area. [b] Calculated by single point pore volume. [c] Pore size distribution maxima calculated by NL-DFT.

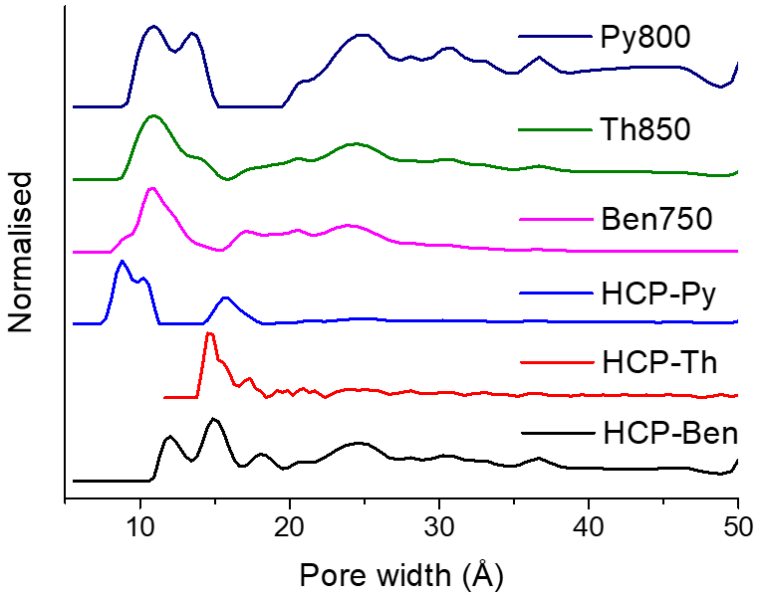

Figure 5.4 Pore size distribution of HCPs and carbons calculated by NL-DFT.

The nitrogen isotherms and pore size distributions for the synthesised carbons are shown in **Figure 5.5**. The carbonisation products of HCP-Ben at 700 °C and 750 °C show Type Ib isotherms, indicating high microporosity (**Figure 5.5a**). As the carbonisation temperature was raised to 850 °C, the isotherms display some Type IVa character with a hysteresis loop gradually appearing at $P/P_0 = 0.5$, this is accompanied by a widening of the pore size distribution (**Figure 5.5b**) and is due to the formation of mesopores at higher activation temperatures. The higher temperatures led to a decrease in surface area from 3105 $m^2\ g^{-1}$ for Ben750 to 3049 $m^2\ g^{-1}$ and 2730 $m^2\ g^{-1}$ for Ben800 and Ben850, respectively (**Table 5.2**). At 900 °C, the isotherm is Type IVa, indicating of a mesoporous material. When the carbonisation temperature is increased from 850 °C to 900 °C, the surface area drops from 2730 $m^2\ g^{-1}$ to 1584 $m^2\ g^{-1}$; this is primarily due to a reduction in the micropore volume from 0.76 $cm^3\ g^{-1}$ to

0.31 $cm^3 g^{-1}$; the total pore volume remains approximately constant. Increasing the carbonisation temperature to 1000 °C resulted in a substantial loss of porosity, with the isotherm displaying Type II characteristics, indicating the presence of mostly macropores and a surface area loss of only 196 $m^2 g^{-1}$ due to the collapse of most micro- and mesopores. In general, the average pore size distribution shifts from being micro- to mesoporous as more material is removed with increasing temperature, this eventually leads to pore collapse and the formation of lower surface area carbons.

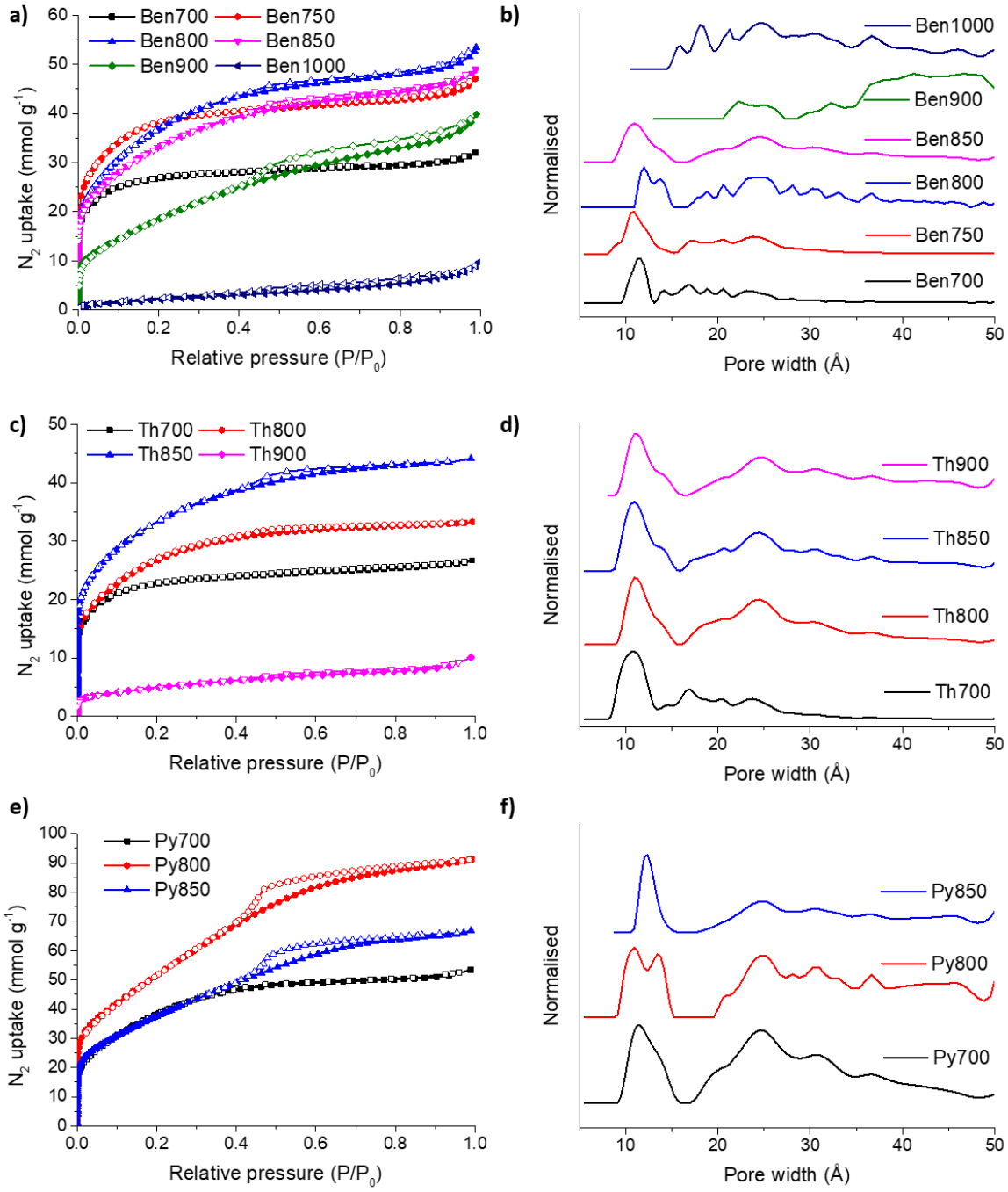

Figure 5.5 Nitrogen adsorption–desorption isotherms of carbonised (a) BenΔ, (c) ThΔ, and (e) PyΔ at 77.3 K (the adsorption and desorption branches are labelled with filled and empty symbols, respectively). Pore size distributions of (b) BenΔ, (d) ThΔ, and (f) PyΔ calculated by NL-DFT.

Table 5.2 Physical properties of carbonised HCP-Ben, HCP-Th and HCP-Py at various temperatures.

		Pore volume (cm^3 g^{-1})[b]		
Sample	Surface area[a]	Total pore volume	Micropore volume	Pore size (Å)[c]
Ben700	2219	1.08	0.77	12
Ben750	3105	1.58	1.00	12
Ben800	3049	1.80	0.77	13/14/25
Ben850	2730	1.67	0.76	12/25
Ben900	1584	1.32	0.31	36-55
Ben1000	196	0.31	0.02	15-45
Th700	1593	0.93	0.78	12
Th800	2138	1.15	0.66	12/20-32
Th850	2682	1.51	0.70	12/20-30
Th900	403	0.29	0.10	12/20-30
Py700	3122	1.82	0.78	12/22-37
Py800	4334	3.14	1.05	12/14/23-48
Py850	3112	2.29	0.71	13

[a] BET surface area. [b] Calculated by single point pore volume. [c] Pore size distribution maxima calculated by NL-DFT.

Carbonised samples produced from HCP-Th and HCP-Py show a similar trend with increasing temperature. HCP-Th carbonised at 700 °C and 800 °C show Type Ib isotherms suggesting a mainly microporous material with surface areas of 1593 m^2 g^{-1} and 2138 m^2 g^{-1}, respectively (**Figure 5.5c**). Upon raising the carbonisation temperature to 850 °C, the isotherm shifts to Type IVa indicating mesopores with a large surface area of 2682 m^2 g^{-1}; the micropore content was still relatively high constituting about 46% of the total pore volume. A further increase in temperature to 900 °C results in a dramatic decrease in surface area to 403 m^2 g^{-1}, and a Type II isotherm. Carbonised HCP-Py at 700 °C displays a Type Ib isotherm with the surface area of 3122 m^2 g^{-1}, primarily ascribed to microporosity. An increase in carbonisation temperature to 800 °C gives a Type IVa isotherm and yields a mesoporous

material with an extremely high surface area of 4334 $m^2 g^{-1}$ (**Figure 5.5e**). Upon a further increase in temperature to 850 °C, the material still possesses a Type IVa isotherm, though the micropore and total pore volumes are decreased, resulting in a lower surface area of 3112 $m^2 g^{-1}$. At higher temperatures, the poor mass recovery of the carbons precluded porosity testing. All ThΔ and PyΔ carbons retain some of their respective parent heteroatoms showing that the incorporation of heteroatoms is possible using selected heteroatom containing precursors (**Table 5.3**).

Table 5.3 Carbonisation yields and CHNS elemental analysis of HCPs and porous carbon products.

Sample	Yield[a]	C (%)	H (%)	N (%)	S (%)
HCP-Ben	-	85.50	5.45	-	-
HCP-Th	-	52.79	3.2	-	23.40
HCP-Py	-	58.80	5.10	11.02	-
Ben700	51	90.09	0.67	-	-
Ben750	47	93.81	0.53	-	-
Ben800	28	93.71	0.41	-	-
Ben850	15	90.99	0.48	-	-
Ben900	8	78.42	1.06	-	-
Th700	21	76.52	0.51	-	14.46
Th800	20	82.71	0.51	-	11.92
Th850	16	89.18	0.31	-	5.32
Py700	15	77.65	0.88	2.35	-
Py800	12	87.78	0.46	1.42	-
Py850	11	87.82	0.43	1.09	-

[a] Yield calculated from final mass against the starting precursor mass.

FE-SEM was used to study the morphology of the HCPs and various carbonised products. The images all show similar morphologies for the carbonised samples at 800 °C and their precursor polymers (**Figure 5.6**). It can be concluded that the morphology is generally retained with these carbonisation conditions.

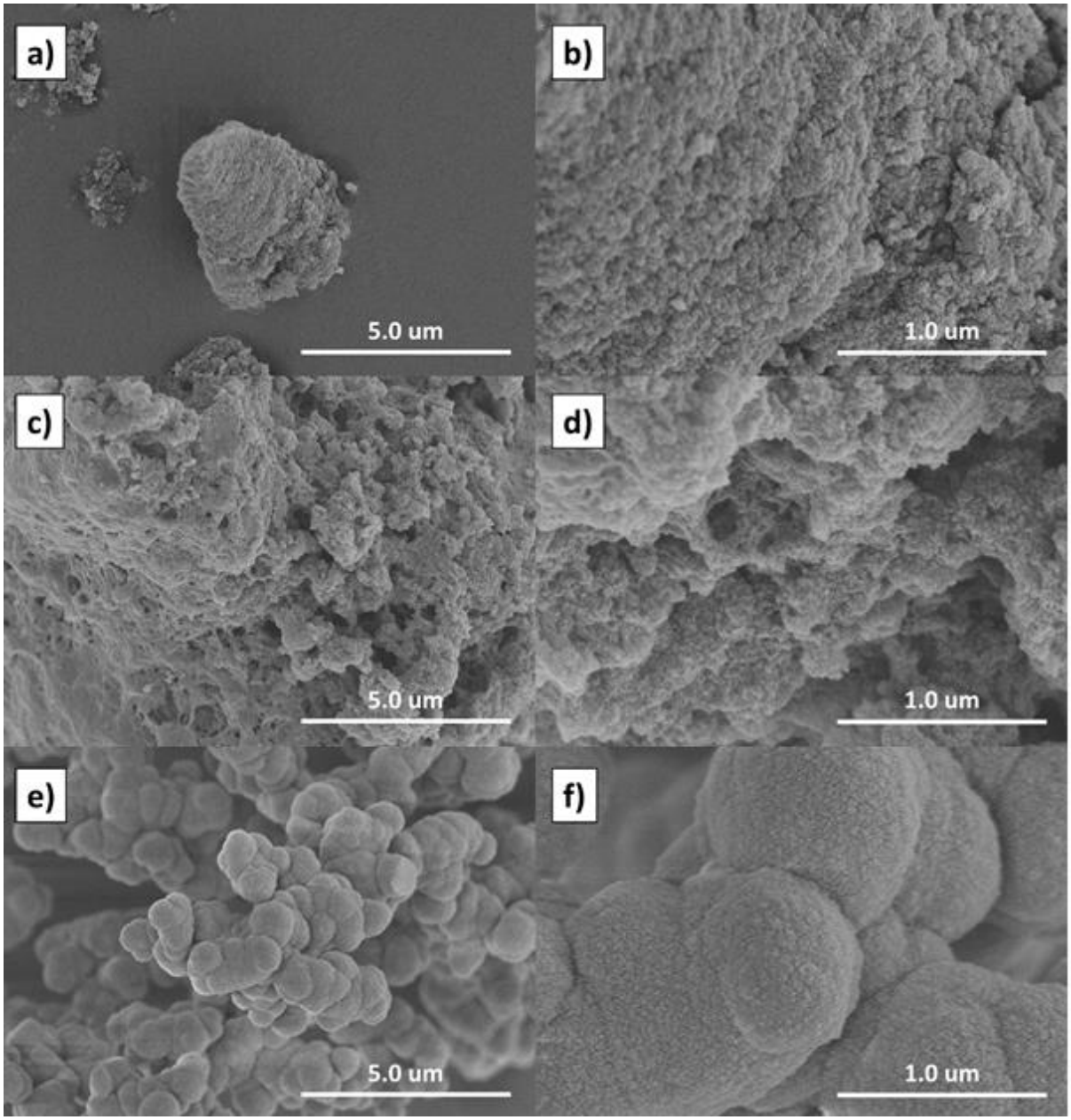

Figure 5.6 FE-SEM images of (a, b) HCP-Ben, (c, d) Ben800, and (e, f) HCP-Th, at low and high magnifications, respectively.

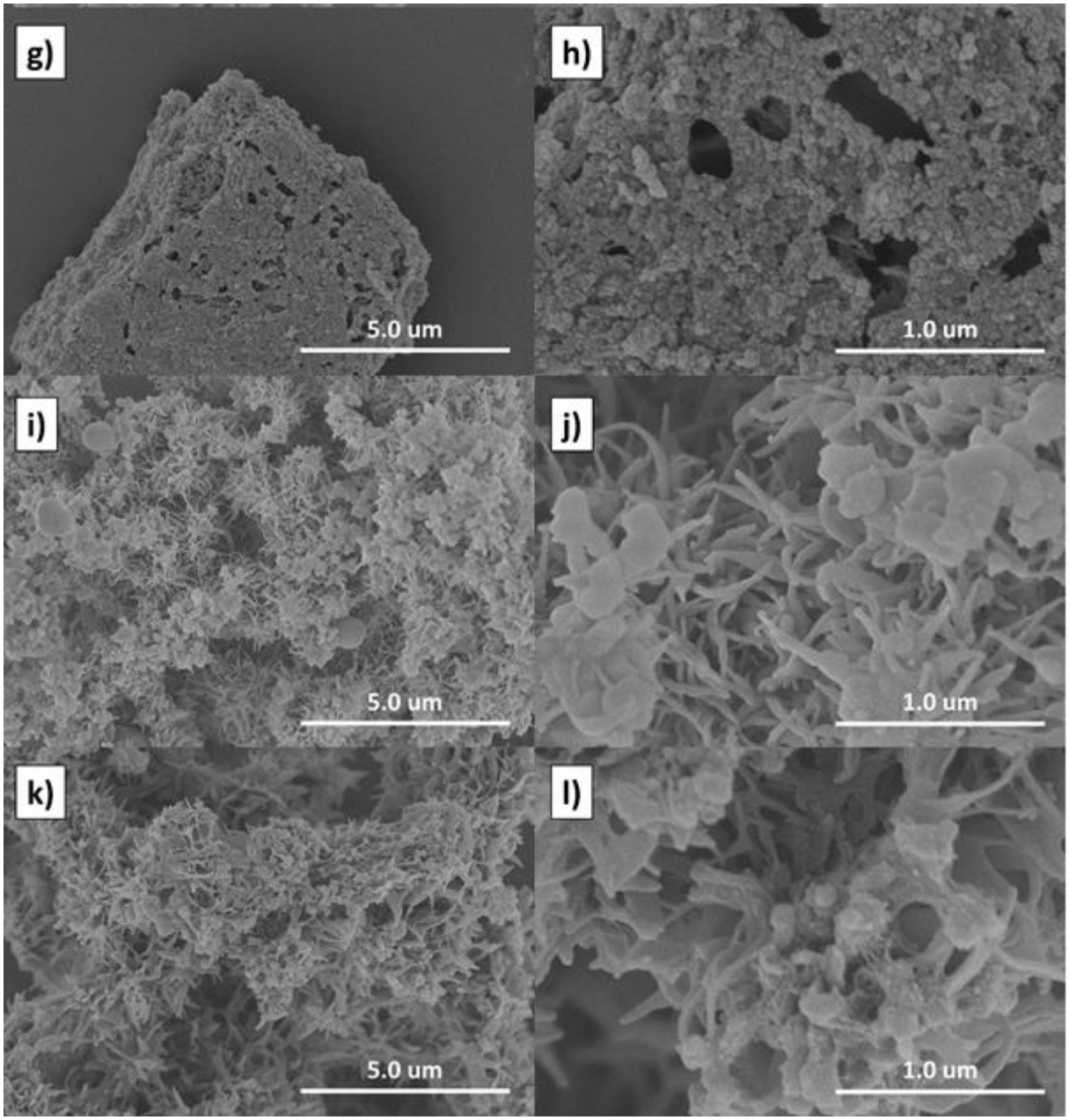

Figure 5.6 FE-SEM images of (g, h) Th800, (i, j) HCP-Py, and (k, l) Py800 at low and high magnifications, respectively.

PXRD patterns of the HCPs and their carbonised products (**Figure 5.7**) exhibit a characteristic peak located at 44°, corresponding to the (101) plane of hexagonal graphite, thus revealing their amorphous nature and low degree of graphitisation.[33]

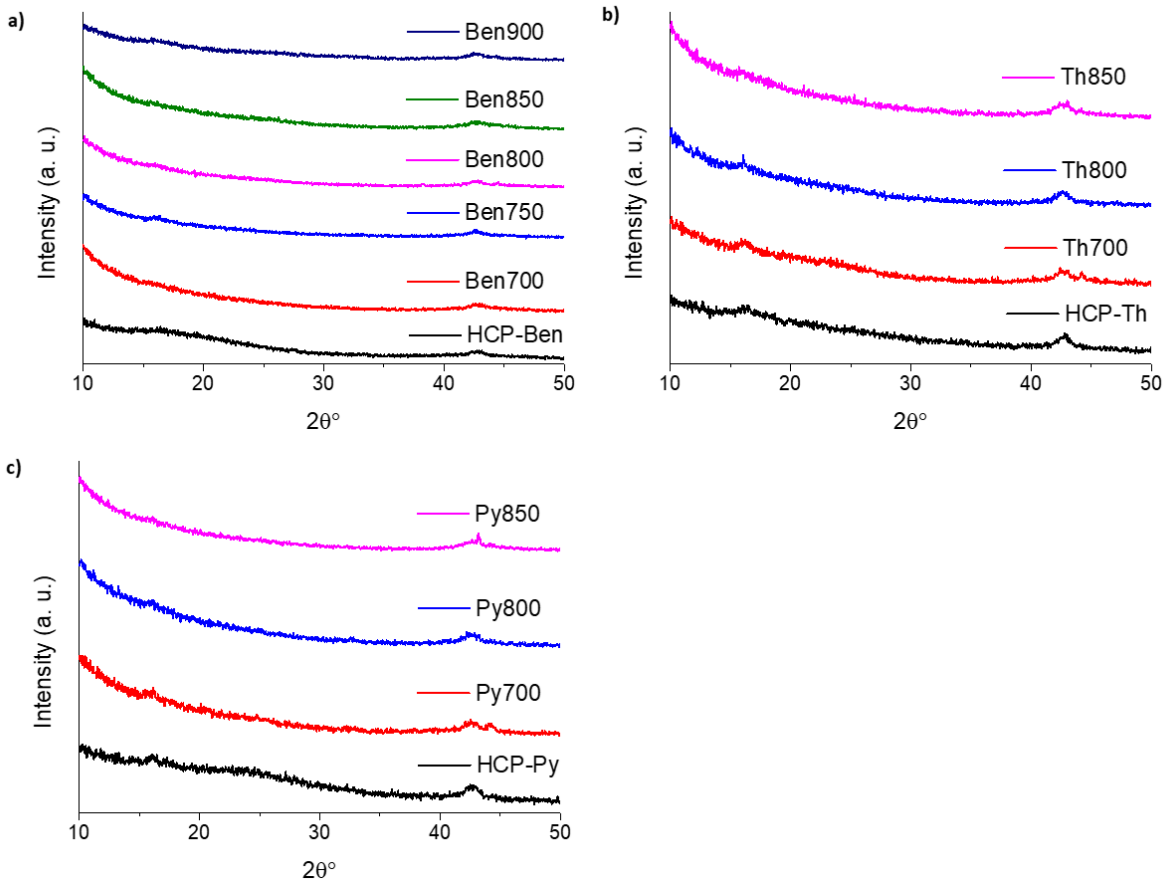

Figure 5.7 PXRD of (a) HCP-Ben and BenΔ, (b) HCP-Th and ThΔ and (c) HCP-Py and PyΔ samples.

The Raman spectra of Ben800, Th800, and Py800 present two first-order Raman bands for *D* at ~1350 cm^{-1} and *G* carbon at ~1590 cm^{-1} attributed to the breathing mode of *k*-point phonons of A_{1g} symmetry and the in-plane stretching motion of symmetric sp^2 C–C bonds respectively (**Figure 5.8**).[24, 34]

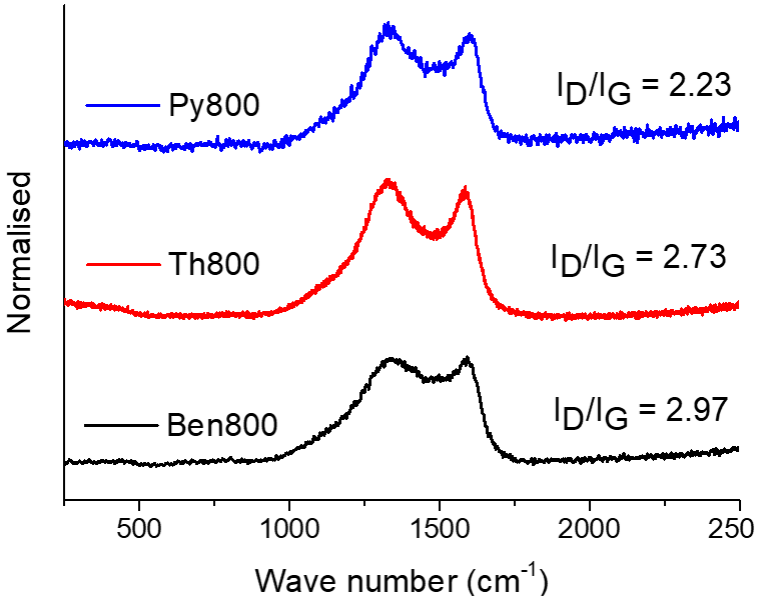

Figure 5.8 Raman spectra of Ben800, Th800, and Py800 with peaks at 1350 cm^{-1} and 1596 cm^{-1} assigned to the *D* band and *G* band respectively.

ICP-OES was also investigated for Ben750, Th850, and Py800 and detected only trace amounts of Fe and K (**Table 5.4**). Due to this, we can exclude its influence on gas absorption measurements.

Table 5.4 Residual metal content from ICP-OES analysis.

Sample	Fe (wt%)	K (wt%)
Ben750	0.020	0.017
Th850	0.058	0.063
Py800	0.022	0.056

The composition of the precursor polymers and the resultant carbonaceous materials were investigated by XPS (**Table 5.5**–**9**, **Figure 5.9**–**13**).

Table 5.5 Elemental ratios from XPS peak areas.

Sample	C 1s (%)	O 1s (%)	N 1s (%)	S 2p (%)	Cl 2p
HCP-Ben	89.5	10.3	0.0	0.0	0.3
HCP-Th	73.1	16.7	0.0	9.7	0.5
HCP-Py	74.4	14.0	10.4	0.0	1.2
Ben800	92.0	8.0	0.0	0.0	0.0
Th800	89.6	6.6	0.0	3.8	0.0
Py800	89.2	9.8	1.0	0.0	0.0

HCP-Ben and its carbonised product, Ben800 contains C and O, while HCP-Th and Th800 also contain S and HCP-Py and Py800 N (**Figure 5.9**).

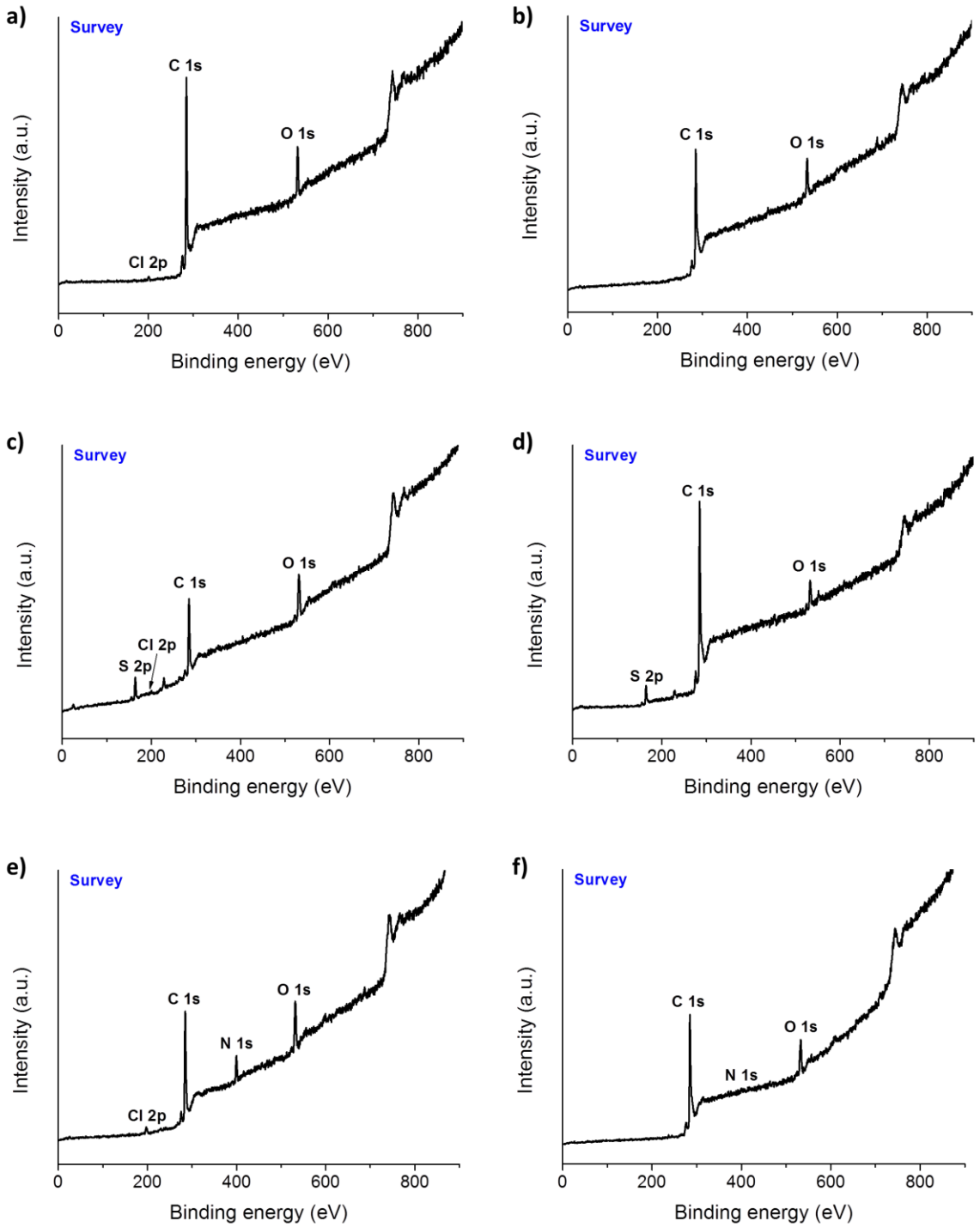

Figure 5.9 XPS survey scan spectras for (a) HCP-Ben, (b) Ben800, (c) HCP-Th, (d) Th800, (e) HCP-Py, and (f) Py800.

Residual Fe was not detected in any of the samples, however trace amounts of Cl remain in the polymer after synthesis (**Table 5.6**), though this appears to be removed in the carbonisation process and was not detected in any of the carbons. HCP-Ben shows a Cl 2p peak at 200.1 eV representative of C-Cl, HCP-Th a peak at 199.7 eV suggest low levels of FeCl, and HCP-Py a peak at 196.8 eV and 200.1 eV for N-Cl and C-Cl, respectively (**Figure 5.10**).[35-37]

Table 5.6 Ratio of chlorine groups from XPS of Cl 2p.

		Amount (%)					
Binding energy (eV)	Assignment	HCP-Ben	Ben800	HCP-Th	Th800	HCP-Py	Py800
196.8	N Chloride[36, 37]	0	0	0	0	78	0
199.7	Fe-Cl[35]	0	0	100	0	0	0
200.1	Organic chloride[36]	100	0	0	0	22	0

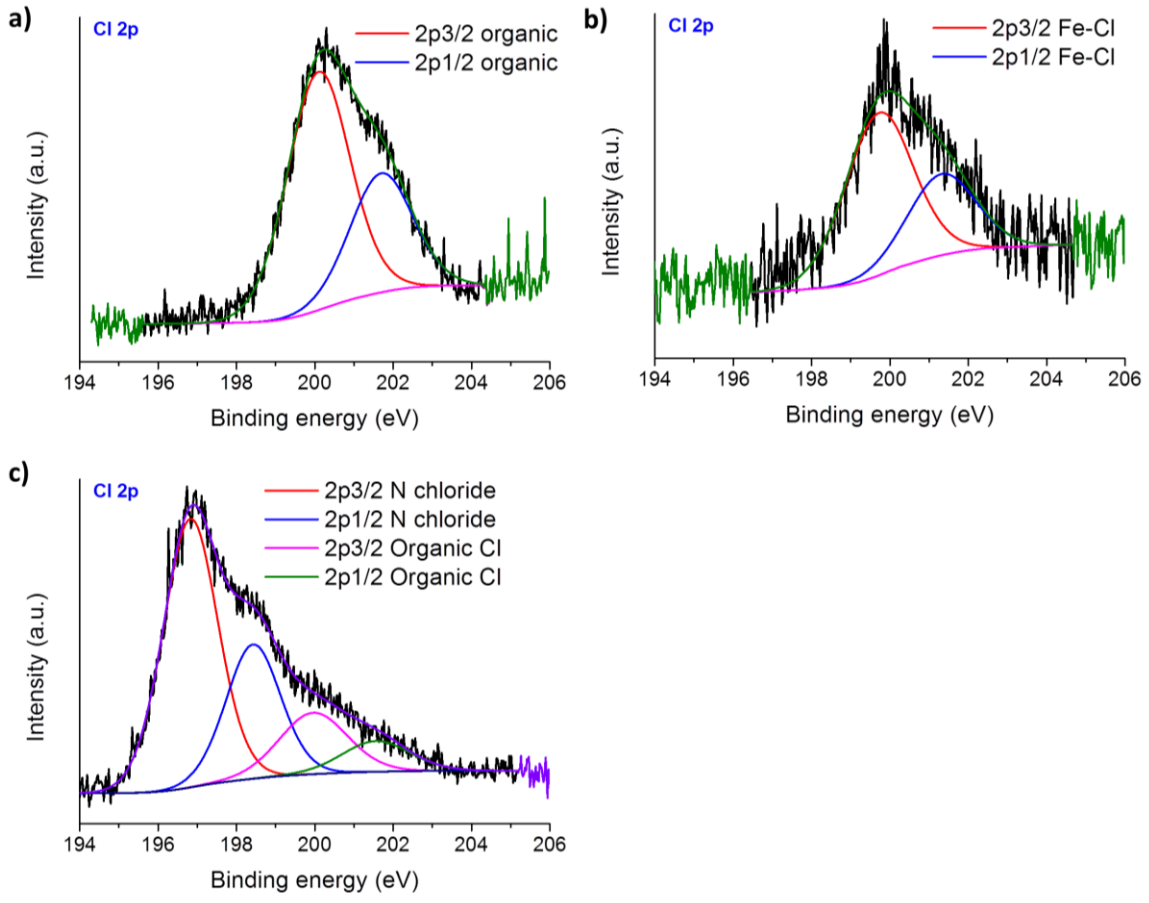

Figure 5.10 XPS Cl 2p core-level spectras for (a) HCP-Ben, (b) HCP-Th, and (c) HCP-Py.

A primary peak was observed for C 1s for all samples at 284.5 eV corresponding to C-C and C-H species, followed by peaks at 286.0 eV, 287.5 eV, 289.2 eV, and 290.9 eV for C-O and C-N, C=O,

carbonates, and π to π* transitions, respectively (**Figure 5.11**).[36, 38, 39] The increase in π to π* after carbonisation is likely due to the material becoming more graphitic in nature.

Table 5.7 Ratio of carbon groups from XPS of C 1s.

		Amount (%)					
Binding energy (eV)	Assignment	HCP-Ben	Ben800	HCP-Th	Th800	HCP-Py	Py800
284.5	C-C, C-H[39]	84	57	77	66	72	55
286.0	C-O, C-N[39, 40]	11	23	17	20	22	27
287.5	C=O[39]	0	8	2	5	4	6
289.2	Carbonate[36]	3	7	4	6	3	8
290.9	π to π transition[38]	3	4	0	3	0	4

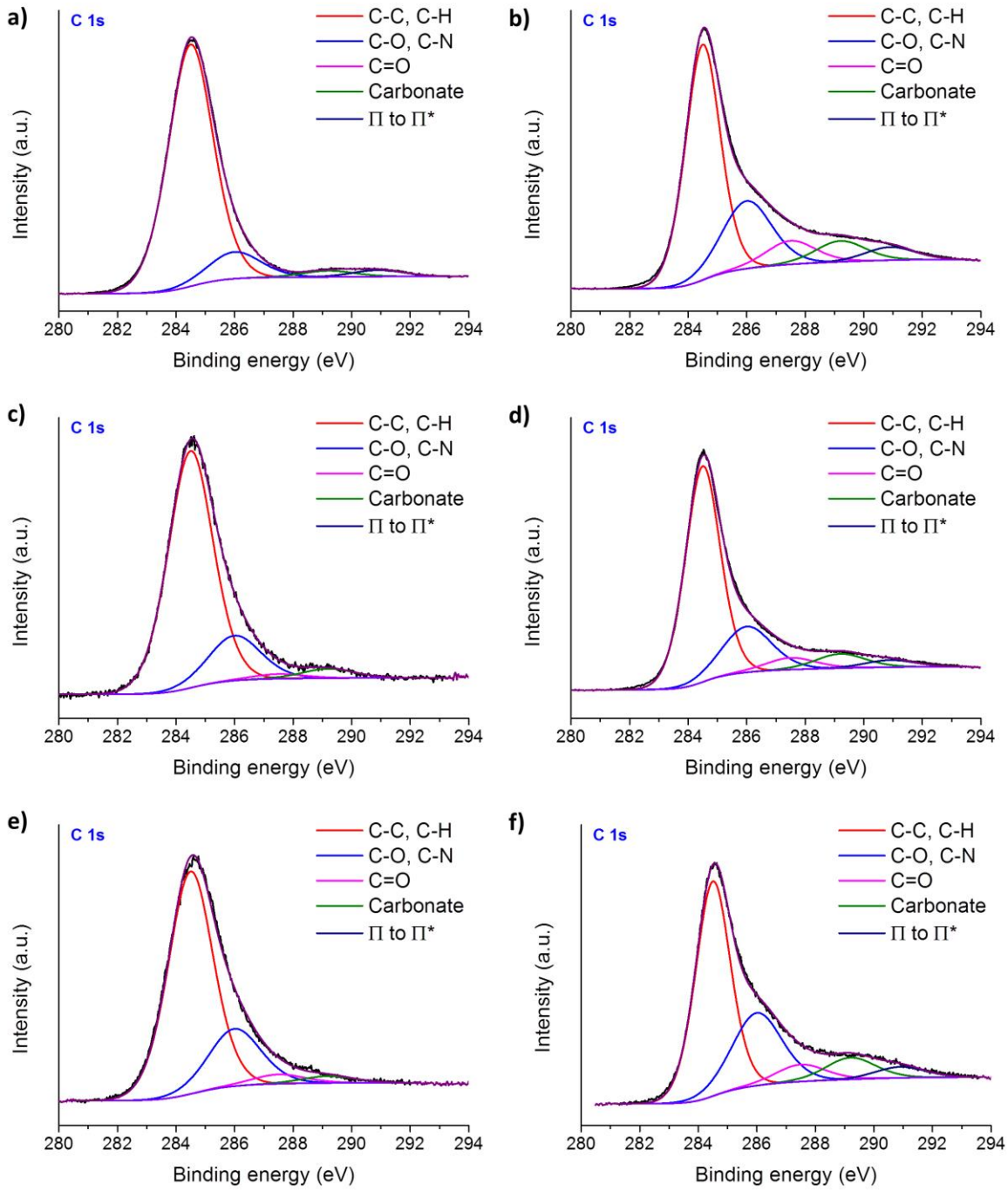

Figure 5.11 XPS C 1s core-level spectras for (a) HCP-Ben, (b) Ben800, (c) HCP-Th, (d) Th800, (e) HCP-Py, and (f) Py800.

Peaks for O 1s were observed at 530.7 eV, 532.1 eV, 533.5 eV, and 535.5 eV which correspond to oxides, carbonates, C=O, and C-O-H, respectively (**Figure 5.12**).[36]

Table 5.8 Ratio of oxygen groups from XPS of O 1s.

		Amount (%)					
Binding energy (eV)	Assignment	HCP-Ben	Ben800	HCP-Th	Th800	HCP-Py	Py800
530.7	Oxide[36]	0	4	22	6	8	22
532.1	Carbonate[36]	56	35	62	51	68	34
533.5	C=O[36]	44	44	17	39	13	49
535.5	C-O-H[36]	0	17	0	4	1	9

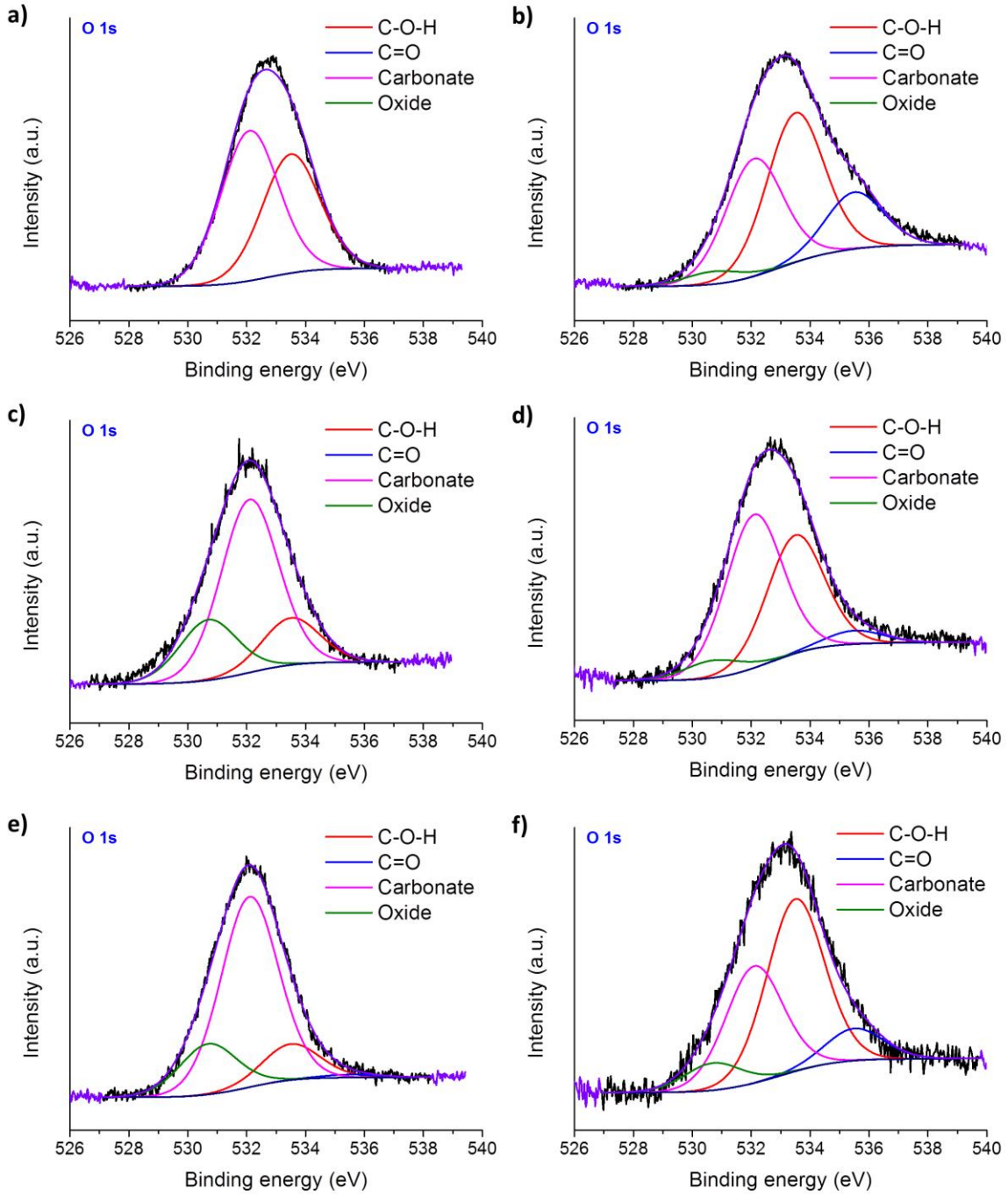

Figure 5.12 XPS O 1s core-level spectras for (a) HCP-Ben, (b) Ben800, (c) HCP-Th, (d) Th800, (e) HCP-Py, and (f) Py800.

XPS of HCP-Th shows S 2p peaks at 163.4 eV and 163.9 eV for C-S-H and C-S-C species respectively (**Figure 5.13**). Upon carbonisation, Th800 loses all C-S-H species as expected, and gives rise to two new species at 165.1 eV and 168.1 eV for R_2-SO and a sulfate/sulfone species, respectively.[36, 41]

Table 5.9 Ratio of sulfur groups from XPS of S 2p.

		Amount (%)					
Binding energy (eV)	Assignment	HCP-Ben	Ben800	HCP-Th	Th800	HCP-Py	Py800
163.4	C-S-H[41]	0	0	83	0	0	0
163.9	C-S-C[41]	0	0	17	80	0	0
165.1	R2-SO[41]	0	0	0	7	0	0
168.1	Sulfate/Sulfone[36]	0	0	0	12	0	0

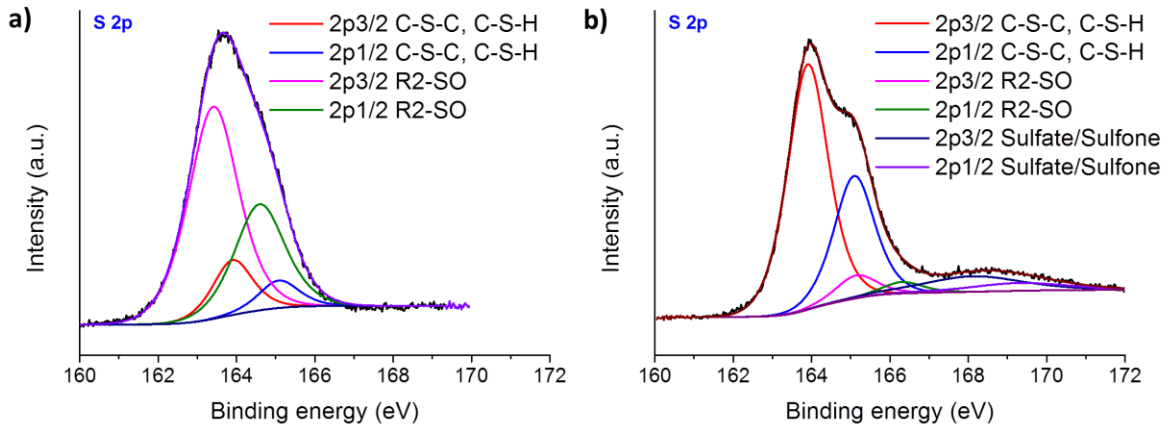

Figure 5.13 XPS S 2p level spectras for (a) HCP-Th and (b) Th800.

The XPS of HCP-Py shown a largely pyrrolic peak at 399.7 eV, followed by peaks at 398.2 eV and 400.9 eV for pyridinic and graphitic-nitride, respectively (**Figure 5.14**).[42-45] Following carbonisation, the graphitic-nitride content increases from 7% in HCP-Py to 19% in to Py800, in line with what we expect (**Table 5.10**).

Table 5.10 Ratio of nitrogen groups from XPS of N 1s.

		Amount (%)					
Binding energy (eV)	Assignment	HCP-Ben	Ben800	HCP-Th	Th800	HCP-Py	Py800
398.2	Pyridinic[42, 44-46]	0	0	0	0	21	34
399.7	Pyrrolic[43-46]	0	0	0	0	72	47
400.9	Graphitic-N[42, 44, 46]	0	0	0	0	7	19

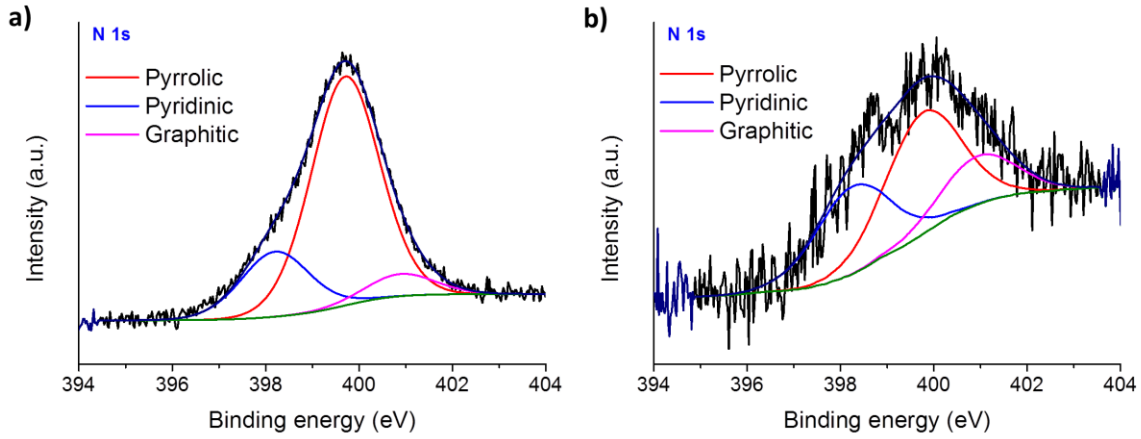

Figure 5.14 XPS N 1s core-level spectras for (a) HCP-Py and (b) Py800.

5.4.3 CO_2 Storage Capabilities of Hypercrosslinked Polymer-Derived Activated Carbons

The CO_2 uptake of each carbonised HCP was tested at room temperature (298 K) and these results are shown in **Figure 5.15a** with the full CO_2 uptake isotherms for the three HCPs and the highest surface area carbons, Ben750, Th850, and Py800, shown in **Figure 5.15b**. **Table 5.11** summarises the amount of CO_2 adsorbed by the materials at a pressure of 1 bar and 10 bar.

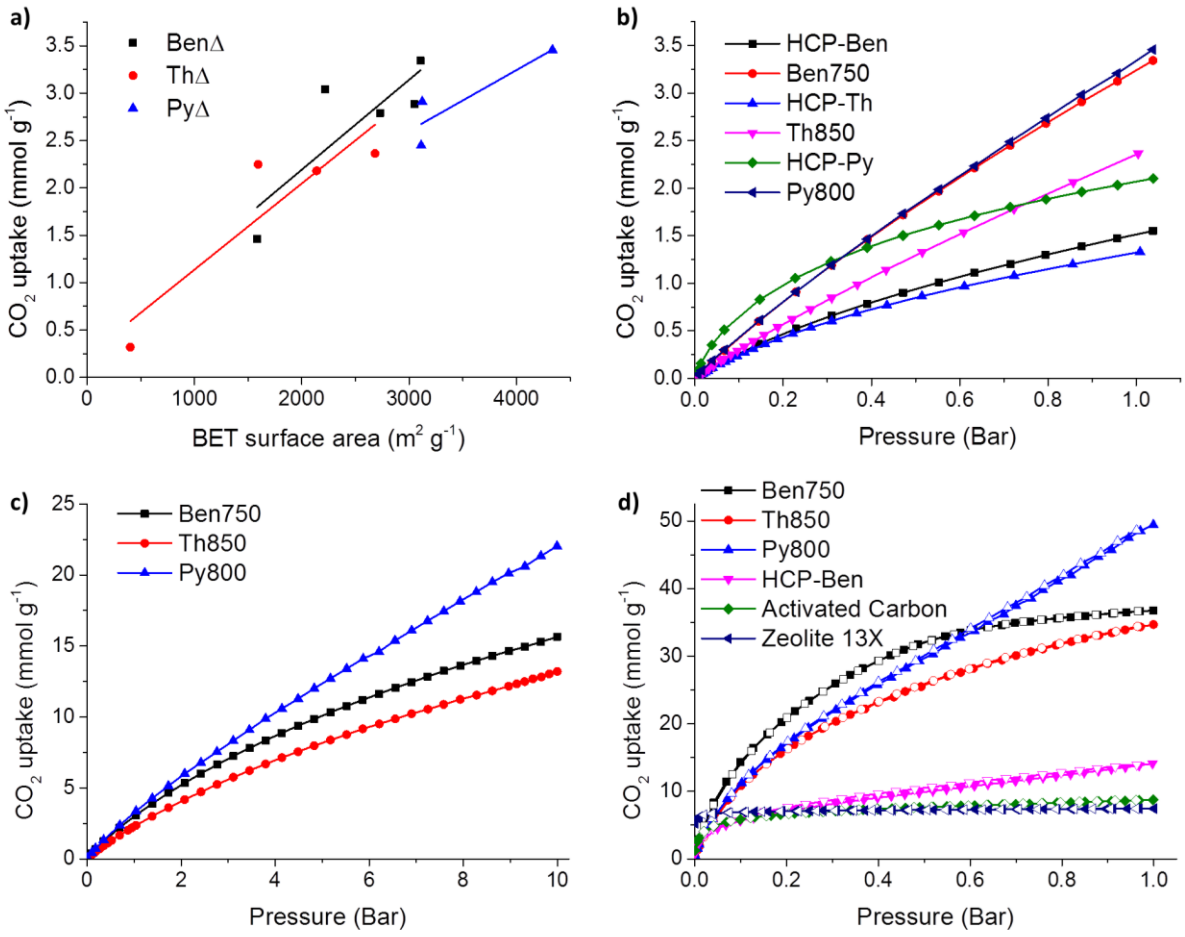

Figure 5.15 (a) Correlation of CO_2 uptake with BET surface area for carbonised HCPs at 1 bar; (b) CO_2 sorption isotherms at 298 K over pressure range 0 to 1 bar; (c) CO_2 sorption isotherms at 298 K over pressure range of 0 to 10 bar; (d) CO_2 adsorption-desorption isotherms at 195 K and 1 bar (the adsorption and desorption branches are labelled with filled and empty symbols, respectively).

Table 5.11 BET surface areas and CO_2 uptake of HCPs and optimised carbons.

		CO_2 uptake[a] (mmol g^{-1})	
Sample	Surface area	1 bar CO_2	10 bar CO_2
HCP-Ben	1382	1.6	-
HCP-Th	484	1.3	-
HCP-Py	322	2.1	-
Ben750	3105	3.3	15.6
Th850	2682	2.4	13.2
Py800	4334	3.5	22.0

[a] CO_2 uptake at 298 K at various pressures.

HCP-Ben adsorbs 1.6 mmol g^{-1} of CO_2 at 1 bar.[29] HCP-Th has a lower uptake of 1.3 mmol g^{-1} of CO_2 at 1 bar, likely due its reduced surface area and the low affinity of S with CO_2. Although the HCP-Py has the lowest surface area of 322 m^2 g^{-1} of the three HCPs, it has the highest CO_2 uptake of 2.1 mmol g^{-1} at 1 bar, possibly due to the presence of the N-containing heterocycles in the polymer, which are known to aid in CO_2 adsorption.[47] The CO_2 uptakes of all HCPs were increased through carbonisation with KOH activation. It was found that the CO_2 uptake is, approximately, linearly proportional to the surface areas of the carbons irrespective of the carbonisation precursor (**Figure 5.15a**). The CO_2 sorption isotherms for the carbonised HCPs all have a similar shape and show a roughly linear uptake of CO_2 with increasing pressure (**Figure 5.15b**) up to 1 bar. The CO_2 adsorption performance of these carbons was also evaluated at up to 10 bar (**Figure 5.15c**). The isotherms shapes are all similar over this pressure range, and none of the materials are close to saturation at 10 bar. Py800, in particular, shows a CO_2 isotherm that is almost linear with pressure. The highest CO_2 uptake at 10 bar was recorded for Py800, which adsorbs up to 22.0 mmol g^{-1} of CO_2 at 10 bar; these are very high CO_2 uptakes in comparison to other leading materials under these conditions, such as MOF-205 (10.9 mmol g^{-1}),[48] PPN-4 (11.6 mmol g^{-1}),[49] Maxsorb (13.5 mmol g^{-1}),[50] CN-2800 (13.9 mmol g^{-1}),[13] and COF-102 (15.5 mmol g^{-1}).[51] Ben750 and Th850 also have high CO_2 uptakes of 15.6 mmol g^{-1} and 13.2 mmol g^{-1}, respectively. A similar isotherm shape was observed previously for swellable HCPs, although the CO_2 uptake was lower (6.8 mmol g^{-1}).[29] HCP-Ben was shown to swell visibly in the presence of CO_2, with the degree of swelling being related directly to the CO_2 density. This could pose design problems for some practical applications; for example, swelling could increase the working back-pressure. Carbonisation removes the flexibility of the HCPs, and observation of Ben750, derived from HCP-Ben, in a high-pressure view cell (40 bar of pure CO_2, 298 K) gave no evidence of any swelling (**Figure 5.16**). Hence, swelling can be eliminated and CO_2 adsorption increased via carbonisation. For example, the CO_2 uptake for HCP-Ben was 15.3 mmol g^{-1} at 40 bar,[29] while Ben750 adsorbs a greater quantity of CO_2 (15.6 mmol g^{-1}) at only 10 bar.

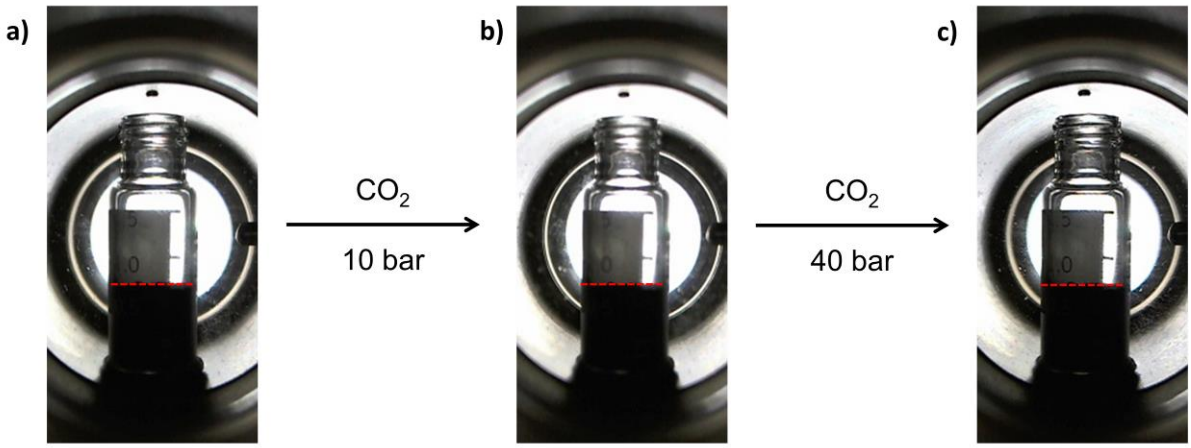

Figure 5.16 Photographs show the absence of swelling of Ben750 in a pure CO_2 atmosphere when the pressure was increased from (a) 1 bar to (b) 10 bar, and finally (c) 40 bar.

Since the CO_2 isotherms were not fully saturated at 10 bar, the adsorption temperature was lowered to investigate the maximum possible CO_2 adsorption capacity for these carbons (195 K / 1 bar). Ben750 and Th850 retains a Type Ib isotherm and Py800 retains a Type IVa isotherm (**Figure 5.15d**). These carbonised materials show remarkable CO_2 uptakes of 36.8 mmol g^{-1}, 34.7 mmol g^{-1}, and 49.4 mmol g^{-1} for Ben750, Th850, and Py800, respectively. These uptake results are far higher than other comparison materials under the same conditions such as the non-carbonised HCP-Ben (14.1 mmol g^{-1}), a commercial activated carbon (8.7 mmol g^{-1}), and zeolite 13X (7.4 mmol g^{-1}).

5.4.4 H_2 Storage Capabilities of Hypercrosslinked Polymer-Derived Activated Carbons

The H_2 uptake capacities of the carbonised HCPs were also investigated at pressures up to 10 bar (**Table 5.12**). For all carbons, irrespective of the carbonisation precursor or temperature, a roughly linear relationship between the apparent BET surface areas and the H_2 uptake was observed in 1 bar at 77.3 K (**Figure 5.17a**).

Table 5.12 BET surface areas and H_2 uptake of HCPs and optimised carbons.

		H_2 uptake[a] (wt%)	
Sample	Surface area	1 bar H_2	10 bar H_2
HCP-Ben	1382	1.1	-
HCP-Th	484	0.9	-
HCP-Py	322	1.0	-
Ben750	3105	3.0	4.0
Th850	2682	2.5	3.7
Py800	4334	3.6	5.6

[a] H_2 uptake at 77.3 K at various pressures.

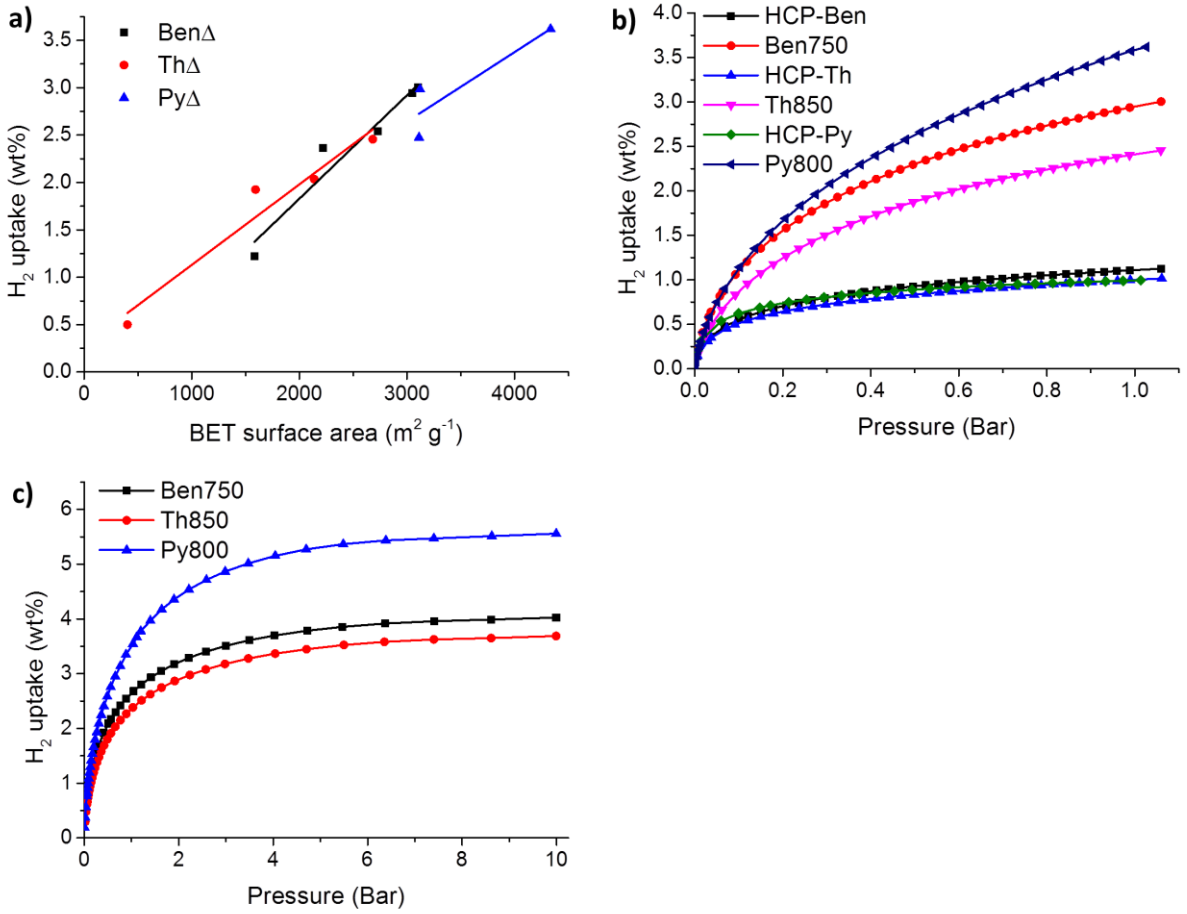

Figure 5.17 (a) Correlation of H_2 uptake with BET surface area for carbonised HCPs at 1 bar; (b) H_2 sorption isotherms at 77.3 K over pressure range 0 to 1 bar and (c) H_2 sorption isotherms at 77.3 K over pressure range of 0 to 10 bar.

Py800, demonstrated the highest H_2 uptake of 3.6 wt% at 1 bar and 77.3 K. The H_2 uptake was significantly improved by carbonisation, with HCP-Ben, HCP-Th, and HCP-Py showing H_2 uptakes of

1.1 wt%, 0.9 wt%, and 1.0 wt%, respectively (**Figure 5.17b**). Ben750, Th850, and Py800 also show high H_2 uptakes of 4.0 wt%, 3.7 wt%, and 5.6 wt%, respectively at 10 bar and 77.3 K, and all materials reach saturation under these conditions (**Figure 5.17c**). These are amongst the highest H_2 uptakes reported to date for any porous carbon materials at 10 bar,[13, 52] and these relatively inexpensive materials outperform zeolite-,[53] carbide-,[54] and MOF-derived carbons.[55] Ben750 and Py800 also outperforms a previously reported carbonised N-rich HCP, synthesised from a non-commercial monomer, which adsorbed 2.6 wt% H_2 at 1 bar and 77.3 K.[56]

5.5 Conclusions and Outlook

Carbonisation of HCPs with KOH activation can be used to generate highly porous carbons that show attractive properties for CO_2 and H_2 adsorption. This method can produce porous carbonaceous materials with surface areas as high as 4334 $m^2 g^{-1}$ using low cost precursors while allowing heteroatoms to be incorporated by the choice of feedstock. The almost limitless choice of aromatic molecules to produce HCPs give a wide potential for further HCP-derived materials to be produced. Thus, it is likely that other HCP precursors might yield even better materials, not only as sorbents but also for other applications such as energy storage, catalysis, and gas separations.

There is much scope to produce even higher surface area materials either by further attempts of HCP activated carbonisations, or by improving the HCP chemistry. Recently, high surface area HCPs were reported through a solvent knitting approach which produces 2-D HCPs with BET surface areas of up to 3002 $m^2 g^{-1}$.[57] Although a high porosity HCP was produced, this polymer only exhibited a CO_2 sorption capacity of 2.57 mmol g^{-1} at 298 K and 1 bar (*c.f.*, Ben750 with a BET of 3105 mmol g^{-1} and CO_2 sorption of 3.3 mmol g^{-1}). Thus, further syntheses need to be attempted for a pristine HCP to show very high gas storage capabilities which can outperform carbon. A direct relationship on how the choice of carbonisation precursor affects the result porosity of the activated carbon has also yet to be reported. This could be performed by further systematic syntheses and carbonisations, and then new design rules developed based upon these results.

5.6 References

[1] S. Subramoney, *Adv. Mater.* **1998**, *10*, 1157.

[2] H. W. Kim, H. W. Yoon, S.-M. Yoon, B. M. Yoo, B. K. Ahn, Y. H. Cho, H. J. Shin, H. Yang, U. Paik, S. Kwon, J.-Y. Choi, H. B. Park, *Science* **2013**, *342*, 91; A. F. Ismail, L. I. B. David, *J. Membr. Sci*. **2001**, *193*, 1.

[3] K. Konieczny, G. Klomfas, *Desalination* **2002**, *147*, 109; M. A. Shannon, P. W. Bohn, M. Elimelech, J. G. Georgiadis, B. J. Marinas, A. M. Mayes, *Nature* **2008**, *452*, 301.

[4] Y. Yang, K. Chiang, N. Burke, *Catal. Today* **2011**, *178*, 197; J.-S. Yu, S. Kang, S. B. Yoon, G. Chai, *J. Am. Chem. Soc*. **2002**, *124*, 9382.

[5] D. D. L. Chung, *Carbon* **2001**, *39*, 279; M. H. Al-Saleh, U. Sundararaj, *Carbon* **2009**, *47*, 1738.

[6] A. D. Roberts, X. Li, H. Zhang, *Chem. Soc. Rev.* **2014**, *43*, 4341.

[7] L. Qie, W. Chen, H. Xu, X. Xiong, Y. Jiang, F. Zou, X. Hu, Y. Xin, Z. Zhang, Y. Huang, *Energy Environ. Sci.* **2013**, *6*, 2497.

[8] B. Fang, J. H. Kim, M. Kim, J.-S. Yu, *Chem. Mater.* **2009**, *21*, 789.

[9] A. Stein, Z. Wang, M. A. Fierke, *Adv. Mater.* **2009**, *21*, 265.

[10] M. Sevilla, R. Mokaya, *Energy Environ. Sci.* **2014**, *7*, 1250; J. Wang, S. Kaskel, *J. Mater. Chem.* **2012**, *22*, 23710; C. Bouchelta, M. S. Medjram, O. Bertrand, J.-P. Bellat, *J. Anal. Appl. Pyrolysis* **2008**, *82*, 70.

[11] B. Adeniran, R. Mokaya, *Nano Energy* 2015, *16*, 173; Y. Yuan, I. Cabasso, H. Liu, J. *Phys. Chem. B* **2008**, *112*, 14364.

[12] A. Silvestre-Albero, J. Silvestre-Albero, M. Martínez-Escandell, F. Rodríguez-Reinoso, *Ind. Eng. Chem. Res.* **2014**, *53*, 15398.

[13] B. Adeniran, R. Mokaya, *J. Mater. Chem. A* **2015**, *3*, 5148.

[14] Y. Zhu, S. Murali, M. D. Stoller, K. J. Ganesh, W. Cai, P. J. Ferreira, A. Pirkle, R. M. Wallace, K. A. Cychosz, M. Thommes, D. Su, E. A. Stach, R. S. Ruoff, *Science* **2011**, *332*, 1537.

[15] K. S. Park, Z. Ni, A. P. Côté, J. Y. Choi, R. Huang, F. J. Uribe-Romo, H. K. Chae, M. O'Keeffe, O. M. Yaghi, *Proc. Natl. Acad. Sci.* **2006**, *103*, 10186.

[16] H.-C. Zhou, S. Kitagawa, *Chem. Soc. Rev.* **2014**, *43*, 5415.

[17] T. Ben, H. Ren, S. Ma, D. Cao, J. Lan, X. Jing, W. Wang, J. Xu, F. Deng, J. M. Simmons, S. Qiu, G. Zhu, *Angew. Chem., Int. Ed.* **2009**, *48*, 9457.

[18] A. I. Cooper, *Adv. Mater.* **2009**, *21*, 1291.

[19] C. D. Wood, B. Tan, A. Trewin, H. Niu, D. Bradshaw, M. J. Rosseinsky, Y. Z. Khimyak, N. L. Campbell, R. Kirk, E. Stöckel, A. I. Cooper, *Chem. Mater.* **2007**, *19*, 2034.

[20] W. Chaikittisilp, M. Hu, H. Wang, H.-S. Huang, T. Fujita, K. C. W. Wu, L.-C. Chen, Y. Yamauchi, K. Ariga, *Chem. Commun.* **2012**, *48*, 7259.

[21] S. Zhao, H. Yin, L. Du, L. He, K. Zhao, L. Chang, G. Yin, H. Zhao, S. Liu, Z. Tang, *ACS Nano* **2014**, *8*, 12660; K. Xi, S. Cao, X. Peng, C. Ducati, R. Vasant Kumar, A. K. Cheetham, *Chem. Commun.* **2013**, *49*, 2192.

[22] T. Ben, Y. Li, L. Zhu, D. Zhang, D. Cao, Z. Xiang, X. Yao, S. Qiu, *Energy Environ. Sci.* **2012**, *5*, 8370; Y. Li, T. Ben, B. Zhang, Y. Fu, S. Qiu, *Sci. Rep*. **2013**, *3*, 2420.

[23] K. Yuan, P. Guo-Wang, T. Hu, L. Shi, R. Zeng, M. Forster, T. Pichler, Y. Chen, U. Scherf, *Chem. Mater*. **2015**, *27*, 7403; M. E. Bhosale, R. Illathvalappil, S. Kurungot, K. Krishnamoorthy, *Chem. Commun.* **2016**, *52*, 316.

[24] J.-S. M. Lee, T.-H. Wu, B. M. Alston, M. E. Briggs, T. Hasell, C.-C. Hu, A. I. Cooper, *J. Mater. Chem. A* **2016**, *4*, 7665.

[25] L. D. Asnin, V. A. Davankov, A. V. Pastukhov, Y. A. Shchurov, *Russ. Chem. Bull*. **2009**, *58*, 2217; K. Song, Z. Zou, D. Wang, B. Tan, J. Wang, J. Chen, T. Li, *J. Phys. Chem. C* **2016**, *120*, 2187.

[26] W. Li, A. Zhang, H. Gao, M. Chen, A. Liu, H. Bai, L. Li, *Chem. Commun.* **2016**, *52*, 2780; V. A. Davankov, M. P. Tsyurupa, *React. Polym.* **1990**, *13*, 27; N. A. Peppas, K. P. Staller, *Polym. Bull.* **1982**, *8*, 233; M. P. Tsyurupa, V. A. Davankov, *React. Funct. Polym.* **2002**, *53*, 193.

[27] B. Li, R. Gong, W. Wang, X. Huang, W. Zhang, H. Li, C. Hu, B. Tan, *Macromolecules* **2011**, *44*, 2410.

[28] R. Dawson, T. Ratvijitvech, M. Corker, A. Laybourn, Y. Z. Khimyak, A. I. Cooper, D. J. Adams, *Polym. Chem.* **2012**, *3*, 2034.

[29] R. T. Woodward, L. A. Stevens, R. Dawson, M. Vijayaraghavan, T. Hasell, I. P. Silverwood, A. V. Ewing, T. Ratvijitvech, J. D. Exley, S. Y. Chong, F. Blanc, D. J. Adams, S. G. Kazarian, C. E. Snape, T. C. Drage, A. I. Cooper, *J. Am. Chem. Soc*. **2014**, *136*, 9028.

[30] M. Thommes, K. Kaneko, A. V. Neimark, J. P. Olivier, F. Rodriguez-Reinoso, J. Rouquerol, K. S. W. Sing, *Pure Appl. Chem.* **2015**, *87*, 1051.

[31] V. A. Davankov, M. P. Tsyurupa, *Hypercrosslinked Polymeric Networks and Adsorbing Materials: Synthesis, Properties, Structure, and Applications*, Elsevier, **2011**.

[32] M. Jordá-Beneyto, F. Suárez-García, D. Lozano-Castelló, D. Cazorla-Amorós, A. Linares-Solano, *Carbon* **2007**, *45*, 293.

[33] J. Han, G. Xu, H. Dou, D. R. MacFarlane, *Chem. Eur. J* **2015**, *21*, 2310.

[34] N. J. Bell, Y. H. Ng, A. Du, H. Coster, S. C. Smith, R. Amal, *J. Phys. Chem. C* **2011**, *115*, 6004.

[35] A. P. Grosvenor, B. A. Kobe, M. C. Biesinger, N. S. McIntyre, *Surf. Interface Anal.* **2004**, *36*, 1564.

[36] J. F. Moulder, J. Chastain, *Handbook of X-ray Photoelectron Spectroscopy: A Reference Book of Standard Spectra for Identification and Interpretation of XPS Data*, Physical Electronics, **1995**.

[37] K. L. Tan, B. T. G. Tan, E. T. Kang, K. G. Neoh, *Phys. Rev. B* **1989**, *39*, 8070.

[38] A. Mezzi, S. Kaciulis, *Surf. Interface Anal.* **2010**, *42*, 1082.

[39] B. P. Payne, M. C. Biesinger, N. S. McIntyre, *J. Electron Spectrosc. Relat. Phenom.* **2011**, *184*, 29.

[40] R. J. J. Jansen, H. van Bekkum, *Carbon* **1995**, *33*, 1021.

[41] B. J. Lindberg, K. Hamrin, G. Johansson, U. Gelius, A. Fahlman, C. Nordling, K. Siegbahn, *Phys. Scr.* **1970**, *1*, 286.

[42] T. Kondo, D. Guo, T. Shikano, T. Suzuki, M. Sakurai, S. Okada, J. Nakamura, *Sci. Rep.* **2015**, *5*, 16412.

[43] S. Kundu, W. Xia, W. Busser, M. Becker, D. A. Schmidt, M. Havenith, M. Muhler, *Phys. Chem. Chem. Phys.* **2010**, *12*, 4351.

[44] A. Muthukrishnan, Y. Nabae, T. Hayakawa, T. Okajima, T. Ohsaka, *Catal. Sci. Technol.* **2015**, *5*, 475.

[45] L. R. Radovic, I. F. Silva, J. I. Ume, J. A. Menéndez, C. A. L. Y. Leon, A. W. Scaroni, *Carbon* **1997**, *35*, 1339.

[46] H. Wang, T. Maiyalagan, X. Wang, *ACS Catal.* **2012**, *2*, 781.

[47] M. G. Plaza, C. Pevida, A. Arenillas, F. Rubiera, J. J. Pis, *Fuel* **2007**, 86, 2204; G.-P. Hao, W.-C. Li, D. Qian, A.-H. Lu, *Adv. Mater.* **2010**, *22*, 853.

[48] H. Furukawa, N. Ko, Y. B. Go, N. Aratani, S. B. Choi, E. Choi, A. Ö. Yazaydin, R. Q. Snurr, M. O'Keeffe, J. Kim, O. M. Yaghi, *Science* **2010**, *329*, 424.

[49] D. Yuan, W. Lu, D. Zhao, H.-C. Zhou, *Adv. Mater.* **2011**, *23*, 3723.

[50] S. Himeno, T. Komatsu, S. Fujita, *J. Chem. Eng. Data* **2005**, *50*, 369.

[51] H. Furukawa, O. M. Yaghi, *J. Am. Chem. Soc.* **2009**, *131*, 8875.

[52] H. Wang, Q. Gao, J. Hu, *J. Am. Chem. Soc.* **2009**, *131*, 7016; Z. Weigang, F. Vanessa, E. Aylon, M. T. Izquierdo, C. Alain, *J. Phys. Conf. Ser.* **2013**, *416*, 012024.

[53] N. Alam, R. Mokaya, *Energy Environ. Sci.* **2010**, *3*, 1773; H. Nishihara, P.-X. Hou, L.-X. Li, M. Ito, M. Uchiyama, T. Kaburagi, A. Ikura, J. Katamura, T. Kawarada, K. Mizuuchi, T. Kyotani, *J. Phys. Chem. C* **2009**, *113*, 3189; M. Armandi, D. Drago, M. Pagani, B. Bonelli, M. Santarelli, *Int. J. Hydrogen Energy* **2012**, *37*, 1292.

[54] M. Sevilla, R. Foulston, R. Mokaya, *Energy Environ. Sci.* **2010**, *3*, 223; Y. Gogotsi, C. Portet, S. Osswald, J. M. Simmons, T. Yildirim, G. Laudisio, J. E. Fischer, *Int. J. Hydrogen Energy* **2009**, *34*, 6314.

[55] H. Jiang, Y. Feng, M. Chen, Y. Wang, *Int. J. Hydrogen Energy* **2013**, *38*, 10950; W. Wei, Z. Xia, Q. Wei, G. Xie, S. Chen, C. Qiao, G. Zhang, C. Zhou, *Microporous Mesoporous Mater.* **2013**, *165*, 20.

[56] X. Yang, M. Yu, Y. Zhao, C. Zhang, X. Wang, J.-X. Jiang, *J. Mater. Chem. A* **2014**, *2*, 15139.

[57] S. Wang, C. Zhang, Y. Shu, S. Jiang, Q. Xia, L. Chen, S. Jin, I. Hussain, A. I. Cooper, B. Tan, *Sci. Adv.* **2017**, *3*, 3.

Chapter 6

Inverse Vulcanised Polymer-Derived Carbons for Heavy Metal Capture

Some of the contents in this chapter are taken from **Paper V**.

J.-S. M. Lee, D. J. Parker, A. I. Cooper, T. Hasell, "High Surface Area Sulfur-Doped Microporous Carbons from Inverse Vulcanised Polymers". *J. Mater. Chem. A* **2017**, *5*, 18603–18609.

6.1 Background and Context

Microporous materials have many important potential applications, such as to store H_2 as a greener fuel, CO_2 capture, to prevent global warming, and the filtration of toxic compounds from waste water and gas streams to prevent environmental pollution. However, to be relevant to these applications any potential material must be not only effective, but also low enough in cost to allow large scale production and use. However, many proposed microporous materials, such as MOFs or COFs, suffer from a high cost of production due to the cost of the starting materials — often comprising costly metals or rare organic molecules (*e.g.*, hexahydroxytriphenylene used in COF-5 costs 75,600 $/kg, TCI Chemicals), which require complex synthesis. Mercury is one of the most toxic metals that can be found in industrial waste water, which is a significant and current global health concern, especially in lower and middle-income countries. Inverse vulcanised polymers, which are high in sulfur, can be produced very cheaply from waste by-products. By engineering the carbonisation, high surface area and high sulfur-doped materials can be obtained which show excellent uptakes of both H_2 and CO_2, outperforming many more expensive commercial and academic materials. Furthermore, sulfur incorporated into these materials, itself a by-product of the petrochemicals industry, affords a high affinity for heavy metals such as mercury or gold. Gold extraction by hydrometallurgy is a widely used practice to recover gold from natural ore,[1] or increasingly from electrical waste.[2] In this method lixiviants are used to solubilise the gold in an aqueous phase before it is recovered onto a solid support, commonly activated carbon.[3] The high adsorption of metals were shown not to be due to porosity alone but benefitted by the high sulfur functionality which plays a key factor.

6.2 Introduction

Coal is the most abundant fossil fuel on the planet, responsible for ~41% of the world's electricity needs and 29% of the total world energy use.[4] There is currently ~900 billion metric tonnes of coal reserves which is sufficient to meet the current energy demands for the next 200 years.[5] In addition to the serious global concerns of the release of greenhouse gases during coal combustion, the process also releases volatile trace metals such as mercury (Hg), selenium, and arsenic, with worldwide emissions of Hg reaching 5000 tonnes annually.[6] Studies report that the Hg content varies between 0.01 to 1.5 g per tonne of coal,[7] with the global coal consumption in 2016 estimated at 5331 million tonnes.[8] The toxicity of coal burning emissions poses a global health threat. Mercury is considered to be one of the most toxic metals found in the environment. It is relatively water soluble and can accumulate in rivers and lakes, where it can be readily converted by microbes into methylmercury, a neurotoxin that bioaccumulates in fishes and animals.[9] Exposure to mercury has serious health implications in humans,

such as changes in the central nervous system, irritability, fatigue, behavioural changes, tremors, headaches, hearing and cognitive loss, dysarthria, incoordination, hallucinations, and death.[10]

With the high levels of global coal consumption, it is of great importance to improve methods which can reduce and minimise the levels of toxic waste metals released. There are a number of methods for the removal of heavy metal ions:[11]

- **Membrane filtration** utilises a permeable membrane, generally with a pore size of 5–20 nm, for separations.[12] In addition to heavy metals, the method can also remove suspended solids and organic compounds.
- **Ion exchange** attracts soluble ions from the liquid phase to the solid phase. The method is cost-effective and is known for treating water with low metal concentrations.[13]
- **Electrolysis** passes an electrical current through a metal-containing electrolyte solution in order to precipitate the metal ions as hydroxides.[14]
- **Electrodialysis** is a membrane separation method where ionised species in water is passed through an ion exchange membrane via application of an electric potential. When ions are passed through the cell, the anions attract towards the anode and the cations toward the cathode, whilst passing through the anion exchange and cation exchange membranes, respectively.[15] However, the membranes must be readily replaced and commonly corrode.[16]
- **Chemical precipitation** involves producing insoluble precipitates of heavy metals as hydroxide, sulfide, carbonate, and phosphate. The precipitants which form coagulates and flocculates which increases their particle size and can be removed as sludge.[17]
- **Absorption on sorbents** is a mass transfer process of ions from water to a solid phase and becomes bound by physical and/or chemical interactions.[18] Various low-cost absorbents derived from industrial by-products, natural materials, and modified biopolymers has been utilised for waste water treatment.[19]

Sorbent materials are advantageous as not only can they capture waste directly from the environment, but also prevent the release of toxic waste products. Activated carbon is known as an effective absorber of mercury ions from flue gas streams, due to its high surface areas, microporous structure, and small levels of mesopores.[20] The low-cost of activated carbons are advantageous, however, they generally suffer from low capacities and weak binding affinities for mercury. Heteroatom doping of carbon materials has been suggested as the “Next Big Thing” in materials science and has gained a great deal of attention in the last few years.[21] While carbonaceous materials that contain hydrogen, oxygen, and nitrogen elements have been heavily studied, sulfur has been explored to a much lesser extent. The properties of porous carbons are influenced strongly by their surface functionalities. S-doped

carbonaceous materials have most commonly been produced by melt diffusion of sulfur into porous carbon materials,[22] but this approach requires an additional synthetic step and commonly reduces the porosity of the material. It would be more efficient to use a carbonisation precursor with a high initial S-content to produce a porous, S-doped carbon directly. It is known that selective capture of mercury can be enhanced by incorporation of sulfur onto the surface of the porous material,[23] though the adsorption capacities are still currently relatively low.

Recently, MOFs have been explored for their potential in mercury removal due to their high surface areas,[24, 25] though they usually suffer from poor stability in water or to a wide pH range.[25] Traditional POP networks have an advantage over MOFs in which they are much more stable in water, in addition to being easily functionalised with sulfur to target mercury capture. This route has shown exceptional uptake capacities for Hg(II) of up to 1000 mg g^{-1},[26] however, traditional POP networks can be considered expensive for waste water treatment application.

Although sulfur has many applications, supply greatly outweighs demand, thus creating large unwanted stockpiles and a global issue in the petrochemical industry known as the "excess sulfur problem" (**Figure 6.1**).[27]

Figure 6.1 Example of excess sulfur produced from hydrodesulfurisation in the petroleum refining processes. The large abundance of sulfur opens important opportunities for utilisation of this inexpensive by-product.

Sulfur is a waste by-product from the purification of crude oil and gas reserves, which produces ~70 million tons of elemental sulfur annually. This quantity will likely increase as demand for energy pushes the need to use more contaminated petroleum feed-stocks. There has been interest in the use of

this un-tapped, low-cost sulfur into useful materials for applications, with the most significant advancement being a recent development known as "inverse vulcanisation".[27-29] The process enables the production of high-sulfur containing polymers by the ring-opening of S_8 — a cyclic ring of 8 sulfur atoms, with the addition of a small organic molecule crosslinker, typically a diene (**Scheme 6.1**).[28]

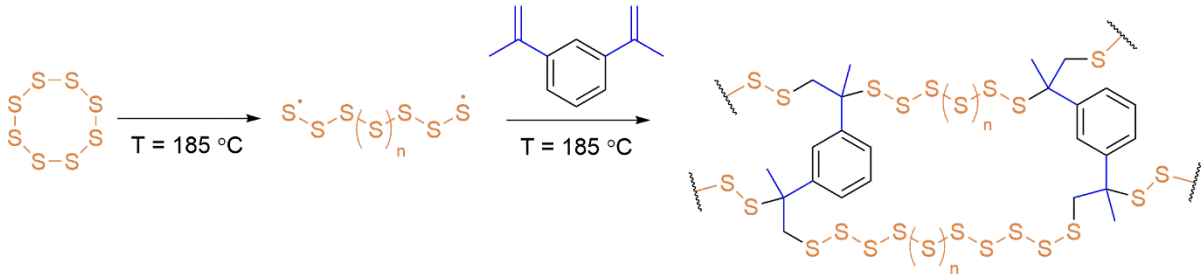

Scheme 6.1 Inverse vulcanisation polymerisation of S_8 with 1,3-diisopropenylbenzene (DIB) to produce poly(S-DIB) copolymer. DIB trades at ~225,000 $ per tonne.

This crosslinks the sulfur chains and stabilises the product against de-polymerisation. This is because although high molecular weight polymeric sulfur is formed via thermal ring-opening polymerisation, the diradical species present can result in depolymerisation back to monomeric and oligomeric sulfur allotropes. The conversion of sulfur into useful polymers and related materials is an advance in waste valorisation.[30] Therefore, co-polymerisation of sulfur with renewable monomers represents an additional contribution to sustainability; in addition these reactions are often solvent free and benefit from full atom economy, further supplementing their Green Chemistry credentials.[30] Suggested applications for these high sulfur polymers are diverse.[27, 31] Optical applications arise from the high refractive index and IR transparency of the materials.[32] Polymeric electrodes can be produced from inverse vulcanisation to give Li-S batteries with enhanced capacities and lifetimes.[33] These sulfur polymers have also shown potential for mercury capture,[34] which is enhanced if they are made macroporous.[35]

To date, only two reports have described microporous materials synthesised directly from elemental sulfur. The first involved inverse vulcanisation of sulfur with either 1,3-diisopropenyl benzene (DIB) or limonene, followed by direct carbonisation.[36] The second route involved the reaction of aromatic methyl and amine-substituted monomers with elemental sulfur directly at elevated temperatures to make benzothiazole polymers.[37] Both of these routes gave materials with narrow pore size distributions, which can be beneficial in gas separations, but also with relatively low BET surface areas: 537 $m^2\ g^{-1}$ (by nitrogen) as the highest for carbonised S-DIB co-polymer, and 751 $m^2\ g^{-1}$ for the benzothiazole polymers (by argon). The organic precursors for the S-DIB and benzothiazole polymers are also considerably more expensive in comparison with sulfur.

Recently, the use of a low-cost bulk industrial feed-stock, dicyclopentadiene (DCPD) was reported as a crosslinker for the inverse vulcanisation of sulfur.[38] DCPD is readily available since it is co-produced in large quantities as a by-product in the steam cracking of naphtha and gas oils to ethylene. In this chapter, it was shown that S-DCPD copolymers can be used to produce low cost S-doped microporous carbons with much higher surface areas (>2200 m^2 g^{-1}) than previously reported. The combination of high surface area and S-functionality allowed not only high H_2 and CO_2 uptakes, but selective uptakes for Hg, in addition to Au.

6.3 Experimental

6.3.1 Chemical Reagents

Dicyclopentadiene (DCPD) was purchased from Tokyo Chemicals Industry. Sulfur, potassium hydroxide, chloroauric acid, mercury(II) chloride, copper(II) nitrate hydrate, cobalt(II) nitrate hexahydrate, nickel(II) nitrate hexahydrate, chromium(III) nitrate nonahydrate, manganese(II) chloride tetrahydrate, iron(III) chloride hexahydrate, and activated carbon (DARCO® FGL) were purchased from Sigma Aldrich. High purity nitrogen was purchased from BOC. All chemical precursors were used as received without any further purification. DI water was used in filtration and washing steps of the resultant materials.

6.3.2 Synthesis

Preparation of S-DCPD

Polymerisation was performed as previously reported.[38] Briefly: Sulfur (10 g) was heated at 160 °C in a glass vessel with stirring, until molten, before adding DCPD (10 g). Heating and stirring were maintained until the reaction mixture became a homogeneous phase (typically ~20–40 minutes) before decanting into a silicone mould and curing at 140 °C for 12 h.

Synthesis of Directly Carbonised Materials

In a typical procedure, S-DCPD (300 mg) was homogeneously ground using a pestle and mortar. The polymer was placed in a ceramic boat and inserted into a tube furnace. The furnace was purged with N_2 at room temperature for 30 min, heated to the specified temperature at a rate of 5 °C min^{-1}, held at the set temperature for the associated time, and finally cooled to room temperature. The material was used without further purification.

Synthesis of KOH Activated Carbonised Materials

In a typical procedure, S-DCPD (1.0 g) and the associated amount of KOH was homogeneously ground using a pestle and mortar. The mixture was placed in a ceramic boat and inserted within a tube furnace. The furnace was purged with N_2 at room temperature for 30 min, heated to the specified temperature at a rate of 5 °C min^{-1}, held at the set temperature for 2 h, and finally cooled to room temperature. The residue was washed thoroughly with deionised water until the filtrate attained pH 7. The resultant carbons were dried under vacuum for 1 day at 70 °C

6.3.3 Metal Ion Uptake Studies

Mercury and Gold Ion Uptakes

A 1000 ppm solution (250 mL) was made up from a stock solution of chloroauric acid ($HAuCl_4$) or mercury(II) chloride ($HgCl_2$) and DI water, with the pH adjusted to 3–4 with the addition of HCl. For mercury, this was then used to prepare further solutions of 20, 100, 500, and 750 ppm by serial dilutions. Activated carbon (measured at 594 m^2 g^{-1}) and 1K-S-DCPD-750 were coarsely ground and screened through a 45 mesh sieve to ensure particles no larger than 350 microns. 12 mL of each solution was decanted into a series of glass vials along with either 15, 30, or 60 mg of 1K-S-DCPD or activated carbon (for the Hg tests), or 10, 20, 40 and 80 mg (for the Au tests). The vials were then capped and placed on a roller for 1 h at room temperature. After 1 h, the vials were removed and the test solutions filtered into clean sample vials using a 0.22 µm filter and a polypropylene syringe. Samples were analysed along with a water blank and a 1000 ppm control sample using the same calibration method on the ICP-OES, with the data being corrected post collection. The data were fitted to a Langmuir isotherm, $q_A = (K \times C_e \times Q_{sat})/(1+K \times C_e)$, where q_A = mg adsorbate per g adsorbent (mg g^{-1}), K = adsorption parameter (L mg^{-1}), C_e = equilibrium concentration (mg L^{-1}) and Q_{sat} = maximum capacity (mg g^{-1}).

Other Metal Ion Uptakes

Tests were carried out on a range of other metals to determine if the high uptake of mercury on 1K-S-DCPD-750 was a function of the sulfur loading, or merely the higher surface area. 100 ppm solutions (50 mL) of copper, cobalt, nickel, chromium, manganese, and iron were made up from stock solutions respective metal salts (copper(II) nitrate hydrate, cobalt(II) nitrate hexahydrate, nickel(II) nitrate hexahydrate, chromium(III) nitrate nonahydrate, manganese(II) chloride tetrahydrate, and iron(III) chloride hexahydrate) and DI water. Activated carbon and 1K-S-DCPD-750 were coarsely ground and screened through a 45 Mesh sieve to ensure that all tests would contain particles no larger than 350 microns. 15 mL plastic vials were loaded with 30 mg of either 1K-S-DCPD-750 or activated

carbon and 12 mL of the chosen metal solution, the tubes were then capped and placed on a roller for 1 h at room temperature. Multiple metals were tested at a time by conducting tests in parallel. After 1 h, the vials were removed and stood in a rack to allow the particulates to settle, whilst a 1 mL aliquot was removed for analysis. The samples were diluted by a factor of 10 by adding the 1 mL aliquots each to a vial containing 9 mL of DI water. Samples were analysed along with a water blank and 100 ppm control samples of each metal using the same calibration method on the ICP-OES, with the data being corrected post collection.

6.4 Results and Discussion

6.4.1 Design and Porosity of S-Doped Carbons

S-DCPD was initially carbonised under a flow of nitrogen at 750 °C for 1 h as a direct comparison with the previously reported carbonised inverse vulcanised polymer,[36] and the product was denoted as S-DCPD-750-1. This material became microporous with a surface area of 403 $m^2 g^{-1}$. A yellow powder appeared in the tube furnace exhaust due to the leaching of elemental sulfur, and the resultant material was a shiny grey-black monolith (**Figure 6.2**).

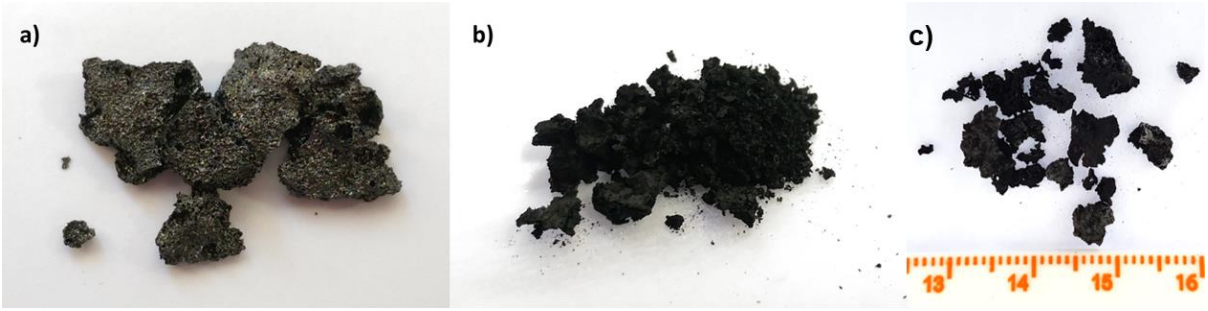

Figure 6.2 Photographs of (a) directly carbonised S-DCPD resulting in a large grey metallic monolith and (b) KOH activated S-DCPD carbon black powder. (c) Additional photo of S-DCPD showing scale (graduations are mm) to allow observation of particle size.

With the aim of increasing the surface areas, S-DCPD was also carbonised for 2 h at 750 °C and 850 °C, denoted as S-DCPD-750-2 and S-DCPD-850, respectively. The nitrogen sorption isotherms for S-DCPD-750-1 and S-DCPD-750-2 were very similar (**Figure 6.3**); both exhibited Type Ia behaviour with most of the nitrogen uptake occurring at $P/P_0 < 0.02$, which indicates the presence of narrow micropores (**Figure 6.4**). The surface area of S-DCPD-750-2 was 415 $m^2 g^{-1}$, comparable with that obtained for S-DCPD-750-1. S-DCPD-850 also showed a Type Ia isotherm but has a somewhat larger

gas uptake in the microporous region, resulting in a higher surface area of 511 m^2 g^{-1}. These surface areas are comparable to previously reported carbonised inverse vulcanised polymers,[36] but are somewhat low for many applications.

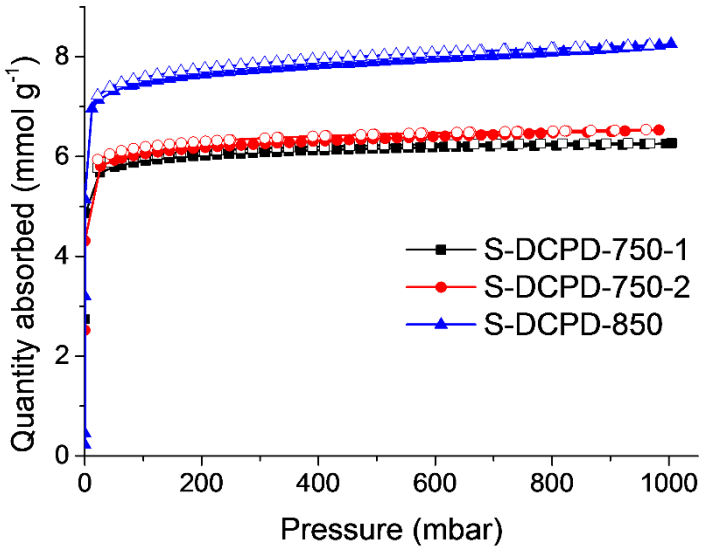

Figure 6.3 Nitrogen adsorption–desorption isotherms of directly carbonised S-DCPD at 77.3 K (the adsorption and desorption branches are labelled with filled and empty symbols, respectively).

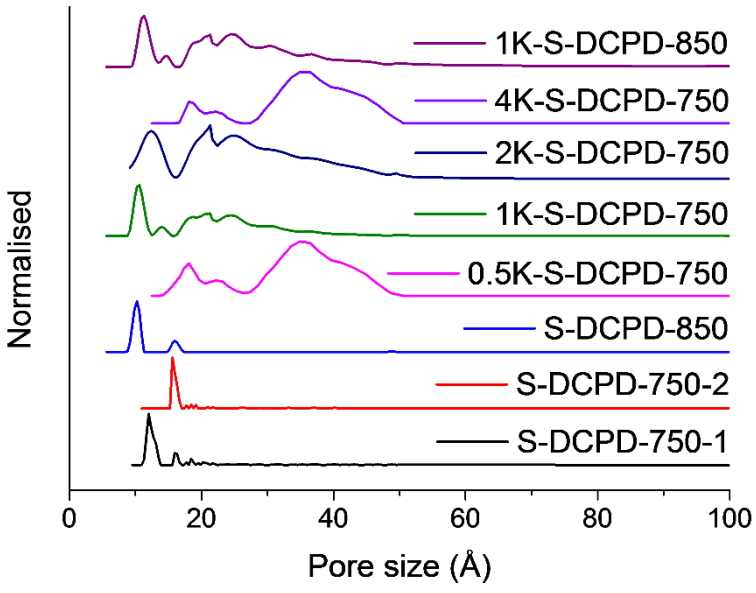

Figure 6.4 Pore size distributions of carbonised S-DCPD calculated by NL-DFT, from the nitrogen sorption isotherms. It can be seen that without KOH present, only micropores are generated (<2 nm). However, addition of KOH also generates mesopores (2–50 nm), therefore creating hierarchical porosity.

Therefore, an alternative carbonisation approach was adopted with the aid of KOH as a chemical activating agent to target higher surface area S-doped carbons. It is known that the use of KOH aids in porosity generation via the reaction 6 KOH + 2 C → 2 K + 3 H_2 + 2 K_2CO_3, followed by the production of CO_2 through the decomposition of K_2CO_3 which generates further porosity.[39]

S-DCPD was synthesised and thoroughly mixed with varying amounts of KOH before being carbonised under a nitrogen flow for 2 h (**Scheme 6.2**). The carbons are referred to as *n*K-S-DCPD-Δ where *n* is the weight ratio of KOH to S-DCPD and Δ signifies the carbonisation temperature.

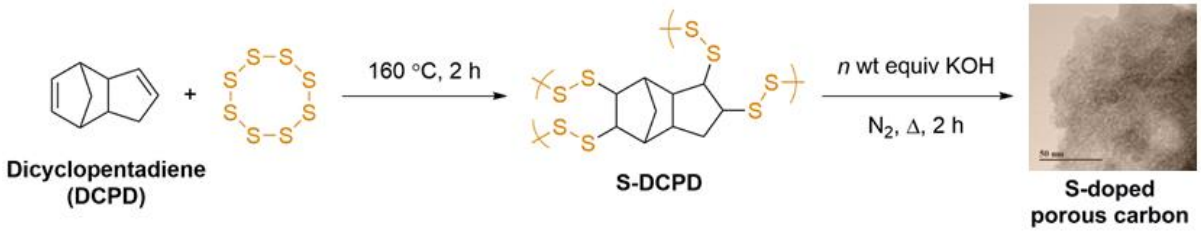

Scheme 6.2 Synthesis of the inverse vulcanised polymer and subsequent carbonisation method.

TGA curves of a representative sample indicated a residual mass of 1.5% (**Figure 6.5**), which is normal for KOH activated carbons.[40]

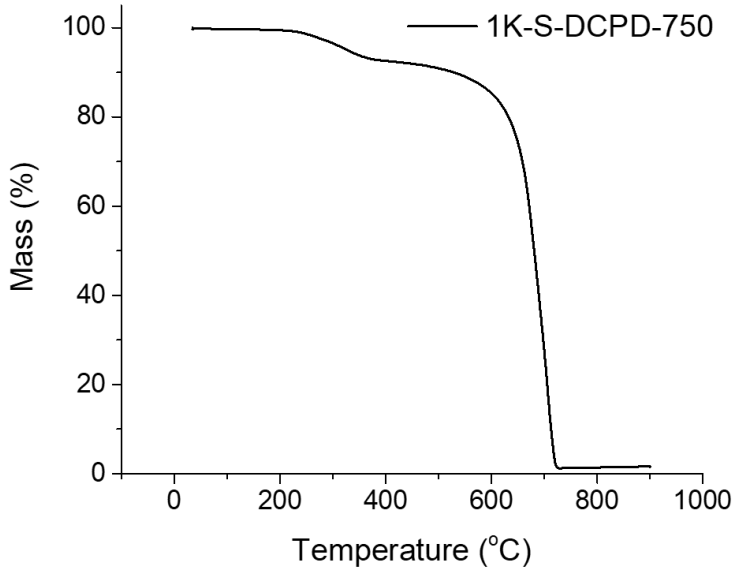

Figure 6.5 TGA analysis of inverse vulcanised polymer-derived activated carbon heated in air.

The nitrogen sorption isotherms of the KOH-activated carbonised S-DCPD showed high levels of microporosity in all samples (**Figure 6.6**). The physical properties of these carbons are summarised in **Table 6.1**.

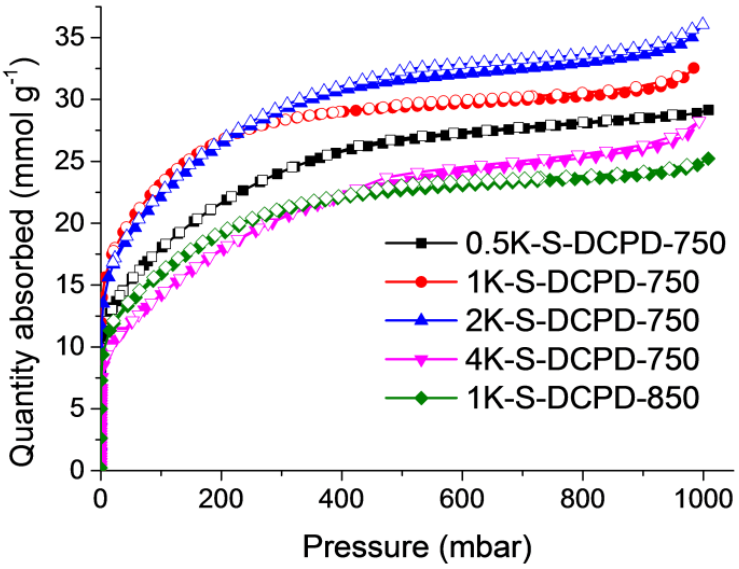

Figure 6.6 Nitrogen adsorption–desorption isotherms of KOH activated S-DCPD carbons at 77.3 K (the adsorption and desorption branches are labelled with filled and empty symbols, respectively).

Table 6.1 Physical properties of S-DCPD carbons.

		Pore volume[b] (cm^3 g^{-1})			Elemental analysis (%)		
Sample	Surface area (m^2 g^{-1})[a]	Total pore volume	Micropore volume	Yield (%)	C	H	S
S-DCPD-750-1	403	0.21	0.20	36	75.85	0.66	18.16
S-DCPD-750-2	415	0.21	0.21	35	77.25	0.63	17.67
S-DCPD-850	511	0.28	0.25	32	81.86	0.50	11.89
0.5K-S-DCPD-750	1792	1.00	0.51	23	74.91	0.35	13.54
1K-S-DCPD-750	2216	1.09	0.80	34	74.14	0.55	13.27
2K-S-DCPD-750	2197	1.21	0.68	14	78.37	0.95	12.77
4K-S-DCPD-750	1520	0.92	0.26	16	77.98	0.55	12.73
1K-S-DCPD-850	1599	0.84	0.48	34	69.40	0.87	9.55

[a] BET surface area. [b] Calculated by single point pore volume.

0.5K-S-DCPD-750 showed a Type Ib isotherm indicating high levels of microporosity with pore size distributions over a broader range compared with the directly carbonised samples (**Figure 6.4**). As the KOH to S-DCPD ratio was increased to 1:1 in 1K-S-DCPD-750, the nitrogen sorption increases, especially in the $P/P_0 < 0.02$ microporous region, resulting in a higher micropore volume (0.80 *vs.* 0.51 cm^3 g^{-1}) and an increase in surface area (2216 m^2 g^{-1} *vs.* 1792 m^2 g^{-1}). Further increases in the KOH quantity in 2K-S-DCPD-750 and 4K-S-DCPD-750 resulted in some Type IVa character, where a hysteresis loop gradually appeared at $P/P_0 = 0.5$ indicative of the development of mesopores. The surface area values for these hierarchically-porous materials were 2197 and 1520 m^2 g^{-1}, respectively.

The micropore percentage fell from 73% in 1K-S-DCPD-750 to 56% in 2K-S-DCPD-750, and 28% in 4K-S-DCPD-750, perhaps because of an oversaturation of the KOH activating agent causing micropore collapse. Since S-DCPD contains 50 wt% sulfur, smaller quantities of KOH activating agent are required compared with conventional carbonisations, where the precursor contains a much higher carbon content.[41] Higher carbonisation temperatures (850 °C) were also tested with 1K-S-DCPD-850 since it is known that higher surface areas can be achieved with temperature optimisation,[42] but the resulting carbon yielded a Type Ib isotherm with a surface of 1599 $m^2 g^{-1}$. The carbonised S-DCPD materials retain a significant amount of their parent sulfur heteroatom in their structure—up to 18.16 wt%—showing that incorporation of sulfur into the porous carbon is possible when using inverse vulcanised polymers as a carbonisation precursor (**Table 6.1**). The surface area of 2216 $m^2 g^{-1}$ for 1K-S-DCPD-750 outperforms other microporous S-doped carbons,[43] including carbonisation precursors that were inherently porous and more costly.[44]

6.4.2 Characterisation of Inverse Vulcanised Polymer-Derived Carbons

FE-SEM and TEM was used to study the morphology of carbonised S-DCPD products (**Figure 6.7**). The shiny, monolithic structure from directly carbonising S-DCPD in S-DCPD-850 is shown in **Figure 6.7a**. The observed structure was smooth with few signs of pores on the surface. TEM of the sample also backed up this observation since the white spots that are typically indicative of pores were not apparent (**Figure 6.7b**). The KOH-activated carbonised product, 1K-S-DCPD-750, was a black powder (**Figure 6.2b**) and its rough, particulate surface was apparent under FE-SEM (**Figure 6.7c&e**). As made, the particle size is in the mm-cm range (**Figure 6.2c**), though the powder can be easily sieved/ground to fractionate into a desired size range.

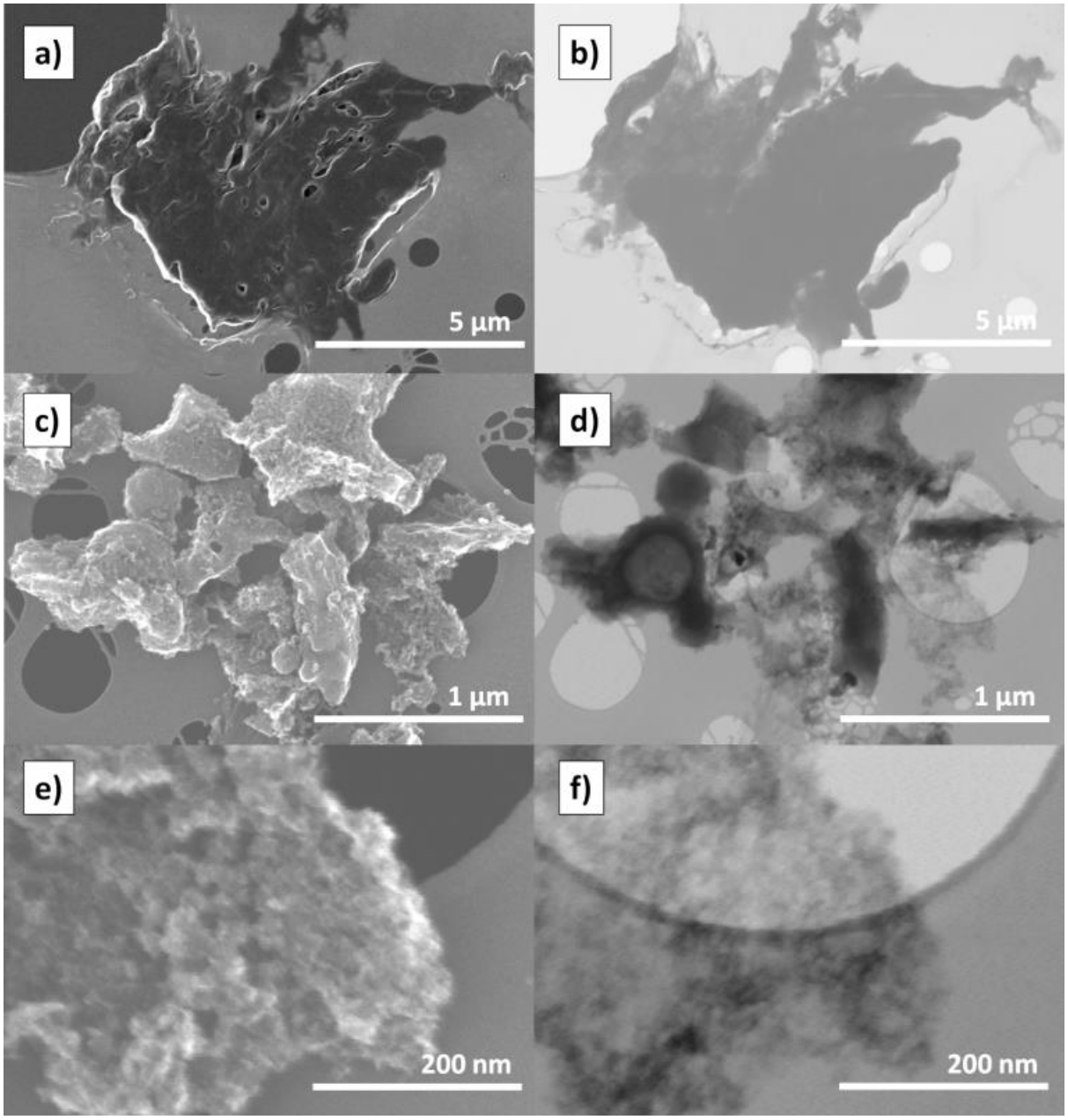

Figure 6.7 FE-SEM images of (a) S-DCPD-850 and (c) 1K-S-DCPD-750. TEM images of (b) S-DCPD-850 and (d) 1K-S-DCPD-750. Higher (e) FE-SEM and (f) TEM magnification of 1K-S-DCPD-750.

Bulk density was determined by measuring the volume and mass of tamped powder in a graduated glass cylinder. The bulk density of the1K-S-DCPD-750 depends on the particle size and packing, but is in the range of 0.4–0.5 g cm^{-3}, comparable to other activated carbons. The skeletal density, measured by nitrogen pycnometry, is 2.2 g cm^{-3}, slightly higher than is usual for activated carbons, which tend to be between 2.0 and 2.1 g cm^{-3}. However, this increase in density could be attributed to the higher mass of sulfur relative to carbon. The TEM of the KOH-activated porous carbon indicated high porosity, showing lower density structure compared to the non-activated sample (**Figure 6.7d&f**). HR-TEM

showed that KOH-activation resulted in a more fibrous network, presumably as a result of its greater porosity (**Figure 6.8**). The morphology of the KOH-activated sample was also observed to be more homogeneous when scanning across the material compared to the directly carbonised sample, which can be advantageous.

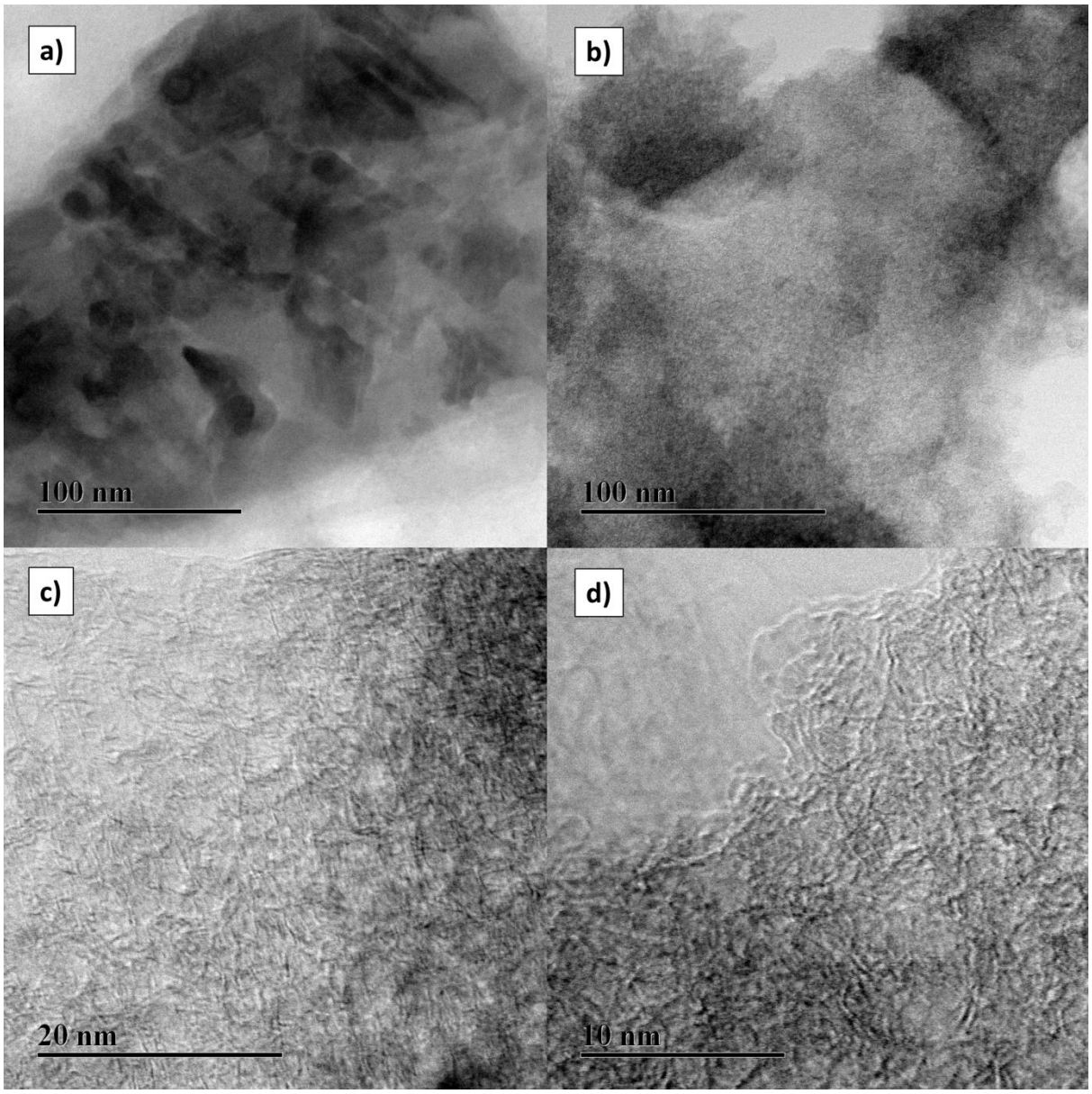

Figure 6.8 HR-TEM images of (a) S-DCPD-850 and (b) 1K-S-DCPD-750 with higher resolution images of 1K-S-DCPD-750 at (c) 20 nm and (d) 10 nm scale.

PXRD patterns of the carbonised products showed two broad characteristic peaks located at 25 and 43° (**Figure 6.9**), corresponding to the (002) and (100) planes of hexagonal graphite, respectively, revealing the presence of an amorphous structure and a low degree of graphitisation.[45]

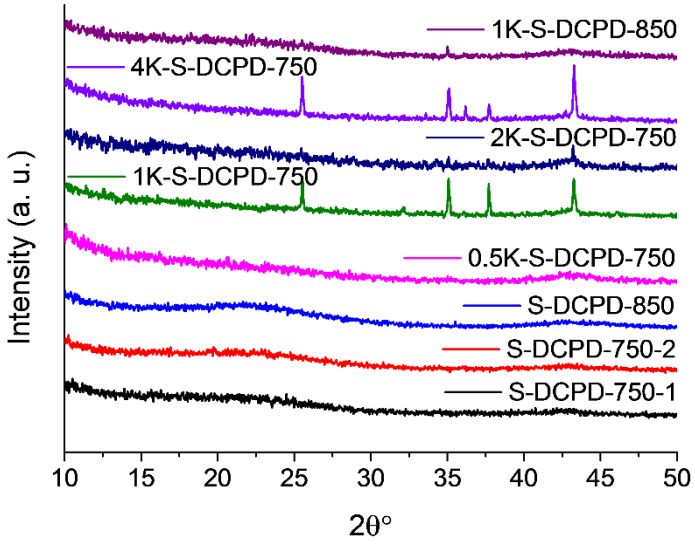

Figure 6.9 PXRD patterns of carbonised S-DCPD samples. Samples 1K-S-DCPD-750 and 4K-S-DCPD-750 contain additional alumina peaks at 26°, 35°, 37°, and 43° associated from the ceramic boat and/or use of pestle and mortar.

6.4.3 CO_2, CH_4, and H_2 Storage Properties of Inverse Vulcanised Polymer-Derived Carbons

Gas sorption isotherms of CO_2, CH_4, and H_2 with the S-DCPD carbons were studied (**Figure 6.10**). The CO_2 uptakes for the KOH-activated materials were tested at room temperature (298 K) with the full isotherms shown in **Figure 6.10a**. **Table 6.2** summarises the amount of CO_2 absorbed by each material at a pressure of 1 bar.

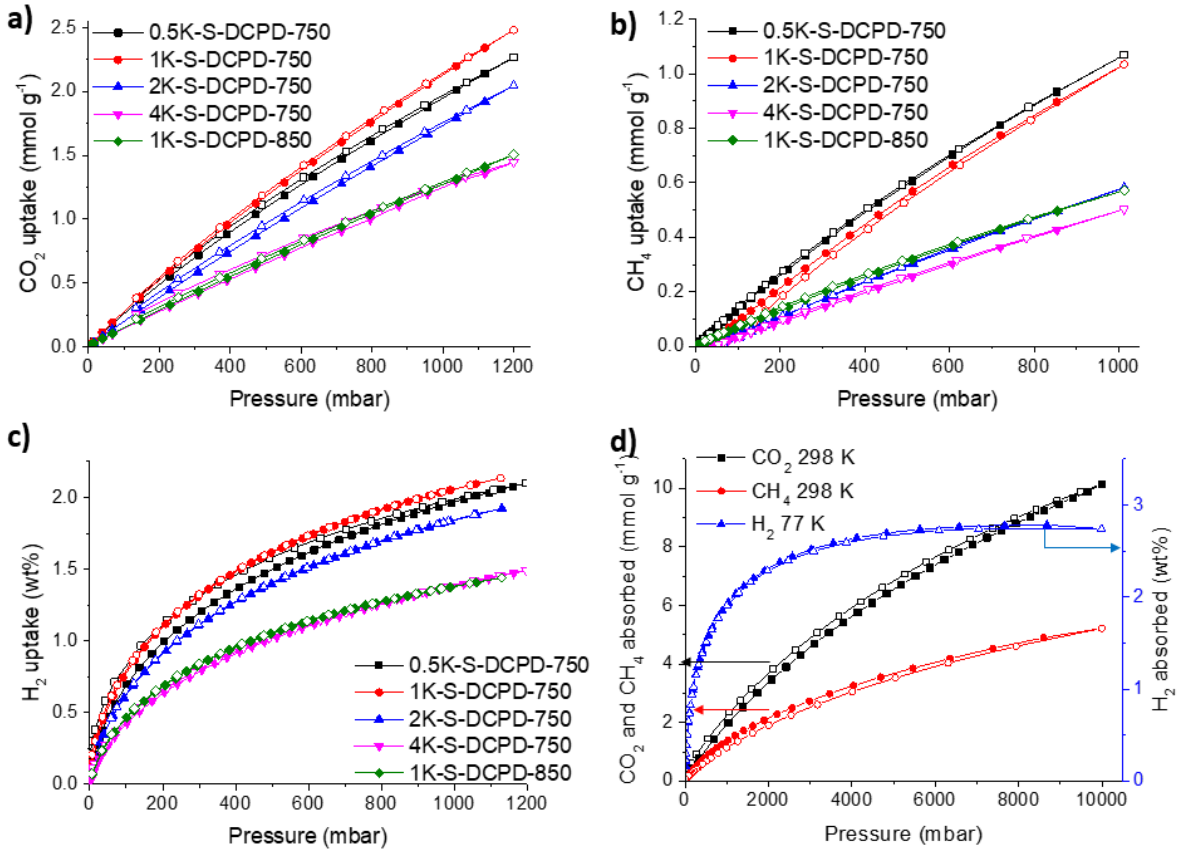

Figure 6.10 (a) CO_2 sorption isotherms at 298 K over pressure range 0–1 bar. (b) CH_4 sorption isotherms at 298 K over pressure range 0–1 bar. (c) H_2 sorption isotherms at 77 K over pressure range 0–1 bar. (d) CO_2 and CH_4 sorption isotherms at 298 K and H_2 sorption isotherms at 77 K of 1K-S-DCPD-750 over pressure range 0–10 bar. The adsorption and desorption branches are labelled with filled and empty symbols, respectively.

Table 6.2 BET surface area, H_2, CO_2, and CH_4 uptake of KOH activated S-DCPD carbons.

		Gas uptake		
Sample	Surface area ($m^2\ g^{-1}$)[a]	CO_2[b] (mmol g^{-1})	CH_4[c] (mmol g^{-1})	H_2[d] (wt%)
0.5K-S-DCPD-750	1792	2.01	1.07	1.99
1K-S-DCPD-750	2216	2.20	1.03	2.09
2K-S-DCPD-750	2197	1.79	0.58	1.88
4K-S-DCPD-750	1520	1.29	0.50	1.40
1K-S-DCPD-850	1599	1.31	0.57	1.41

[a] BET surface area. [b] CO_2 uptake at 298 K and 1 bar. [c] CH_4 uptake at 298 K and 1 bar. [d] H_2 uptake at 77 K and 1 bar.

The CO_2 uptake was roughly proportional to the surface area of each material, with a CO_2 uptake of up to 2.20 mmol g^{-1} for 1K-S-DCPD-750, outperforming recent reports of sulfur-containing microporous polymers,[37] previous carbonised inverse-vulcanised polymers,[27] sulfur-containing hypercrosslinked microporous polymers,[46] and microporous networks: COF-6,[47] CMP-1,[48] and highly porous PAF-1.[49] The CH_4 sorption behaviour was also tested at 298 K and 1 bar with an uptake of up to 1.07 mmol g^{-1} for 0.5K-S-DCPD-750 (**Figure 6.10b**). H_2 uptakes tested at 77 K and 1 bar were high with all KOH-activated samples, with an uptake of 2.09 wt% observed from 1K-S-DCPD-750 (**Figure 6.10c**). The large uptakes are due to H_2 being purely attracted to a large surface via physisorption as a result of weak van der Waals interactions. The H_2 uptake is more than three times larger than the previously reported carbonised inverse vulcanised polymers; this a dramatic improvement for this cheap synthetic method,[36] although more striking results were found at higher gas pressures. The absorption of small gases were evaluated at pressures of up to 10 bar for the best performing sample, 1K-S-DCPD-750 (**Figure 6.10d**). This material adsorbed up to 10.1 mmol g^{-1} of CO_2 at 298 K with no sign of saturation, matching and outperforming more costly materials such as carbonised polyacrylonitrile AC-3000,[50] mesoporous silica templated carbon IBN-9,[51] and directly carbonised MOF-74 and MIL-53.[52] 1K-S-DCPD-750 adsorbs 2.74 wt% H_2 at 77 K and 10 bar, outperforming industrial BPL activated carbon,[47] and exceeding porous carbons 12ACA-800 (made from carbon aerogel via subcritical drying),[53] AC-C4 (activated at very high temperatures with further activation using CO_2 gas),[54] and even porous carbons measured at high pressures of over 60 bar.[55]

6.4.4 Heavy Metal Ion Capture Studies with the Inverse Vulcanised Polymer-Derived Carbon

The S-doping in the structure of these microporous carbons may have further benefits, such as providing anchor sites for metal catalysts. The combination of high surfaces areas, hierarchical porosity, and high sulfur loading is also very attractive for the removal of trace heavy metal ions from water. Mercury pollution from industrial wastewater is a significant global health concern because of its relatively high solubility in water and tendency to bioaccumulate and cause severe toxic effects.[56] Sulfur is known to have a high affinity for mercury, and therefore 1K-S-DCPD-750 was tested for the capture of $HgCl_2$ from water (**Figure 6.11**). The material was tested against a commercial activated carbon, DARCO® FGL, a lignite coal-based activated carbon which is manufactured specifically for the removal of heavy metal ions and other contaminants from gas emission streams. The physical properties of the activated carbon are listed in **Table 6.3**.

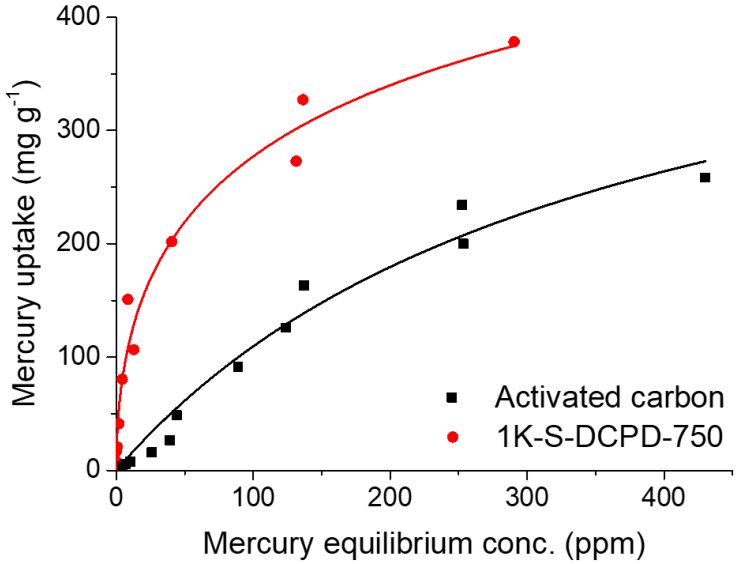

Figure 6.11 The adsorption isotherm of mercury (as aqueous $HgCl_2$) into samples of conventional activated carbon and carbonised sulfur polymer, with Langmuir isotherm fittings.

Table 6.3 Physical properties of DARCO® FGL activated carbon.

Sample	Surface area (m^2 g^{-1})[a]	Pore volume (cm^3 g^{-1})[b]		Bulk density (g cm^{-3})[c]
		Total pore volume	Micropore volume	
DARCO® FGL	594	0.40	0.22	0.63

[a] BET surface area. [b] Calculated by single point pore volume. [c] Tamped apparent.

1K-S-DCPD-750 showed a greatly enhanced uptake of mercury in comparison to activated carbon, especially at low mercury concentrations. The higher uptake of Hg by 1K-S-DCPD-750 is not simply a result of the higher surface area, as this enhancement is not observed with other metals (**Figure 6.12**), but instead is a result of the incorporation sulfur functional groups.

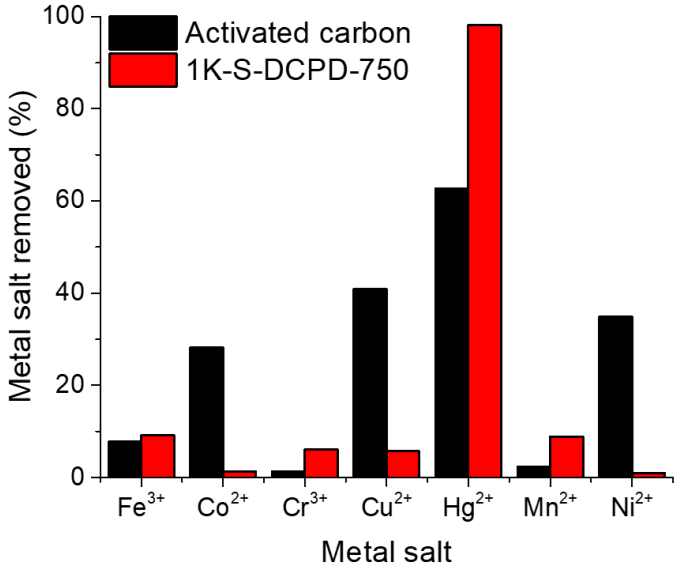

Figure 6.12 Metal ion uptake of conventional activated carbon and carbonised sulfur polymer (30 mg) for a series of metal salts (100 ppm, 12 mL). The higher uptake of the activated carbon for many of the metals suggests that the higher metal uptake of 1K-S-DCPD-750 for Hg is not merely a function of its higher surface area, but is instead related to the specific affinity of Hg with the sulfur present in the material.

Activated carbons are frequently used for the adsorption of mercury ions from wastewater, and they generally show maximum Hg uptakes in the ~10–500 mg g^{-1} range.[57] Activated carbons post-synthetically doped with sulfur tend to also fall within this range, *e.g.*, a recent optimisation study on commercially available activated carbon impregnated with sulfur showed a maximum adsorption capacity of 294 mg g^{-1}.[58] At an equilibrium Hg concentration of ~10 ppm, 1K-S-DCPD-750 absorbed over 15 times more Hg than the activated carbon control (151 mg g^{-1} *vs.* 7.8 mg g^{-1}). Fitting these data to a Langmuir isotherm also indicated a higher maximum saturation capacity for the sulfur loaded material (850 mg g^{-1} *vs.* 498 mg g^{-1}) and adsorption parameters that were over 20 times higher (0.058 L mg^{-1} *vs.* 0.0028 mg g^{-1}). Absorption of mercury ions at low concentrations (<1 mg g^{-1}) has particular practical relevance. For example, the Environmental Protection Agency has set a maximum contaminant level goal for mercury of 0.002 mg L^{-1}, or 1 x 10^{-6} mg g^{-1}.[59]

The precipitation of gold from chloride solutions by activated carbon is of interest not only for the recovery and concentration of gold in hydrometallurgical extraction, but also in catalysis, electronics, and biotechnology.[3] This higher surface area, and specific affinity of the incorporated sulfur for Au ions, gives the 1K-S-DCPD-750 a much higher uptake of gold in comparison to a standard activated carbon (**Figure 6.13**). Fitting these data to a Langmuir isotherm gave saturation capacities of 1497 mg g^{-1} for the sulfur loaded material compared to 541 mg g^{-1} for standard activated carbon, with corresponding adsorption parameters of 1.3 L mg^{-1} and 0.6 L mg^{-1}, respectively.

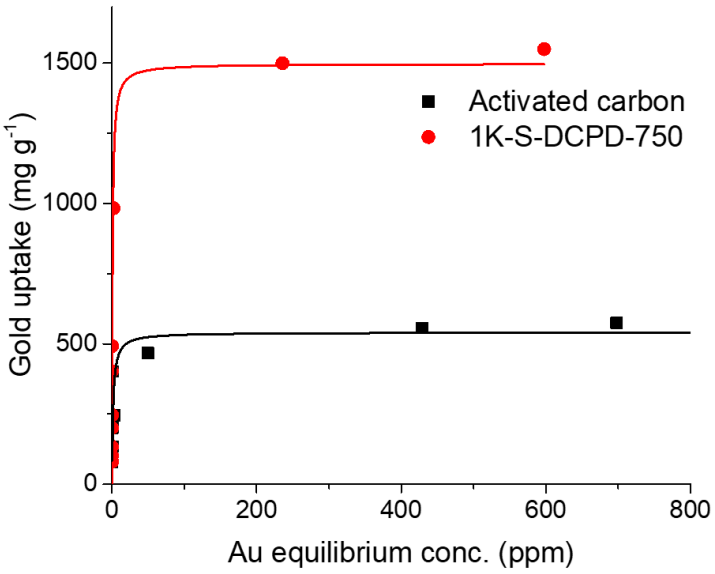

Figure 6.13 The adsorption isotherm of gold (as aqueous $HAuCl_4$) into samples of conventional activated carbon and carbonised sulfur polymer, with Langmuir isotherm fittings.

6.5 Conclusions and Outlook

Porous carbons with surface areas greater than 2200 m^2 g^{-1} with high levels of S-doping have been produced from inverse vulcanised polymers. Synthesis was performed from starting materials that consist entirely of low-cost industrial by-products; sulfur and DCPD trade at ~100 and ~800 $ per tonne, respectively; matching that of commercial activated carbons (350–3200 $ per tonne). The use of KOH as a chemical activating agent resulted in vastly improved porosity and morphology. The resultant carbons show attractive properties for small gas adsorption, outperforming many commercial porous materials, particularly at higher pressures. The materials show mercury ion capture potential in the practically-relevant, low-concentration range. Up to 150% of the materials weight in gold can be adsorbed from solution; this is three times the capacity seen for common activated carbon. The applicability of these porous S-doped carbons should not only be limited to gas sorption and water purification materials; they are also potentially relevant as catalyst supports, in lithium-sulfur batteries, and as supercapacitors. There is great scope for variation in the organic crosslinkers used in inverse vulcanisation and, with further optimisation of the carbonisation process, this new route to microporous S-doped carbons should yield a range of scalable materials with improved properties in the future.

6.6 References

[1] S. S. Konyratbekova, A. Baikonurova, A. Akcil, *Min. Proc. Ext. Met. Rev*. **2015**, *36*, 198.

[2] J. Cui, L. Zhang, *J. Hazard. Mater.* **2008**, *158*, 228.

[3] S. I. Tsyganova, V. V. Patrushev, G. N. Bondarenko, *Russ. J. Appl. Chem*. **2013**, *86*, 534.

[4] Coal, International Energy Agency. Retrieved from https://www.iea.org/about/faqs/coal/

[5] S. Ansolobehere, J. Beer, J. Deutch, A. D. Ellerman, J. Friedman, H. Herzog, H. Jacoby, P. Joskow, G. McRae, R. Lester, E. Moniz, E. Steinfeld, *The Future of Coal: Options for a Carbon-Constrained World, an interdisciplinary MIT study*, Massachusetts Institute of Technology, **2007**.

[6] X. Guo, C.-G. Zheng, M. Xu, *Energy Fuels* **2007**, *21*, 898.

[7] N. Pirrone, S. Cinnirella, X. Feng, R. B. Finkelman, H. R. Friedli, J. Leaner, R. Mason, A. B. Mukherjee, G. B. Stracher, D. G. Streets, K. Telmer, *Atmos. Chem. Phys*. **2010**, *10*, 5951.

[8] Coal consumption, BP Global. Retrieved from https://www.bp.com/en/global/corporate/energy-economics/statistical-review-of-world-energy/coal/coal-consumption.html

[9] J. A. Sorensen, G. E. Glass, K. W. Schmidt, J. K. Huber, G. R. Rapp, *Environ. Sci. Technol.* **1990**, *24*, 1716.

[10] B. Fernandes Azevedo, L. Barros Furieri, F. M. Pecanha, G. A. Wiggers, P. Frizera Vassallo, M. Ronacher Simoes, J. Fiorim, P. Rossi de Batista, M. Fioresi, L. Rossoni, I. Stefanon, M. J. Alonso, M. Salaices, D. Valentim Vassallo, *J. Biomed. Biotechnol.* **2012**, *2012*, 11.

[11] A. Dąbrowski, Z. Hubicki, P. Podkościelny, E. Robens, *Chemosphere* **2004**, *56*, 91.

[12] S. Vigneswaran, H. H. Ngo, D. S. Chaudhary, Y.-T. Hung, in *Physicochemical Treatment Processes*, (Eds: L. K. Wang, Y.-T. Hung, N. K. Shammas), Humana Press, Totowa, NJ **2005**, 635.

[13] N. Dizge, B. Keskinler, H. Barlas, *J. Hazard. Mater.* **2009**, *167*, 915.

[14] H. Y. Shim, K. S. Lee, D. S. Lee, D. S. Jeon, M. S. Park, J. S. Shin, Y. K. Lee, J. W. Goo, S. B. Kim, D. Y. Chung, *J. Agric. Chem. Environ.* **2014**, *3*, 130.

[15] P. H. Wolf, S. Siverns, S. Monti, *Desalination* **2005**, *182*, 293.

[16] T. A. Kurniawan, G. Y. S. Chan, W.-H. Lo, S. Babel, *Chem. Eng. J.* **2006**, *118*, 83.

[17] F. Fu, Q. Wang, *J. Environ. Manage.* **2011**, *92*, 407.

[18] S. Babel, T. A. Kurniawan, *Chemosphere* **2004**, *54*, 951.

[19] M. A. Barakat, *Arab. J. Chem.* **2011**, *4*, 361.

[20] I. Diamantopoulou, G. Skodras, G. P. Sakellaropoulos, *Fuel Process. Technol*. **2010**, *91*, 158.

[21] W. Kiciński, M. Szala, M. Bystrzejewski, *Carbon* **2014**, *68*, 1.

[22] D.-W. Wang, Q. Zeng, G. Zhou, L. Yin, F. Li, H.-M. Cheng, I. R. Gentle, G. Q. M. Lu, *J. Mater. Chem. A* **2013**, *1*, 9382.

[23] S. R. Shewchuk, R. Azargohar, A. K. Dalai, *J. Environ. Anal. Toxicol*. **2016**, *6*, 379.

[24] F. Ke, L.-G. Qiu, Y.-P. Yuan, F.-M. Peng, X. Jiang, A.-J. Xie, Y.-H. Shen, J.-F. Zhu, *J. Hazard. Mater*. **2011**, *196*, 36.

[25] K.-K. Yee, N. Reimer, J. Liu, S.-Y. Cheng, S.-M. Yiu, J. Weber, N. Stock, Z. Xu, *J. Am. Chem. Soc*. **2013**, *135*, 7795.

[26] B. Li, Y. Zhang, D. Ma, Z. Shi, S. Ma, *Nat. Comm*. **2014**, *5*, 5537.

[27] J. J. Griebel, R. S. Glass, K. Char, J. Pyun, *Prog. Polym. Sci.* **2016**, *58*, 90.

[28] W. J. Chung, J. J. Griebel, E. T. Kim, H. Yoon, A. G. Simmonds, H. J. Ji, P. T. Dirlam, R. S. Glass, J. J. Wie, N. A. Nguyen, B. W. Guralnick, J. Park, A. Somogyi, P. Theato, M. E. Mackay, Y.-E. Sung, K. Char, J. Pyun, *Nat. Chem*. **2013**, *5*, 518.

[29] M. Arslan, B. Kiskan, Y. Yagci, *Macromolecules* **2016**, *49*, 767.

[30] M. J. H. Worthington, R. L. Kucera, J. M. Chalker, *Green Chem.* **2017**, *19*, 2748.

[31] D. A. Boyd, *Angew. Chem., Int. Ed.* **2016**, *55*, 15486.

[32] J. J. Griebel, S. Namnabat, E. T. Kim, R. Himmelhuber, D. H. Moronta, W. J. Chung, A. G. Simmonds, K. J. Kim, J. van der Laan, N. A. Nguyen, E. L. Dereniak, M. E. Mackay, K. Char, R. S. Glass, R. A. Norwood, J. Pyun, *Adv. Mater*. **2014**, *26*, 3014.

[33] A. G. Simmonds, J. J. Griebel, J. Park, K. R. Kim, W. J. Chung, V. P. Oleshko, J. Kim, E. T. Kim, R. S. Glass, C. L. Soles, Y. E. Sung, K. Char, J. Pyun, *ACS Macro Lett*. **2014**, *3*, 229.

[34] M. P. Crockett, A. M. Evans, M. J. H. Worthington, I. S. Albuquerque, A. D. Slattery, C. T. Gibson, J. A. Campbell, D. A. Lewis, G. J. L. Bernardes, J. M. Chalker, *Angew. Chem., Int. Ed.* **2016**, *55*, 1714.

[35] M. W. Thielke, L. A. Bultema, D. D. Brauer, B. Richter, M. Fischer, P. Theato, *Polymers* **2016**, *8*, 266; T. Hasell, D. J. Parker, H. A. Jones, T. McAllister, S. M. Howdle, *Chem. Commun.* **2016**, *52*, 5383.

[36] J. C. Bear, J. D. McGettrick, I. P. Parkin, C. W. Dunnill, T. Hasell, *Microporous Mesoporous Mater*. **2016**, *232*, 189.

[37] S. H. Je, O. Buyukcakir, D. Kim, A. Coskun, *Chem* **2016**, *1*, 482.

[38] D. J. Parker, H. A. Jones, S. Petcher, L. Cervini, J. M. Griffin, R. Akhtar, T. Hasell, *J. Mater. Chem. A* **2017**, *5*, 11682.

[39] S. J. Yang, H. Jung, T. Kim, C. R. Park, *Prog. Nat. Sci. Mater*. **2012**, *22*, 631.

[40] M. Cox, R. Mokaya, *Sus. Energ. Fuels* **2017**, *1*, 1414.

[41] Y. Li, T. Ben, B. Zhang, Y. Fu, S. Qiu, *Sci. Rep.* **2013**, *3*, 2420.

[42] J.-S. M. Lee, M. E. Briggs, T. Hasell, A. I. Cooper, *Adv. Mater.* **2016**, *28*, 9804.

[43] Y. Xia, Y. Zhu, Y. Tang, *Carbon* **2012**, *50*, 5543.

[44] J. P. Paraknowitsch, A. Thomas, J. Schmidt, *Chem. Commun*. **2011**, *47*, 8283.

[45] L. Qie, W.-M. Chen, Z.-H. Wang, Q.-G. Shao, X. Li, L.-X. Yuan, X.-L. Hu, W.-X. Zhang, Y.-H. Huang, *Adv. Mater.* **2012**, *24*, 2047.

[46] S. K. Kundu, A. Bhaumik, *ACS Sustain. Chem. Eng.* **2016**, *4*, 3697.

[47] H. Furukawa, O. M. Yaghi, *J. Am. Chem. Soc.* **2009**, *131*, 8875.

[48] R. Dawson, D. J. Adams, A. I. Cooper, *Chem. Sci.* **2011**, *2*, 1173.

[49] T. Ben, H. Ren, S. Ma, D. Cao, J. Lan, X. Jing, W. Wang, J. Xu, F. Deng, J. M. Simmons, S. Qiu, G. Zhu, *Angew. Chem., Int. Ed.* **2009**, *48*, 9457.

[50] T. C. Drage, J. M. Blackman, C. Pevida, C. E. Snape, *Energy Fuels* **2009**, *23*, 2790.

[51] Y. Zhao, L. Zhao, K. X. Yao, Y. Yang, Q. Zhang, Y. Han, *J. Mater. Chem.* **2012**, *22*, 19726.

[52] G. Srinivas, V. Krungleviciute, Z.-X. Guo, T. Yildirim, *Energy Environ. Sci.* **2014**, *7*, 335.

[53] C. Robertson, R. Mokaya, *Microporous Mesoporous Mater.* **2013**, *179*, 151.

[54] H. Wang, Q. Gao, J. Hu, *J. Am. Chem. Soc.* **2009**, *131*, 7016.

[55] E. Terrés, B. Panella, T. Hayashi, Y. A. Kim, M. Endo, J. M. Dominguez, M. Hirscher, H. Terrones, M. Terrones, *Chem. Phys. Lett.* **2005**, *403*, 363.

[56] L. Jarup, *Brit. Med. Bull.* **2003**, *68*, 167.

[57] P. Hadi, M. H. To, C. W. Hui, C. S. K. Lin, G. McKay, *Water Res.* **2015**, *73*, 37.

[58] K. Rashid, K. Suresh Kumar Reddy, A. A. Shoaibi, C. Srinivasakannan, *Clean Technol. Envir.* **2013**, *15*, 1041.

[59] National Primary Drinking Water Regulations United States Environmental Protection Agency. Retrieved from https://www.epa.gov/ground-water-and-drinking-water/national-primary-drinking-water-regulations#Inorganic

Chapter 7

Summary and Conclusions

In this thesis, the relationship between porosity, electrical conductivity, and chemical functionality in organic polymers and carbons was explored for supercapacitor, gas storage, and heavy metal capture applications. Although pristine porous organic polymers and inverse vulcanised polymers are exceptional materials with many inherent properties, they can have limitations in these applications. It was demonstrated that through controlled carbonisation procedures, the fundamental properties of the parent polymers could be enhanced, often dramatically.

Chapter 3 showed that we can impart electrical conductivity into non-conducting CMPs by carbonisation for supercapacitive energy storage. The porosity and functionality of pristine CMPs can be controlled through the choice of monomers. CMP-1, the first reported CMP, was chosen as the carbonisation precursor to exemplify the applicability of this carbonisation method. It was found that both the pore structure and the heteroatoms present in the parent CMP could be retained in the resultant carbon. This route allows for carbons that can have their pore structure engineered and pre-determined by the choice of carbonisation precursor. Pore structure design is especially important for the diffusion of electrolyte through the material. By optimisation of the carbonisation procedure and electrolyte choice, ideal and high-performance supercapacitors were obtained. The route presented here opens up a new method to access electro-active properties from CMPs. Further optimisation of these initial findings (*e.g.*, by choice of CMP) is expected to lead to supercapacitors with improved properties, or other electrochemical applications such as oxygen reduction reactions.

Following on from this, Chapter 4 presents the application of electrical conductivity to HCPs using a similar strategy and their performance as supercapacitors were assessed. HCPs are promising materials due to their synthetic diversity, low-cost, and scalability. Non-heteroatom (benzene), and heteroatom-containing HCPs (S: thiophene; N: pyrrole, aniline) were used as carbonisation precursors to examine their influence on the supercapacitor performance. It was found that the incorporation of N-functionality had the highest contribution to performance, followed by S-functionality, due to the pseudocapacitive contributions. The carbonisation conditions were optimised to produce two best performing materials, one strongly electric double-layer capacitive and one strongly pseudocapacitive. The first material shows fast charging kinetics and high capacitive retention with faster charging rates, while the second shows very high capacitance. The materials show ideal performance, even in a two-electrode setup, and outperform many top organic-based supercapacitors in literature. The EDLC and PC contributions of each material (20 samples) were quantified through partitioning methods and design rules were made for controlling EDLC and PC in the material synthesis. These rules are not only applicable for HCPs, but many materials in general which aim to exploit both EDLC and PC mechanisms in supercapacitors.

Chapter 5 presented a route to greatly enhance the porosity and gas storage capabilities of HCPs via chemical activated carbonisation. As discussed previously, HCPs have many positive properties and show favourable gas storage properties. However, HCPs swell with absorption which can be disadvantageous in practical applications, *e.g.*, increases the working back-pressure. Three HCPs based on benzene, thiophene, and pyrrole were chosen for this study. Through chemical activated carbonisation, both the surface areas can be increased and swelling eliminated simultaneously. This produced a highly porous carbon of over 4300 $m^2 g^{-1}$, the highest for an organic polymer-derived carbon. The material, synthesised from low-cost materials, showed record uptakes for CO_2 and H_2 at 10 bar, outperforming many expensive benchmark materials. It is likely that other HCP precursors might yield even better materials than the three tested here since the available pool of aromatic monomers is huge. Further highly porous carbons are envisioned not only as sorbents but for other applications such as energy storage, catalysis, and gas separations.

Chapter 6 presents a route to create porosity in order to allow increased efficiency and effectiveness in capturing heavy metal ions. Inverse vulcanised polymers can be produced from low-cost industrial by-products, sulfur and DCPD, which trade at ~100 and 800$ per tonne, respectively. As synthesised, inverse vulcanised polymers are dense in sulfur but have no porosity. By optimising the chemical activated carbonisation of these polymers, high surface areas materials were produced that still retain high amounts of sulfur. These high surface area S-doped carbons showed higher CO_2 and H_2 uptakes than many expensive academic materials. The most porous sample absorbed over 15 times more mercury than activated carbon in low, practically relevant concentrations in water. It was also discovered to have a gold saturation capacity of ~3 times more than activated carbon; that is up to one and a half times of the material's weight in gold. It was shown that the high uptakes were not simply a result of the higher surface area, but due to the incorporation of sulfur functional groups into the carbon. There is huge scope for variation of organic crosslinkers used in inverse vulcanisation and further optimisation of the carbonisation process built upon this route to produce scalable microporous S-doped carbons. The applicability of S-doped carbons is not limited to gas storage and water purification, but also as catalyst supports, Li-S batteries, and supercapacitors.

Overall, the research presented in this thesis highlights developments in the carbonisation of porous organic polymers and inverse vulcanised polymers towards targeted energy and environmental applications – this shows that carbon materials, while old, are far from dead. The choice of precursor and carbonisation method is key to obtaining high performing materials. It is the author's hope that many groups will build on the results presented in this thesis to achieve even better materials.